UNIVERSITY OF SOUTHAMPTON

Broad-Band Spectral Analysis of a Complete Sample of Type 1 AGN Detected by *INTEGRAL*

Manuela Molina
Submitted for the degree of Doctor of Philosophy
School Of Physics and Astronomy
FACULTY OF ENGINEERING, SCIENCE & MATHEMATICS

February 10, 2009

To my family: my mum Franca, my sister Claudia, my husband Bruno. And to my dad, Antonio, who is always in my heart.

UNIVERSITY OF SOUTHAMPTON

ABSTRACT

FACULTY OF ENGINEERING, SCIENCE & MATHEMATICS

School Of Physics and Astronomy

Doctor of Philosophy

Broad-Band Spectral Analysis of a Complete Sample of Type 1 AGN Detected by *INTEGRAL*

by Manuela Molina

This thesis contains results on type 1 Active Galactic Nuclei detected and studied with *INTEGRAL*. The sample of sources analysed in the present thesis is based on a complete sample of type 1 AGN extracted from the 3rd IBIS/ISGRI catalogue. Archival X-ray data taken from several observatories, such as *XMM-Newton*, *Chandra*, *Swift/XRT* and *ASCA*, have been combined together with IBIS spectra, providing for the first time a broad-band spectral analysis of a hard X-ray detected complete sample of type 1 AGN. The principal aim of this work is to study the continuum properties of type 1 AGN, i.e. power law slope, reflection fraction and high energy cut-off, and their relation to spectral modelling of AGN and to synthesis models of the Cosmic Diffuse X-ray Background.

The analysis presented in this work covers two subclasses of type 1 AGN: Broad Line Radio Galaxies (BLRG) and Radio Quiet (RQ) type 1 sources. In particular, among BLRG, IGR J21247+5058 is studied in great depth (see chapter 5). This is in fact a very peculiar source, displaying very complex absorption, in the form of two layers partially covering the central emitting source. So far, only one other BLRG was known to require such complexity regarding absorption (namely 4C 445), making IGR J21247+5058 indeed a very peculiar and almost unique AGN.

Broad-band spectra of the other seven BLRG present in the *INTEGRAL* complete sample have been analysed in search for a dichotomy between this population (chapter 6) and their radio quiet counterparts (chapter 7). Several studies have in fact shown in the past that BLRG might behave differently than radio quiet AGN, displaying weaker reprocessing features (i.e. the reflection component and the strength of the iron line), possibly associated with the presence of the jet. In the present study, however, such diversity is not found to be very striking, with the reprocessing features of the analysed sources not being as weak as expected. This could imply a different scenario for the dilution of these features, not involving a jet but rather a different geometry and/or accretion flow efficiency in the accretion disk.

The analysis of the complete sample of type 1 AGN also allows a general picture of the average properties of this class of sources to be obtained. The mean power law slope is found to be Γ=1.86±0.01, in good agreement with the generally accepted canonical spectral index of 1.9. The average cut-off energy is E_c=104 keV, lower than previously found in other works; the mean reflection fraction is 1.08±0.14. Correlations between the spectral parameters have also been investigated, but most of them remain still to be proven. When considering these results in the framework of AGN spectral modelling, we found that the average Comptonising plasma temperature is typically $\sim$50 keV with an optical depth ranging from 2 to 5, i.e. the plasma is not too thick. As far as the Cosmic X-ray Diffuse Background is concerned, synthesis models have so far assumed a spectral shape for the CXB with Γ=1.9 with no dispersion in values and a high energy cut-off of at least 200 keV. However, the value of Γ=1.86 with a dispersion of 0.2 and a cut-off energy with a narrow range of values around 100 keV, as found in the present thesis, could provide a self-consistent modelling of the CXB. The implementation of the information provided in this thesis is clearly very important for CXB synthesis models and represents the next step of this work.

Publications

The following list reports the papers directly related to this thesis and written from the work made during the three years of my Ph.D. course. They correspond to part of chapter 4, chapter 5 and 6; the papers listed here have been accepted for publication on the refereed journals Astrophysical Journal and Monthly Notices of The Royal Astronomical Society.

1. **Molina M.**, Bassani L., Malizia A. et al. 2008, MNRAS, 390, 1217
   A broad-band spectral analysis of eight radio loud type 1 AGN selected in the hard X-ray band.

2. **Molina M.**, Giroletti M., Bassani L. et al. 2007, MNRAS, 382, 937
   Broad-band X-ray spectrum of the newly discovered broad-line radio galaxy IGR J21247+5058.

3. **Molina M.**, Malizia A., Bassani L. et al. 2006, MNRAS, 371, 821
   INTEGRAL observations of active galactic nuclei obscured by the Galactic plane.

4. Bassani L., **Molina M.**, Malizia A. et al. 2006 ApJ, 636L, 65
   INTEGRAL IBIS Extragalactic Survey: Active Galactic Nuclei Selected at 20-100 keV.

The following list reports the papers not directly related to this thesis, for which I gave a contribution as a member of the IBIS survey team, during the three years of my Ph.D. course.

1. Capitanio F., Giroletti M., **Molina M.** et al. 2008, accepted for publication on ApJ, astroph/0809.2180
   The two INTEGRAL X-ray transients IGR J17091–3624 and IGR J17098–3628: a multi-wavelength long term campaign.

2. Malizia, A., Bassani, L., Bird, A. J., Landi R., Masetti N., de Rosa A., Panessa F., **Molina, M.** et al. 2008, MNRAS, 389, 1360
   First high-energy observations of narrow-line Seyfert 1s with INTEGRAL/IBIS
3. Panessa F., Bassani L., de Rosa A., Bird A. J., Dean A. J., Fiocchi M., Malizia A., **Molina M.** et al. 2008, A&A, 483, 151
   The broad-band XMM-Newton and INTEGRAL spectra of bright type 1 Seyfert galaxies.
4. Hill A. B., Bird A. J., Dean A. J., McBride V. A., Sguera V., Clark D. J., **Molina M.** et al. 2007, MNRAS, 381, 1275
   An unexpected outburst from A0535+262.
5. Landi R., Malizia A., Masetti N., de Rosa A., Gianní S., Dean A. J., **Molina M.** et al. 2007, ATel 1310
   Swift/XRT follow-up observation of IGR J12131+0700 (not NGC 4180).
6. Landi R., Masetti N., Stephen J. B., de Rosa A., Capitanio F., **Molina M.** et al. 2007, ATel 1288
   Swift/XRT follow-up observations of INTEGRAL/IBIS AGN candidates.
7. Landi R., Malizia A., Masetti N., de Rosa A., Gianní S., Dean A. J., **Molina M.**
   Swift/XRT follow-up observations of INTEGRAL detected AGN.
8. Malizia A., Landi R., Bassani L., Bird A. J., **Molina M.** et al. 2007, ApJ, 668, 81
   Swift XRT Observation of 34 New INTEGRAL IBIS AGNs: Discovery of Compton-Thick and Other Peculiar Sources.
9. Bird A. J., Malizia A., Bazzano A., Barlow E. J., Bassani L., Hill A. B., Bélanger G., Capitanio F., Clark D. J., Dean A. J., Fiocchi M., Götz D., Lebrun F., **Molina M.** et al. 2007, ApJS, 170, 175
   The Third IBIS/ISGRI Soft Gamma-Ray Survey Catalog.
10. Landi R., Masetti N., Gehrels N., Perri M., **Molina M.**, de Rosa A. 2007, ATel 990
    Swift/XRT observations confirm the AGN nature of IGR J14175-4641 IGR J14552-5133 and IGR J16351-5806.
11. Sguera V., Bird A. J., Dean A. J., Bazzano A., Ubertini P., Landi R., Malizia A., Barlow E. J., Clark D. J., Hill A. B., **Molina M.** 2007 A&A, 462, 695
    INTEGRAL and Swift observations of the supergiant fast X-ray transient AX J1845.0-0433 = IGR J18450-0435.

12. Barlow E. J., Knigge C., Bird A. J., Dean A.J, Clark D. J., Hill A. B., **Molina M.**, Sguera V. 2006, MNRAS, 372, 224
    20-100 keV properties of cataclysmic variables detected in the INTEGRAL/IBIS survey.

13. Sguera V., Bazzano A., Bird A. J., Dean A. J., Ubertini P., Barlow E. J., Bassani L., Clark D. J., Hill A. B., Malizia A., **Molina M.**, Stephen J. B. 2006, ApJ, 646, 452
    Unveiling Supergiant Fast X-Ray Transient Sources with INTEGRAL.

14. Bird A. J., Barlow E. J., Bassani L., Bazzano A., Bélanger G., Bodaghee A., Capitanio F., Dean A. J., Fiocchi M., Hill A. B., Lebrun F., Malizia A., Mas-Hesse J. M., **Molina M.** et al. 2006, ApJ, 636, 765
    The Second IBIS/ISGRI Soft Gamma-Ray Survey Catalog.

15. Bassani L., De Rosa A., Bazzano A., Bird A. J., Dean A. J., Gehrels N., Kennea J. A., Malizia A., **Molina M.** et al. 2005, ApJ, 634, 21
    Is the INTEGRAL IBIS Source IGR J17204-3554 a Gamma-Ray-emitting Galaxy Hidden behind the Molecular Cloud NGC 6334?

16. Bassani L., Malizia A., **Molina M.** et al. 2005, ATel 537
    Candidate AGN in the 2nd IBIS/ISGRI survey catalogue.

17. Stephen J. B., Bassani L., **Molina M.** et al. 2005, A&A, 432, 49
    Using the ROSAT Bright Source Catalogue to find counterparts for IBIS/ISGRI survey sources.

Declaration

The Author, Manuela Molina, is a member of the IBIS survey team with the principal role of studying Active Galactic Nuclei detected by IBIS. The work presented in this thesis represents the result of three years of research performed by the Author. However, this work was not completed in isolation, being carried out within the IBIS survey project which is a multi-national collaboration. The contribution of other people is indicated below:

- The Author worked jointly with Dr. M. Giroletti (IRA/INAF Bologna, Italy) for the radio analysis of IGR J21247+5058.
- The Author worked jointly with Dr. L. Bassani and Dr. A. Malizia (IASF/INAF Bologna, Italy) for the broad-band analysis of the complete sample of sources analysed in this thesis.
- Dr. N. Masetti (IASF/INAF Bologna, Italy) was responsible for the reported optical characteristics of the newly detected AGN analysed in this thesis.
- Dr. R. Landi (IASF/INAF Bologna, Italy) provided all the *Swift*/XRT data reduction presented in this thesis. The Author was responsible for their spectral analysis (in chapter 5, 6 and 7).
- Dr. V. McBride (IBIS Team Southampton) provided the *Chandra* data reduction for QSO B0241+62 (chapter 6). The Author was responsible for their spectral analysis.
- Dr. J.B. Stephen (IASF/INAF Bologna, Italy) provided the complete sample of AGN on which this thesis is based upon.

Acknowledgements

First of all I would like to thank my supervisor, Professor Tony Dean, for encouraging and supporting me during my time in Southampton.

A big thank you should also go to Dr. Tony Bird, for his patience, his technical and scientific help, for the irony and for always letting me know when my English was improving... cheers Ralph!

My gratitude also goes to Dr. Loredana Bassani and to Dr. Angela Malizia, for their invaluable scientific and moral support and also for being so helpful, and to the other people at IASF in Bologna.

Then, of course, I have to thank my wonderful family, who have always supported me through the highs and lows of the past three years. I would never have made it without my mum, Franca, and my sister, Claudia. A very special thank you goes to my very patient husband, Bruno, who had the will (and strength) to travel back and forth for three years (I bet low cost companies are extremely grateful to him!).

Another special thanks goes to Andrea, one of the best friends I could ever have found! Hers and Hardo's support was invaluable, as were the many coffees we had together!

Thanks to the guys in the office: Vanessa, one of the nicest persons I've ever met, Adam (whom I am still thanking for my degree thesis!), and, of course, the Italian guys: Simone and Vito (*beato te che non capisci niente...*). Thanks also to the guys next door: Dave, Omar, Simon and everybody else I have forgotten!

It's been three very interesting years...

Contents

List of Figures

List of Tables

Chapter 1

Scientific Framework

1.1 Introduction

For most of the past century, optical astronomy has been the dominant field in astrophysical research. In the last 50 or 60 years, however, other branches of astronomy have greatly developed, opening new windows on the radio, millimetre, infrared, UV, X-ray and gamma-ray Universe. In particular, X-ray and gamma-ray astronomy have known a dramatic development that has made them part of mainstream astrophysics in their own right. In little more than 20 years, the high energy sky has proven to be populated by the most energetic and extreme phenomena ever observed in the Universe: from violently interacting binary systems, to black holes, gamma-ray bursts (GRBs) and Active Galactic Nuclei (AGN).

A number of physical processes are responsible for the production of high energy radiation. In the following, some of the principal ones are listed.

- **Blackbody Emission.** The blackbody spectrum is represented by the Planck function, that can be written in the form:

  $$B_\nu(T) = \frac{2h\nu^3}{c^2}\frac{1}{(e^{h\nu/kT}-1)}\ \mathrm{erg\,cm^{-2}\,s^{-1}\,Hz^{-1}} \tag{1.1}$$

  Two regimes are identified for the blackbody emission, one described by the Rayleigh-Jeans Law and the other one by Wien's Law. The former describes regimes for which $h\nu/kT \ll 1$ and the Planck function is then written as $B_\nu(T)=2(\nu c)^2 kT$ erg $cm^{-2}s^{-1}Hz^{-1}$; the latter is applied when $h\nu/kT \gg 1$ and the Planck function becomes $B_\nu(T)=(2h\nu^3/c^2)e^{-h\nu/kT}$ erg $cm^{-2}s^{-1}Hz^{-1}$. Since optically thick thermal emission in the Universe has not been found at temperatures exceeding 4×10^7K, only the Wien tails from the hottest acretion discs are likely to be detected at soft gamma-ray energies.

- **Bremsstrahlung.** Bremsstrahlung (braking) radiation originates from the acceleration of electrons in Coulomb collisions with other electrons and with ions and nuclei. It is analogous to free-free emission and the radiation corresponds to transition between unbound states in the field of the nucleus. If electrons have a spectrum N(E)dE=N$_0$E$^{-\gamma}$dE, then the photon flux is:

$$dI_\nu = F(\gamma)\frac{c}{4\pi R^2}\frac{\bar{n}M}{X_0}N_0E_\nu^{-\gamma}dE_\gamma \ \mathrm{erg\,cm^{-2}\,s^{-1}} \tag{1.2}$$

where M is the atomic mass of the gas atoms, R is the distance to the source, $\bar{n}$ is the number density of target atoms, X$_0$ is the radiation length and F(γ) is a constant. In hot gas regions (i.e. plasma), the so-called thermal Bremsstrahlung radiation is produced, which emits a characteristic spectrum. Each collision produces a photon, whose energy corresponds approximately to the energy loss caused by the collision. The distribution of photon energies thus reflects the electron energy distribution and its average is proportional to the temperature. The electrons follow a Maxwell-Boltzman distribution and therefore the probability that an electron has a velocity v in the range d^{3}v is given by:

$$dP = (\frac{m}{2\pi kT})^{3/2}e^{\frac{-mv^2}{2kT}}d^3v \tag{1.3}$$

If the velocities are isotropically distributed, then d^{3}v=4πv^{2}dv and dP$\propto$v^{2}exp(-mv^2/2kT)dv, leading to a thermal Bremsstrahlung spectrum of photons described by the relation

$$dI_\nu = \frac{K}{\sqrt{T}}e^{\frac{-mv^2}{2kT}}d\nu \ \mathrm{erg\,cm^{-2}\,s^{-1}} \tag{1.4}$$

commonly found in the X-ray domain.

- **Synchrotron Radiation.** Synchrotron radiation is caused by accelerated relativistic electrons spiralling around the field lines of a magnetic field; when considering non-relativistic electrons, cyclotron radiation is instead emitted. The force felt by the electron in the magnetic field is perpendicular to the direction of the field and to the direction of the particle's velocity and this causes the electron to change its direction. The produced radiation is compressed into a small range of angles around the instantaneous velocity vector of the particle, causing the so-called "beaming". As the electrons spiral in the magnetic field, they radiate photons of a characteristic energy; the frequency of the emitted radiation corresponds to the revolving frequency and is proportional to the magnetic field intensity and the electron charge and inversely proportional to the electron rest mass. The rate of energy loss by the relativistic electrons can be written as:

$$\frac{dE}{dt} = -\frac{4}{3}\sigma_T c \frac{B^2}{2\mu_0}\gamma^2 \text{ erg s}^{-1} \tag{1.5}$$

where γ is the Lorentz factor and σ_T is the Thomson cross-section. If the emission is represented by a delta function, then the mean frequency is ν_m=4.6×10^{-6}B$_p$E^2(eV) Hz, where B$_p$ is the magnetic field intensity orthogonal to the direction of motion of the electron. If the electrons have a power law distribution N(E)dE=K$_e$E$^{-\gamma}$dE (cm^{-2} s^{-1} keV), the resulting spectrum of the photons is:

$$dI_\nu = kK_e B^{\frac{\gamma+1}{2}} \nu^{-(\frac{\gamma-1}{2})} d\nu \text{ ph cm}^{-2}\text{ s}^{-1}\text{ keV}^{-1} \tag{1.6}$$

If the electrons and the magnetic field are energetic enough, the emitted radiation can be in the form of gamma-rays.

- **Inverse Compton Scattering** takes place when high energy relativistic electrons upscatter low energy photons. This process requires high photon densities in order to take place. In the case of relativistic electrons where multiple scatterings occur, the frequency of the upscattered photons is proportional to E$_\gamma$=$\gamma_e^2 h\nu$, where γ_e^2 is the electron Lorentz factor and ν is the initial photon frequency. The rate of energy loss by the electrons is given by:

  $$\frac{dE}{dt} = -K_c\sigma_T \overline{n}_{ph}(h\nu_0)\gamma^2 \text{ erg s}^{-1} \tag{1.7}$$

  where $\overline{n}_{ph}$ is the number density of photons and σ_T is the Thomson cross-section. If the electrons have a spectrum described by:

  $$N(E)dE = K_e E^{-\gamma} dE \text{ electrons cm}^{-2}\text{ s}^{-1}\text{ keV} \tag{1.8}$$

  Then the emitted spectrum will be:

  $$I(\nu)d\nu = n_{ph}K_cK_e\nu^{-\frac{\gamma-1}{2}} \text{ ph cm}^{-2}\text{ s}^{-1}\text{ keV}^{-1} \tag{1.9}$$

  In many astronomical sources, electrons can reach Lorentz factors of about 100-1000, and consequently scatter low energy photons to very high energies if they pass through a region with a high electron column density. For example, an optical photon with ν=4×10^{14} Hz, when interacting with an electron with γ_e=1000, becomes a gamma-ray photon with ν=4×10^{20} Hz (∼1.6 MeV). An important process, above all in AGN, is the so-called synchro-self Compton, where synchrotron electrons can inverse-Compton scatter low energy photons up to X-ray and gamma-ray frequencies. In this process, the photons for the Compton scattering come from synchrotron radiation by the same electrons which are involved in the Compton scattering. In the external Inverse Compton scattering model, which is relevant for AGN jets located near broad line regions or bright accretion disks, the target photons for the inverse Compton scattering are derived from optical/UV light coming, for instance, from the nucleus of the active galaxy, or Cosmic Microwave Background photons.

- **Electron-Positron Annihilation.** When an electron encounters its antiparticle, the positron, they annihilate, producing two gamma-ray photons each carrying an energy of 511 keV. Depending on the temperature of the surrounding environment, it can sometimes happen that the annihilation is preceded by the creation of positronium, similar to a hydrogen atom but with a positron instead of a proton. Positronium is unstable and has two states: the singlet and the triplet. The singlet state decays into two 511 keV gamma-ray photons, while the triplet decays in three gamma-ray photons with a continuum energy extending below the 511 keV line.

There are also several methods in which gamma-rays interact with matter, such as the photoelectric effect, the Compton effect and pair production. The dominant process is strongly dependent on the energy of the interacting gamma-ray photon and on the atomic number Z of the absorbing material. In the following, two of these processes directly relevant to the soft gamma-rays photons studied by *INTEGRAL* are explained.

- **The Photoelectric Effect** occurs when a low energy gamma-ray photon interacts with a tightly bound electron. This process is important for E_γ<1 MeV and for high Z materials. The energy carried by the photon is transferred to an atomic electron, resulting in the ejection of the electron from the atom with an energy E_e, given by $E_e = h\nu - E_b$, where $h\nu$ is the absorbed gamma-ray photon energy and E_b is the binding energy of the electron in its shell; as it is evident from the formula, the energy of the ejected electron depends solely on the frequency of the incident photon. As the electron is ejected, a vacancy is produced and then filled by another electron from a higher orbit. The process emits X-rays, in turn absorbed by the material, resulting in all the initial photon's energy being absorbed in the material.

The probability of photoelectric absorption is $\tau \propto Z^5$, where Z is the atomic number of the material and τ is the probability.

- **Compton Scattering** is an elastic collision between a free electron and a gamma-ray photon and is the dominant process occurring between E=0.1 MeV and 1 MeV, that corresponds to the energy at which atomic electrons can be considered free. The collision causes the gamma-ray photons to lose part of their energy and momentum; the energy of the scattered photon is given by:

$$E'_\gamma = \frac{E_\gamma}{1 + \frac{E_\gamma}{mc^2}(1 - cos\theta)} \text{ erg} \tag{1.10}$$

where E_γ is the energy of the incident photon, m is the rest mass of the electron and θ is the scattering angle of the photon. The Compton effect cross-section depends only on the number of free electrons and not on the material atomic number.

1.2 Energy Produced in Accretion

The accretion of matter onto a compact object is one of the main causes of the powerful high energy emission observed both in Galactic and extragalactic sources. The huge observed power is thought to be provided by the release of gravitational energy as gas spirals inward towards the compact object (generally a black hole or a neutron star in the case of Galactic sources or a supermassive black hole in the case of active galactic nuclei). The gravitational potential energy E released by accretion of a mass m onto the "surface" of a compact object of mass M_c and radius R_c is given by:

$$E_{acc} = \frac{GM_c m}{R_c} \text{ erg} \tag{1.11}$$

If matter is continuously supplied over time, then the luminosity produced by accretion is:

$$L_{acc} = \frac{GM_c}{R_c}\frac{dm}{dt} \text{ erg s}^{-1} \tag{1.12}$$

As matter is accreted, the gravitational potential energy U is released as thermal energy, heating the material in the accretion disk. Equation 1.12 can then be rewritten as:

$$L_{acc} = \frac{dU}{dt} = \frac{d}{dt}\frac{GM_c m}{R_c} = \frac{GM_c}{R_c}\dot{m} = \eta \dot{m} c^2 \tag{1.13}$$

where the quantity $\eta = GM_c/R_c c^2$ is the efficiency of accretion and $\dot{m} = dm/dt$ is the accretion rate. η depends on the compactness of the system: the more compact the system, the more efficient the accretion process is. For example, for a neutron star with M_c=1.4$M_\odot$ and R_c=10 km, the efficiency is ~0.1, hence making the neutron star a powerful energy source. If a prograde Kerr black hole instead of a neutron star is considered, the efficiency improves to η~0.4, while for a non-rotating Schwarzschild black hole the efficiency is around 0.06.

There is however a limit to the luminosity produced during the accretion process: in fact, if the luminosity is too high, radiation pressure blows away the infalling material. The limiting luminosity (in the case of spherical accretion) is known as Eddington luminosity and is obtained by balancing the inward force of gravity against the outward radiation pressure:

$$L_{Edd} = \frac{4\pi G M_c m c}{\sigma_T} = 1.38 \times 10^{38} (\frac{M}{M_\odot}) \text{erg s}^{-1} \tag{1.14}$$

where M_c is the mass of the compact object, m is the mass of an accreting particle (~ the proton mass) and σ_T=6.65×10^{-25} cm^{-2} is the Thomson cross-section.

1.3 Active Galactic Nuclei

Active Galactic Nuclei (AGN) are the most violent, long lived objects in the Universe and are the sites of energy released on the most powerful sustained rates we know of. Active nuclei can be found in the cores of “normal” galaxies, but their emission is so powerful to outshine that of their host galaxy. Such strong emission cannot be, in general, related to stellar activity, but has instead to be traced back to the central engines responsible for the energy production. The huge observed power is thought to be provided by the release of gravitational energy as the gas in the galaxy spirals towards a Super Massive Black Hole (SMBH), which can have a mass of typically 10^7 M$_\odot$ or more.

AGN continuum spectra look dramatically different from those of normal galaxies. They produce a large amount of energy on small spatial scales and their emission spans the electromagnetic spectrum from radio frequencies up to gamma-rays, with peaks in the ultraviolet and a high percentage of the bolometric luminosity emitted both in the infrared and in the X-rays. High energy emission is arguably one of the most important aspects to understand AGN, because of its unambiguous association with nuclear activity and diagnostic capability to study accretion mechanisms.

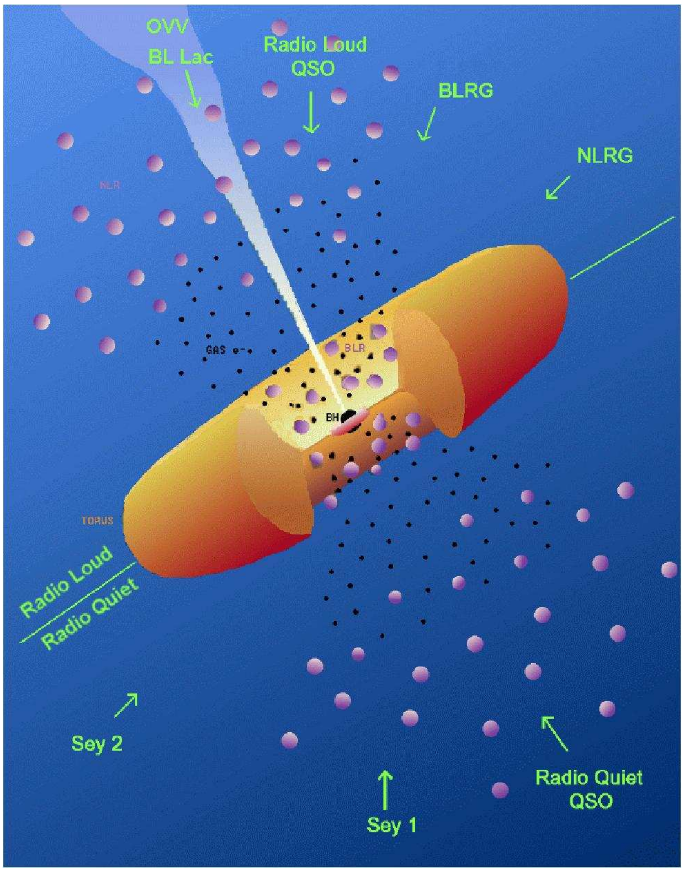

Figure 1.1: A schematic view of the AGN Unified Model based on obscuration-by-orientation (Urry & Padovani 1995).

1.3.1 AGN Unification

As already mentioned, AGN derive their power from accretion onto a super massive black hole, with the primary continuum emission peaking at UV/soft X-ray wavelengths, with a tail in the optical and extending up to several hundreds keV. Many different types of AGN are observed; however, all these classes seem to have some common underlying characteristics, thus representing different aspects of the same astrophysical phenomenon. A unified scenario has been developed both for radio loud (Urry & Padovani 1995) and Seyfert galaxies (Antonucci & Miller 1985), which is explained in the following and in figure 1.1.

The structure of an AGN can be characterised by the presence of the following regions:

•**Black Hole and Accretion Disk**: kinematic observations of a significant number of galaxies show evidence for central black holes with masses between 10^6 and 10^9 $M_{\odot}$ (Kormendy & Richstone 1995). Around the central black hole, the accretion disk is where the primary emission comes from, although its structure and emission mechanisms are still a matter of debate. Shakura & Sunyaev (1973) proposed a model in which the accretion disk is optically thick but geometrically thin. In this model, the efficiency of the accretion process, i.e. the ratio between the average radiated energy per particle and the particle rest energy, can reach the maximum allowed by a general relativistic gravitational potential. Another model, proposed by Narayan et al. in 1998, involves the *Advection Dominated Accretion Flow* mechanism (ADAF). In this scenario, the energy transfer from baryons (which gain much of the gravitational energy) to electrons (which radiate most efficiently) is highly inefficient. Therefore baryons fall into the last stable orbit maintaining most of their energy and the ratio between the radiated luminosity and the accretion mass is low. This mechanism is the favoured one for explaining the accretion geometry of the lowest luminosity AGN.

•**Broad Line Region (BLR)**: the broad lines observed in Seyfert galaxies optical/UV spectra have typical widths of 5000 km s^{-1} up to 10^4 km s^{-1}. These large widths are interpreted as due to Keplerian velocities of large numbers of clouds rotating around the central black hole at distances of 0.01-0.1 pc. The density of this gas is believed to be very high ($\rho \geq 10^9$ cm^{-3}), as required by the observed ratio between the permitted and forbidden emission line transitions. The typical processes involved in the BLR are mainly photoionisation heating and Bremsstrahlung cooling.

•**Narrow Line Region (NLR)**: narrow lines, which are also commonly observed in AGN, have much smaller widths (~100 km s^{-1}) than broad lines. This can be explained if these lines are produced by material placed further away from the central black hole, extending on scales of typically 100 pc. The gas is also less dense ($\rho \sim 10^3$-10^6 cm^{-3}) than that present in the BLR.

•**Obscuring Molecular Torus**: this is the key component of unification schemes. It prevents the direct observation of the BLR if the line of sight intercepts it and it is usually located at ~1 pc from the central black hole. It is thought to be made of a thick toroidal wall of dust and molecular gas, whose vertical axis is perpendicular to the equatorial plane of the accretion disk. According to the unified model developed by Antonucci & Miller in 1985, type 2 galaxies harbour a bright type 1 nucleus hidden from our view by an optically and geometrically thick torus. This picture implies that type 1 and 2 AGN are essentially the same objects viewed at different inclination angles. Direct observational evidence for this unified model came from spectro-polarimetric observations of some narrow line objects, revealing hidden polarised broad lines (Antonucci & Miller 1985; Tran 2001), scattered by free electrons in a mirror of ionised gas located just outside the opening of the torus, as well as from detection of maser-like structures orbiting around a central super massive object on scales of 0.1-1 pc in some nearby AGN (Greenhill et al. 1996).

Additional strong support has been obtained from X-ray observations of Seyfert 2 nuclei showing heavy photoelectric absorption due to cold gas, likely associated with the dusty torus (Matt et al. 2003; De Rosa et al. 2008). Variability in the X-ray column density of type 2 sources (Risaliti et al. 2002), associated with clouds in close proximity to the AGN (<0.1 pc) also suggests that X-ray absorption, broad line emission, dust obscuration and reprocessing are produced by a single, continuous distribution of clouds. According to a recent model (Elitzur 2008) the torus can also be considered as made of dust-free clouds that absorb X-rays. In this scenario, the torus is also considered as a continuation of the Broad Line Region, that extends to the inner boundary of the torus, and not a separate entity, as suggested also by IR reverberation observations (Suganuma et al. 2006).

Beside orientation, the bimodality of the radio luminosity of AGN (when normalised to their optical power) has also led to the distinction between radio loud and radio quiet objects. A unification model which takes into account the different properties observed among radio loud AGN, also including the presence of a relativistic jet, has been proposed by Urry & Padovani (1995). According to these authors, radio jets in radio loud AGN introduce another element of anisotropy in addition to the torus. Because of relativistic beaming effects, if our line of sight is along the radio jet direction, then its emission completely dominates the underlying nuclear continuum emission and the source is classified as a *Blazar*. As the viewing angle increases, the strength of the beamed component decreases, thus explaining the different spectral characteristics observed along the sequence Blazar-RL quasar-Broad Line Radio Galaxy-Narrow Line Radio Galaxy. The latter two classes can be considered as the radio loud counterparts of Seyfert 1 and Seyfert 2 galaxies respectively. In table 1.1, a schematic overview of the so-called “AGN-zoo” is outlined.

	Emission Line Properties		
	Type 1 (Broad Lines)	Type 2 (Narrow Lines)	Peculiar Objects
RQ Objects	Seyfert 1s RQ QSOs LINER 1s	Seyfert 2s RQ QSO 2s LINER 2s	BAL QSOs
RL Objects	BLRGs RL QSOs	NLRGs RL QSO 2s	Blazars

Table 1.1: The AGN Zoo.

It is worth noting that the unification model illustrated above is very simplified: over the years, detailed observations have suggested an indeed more sophisticated structure for the innermost regions of AGN, accounting for all the different AGN “flavours” seen in the sky and at different wavelengths.

1.4 Seyfert Galaxies

The class of AGN consists of objects showing some well-defined and distinctive features, such as:

- High nuclear luminosity (10^{41}-10^{47} erg s^{-1}), frequently outshining that of a normal galaxy of a different morphological type.
- The presence of strong high ionisation lines in their optical spectra.
- A broad-band continuum emission extending from radio to gamma-rays.
- Rapid variability in the optical continuum as well as in the emission lines.

Such complexity led to an heterogeneous classification based on the continuum, spectral and variability properties. AGN are firstly divided in *radio quiet* (90% of the population) and *radio loud*. Radio quiet objects are further divided in subclasses: high luminosity radio quiet AGN (quasars), Seyfert galaxies, low luminosity AGN and LINERS (Low-Ionisation Nuclear Emission-lines Regions). Radio loud AGN are mainly quasars or blazar type sources. Among all these different types of sources, Seyfert galaxies, which are the focus of this thesis, represent a major class consisting of AGN which are luminous and located in the nearby Universe, i.e. at $z<0.5$.

Seyfert galaxies were first recognised as a separate class of objects by Carl Seyfert in 1943, who found that the optical spectra of these objects were characterised by high ionisation emission lines, with widths up to several thousands km/sec. All Seyfert galaxies show narrow high ionisation emission lines in their optical spectra, indicating the presence of strong ionising radiation. However, some Seyfert galaxies (type 1 Seyferts) also show a broadening of the permitted lines, suggesting the presence of a dense ($\rho \geq 10^9$ cm^{-3}) and fast moving gas ($v \sim 10^4$ km s^{-1}). Sources which instead show only narrow emission lines are classified as type 2 Seyferts. In between type 1 and 2 Seyferts there is a wide variety of intermediate types, where the broad line components are weakly observable.

1.5 The X-ray Continuum Emission

The source of X-rays in AGN is located in the very inner nuclear region of the accretion disk, where most of the gravitational energy is released. Thermal emission emerges from an optically thick disk, providing the bulk of photons with energies spanning from the optical to the extreme UV/soft X-ray range. The Comptonisation of such photons occurs in a hot optically thin corona made of “thermal” mildly relativistic electrons (i.e. with $kT_e \sim 200$ keV) which extends above the accretion disk. There is a general consensus in indicating successive inverse-Compton scatterings of softer seed photons as the main production mechanism of X-rays.

The particle acceleration, i.e. the coronal heating mechanism, is often said to be due to dissipation of accretion energy generated in magneto-rotational instabilities in the disk and eventually transferred in the corona via reconnection of magnetic loops. However, this issue is far from being clear and also the geometry of the corona itself is almost unknown. The irradiated energy from the corona, in turn, is believed to be the main source of heating for the disk, introducing a coupling between the corona and the disk.

The above scenario has been first proposed by Haardt & Maraschi (1993) and is usually referred to as the “two-phase” disk model (see figure 1.2). The existence of a cold phase, occurring in the accretion disk, and a hot phase, occurring in the corona, are indeed the main ingredients of this model.

The key physical parameters are the temperature and the optical depth of the corona and the temperature of the accretion disk. The energy balance between the cold and the hot phases determines the values of these key parameters and, in turn, the shape of the emerging X-ray spectrum.

However, in its simplest version, such a model with a cold disk covered by a uniform hot corona cannot work properly, as it predicts too many Comptonisation photons for a given number of seed photons from the disk. In fact, many observations indicate a soft (i.e. UV) luminosity (L_s) several times larger than the hard (i.e. X-ray) luminosity (L_h), at odds with the theoretical prediction of $L_s \sim 2 \times L_h$ (Haardt & Maraschi 1993). These results led Haardt, Maraschi & Ghisellini (1994) and Stern et al. (1995) to propose a more realistic model in which the X-ray emitting active regions are located only in some “blobs” above the surface of the disk (the so-called “patchy” corona). In this way some fraction of the UV radiation emerging from the disk does not interact with the corona, i.e. the X-ray active blobs, and no Comptonisation occurs. In this scenario, viscous heating arising directly from dissipation in the accretion flow also provides an important contribution to the UV bump.

Zdziarski et al. (1990) also proposed an alternative model based on a corona with a non-thermal distribution of electron energies which essentially works like the thermal one. However, the presence of a high energy cut-off (where the cut-off energy points to a Maxwellian temperature of electrons in the corona) observed in most Seyfert galaxies

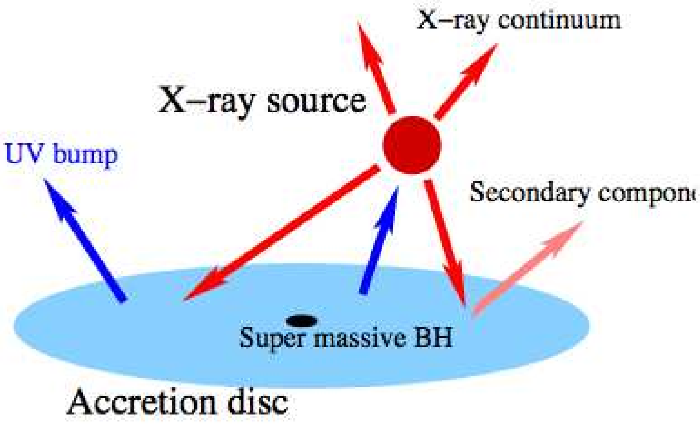

Figure 1.2: Schematic view of the two-phase Comptonisation model assuming a discrete geometry (i.e. patchy and not uniform) for the corona (Petrucci et al. 2002).

(Matt 2000; Perola et al. 2002; Molina et al. 2006), together with the lack of detection of an annihilation line (Johnson et al. 1997) expected to be present in the non-thermal model, have led many to consider it inappropriate and thermal models have been preferred over the non-thermal ones[1].

Comptonisation models account for the overall "first-order" spectral shape of AGN observed in the X-ray band, i.e. a high energy cut-off power law with a photon index $\Gamma \sim$1.8-2. However, a detailed examination of AGN spectra reveals the existence of many additional components to the simple power law model, that have been interpreted as signatures of the reprocessing of the primary nuclear continuum by some material located around the central engine (Mushotzky, Done & Pounds 1993). Understanding where and how these features originate may provide the best means to get a complete description of the geometry and the nature of the accretion process and, hence, how an AGN works and ultimately how it may evolve.

1.5.1 Neutral Absorption

The most striking broad spectral feature observed in the X-ray spectra of Seyfert galaxies is the cut-off in the soft X-ray region due to absorption by material associated with the interstellar medium in our Galaxy and by material local to the active galaxy. This intrinsic material suppresses the primary power law-like continuum via photoelectric absorption. The observed values for the intrinsic absorption column density span from $N_H \sim \text{few} \times 10^{20}$ cm^{-2} up to $N_H > 10^{25}$ cm^{-2} with a distribution peaked at $\sim 10^{23-24}$ cm^{-2}, as reported by

---

[1] However, note that in many Galactic black holes a hard power law tail is sometimes observed.

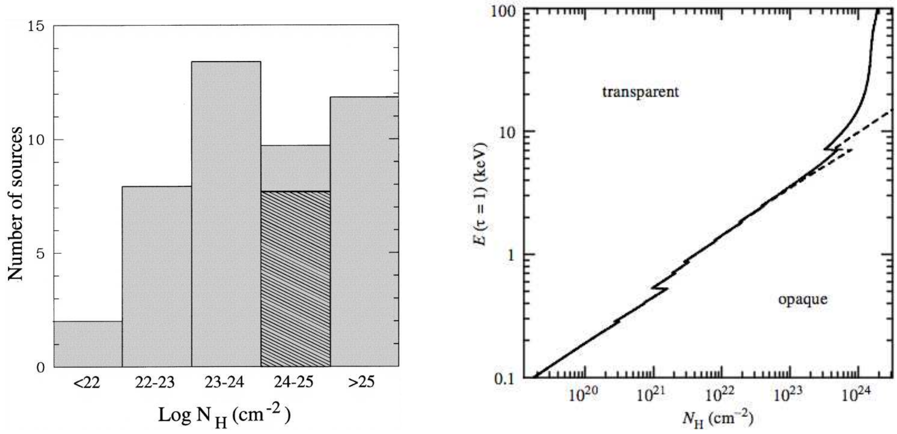

Figure 1.3: Left Panel: Distribution of N$_H$ values among a sample of local Seyfert 2 galaxies from Risaliti et al. (1999). Right Panel: The energy corresponding to an optical depth τ=1 as a function of the column density. The dashed line indicates the case with only photoelectric absorption, while the solid line refers to the case with the inclusion of Compton scattering (Matt 2002).

Risaliti, Maiolino & Salvati (1999) for a large sample of local Seyfert 2s (figure 1.3 left panel). When N$_H$ exceeds 1.5×10^{24}cm^{-2} (i.e. the inverse of the Thomson scattering cross-section), the Compton scattering optical depth equals unity and the source is defined to be “Compton-thick”. In this case the primary emission in the X-ray band is totally absorbed up to several hundreds keV (figure 1.3 right panel). On the other hand, when N$_H$ is lower than 1.5×10^{24}cm^{-2} the source is called “Compton-thin”.

As proposed by Matt (2002), different regions could be associated with the “Compton-thick” and the “Compton-thin” absorbing material: the former might be associated with the circumnuclear torus while the latter could also be associated with larger dust lanes present in the host galaxy (see also Maiolino & Rieke 1995).

Even though somewhat at odds with basic unification models which predict a one-to-one relationship between optical type 1 (type 2) and X-ray unobscured (obscured) sources, many examples of broad line objects suffering from X-ray intrinsic absorption have been found (Maccacaro, Perola & Elvis 1982; Fiore et al. 2001; Wilkes et al. 2002). This fact is puzzling and some possible explanations have been proposed along the years: (*i*) the dust-to-gas ratio of the X-ray absorbing material could be lower than it is in the Galactic interstellar medium (Maiolino et al. 2001a); (*ii*) the dust grains size of this material could be larger than Galactic ones and thus do not extinct efficiently in the optical (Maiolino et al. 2001b); (*iii*) our line of sight does not pass through the torus but intercepts another kind of dust-free material (such as a disk wind) located within the the dust sublimation radius (Weingartner & Murray 2002). Alternatively, as recently proposed by Elitzur (2008) the torus might be “clumpy”, i.e. made of dust-free clouds able to attenuate X-rays but

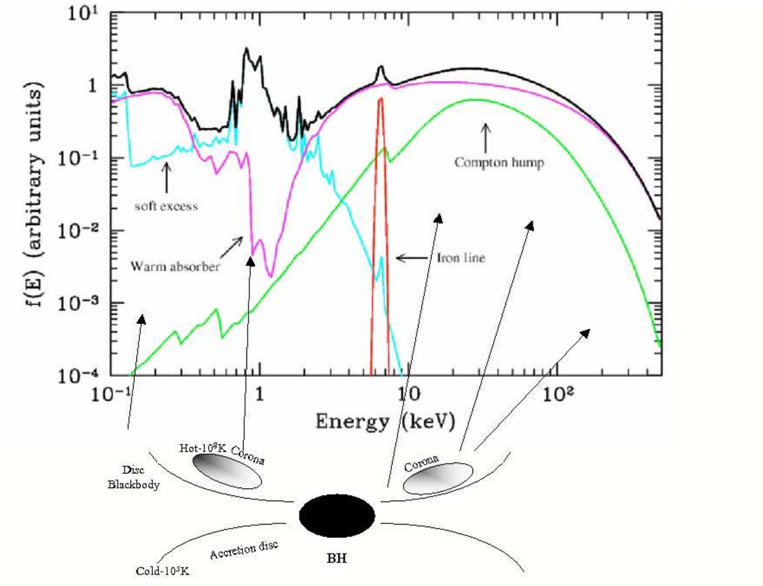

Figure 1.4: Typical X-ray spectrum of Seyfert 1 galaxies, with the individual spectral components highlighted. In the bottom of the figure is reported a schematic picture of the region close to the black hole, indicating the different physical components responsible for the observed spectral features.

transparent to optical and UV wavelengths. In order for clumpyness to be efficient, the size of the clouds has to be much smaller than the mean free path of the photons coming from the central illuminating source. If this model is adopted, then the observed difference between type 1 and type 2 sources strongly depends on the probability of intercepting a more or less large number of clouds in the torus.

1.5.2 Reflection Component

Figure 1.4 shows a typical broad-band X-ray spectrum of a type 1 AGN, indicating the main spectral features as well as the place where they are believed to originate within the framework of the disk-corona model as mentioned previously. The strength of these components varies from object to object on the basis of its peculiarities and also among different subclasses of AGN. However, this spectral "template" seems to be appropriate, at least to the first order, for most non-Blazar type AGN (Nandra & Pounds 1994; Turner et al. 1997; Mineo et al. 2000; Perola et al. 2002), apart from the remarkable difference due to the soft X-ray cut-off seen in type 2 sources.

The optically thick material of the disk is irradiated by the primary X-ray emitting source (see figure 1.2): soft X-ray (<10 keV) photons incident on this material are photoelectrically absorbed by ions of elements such as C, O and Fe and subsequently thermalised. On the other hand, photons with harder energies (>30-40 keV) incident on the disk are backscattered via Compton scattering, transferring only ~10% of their energy to the disk. This scattered emission from the optically thick material (the so-called "reflection" component; Guilbert & Rees 1988; George & Fabian 1991) results in a broad hump, peaking at ~30-40 keV, due to the combination between Compton scattering at high energies and absorption at low energies (figures 1.4 and 1.5). It must be pointed out that some observations (see Fabian et al. 2000 for a review) also suggest that a reflection component can also originate from the molecular torus; reflection on the outermost regions of the AGN (i.e. the putative molecular torus) might result in a narrow emission line component at an energy close to the Fe Kα line (see next section). The reflection hump has been effectively observed in most bright Seyfert galaxies, first with *Ginga* (Nandra & Pounds 1994), then with *BeppoSAX* (Perola et al. 2002) and now with *INTEGRAL* (Panessa et al. 2008; De Rosa et al. 2008), thanks to their wide spectral coverage extending above 10 keV. The intensity of the reflection hump suggests that the material covers $\sim 2\pi$ sr of the sky as seen by the X-ray source.

1.5.3 Fluorescent Emission Lines

A simulated spectrum of a "reflection" component (calculated assuming a power law model for the incident X-ray emission and a plane-parallel slab geometry for the illuminated cold material) is shown in figure 1.5.

In this figure several emission lines can be noted: they originate via photoelectric absorption followed by fluorescence emission from several atomic species. The most prominent among these lines is the typically narrow Fe Kα one emerging at 6.4 keV in the case of neutral iron. This value slowly rises up to 6.9 keV in the case of fully ionised iron. The combination of fluorescence yield ($\propto Z^4$) and relative abundance of iron justifies the strength of this feature. A line arising from a rotating disk is expected to have a double-peaked profile (e.g. Fabian et al. 2002): however, the detailed profile of the observed line strongly depends on several parameters such as the geometry assumed for the primary X-ray source, the inclination of the emitting region with respect to our line of sight and/or the disk emissivity law. Moreover, contributions to the Fe Kα emission are also expected from reflection onto the optically thick torus and onto the BLR and NLR clouds (Ogle et al. 2000). Hence the final profile as well as the intensity of the line are both quite difficult to interpret.

The determination of the properties of the Fe Kα line has been the object of much theoretical work (e.g. Matt, Perola & Piro 1991; Ghisellini, Haardt & Matt 1994). Detailed

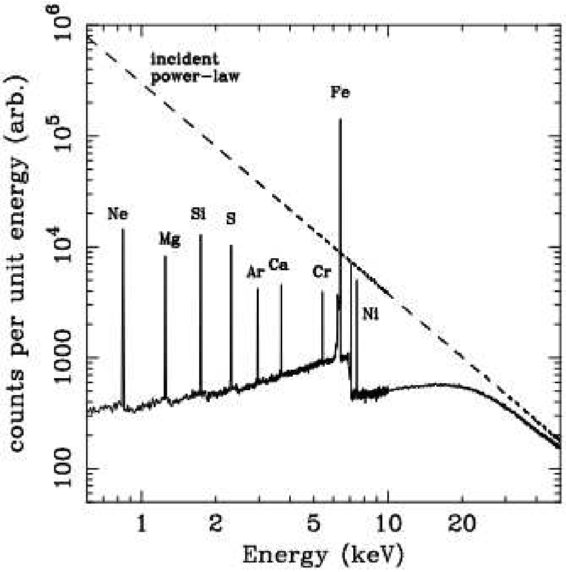

Figure 1.5: The spectrum of the reflected X-rays expected assuming a power law X-ray spectrum (dashed line) irradiates a semi-infinite slab of cold matter. Solar abundances are assumed (Reynolds 1997).

calculations have predicted an average line equivalent width EW∼150-230 eV, which roughly increases linearly with the covering factor and decreases as the inclination increases. These values are in rough agreement with the observations. From a compilation of archival results of Seyfert galaxies observed both by *Ginga* and *ASCA*, Gilli et al. (2000) found an EW=267±186 eV (EW=154± 89 eV) for type 1s and EW=363±254 eV (EW=300±163 eV) for type 2s with *ASCA* (*Ginga*). Also Guainazzi et al. (2006) found a similar range in EW values for their sample of 102 AGN detected by *XMM-Newton*.

Note that type 2 AGN are expected to have larger Fe Kα EW, since most of their primary continuum is intercepted by the torus and the Fe Kα photons are also produced by transmission through such absorbing material. Moreover, other Fe Kα photons originate by reflection in the inner, farthest, part of the torus. In the most extreme cases (i.e. Compton-thick sources) the direct continuum is completely absorbed, only the reflected component can be observed, thus providing the most extreme values of EWs (up to ∼2 keV, e.g. Levenson et al. 2002).

The advent of *XMM-Newton* and *Chandra* has allowed more detailed investigations of these features to be performed. Using *Chandra* HETGS observations of a sample of Seyfert 1 galaxies, Padmanabhan & Yaqoob (2003) confirmed the complexity in the shape of iron emission lines, which consist of a broad (FWHM∼10^4-10^5 km/s) and/or a narrow component. This latter feature (centered at 6.403±0.062 keV), which is thought to arise in cold iron located in the torus or in the BLR clouds, appears to be a common feature of type 1 AGN.

However, in some cases (such as in MCG-06-30-015, Padmanabhan & Yaqoob 2003; Vaughan & Fabian 2004) the narrow component superimposed onto a broad disk line feature is characterised by very rapid variability, strongly suggesting that it could be the blue peak of the broad disk line itself; Guainazzi et al. (2006) observed, in a sample of 102 AGN detected by *XMM*, that relativistically broadened iron lines could be present in at least 25% of the studied population. Nevertheless, it is worth noting that reprocessing features, both the iron line and the reflection hump above 10 keV, are not commonly observed in the X-ray spectra of radio quiet QSOs and radio loud AGN and, when detected, they are usually weaker than in Seyfert galaxies (Sambruna et al. 1999; Reeves & Turner 2000; Grandi et al. 2006). To explain this effect in radio quiet objects, Iwasawa & Taniguchi (1993) have suggested the existence of an X-ray “Baldwin effect” such that, as the X-ray luminosity increases, the outer layers of the disk progressively become more ionised until any reprocessed feature is suppressed.

The weakness of the reprocessing feature in radio loud AGN can instead be interpreted as the result of dilution of the primary continuum by emission from a jet (e.g. Cappi et al. 1997) and/or the result of a different disk-source geometry, for example where the inner portion of the disk is so hot and ionised to prevent any reprocessing of the incident X-ray photons (Grandi et al. 2000).

1.5.4 Warm Absorber and Soft Excess Emission

The spectrum reported in figure 1.4 shows the presence of two more components occurring in the soft band: the warm absorber and the soft excess. Even though ionised absorbing gas had already been observed with previous X-ray telescopes in many Seyfert 1 galaxies (Reynolds 1997) and in some QSOs (George et al. 2000), only observations performed with grating spectrometers and calorimeters have provided the adequate tool to deeply constrain the physical nature of these features. The high resolution soft X-ray spectra of bright type 1 AGN obtained with both *XMM-Newton* and *Chandra* show many absorption lines and few emission lines from hydrogen-like and helium-like ions of the most common metals (see Krolik & Kriss, 1995, for a theoretical review). The column densities of several atomic species are typically in the range of $\sim 10^{19}$-10^{21} cm^{-2}. Moreover, absorption lines are found to be blueshifted, suggesting that they are emitted from an outflowing wind (Kaspi et al. 2001). The most plausible location for this photoionised gas appears to be a stratified absorber with different ionisation levels, lying a few parsecs from the nucleus and extending up to the NLR. On the basis of *Chandra* and *XMM-Newton* data, Kinkhabwala et al. (2002) and Sako et al. (2001) have found that this warm ionised absorber is also responsible for the soft X-ray scattered emission seen in obscured Seyfert 2 galaxies. The same gas absorbing the primary continuum in face-on (type 1) objects produces the "secondary" emission line spectrum observed in edge-on (type 2) sources. These findings allow to infer many important parameters, such as the geometry and the physical conditions of the innermost regions of AGN and they also provide a further strong support to Unified Models.

As far as the soft excess emission in type 1 objects is concerned, two physical interpretations are given on the basis of the observational properties (Pounds & Reeves 2002). In the case of a "sharp" soft excess, the most plausible explanation is that it originates as reprocessing of the hard X-ray emission by the inner parts of the disk (i.e. the soft X-ray portion of the reflection spectrum, see also Branduardi-Raymont et al. 2001). On the other hand, if the upturn gradually emerges below 2-3 keV ("gradual" soft excess) the emission is believed to be the Comptonised hard tail of the Big Blue Bump (i.e. the thermal emission arising directly from the disk).

1.6 AGN Continuum Spectra

As mentioned above, AGN spectra span a large range in frequencies from hard X-rays to the far infrared and radio, with almost equal power per decade of frequency. The most remarkable features include:

- The X-ray continuum can be broadly described as a power law from energies of ~1 keV up to an eventual cut-off somewhere beyond 100 keV.

- The "Big Blue Bump", which covers the wavelength range from ~4000 Å to at least 1000 Å and can be explained as thermal emission from the gas in the accretion disk within a wide range of temperatures. Whether this feature extends further into the extreme ultraviolet is unclear. Our Galaxy becomes virtually opaque at wavelengths between 912 Å and ~100 Å due to absorption by neutral hydrogen.

- The "near infrared inflection", which appears as a dip between 1 μm and 1.5 μm, corresponding to the sublimation temperature of the refractory gas that envelops the central regions. This is practically the only continuum feature with a well defined wavelength.

- The "infrared bump" is a broad feature longward of the 1 μm inflection.

- The “submillimetre break” marks a sharp drop in emission and is the strongest feature seen in normal quasar continua. The exact location of this feature and the size of the drop varies within the AGN population. In radio loud objects the drop in power output is only ~2 decades, while for the more common radio quiet objects it may be ~5 or 6 decades (Elvis et al. 1994).
- Radio emission is sometimes characterised by a flat spectrum and a compact radio core. Radio emission takes place above all in jets of plasma, resulting in large radio lobes. Jets and lobes are the sources of the continuum radio emission, provided chiefly by synchrotron radiation from relativistic electrons spiralling in magnetic fields in the jets and lobes. Radio emission is a negligible fraction of the bolometric luminosity. It is worth mentioning that all AGN are radio emitters at some level, although in the so-called radio quiet sources the origin of the observed radio emission does not come from a powerful jet, but is probably generated by jets or plasma outflows on much smaller scales.

The origin of these continuum features is not well understood. They cannot in general be satisfactorily fitted with simple thermal or non-thermal emission mechanisms, possibly implying the presence of various production sites and related radiation output. For these reasons, in the following, the various properites observed in Seyfert galaxies in different wavebands, from radio to infrared and optical/UV will be described; the X-ray emission, which was treated before, is omitted.

1.6.1 Radio Emission

Radio emission constitutes a very small fraction of the total bolometric luminosity of Seyfert galaxies, being 5 to 6 orders of magnitude lower than the UV/optical flux continuum. The origin of the radio emission in radio loud AGN is to be traced in kiloparsec-scale jets (Kukula et al. 1995). In radio quiet sources, the radio emission is mostly unresolved on large scales, but sub-arcsecond imaging shows compact radio emission on arcsec scales; radio variability of radio quiet AGN also suggests the presence of a compact non thermal source (Barvainis et al. 2005; Anderson & Ulvestad 2005). This radio emission in radio quiet AGN is thought to originate in a scaled down version of radio loud AGN, i.e. in low power jets that dissipate before leaving the core, thus explaining why no resolved emission is seen. The radio spectrum is typically flat, indicating non thermal emission (Ho & Ulvestad 2001). By virtue of their proximity, a high fraction of Seyfert galaxies are detectable as radio sources but have been traditionally regarded as radio quiet objects. However, it has been recently shown by Ho & Peng (2001) that, on the basis of the radio-to-optical luminosity ratios, a substantial fraction (~60%) of Seyferts are “radio loud”. Traditionally a source is classified as radio loud if it has a radio power density at 5 GHz $P_{5GHz} \geq 10^{32}$ erg s^{-1} Hz^{-1} and and the 5 GHz radio to optical B band flux density ratio $R_B \geq 10$ (i.e. Kellerman et al. 1989); In phenomenological classifications of AGN, type 1 and type 2 Seyferts are often viewed as the radio quiet counterparts of broad line and narrow line radio galaxies respectively (Krolik 1998); however, the search for intrinsic differences between the radio properties of type 1 and type 2 sources is still essentially inconclusive.

1.6.2 Infrared Emission

The infrared emission of Seyfert galaxies is thought to be of thermal origin, due to reprocessing of the primary radiation from dust. Indeed, the presence of a local minimum at ~ 1 μm hints at a thermal emission mechanism. This is likely due to reprocessing from the dust located closer to the nuclear source (~0.1 pc) having a temperature of the order of 2000 K; at higher temperatures, the grains sublimate. On the other hand, the submillimetre break at the end of the far-infrared band can be easily reconciled with the rapid loss of efficiency of dust grains at longer wavelengths.

Infrared continuum variability is also consistent with emission from dust. In the case of the Seyfert galaxy Fairall 9, for instance, the observed delay between infrared and UV continuum is consistent with emission from dust located at ~400 light days (or ~0.3 pc) from the nucleus (Clavel, Wamsteker & Glass 1989).

Many models have proposed a toroidal geometry for the emitting dust (e.g. Pier & Krolik 1992; Granato & Danese 1994; Efstathiou & Rowan-Robinson 1995). These generally extend only to mid-infrared wavelengths and find it difficult to account for the cool far-infrared radiation. This may be produced further out in a circumnuclear starburst. However, the observed correlation between the mid- and far-infrared luminosities indicates that the emission processes must be linked. It is possible that the starburst and AGN are indeed triggered by the same interaction or merger event (Rowan-Robinson 2001).

Whatever the geometry of the emitting dust, it is clear that, for an observer behind the optically thick medium, the view of the central radiating source will be obscured. These AGN will appear very different and may not be immediately recognised as such at all.

1.6.3 Optical-UV Emission

The main feature which dominates the optical-UV spectra of most AGN is the “big blue bump”. The exact shape of this feature is confused by a large number of broad and blended lines thought to be emitted from the fast moving ionised clouds of the BLR and NLR. In particular, superimposed on the continuum between ~2000 Å and 4000 Å is a feature known as the “small blue bump”, made up of the Balmer continuum and blended Balmer and Fe II emission lines.

Contamination by the host galaxy can play a major role in low luminosity AGN, especially if there is a nuclear starburst that is often difficult to resolve. Intrinsic reddening by dust very close to the AGN can also have a dramatic effect on the slope of the observed spectrum. It should also be emphasised that in the extreme UV our Galaxy is for the most part opaque and few data are available in that region of the spectrum.

Most current models interpret the big blue bump as thermal emission from an optically thick, geometrically thin accretion disk. A radial temperature distribution in the disk results in emission approximated by a multi-blackbody spectrum. Therefore, the majority of the flux at different wavelengths is emitted from physically separated and distant regions of the disk. This immediately causes a problem for this type of models as variations in the continuum are observed to be virtually simultaneous at optical and UV wavelengths (Ulrich et al. 1997). Changes would therefore need to propagate at speeds much greater than the sound speed in the optically thick medium. The multi-blackbody model also has problems fitting the optical continuum slope, usually producing spectra that are too “blue” to fit the data.

According to unification models, type 2 objects should be type 1 nuclei heavily obscured by material along the line of sight. Indeed, the main component of the optical continuum of Seyfert 2 galaxies is the starlight from the host galaxy. However, the presence of a “featureless continuum” (i.e. no spectral line features) contributes significantly to the spectrum. This component is interpreted in terms of scattered light from the obscured type 1 nucleus, as found for the broad lines. Nevertheless, this solution seems to explain only 20% of the total UV-optical continuum (Heckman et al. 1995). A number of alternative solutions have been proposed, including starburst emission (Heckman et al. 1995) and reprocessing from NLR clouds (Contini & Viegas 2000).

Chapter 2

The *INTEGRAL* mission

2.1 Introduction

The ESA satellite *INTEGRAL* (*INTErnational Gamma Ray Astrophysics Laboratory*) is dedicated to high resolution spectroscopy (2.5 keV FWHM at 1 MeV) and high resolution imaging (angular resolution: $12'$ FWHM) in the energy range 15 keV-10 MeV. *INTEGRAL* can also perform simultaneous observations of the X-ray (3-35 keV) and optical (V band, 550 nm) bands thanks to two smaller monitors (Winkler et al. 2003).

INTEGRAL, one of ESA's medium size missions within the "*Horizon 2000*" programme, was successfully launched from Baikonour (Kazakhstan) on October 17, 2002. The mission is managed by ESA with contributions from 16 European countries, as well as from Russia (participating with the PROTON launcher) and from NASA (participating with the *Deep Space Network* ground stations).

The satellite (see figures 2.1 and 2.2) was placed in a highly eccentric orbit with a high perigee, so to allow long uninterrupted observations with a practically constant background, far from the radiation belts around the Earth. The initial orbital parameters were: an orbital period of 72 hours with an inclination of 52.2°; perigee at 9000 km; apogee at 154 000 km. In order to reduce the instrumental background, all scientific observations are conducted when the satellite is at a nominal altitude of 60 000 km when approaching the radiation belts and above 40 000 km when moving away from the belts. This means that during a single orbit, the satellite can perform scientific observations for about 90% of the time.

INTEGRAL main scientific objectives are (Winkler et al. 2003):

- studies of compact objects (Black Holes, Neutron Stars, White Dwarves);
- analysis and monitoring of high energy transient sources;

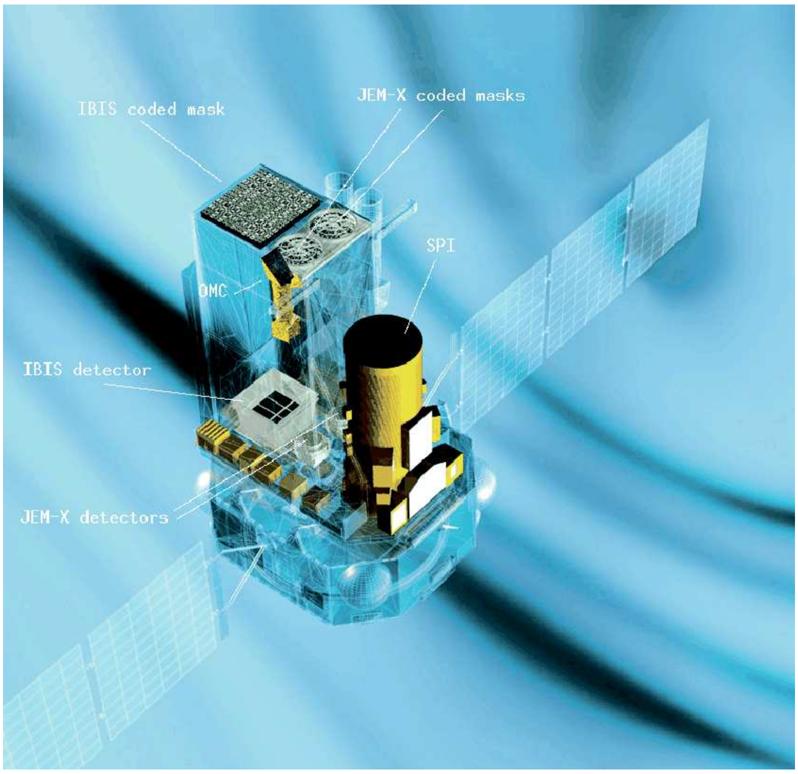

Figure 2.1: The *INTEGRAL* satellite (Winkler et al. 2003).

- studies of the stellar nucleosynthesis (novae and supernovae);
- studies of the Galactic Plane and Centre;
- studies of Galactic structures (clusters, maps of the continuum and of emission lines, interstellar medium, cosmic ray distribution);
- studies of extragalactic sources (Active Galactic Nuclei, nearby galaxies, cluster of galaxies, cosmic diffuse background);
- detection and identification of high energy sources;
- gamma-ray bursts.

These objectives are achieved thanks to the spectroscopic capabilities of the spectrometer SPI, which operates in a wide energy range (0.2-10 MeV) and to the high angular resolution (12′) of the imager IBIS. These instruments also possess a good source position accuracy and a sensitivity of a few mCrab, thus allowing broad-band spectroscopy, which is fundamental for measuring spectral shapes and identifying spectral lines. The production of wide field of view images also allows the identification of the position and

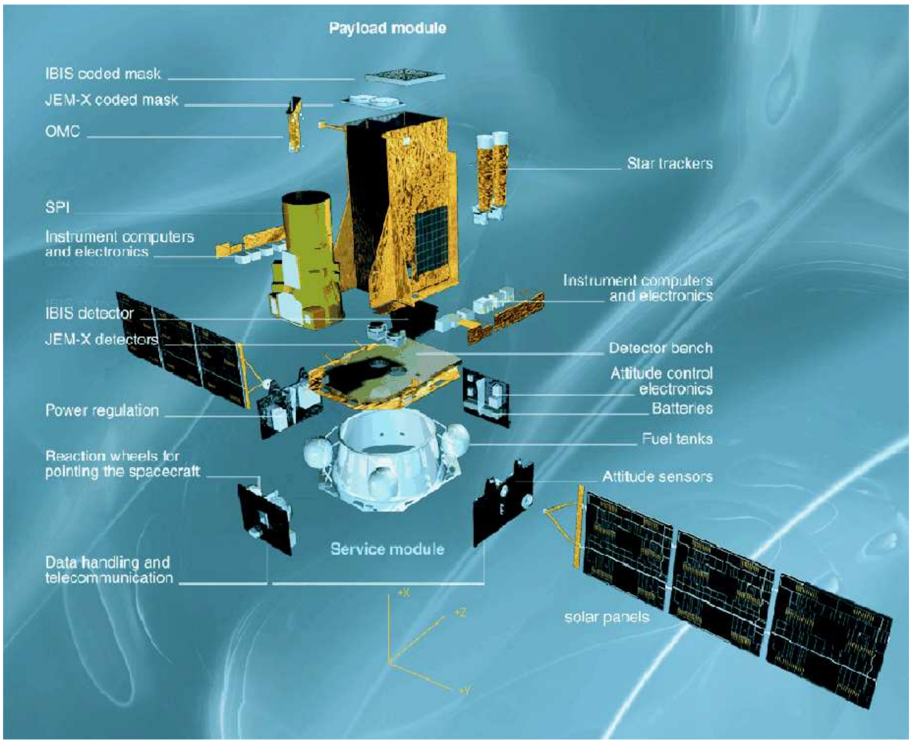

Figure 2.2: A detailed view of *INTEGRAL* (Jensen et al. 2003).

the direction of the incident signal. This is a very important aspect, since once the correct position of an object is known, it is then possible to study it at other wavelengths, such as the radio, the infrared (100-1 μm), the optical/UV (1μm-10 nm) and the X-ray band (below 10 keV). Finally the large fields of view of *INTEGRAL*'s two main instruments, SPI and IBIS, are ideal for survey studies over large areas of the sky, that can be mosaiced together providing an almost complete all-sky coverage.

2.2 Scientific Payload

The overall dimensions of the *INTEGRAL* satellite are $5\times2.8\times3.2$ m. When deployed, the solar panels are 16 m long; the total mass is ~4t, including ~2t of scientific instrumentations. *INTEGRAL* has two main gamma ray instruments on board: a spectrometer, SPI (*Spectrometer on INTEGRAL*; Vedrenne et al. 2003), and an imager, IBIS (*Imager on Board INTEGRAL Satellite*; Ubertini et al. 2003). Two monitors, JEM-X (Lund et al. 2003) for the X-ray band and OMC (Mas-Hesse et al. 2003), operating at optical wavelengths, are also part of the payload. An exploded picture of the satellite can be seen in figure 2.2, where all the instruments are clearly visible. In table 2.1 the technical characteristics are also reported.

Parameter	**SPI**	**IBIS**
Energy Range	18keV-8MeV	15keV-10MeV
Detector	19 Ge detectors of (6×7)cm each cooled to 85K	16384 CdTe detectors of $(4 \times 4 \times 2)$mm each 4096 CsI detectors of $(8.4 \times 8.4 \times 30)$mm each
Detector Area (cm^2)	500	2600 (CdTe), 2890 (CsI)
Spectral Resolution (FWHM)	3keV @ 1.7 MeV	8keV @ 100keV
Continuum Sensitivity ($ph\,cm^{-2}\,s^{-1}\,keV^{-1}$) ($\Delta E = E/2$, 3σ, 10^6s)	5.5×10^{-6} @ 100keV 1.2×10^{-6} @ 1MeV	6×10^{-7} @ 100keV 5×10^{-7} @ 1MeV
Line Sensitivity ($ph\,cm^{-2}\,s^{-1}$) (3σ, 10^6s)	3.3×10^{-5} @ 100keV 2.4×10^{-5} @ 1MeV	1.9×10^{-5} @ 100keV 3.8×10^{-4} @ 1MeV
Field of View (fully coded)	16° (diagonal)	$9° \times 9°$
Angular Resolution (FWHM)	2.5° (point source)	$12'$
Source Positioning (radius)	$\leq 1.3°$	$\leq 1'$ (10σ source)
Temporal Accuracy (3σ)	$\leq 200\mu s$	$\leq 200\mu s$
Mass (kg)	1309	746
Power [max/av](W)	385/110	240/208
Parameter	**JEM-X**	**OMC**
Energy Range	4keV-35keV	500nm-600nm
Detectors	Microstrip Xe/CH_4 gas detectors (1.5bar)	CCD + V filter
Detectors Area (cm^2)	500 for each of the two JEM-X detectors	CCD: (2061×1056)pixels Image area: (1024×1024)pixels
Spectral Resolution (FWHM)	2.0keV @ 22keV	-
Continuum Sensitivity ($ph\,cm^{-2}\,s^{-1}\,keV^{-1}$) ($3\sigma$, 10^6s)	1.2×10^{-5} @ 6keV	-
Line Sensitivity ($ph\,cm^{-2}\,s^{-1}$) (3σ, 10^6s)	1.9×10^{-5} @ 6keV	-
Limit Magnitude (mag) (3σ, 5000s)	-	17.8
Field of View (fully coded)	4.8°	$5° \times 5°$
Angular Resolution (FWHM)	$3'$	$25'$
Source Positioning at 10σ (radius)	$\leq 30''$	$6''$
Temporal Accuracy (3σ)	$\leq 200\mu s$	≥ 1s
Mass (kg)	65	17
Power [max/av](W)	50/37	20/17

Table 2.1: Scientific Payload main parameters (taken from Winkler et al. 2003).

The spectrometer, imager and the X-ray detector share a common principle: they are all, in fact, coded mask telescopes. The coded mask technique is crucial for high energy imaging and for the separation and positioning of sources. Coded mask instruments also offer an almost perfect background subtraction, since, for any pointing direction, the detector pixels can be considered as split into two separate sets: one able to "see" the source and another in which the flux is blocked by the opaque elements of the mask. The latter set provides a simultaneous measurement of the background for the other on-source set under the same conditions.

All the instruments are co-aligned, with overlapping fully-coded fields of view, ranging from 4.8° for JEM-X, to $5^\circ \times 5^\circ$ for OMC, $9^\circ \times 9^\circ$ for IBIS and 16° (diagonal) for SPI. All the instruments on board *INTEGRAL* are designed in order to optimise the satellite performances. Their main characteristics can be summarised as follows:

- they are co-aligned in order to point approximately all in the same direction;
- they can operate one at a time, independently from one another;
- each of the instruments is optimised to operate in a specific energy range, sometimes overlapping those of the other instruments. This allows for a better instrument calibration to be achieved;
- three out of the four instruments operate over a wide energy range, together covering from 3 keV up to 10 MeV.

2.3 The IBIS Imager

IBIS (figure 2.3) is a gamma-ray telescope capable of observing many kinds of celestial objects, ranging from compact Galactic objects to extragalactic high energy sources. It was designed for fine imaging and for source identification; it also has a fairly good spectral sensitivity both for the continuum and for the lines. IBIS covers the entire energy range from 15 keV up to a few MeV; it has a large field of view and is able to localise faint sources at low energies with an accuracy better than a few arcminutes. Since this thesis will concentrate on data obtained by IBIS, in the following this instrument will be described in more detail.

2.3.1 Instrument Description

IBIS is a coded mask telescope, constituted by two main components: a mask which poses as the telescope aperture and a detector for collecting the incident radiation. The

Figure 2.3: IBIS during the last phases of mechanical integration at ESTEC (Ubertini et al. 2003).

detector is positioned on-axis below the mask and consists of two layers: ISGRI (*INTEGRAL Soft Gamma Ray Imager*; Lebrun et al. 2003) and PICsIT (*Pixellated Imaging CsI Telescope*; Labanti et al. 2003). ISGRI is constituted of solid state position sensitive CdTe (Cadmium Telluride) detectors, optimised to operate between 15 keV and 1 MeV. PICsIT is instead made of scintillating CsI (Cesium Iodide) crystals, optimised for a higher energy range between 175 keV and 20 MeV. This double-layer configuration ensures a good continuum and broad line sensitivity over the whole energy range in which IBIS operates. Besides this, the double-layer design allows the tracking of the 3-D path of interacting photons when an event is detected both in ISGRI and PICsIT. The subsequent use of Compton algorithms for such events enables an improvement of the signal-to-noise ratio by rejecting those events with a low probability of being caused by photons emitted by the sources in the field of view. The instrument also possesses an anticoincidence system in order to be able to reject events caused by photons present in the background or produced inside the satellite itself. A collimation system is also present so to keep the low energy response of IBIS; it consists of a passive lateral shield that limits the solid angle (and therefore the cosmic gamma-ray background) viewed directly by the IBIS FOV up to a few hundreds of keV.

2.3.2 The Coded Mask

IBIS coded mask is a rectangle of 1180 × 1142 mm^2 and 114 mm thick, constuted of three main subsystems: the *coded mask* itself, a *support panel* and a *peripheral frame*.

Ideally, a coded mask should have a null thickness in order to avoid auto-collimation effects of the incident radiation; also, opaque elements should be totally opaque and transparent elements should be totally transparent to radiation. In IBIS the closest configuration to the ideal situation has been achieved in the following way. In order to have the maximum opacity, tungsten has been used: this metal has a high atomic number (Z=92), it is very dense (ρ=19.3 g/cm^3) and it is very opaque to high energy photons. As far as the mask is concerned, its thickness has been set to 16 mm in order to maximise the weight while avoiding auto-collimation effects.

The mask consists of a surface made of elements some of which opaque and some transparent to radiation, arranged in a specific pattern. From a mathematical point of view, the mask can be considered as a matrix $\sum_{ij} a_{ij}$ where if a_{ij} is 1, then the mask element is opaque; if it is 0, then the element is transparent. In reality, however, the mask elements are neither completely transparent nor completely opaque to gamma-ray photons; each coded mask instrument has, in fact, a characteristic opacity (or transparency) curve, which describes the capability of the instrument to modulate the radiation as a function of energy, position and interaction of the photon with the mask.

The mask alone is a cuboid of $1064 \times 1064 \times 16$ mm^3, constituted by 95×95 square cells of 11.2×11.2 mm^2 each. The cells form a coded pattern, called *modified uniformly redundant array* (MURA), of 53×53 elements. Approximately half of the cells are opaque to photons in the IBIS energy range, providing an opacity of 70% at 1 MeV. The other half of the cells are open, with an on-axis transparency of 60% at 20 keV (see figure 2.4).

The support panel includes those elements necessary for sustaining the coded pixels, providing the required strength for the launch conditions and the temperatures in orbit. The peripheral frame has the task of keeping together the whole system.

The image produced on the detector plane is coded and a numerical decoding process is thus necessary before performing any scientific analysis on the data. The useful elements required for the image reconstruction are the information on the incident photons direction and on the spatial modulation of the flux in the field of view. In the assumption that a source could be considered as positioned at infinity, when the photons arrive on the mask the opaque elements prevent them from arriving on the detector plane and only where there are transparent elements will the radiation reach the detector. As a consequence, the source casts a shadow of the mask, the so-called *shadowgram,* on the detector plane. The shadow position depends only on the direction of the incident photons and thus on the position of the object in the sky; the intensity of the radiation, and so the contrast of the shadow, depends on the real intensity of the source. Another source in the field of view, in a different position, will cast a different shadow and so on for all other

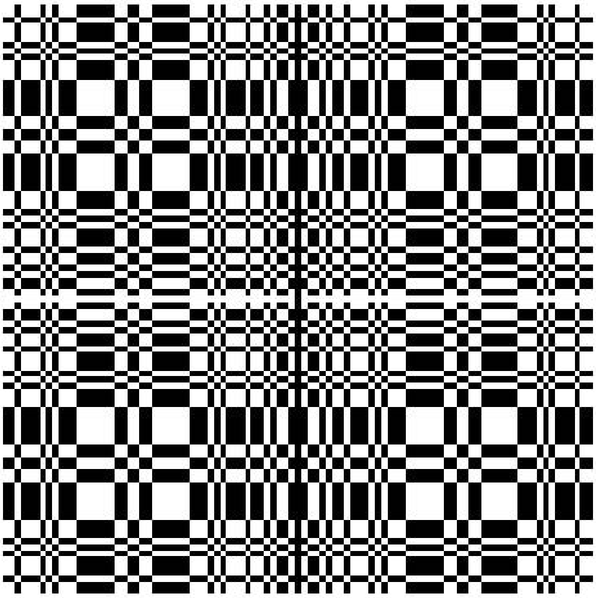

Figure 2.4: The IBIS coded mask pattern (Goldwurm et al. 2003).

sources in the FOV. The detector records several mask shadows, each shifted with respect to one another: these are the coded images of the sources in the FOV. The shadow of the mask is, in other words, shifted with respect to the positions of the sources in the sky. The image decoding process is based on the shifting of the shadows one on top of the other. This is accomplished by knowing the orientation of the satellite in space and by analysing the data from the detector, until the original FOV is reconstructed. Then a specific algorithm is applied, such as a *cross-correlation* algorithm, and the image is finally decoded. In this way, positions and count rates for each source are obtained, appearing as peaks in the correlation function. This type of spatial decoding, which exploits the flux modulation in spatial coordinates, is used in each of the three high energy instruments on board *INTEGRAL*.

2.3.3 The Detection System

As previously mentioned, IBIS is made of two detectors, both position sensitive and independent from one another. Photons can be detected in three ways:

1. Direct detection in ISGRI: a photon arrives on a single pixel of the semi-conductor, interacts and generates an electrical pulse.

2. Direct detection in PICsIT: a photon passes through ISGRI and it is detected in PICsIT, producing one or more scintillation events.

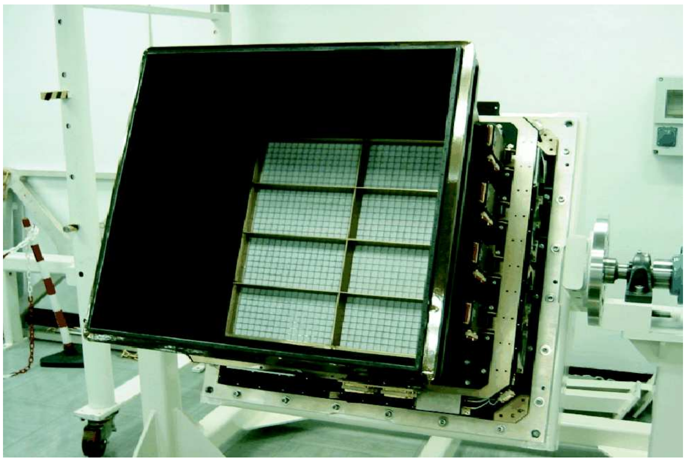

Figure 2.5: The ISGRI detector (Lebrun et al. 2003).

3. Detection in both ISGRI and PCsIT (Compton mode): the photons arrive both in ISGRI and in PICsIT and produce secondary photons through Compton scattering, then are detected by the two instruments. Multiple events occurring only in ISGRI are rejected.

Note, however, that the system cannot determine the order of the interactions, i.e. if the interactions occur first in ISGRI and then in PICsIT or viceversa.

•ISGRI

ISGRI (see figure 2.5) consists of a pixellated array of CdTe semi-conductors, forming a position sensitive detector plane optimised to operate in the 15-1000 keV band. The semi-conductors operate at room temperature, with an optimal temperature range between 0°C and +20°C.

These detectors work in a very simple way: when the photons hit the solid material, electrons are extracted from the metal atoms, thus forming electron-hole pairs. The electrons are then collected under the action of an external electric field. The measure of the generated charge is essentially proportional to the energy of the incident photons, after a correction for the collection time of the electrons is applied.

ISGRI is constituted by 8 identical *Modular Detection Units* (MDUs), each containing 2048 pixels read by 512 *Application Specific Integrated Circuits* (ASICs). Each of the 16348 CdTe pixels of which ISGRI is made have dimensions of 4×4 mm^2 and a thickness of 2 mm. The small pixel area is responsible for the good spatial resolution, even if the pixels relative thinness implies that they can be used only at low energies. ISGRI total area is about 3600 cm^2, while the operative area is 2621 cm^2.

•PICsIT

PICsIT is composed of an array of scintillation counters. In this kind of detectors, the physical process of scintillation is exploited: when a gamma-ray photon enters one of the crystals of the detectors, it interacts with its atoms, extracting electrons via the photoelectric and Compton effects. The extracted electrons, in turn, have enough energy to excite bound electrons that, when de-exited, emit optical radiation. The photons emitted during the de-excitation process are then collected by a photomultiplier which produces a signal proportional to the number of collected photons and therefore also to the energy loss of the incident high energy photon.

PICsIT is made up of a pixellated array of CsI(Tl) bars, optically bound to custom-made PIN photodiodes. The instrument design provides a high degree of modularity; the CsI layer is divided in 8 rectangular modules of 512 detection elements each, for a total of 4064 CsI pixels. Each pixel has dimensions of 8×8 mm^2 and is 3 cm thick; the sensitive area is 2890 cm^2.

2.3.4 The Anticoincidence System

IBIS uses an anticoincidence system to reject or accept events, whether these are photons detected in the field of view or background particles or photons propagated by or induced in the satellite itself.

The anticoincidence system is made of 16 independent modules, the *VETO Detector Modules* (VDM), each constructed from 2 BGO (Bismuth Germanate) crystals 150×75 mm^2 and 20 mm thick; the crystals are coupled together and read out by two photomultipliers. The entire anticoincidence system is divided into two halves: 8 VDMs (2 on each side) shield every side of the detector, while the other 8 VDMs are positioned below the detector array. The structure provides shielding from photons and/or charged particles produced in the satellite; it is also very sensitive to events caused by energetic protons and heavy ions.

2.3.5 The Anticollimation System

The IBIS anticollimation system comprises two mechanically independent subsystems, built with passive materials such as tungsten and lead. The subsystems are the *Hopper*, a 550 mm high structure positioned above the first detector layer, and the *Tube*, made of four walls that link the upper part of the Hopper to the four sides of the coded mask, geometrically defining the field of view of the two detectors and IBIS. The Tube is made of lead, with a variable thickness that becomes progressively thinner towards the mask, adopted in order to minimise the total mass; the Hopper is made of tungsten layers 1.0 mm thick.

2.3.6 The Detector-Mask System

The mask and detector of a coded mask telescope can have several configurations, depending on their relative dimensions:
a) the mask and the detectors have the same dimensions;
b) the detector is larger than the mask;
c) the mask is larger than the detector.

What changes among these configurations is the field of view. The field of view is constituted by two major zones:

- **Fully Coded Field of View** (FCFOV), defined as the solid angle under which the detected flux is completely modulated by the mask. In other words, a source is considered to be in the FCFOV if it projects the whole shadow of the mask pattern on the detector plane. In this case the image will be fully coded.

- **Partially Coded Field of View** (PCFOV), defined as the solid angle under which the detected flux is not fully coded by the mask pattern. This happens for sources that project onto the detector only part of the mask pattern, because some of the projected rays miss the detector plane.

The mask-detector geometry is therefore very important: configuration (a) generally produces a partially coded field of view, except for on-axis sources; configurations (b) and (c) allow for large fully coded fields of view. The most common geometrical configuration used in gamma-ray astronomy is the one with the mask larger than the detector, i.e. configuration (c), which is the one used in IBIS. The reason for choosing configuration (c) instead of (b) resides in the fact that, despite having the same field of view, the former allows for the use of smaller detectors, thus limiting the detection of the gamma-ray background. In configuration (c), the mask is generally made of a mosaic twice as big as the basic pattern, minus a line and a column in order to avoid ambiguity in the signal decoding procedure. In IBIS the FCFOV is $9°\times9°$, while the PCFOV is $29°\times29°$.

At such high energies as in the X-ray and gamma-ray domains where diffraction is negligible, the angular resolution (i.e. the minimum angle at which two nearby sources are distinguishable) depends both on the dimensions of the mask elements and on their distance from the detector. For an on-axis object one will have:

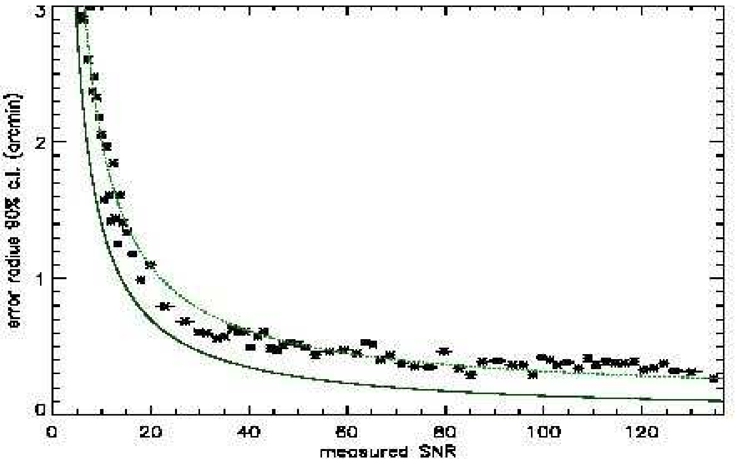

Figure 2.6: PSLA (90% confidence level) as a function of the signal-to-noise ratio (Gros et al. 2003).

$$\Delta\theta = \tan^{-1}(\frac{d}{H}) \tag{2.1}$$

for the point spread function, where *d* is the linear dimension of the mask element and *H* is the distance of the mask from the detector. If the source is instead off-axis at a certain angle φ, the angular resolution is:

$$\Delta\theta = \tan^{-1}(\frac{d}{H}) \times \cos^2\varphi \tag{2.2}$$

The angular resolution is consequently determined by the *d/H* ratio; since in IBIS d=11.2 mm and H=3.2 m, the angular resolution turns out to be $12'$ for on-axis sources and higher for off-axis sources.

Another important parameter is the capability of the detector to localise sources; this parameter is the so-called Point Source Location Accuracy (PSLA) and it is determined by the signal-to-noise ratio (σ), by the pixel area on the detector (Δx) and by the distance (H) between the mask and the detector:

$$\Delta\alpha \simeq (\frac{\Delta x}{\sigma H}) \tag{2.3}$$

Figure 2.6 shows ISGRI PSLA as a function of the signal-to-noise ratio derived from the observations (points) and from theory (lines) as reported by Gros et al. (2003). The absolute localisation (after correcting for bad alignment) is less than $1'$ for sources detected at a significance level higher than 20σ and $3'$ for sources at a significance level of about 7σ.

Instrument	**Background (solar max.)** $\mathbf{ct\,s^{-1}}$	**Crab (on-axis)** $\mathbf{ct\,s^{-1}}$
ISGRI	600	220
PICsIT	3650	7.7

Table 2.2: Ratios between the observed background and the Crab Nebula counts.

2.3.7 The Instrumental Background in IBIS

In the energy range in which IBIS operates, the background is higher than the measured intensity for most of the sources. The main background components in IBIS are:

- the cosmic diffuse gamma-ray background, relevant above all at low energies (below 100 keV). It is a very important component in ISGRI;
- the background due to energetic particles induced by the hadrons in cosmic rays interacting with the satellite. This component is relevant in ISGRI at high energies (above 100 keV) and for PICsIT in the whole operating energy range.

There are also other effects that can influence the background, such as solar activity or the anticoincidence system performance. The solar particle background varies during the solar cycle; it has its minimum during the peak of solar activity, when the solar magnetic field is more intense, preventing the propagation of cosmic rays throughout the inner solar system. The solar background is instead higher by a factor of two during solar minima.

The reduction of the background counts by the anticoincidence system has been evaluated during the verification phase of in-flight IBIS performances. Its value is about 50% for ISGRI and about 40% for PICsIT, compared with when the anticoincidence system is switched off. The ratios of the observed background during the solar maximum and the on-axis Crab Nebula counts are reported in table 2.2. The reported ratios have been determined during the in-flight calibration.

Occasionally a high count number can be observed in some of PICsIT pixels close to the lower energy threshold of the instrument (160-250 keV). In images obtained after few thousands second of integration time, the peaks are not visible because they are uniformly distributed on the entire detector and thus cannot be removed. The contribution of these events is about 30% at low energies and 10% on the whole PICsIT operating energy band.

IBIS is positioned close to SPI and JEM-X, which all have similar configurations. Since gamma-ray photons are highly penetrating, it is possible for them to pass through the satellite or the instruments, as well as through the coded masks, thus being detected by all the instruments. For this reason, off-axis gamma-rays (generally above 300 keV) passing through the SPI coded mask can produce a shadowgram of the mask on the IBIS detectors. Although in this case the IBIS field of view is enhanced, a bright gamma-ray source adds additional counts and modulations to the IBIS histograms, complicating the image reconstruction.

In order to solve the problem of the background determination, an opportune dithering observation strategy has been devised. This strategy consists in a series of pointings 2° off-axis with respect to the target of the observation. The satellite follows the dither pattern continuously during a single observation. There are two different types of dithering:

1. the *rectangular dithering* employs a square pattern centered on the target position (one on-axis pointing and 24 off-axis pointings, each separated by 2° in a rectangular pattern). This mode is used when there are several point sources in the FOV, sources with unknown positions and diffuse extended emission;
2. the *hexagonal dithering* employs a hexagonal pattern centered on the target position (one on-axis pointing and 6 off-axis pointings, each separated by 2° on a hexagonal pattern). This mode is used only for observations of point or isolated sources, with known positions, where no contribution from off-axis sources is expected.

2.3.8 IBIS Sensitivity

The gamma-ray energy band is faced with the unfavourable situation in which the source signal is smaller than the instrumental noise, i.e. $S/N \ll 1$. In this case, the continuum sensitivity can only be computed in a simplified way, assuming both the mask and the detector to be ideal. The expression used, to a first approximation, is:

$$F_{min} = (\sigma/\varepsilon(E_\gamma))\sqrt{4B(E_\gamma)/(A \times T \times \Delta E)} \text{ photons cm}^{-2}\text{ s}^{-1}\text{ keV}^{-1} \tag{2.4}$$

where ΔE is the energy band, B is the background relative to that band (measured in counts $\mathrm{cm^{-2}s^{-1}\ keV^{-1}}$), σ is the significance in the same band, A is the detector area, T is the observing period and $\varepsilon(E_\gamma)$ is the detector efficiency.

As far as the line sensitivity is concerned, it is described approximately by:

$$F_{min} = F(\frac{\sigma}{\varepsilon(E_\gamma)})\sqrt{4B(E_\gamma)\Delta E/(A \times T)} \text{ photons cm}^{-2}\text{ s}^{-1} \tag{2.5}$$

where ΔE is the detector resolution (FWHM) in keV, relative to the considered emission line; F depends on the signal-to-noise ratio and varies between 1.2 (when the background dominates) and 1.0 (when the signal dominates).

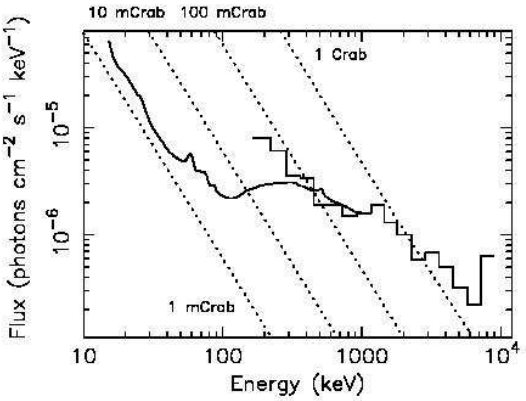

Figure 2.7: IBIS continuum sensitivity, obtained from in-flight background measurements, with an exposure of 10^5 s, 3σ detection level and sampling ΔE=E/2. The solid line refers to ISGRI; the solid-dashed line to PICsIT and dashed line to sources with fluxes of 1, 10, 100 mCrab and 1 Crab (Γ=-2) (Ubertini et al. 2003).

Using these two formulae it is possible to evaluate both ISGRI and PICsIT sensitivities for the continuum and discrete lines (figure 2.7). The plots are relative to a 3σ detection with observing times of 10^5 (continuum) and 10^6 (lines) seconds. The continuum sensitivity is given by ΔE=E/2. The line sensitivity relates to a narrow, unresolved line and to pre-launch estimates. As can be seen from figure 2.7, at low energy even sources with a few mCrab flux can be detected.

2.4 The Other Instruments On-Board *INTEGRAL*

2.4.1 The Spectrometer SPI

The spectrometer SPI is characterised by a high spectral resolution over a very wide energy range (20 keV to 8 MeV, see table 1) and partly overlapping the IBIS energy range. The instruments have especially been designed to work both independently and together: if, on one hand, IBIS provides a good angular resolution, on the other SPI has a good spectral resolution so that, when operated together, the two instruments produce complementary results.

As already mentioned, SPI is a coded mask instrument. The tungsten mask (see figure 2.8) is made of 127 hexagonal blocks, 30 mm thick and 60 mm across the flats, 63 of which are opaque (93% at 1 MeV) and 64 transparent to radiation, i.e. empty (60% at 20 keV, 80% at 60 keV due to support materials). The mask is positioned 1.7 m above the detector and it is held in place by a carbon fibre panel. The detector is made of 19

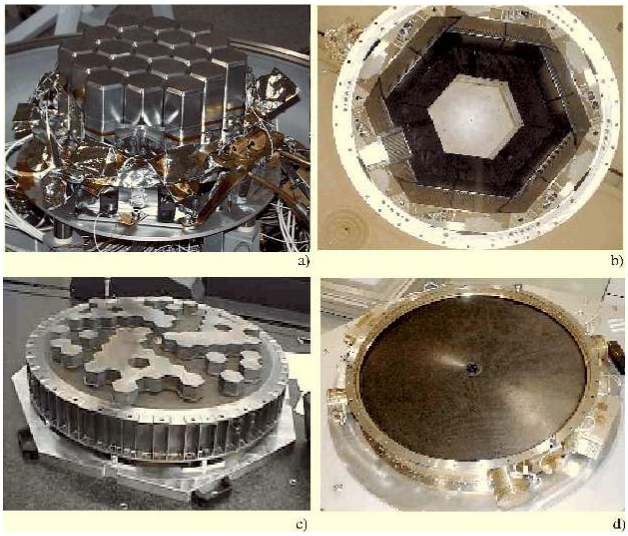

Figure 2.8: The spectrometer SPI (Vedrenne er al. 2003).

hexagonal elements of germanium crystals, 3.2 cm wide across the flats and 7 cm deep, cooled down at 85°. The detector area (500 cm^2) is smaller than that of the mask. The geometry of the detector-mask system allows large portions of the sky to be observed even if with a poor angular resolution of 2.5 degrees. The fully coded field of view is 16 degrees wide, while the partially coded field of view is 31 degrees wide.

Despite the poor angular resolution, SPI offers a better spectral resolution of 2.5 keV at 1.3 MeV when compared with IBIS. The temporal resolution of the two instruments is comparable (52 μs for SPI and 61 μs for IBIS/ISGRI). SPI continuum sensitivity is lower than that of IBIS at low energy, while it is comparable at around 1 MeV, whereas line sensitivity is better in SPI. In the present work, data collected with SPI have not been used, since its poor angular resolution may result in source contamination in the field of view; in this thesis some of the analysed AGN are seen through the Galactic plane and thus are located in very crowed regions, making the probability of a contaminated detection very high.

2.4.2 The X-ray Monitor JEM-X

JEM-X (figure 2.9 and table 1) plays a role in the identification of sources and in the analysis and interpretation of *INTEGRAL* data from X-ray emission of sources. JEM-X can perform simultaneous X-ray observations together with the satellite main instruments, IBIS and SPI, and produces images with an angular resolution of 3$'$ with a 30$''$ PSLA in the 3-35 keV range. JEM-X can thus localise sources more accurately than IBIS; spectra can also be extracted down to 3 keV, i.e. below the IBIS operating energy range, where

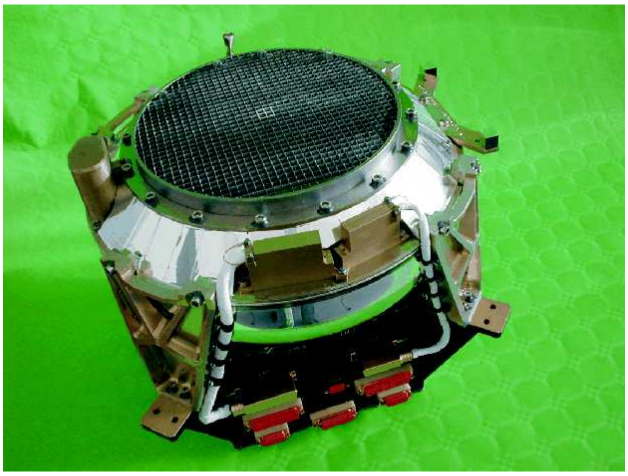

Figure 2.9: The X-ray monitor JEM-X (Lund et al. 2003).

many interesting physical processes occur. However, JEM-X is characterised by a low sensitivity and operates in a narrow energy range; besides, its small field of view implies that a source is visible for a shorter period of time than in IBIS, resulting in a weaker signal from the observed object. For these reasons, data collected with JEM-X have not been used in this thesis, in which we made use of more sensitive instruments like *XMM-Newton* or *Chandra* (see next chapter).

This instrument consists of two identical coded mask telescopes, independent from one another. The tungsten mask is circular, with a diameter of 535 mm and a thickness of 0.5 mm. The mask has about 24247 hexagonal holes 3.3 mm wide. The detectors are gas counters based on a gas proportional Xe/CH_4 counter and employ microstrips to locate the position of X-ray events. The gas in the detector is composed by 90% xenon and 10% methane at a pressure of 1.5 bar, while the main body is made of stainless steel; each of the two detectors has an area of 500 cm^2. The geometry of the mask-detector system allows only a small portion of the sky to be observed at one time ($4.8^\circ \times 4.8^\circ$ FCFOV). The energy resolution is 2 keV at 22 keV, while the temporal accuracy is better than 200 μs. The sensitivity is less than those of the other instruments but it is enough to extend the spectral information to low energies for bright sources observed by IBIS and SPI.

2.4.3 The Optical Monitor OMC

The OMC (figure 2.10 and table 1) allows optical observations to be performed simultaneously with the X-ray and gamma-ray observations carried out by the other instruments on board. The instrument is an optical monitor based around a CCD of 2055×1056 pixels (with an imaging area of 1024×1024 pixels), cooled down to a temperature of -80°C. The

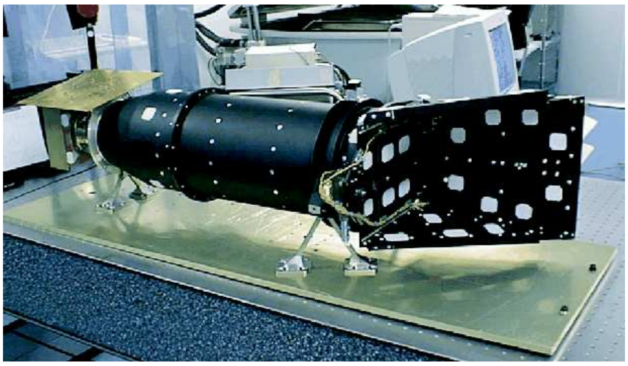

Figure 2.10: The optical monitor OMC (Mas-Hesse et al. 2003).

CCD is placed on the focal plane of a refractive optical system, constituted by a 50 mm lens with a 5°×5° field of view. The filter applied is a Johnson V filter, operating between 550 and 850 nm. The detectable limiting magnitude is 18 for a 5 ksec observation; the angular resolution is 25″ with a 6″ PSLA, while the temporal accuracy is around 1 second.

Chapter 3

X-ray Missions

3.1 Introduction

In order to get a thorough picture of the mechanisms powering AGN, broad-band X- and gamma-ray observations are essential. The analysis of broad-band spectra of AGN allows to study and determine their continuum emission and also those features occurring at high energy, such as the reflection hump and the high energy cut-off. As already mentioned in the previous chapter, in this thesis data collected by the IBIS/ISGRI instrument on-board the *INTEGRAL* satellite are combined together with archival X-ray measurements taken from several X-ray observatories, such as *XMM-Newton*, *Chandra*, *Swift/XRT* and *ASCA*.

The combination of IBIS/ISGRI data with other instruments' measurements poses however the problem of the non-simultaneity of the observations. This problem can be solved by introducing normalisation constants between IBIS and the other instruments. These take into account cross-calibration mismatches and/or intrinsic variability in the spectra of the observed objects.

The instruments chosen for this thesis are all characterised by good sensitivity and good positional accuracy, which in many cases allowed us to localise sources previously not recognised as AGN. Thanks to the accurate positioning of these sources, follow-up optical spectroscopy and subsequent classification has been made possible, enlarging the number of newly discovered, gamma-ray detected active galaxies.

The X-ray telescopes and instruments employed in the following analysis are *XMM*/MOS and pn, *Chandra*/ACIS, *Swift*/XRT and BAT and *ASCA*/GIS; a brief description of each instrument and relevant X-ray detectors is given in the following sections.

Instruments	**EPIC MOS**	**EPIC pn**	**RGS**	**OM**
Bandpass	0.15-12 keV	0.15-15 keV	0.35-2.5 keV	180-600 nm
Orbital target visibility	5-135 ks	5-135 ks	5-135 ks	5-145 ks
Sensitivity	$\sim 10^{-14(a)}$	$\sim 10^{-14(a)}$	$\sim 8\times 10^{-5(b)}$	20.7 mag
Field of View	30′	30′	~5′	17′
PSF (FWHM/HEW)	5″/14″	6″/15″	-	1.4″-2.0″
Pixel size	40 μm (1.1″)	150 μm (4.1″)	81 μm (9×10^{-3} Å)	0.48″
Timeing Resolution	1.5 ms	0.03 ms	0.6 s	0.5 s
Spectral Resolution (at 1 keV)	~ 70 eV	~80 eV	0.04/0.025 Å	$350^{(c)}$

a: in units of erg $\mathrm{cm}^{-2}\ \mathrm{s}^{-1}$; b: O VII 0.57 keV line flux in photons $\mathrm{cm}^{-2}\mathrm{s}^{-1}$;
c: resolving power ($\lambda/\Delta\lambda$) with UV and optical grism.

Table 3.1: *XMM-Newton* Instruments Main Characteristics (from the /emphXMM-Newton User's Handbook).

3.2 The *XMM-Newton* Observatory

The *XMM-Newton* satellite was launched on December 10, 1999 by an Ariane V rocket. The satellite, still in orbit and performing well, was inserted into a highly eccentric orbit with a period of ~48 hours. The perigee is 7000 km and the apogee 114 000 km, with an inclination of ~-40°. This particular orbit was chosen so that the main X-ray instruments could be passively cooled to temperatures between -80° and -100°. Scientific operations can only be performed when the satellite is above altitudes of ~60 000 km, since the lower part of the orbit passes through the Earth's radiation belts. *XMM-Newton* is part of ESA's cornerstone missions within the *Horizon 2000* programme.

The satellite comprises two large payload modules and carries on-board two types of telescopes: three grazing incidence Wolter type I X-ray telescopes, with different X-ray detectors in their focal planes, and a 30 cm optical/UV telescope. The scientific instruments on-board *XMM* are:

- The *European Photon Imaging Camera* (EPIC), which employs 3 CCD cameras for X-ray imaging and also provides moderate resolution spectroscopy and X-ray photometry. The EPIC instrument has two different sets of cameras, MOS and pn, which will be described in more detail later, mounted on the focal planes of the X-ray telescopes.

- The *Reflection Grating Spectrometer* (RGS), made of 2 identical spectrometers for high resolution X-ray spectroscopy and spectro-photometry.

- The *Optical Monitor* (OM), designed for optical/UV imaging and grism spectroscopy.

The satellite main characteristics can be summarised as follows (see also table 3.1):

1. All the instruments can operate simultaneously when conditions are favourable (i.e. brightness constraints). The instruments can also work independently.

2. The X-ray telescopes on-board *XMM-Newton* have a total mirror geometric effective area of 1550 cm^2 at 1.5 keV for each telescope, reaching 4650 cm^2 in total. The very large effective area implies a very high sensitivity.

3. The X-ray telescope Point Spread Function (PSF) is 6$''$ (FWHM), providing a very good angular resolution.

4. The EPIC cameras have a moderate spectral resolution (resolving power: E/ΔE$\sim$20-50). The RGS spectrometers have a much higher spectral resolution with E/ΔE$\sim$200-800.

5. Simultaneous optical/UV observations allow the identification of X-ray sources and provide imaging of the surrounding field.

6. The *XMM-Newton* highly elliptical orbit offers almost continuous target visibility for up to 40 hours.

Since in this thesis only data taken from the EPIC cameras have been employed, in the following a more detailed description of this instrument will be given.

3.2.1 The X-ray Telescopes and the EPIC Cameras

XMM-Newton is equipped with three X-ray telescopes, consisting of 58 grazing incidence Wolter I mirrors, nested in a coaxial and co-focal configuration, providing a large collecting area over a wide energy band (figure 3.1). The mirrors grazing incident angles vary from 17 to 42 arcminutes, their focal length is 7.5 m and the diameter of the largest mirror is 70 cm. The X-ray detectors (i.e. the EPIC cameras) are placed on the focal plane of each telescope.

The *XMM-Newton* EPIC cameras (2 MOS CCDs and a pn CCD; Turner et al. 2001 and Strüder et al. 2001) offer the possibility to perform highly sensitive imaging over a field of view of $\sim 30'$ in the 0.15-15 keV energy range, with moderate spectral and angular resolution. A sketch of the detector layout and the baffled X-ray telescope FOV of the EPIC MOS and pn cameras is shown in figure 3.2.

The two MOS and the pn CCDs operate in photon counting mode, producing an event list which contains every detected photon, its attributes (i.e. x,y position), its arrival time and its energy.

The MOS chip array consists of 7 individual, front illuminated identical CCDs, offset with respect to each other, and each made of 600×600 pixels. The imaging area is

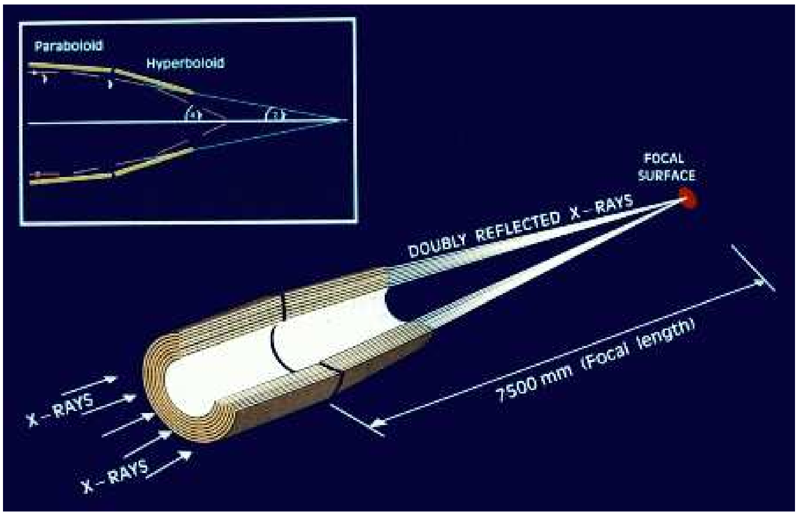

Figure 3.1: The light path in *XMM-Newton*'s open X-ray telescope with the pn camera in focus (not to scale; from the *XMM-Newton* User's Handbook).

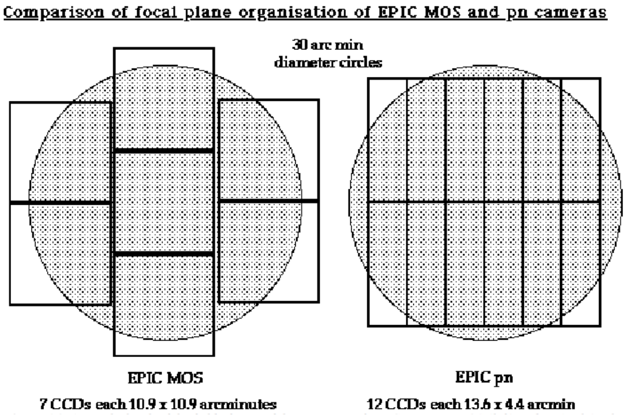

Figure 3.2: A sketch of the field of view of the EPIC MOS and pn cameras. The shaded circle depicts a 30′ diameter area (from the *XMM-Newton* User's Handbook).

$\sim$2.5×2.5 cm^2, so that a mosaic of seven images (1 for each CCD) covers the entire focal plane (62 mm in diameter, corresponding to 28.4′). The pn camera is composed of a single silicon wafer with 12 integrated CCD chips, each made of 64×189 pixels.

The EPIC cameras are designed to produce X-ray images of the sky; the number of images taken depends on the speed at which the detectors are read out from a storage area where data are temporarily collected. There are two main modes of data acquisition:

- "Full Frame" and "Extended Full Frame" (pn only): in both modes all pixels are read out and the entire FOV is covered. The observer can however choose to receive different types of images: a full 600×600 pixels image every 2.6 s, a 300×300 pixels image every 0.9 s (*Large Window Mode*) or a 100×100 pixels image every 0.3 s (*Small Window Mode*).

- "Partial Window". The central CCD of the MOS cameras can be operated in a different data acquisition mode, reading out only part of the CCD. For the pn camera, only half of the area of the 12 CCDs is read out.

- "Timing Mode", in which a 100×1 pixels image is produced every 1.5 ms.

The observer can also choose to employ an optical blocking filter in the low energy part of the passband, influencing the EPIC effective area. The need for using filters is due to the fact that the EPIC CCDs are also sensitive to infrared, visible and UV light. In fact, if a source has a high optical flux, the X-ray signal might be contaminated by the optical photons, giving problems when analysing the data. In order to avoid any problem during data analysis, the EPIC cameras are equipped with aluminased optical blocking filters; there are three types of filters: thick, medium and thin.

As far as the background is concerned, in the EPIC cameras it is essentially made of two components, one due to the cosmic X-ray background and one instrumental. The instrumental background is then divided in two: a component due to the detector noise (important below 0.2 keV) and one due to particles interacting with the satellite or the detectors themselves (important above a few keV). Again, the particle induced background can be further subdivided in two more components: an external flaring component with a strong and rapid variability, and a second internal component. The flaring component can be caused by soft photons, funneled towards the detectors by the mirrors. The internal component can be ascribed to high energy particles interacting with the satellite structure and the detectors.

In the EPIC cameras the centre of the on-axis PSF is narrow and does not vary much over a wide energy range (0.1-4 keV); above 4 keV the PSF is only slightly energy dependent. The PSF is not the same for all the detectors, but it varies from 12.5″ for the pn to ∼4″ for the two MOS cameras. Extended sources in the centre of the FOV could be observed with a spatial resolution of 5″. One of the problems that can affect the PSF is when pile-up occurs (i.e. when two X-ray photons hit the same pixel) and the count rate exceeds a few counts per frame. Another factor affecting the PSF is its dependence on the off-axis angle.

3.3 *Chandra*

The *Chandra* Observatory (figure 3.3), previously known also as *AXAF* (Advanced X-ray Astrophysics Facility), is one of NASA's "Great Observatories" and is the product of a large cooperation between the United States and Europe. The spacecraft, which is still fully operational, was launched on July 23, 1999 by the Space Shuttle *Columbia* and initially deployed on a low-Earth orbit at an altitude of about 240 km. The satellite was subsequently boosted to its operational orbit, with a perigee of 10 000 km and an apogee of 140 000 km. The inclination of the orbit is 28.5 degrees, with an orbital period of 63.5 hours. The satellite remains above the Earth's radiation belts for more than 70% of the orbital period, ensuring, together with the characteristics of the orbit, a high observing efficiency.

The main scientific instrument on-board the satellite is the X-ray telescope, made of concentric, precision-figured, superpolished Wolter-1 telescopes. The telescope PSF is 0.5″ (FWHM) and the Half-Power Diameter (HPD) is less than 1″. On the focal plane is positioned the ACIS (Advanced CCD Imaging Spectrometer; Garmine et al. 2003). The ACIS-I instrument, made of 2-by-2 array of large-format front illuminated CCDs of 2.5 cm^2, is designed for high angular resolution spectrometric imaging over a 17-arcmin-square field of view. The ACIS-S, a 6-by-1 array of 4 front illuminated CCDs and two back illuminated CCDs, serves both as the primary read out detector for the High Energy Transmission Grating (HETG) and also provides high angular resolution spectrometric imaging extending to lower energies over a smaller field of view (8-arcmin-square). The other camera placed on the focal plane of the X-ray telescope is the High Resolution Camera (HRC; Murray et al. 2000), which provides high angular resolution imaging over a 30-arcmin-square field of view. The scientific payload also comprises a Low Energy Transmission Grating (LETG; Brinkman et al. 2000) and a High Energy Transmission Grating (HETG; Market et al. 1994). The LETG provides high resolution spectroscopy ($E/\Delta E>1000$) between 0.07 and 0.15 keV, while the HETG is designed to achieve high resolution spectroscopy from 0.4 to 4 keV (with the Medium Energy Gratings, MEG) and from 0.8 to 8 keV (with the High Energy Gratings, HEG).

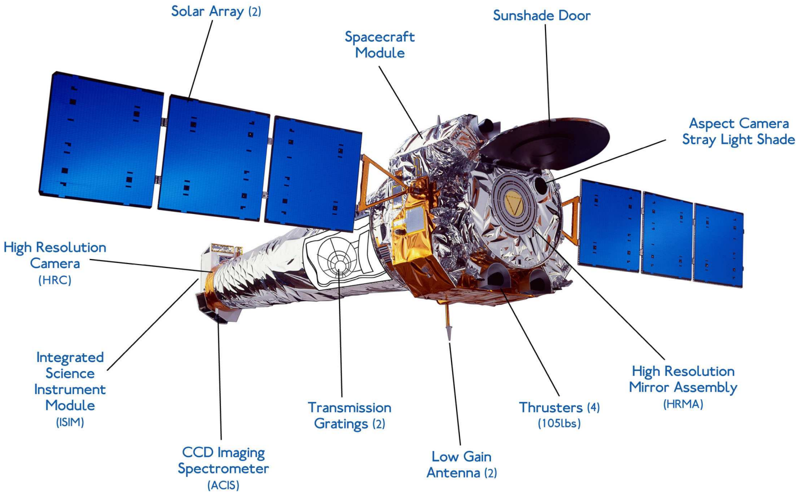

Figure 3.3: A sketch of the *Chandra* Observatory. The main components and scientific instruments are labelled (credits: http://chandra.harvard.edu/).

In this thesis, *Chandra* data have been employed only for one source, namely QSO B0241+62 (see chapter 4 and 6).

3.4 *Swift*

The *Swift* Gamma-ray Burst Explorer (Gehrels et al. 2004) is a NASA's multiwavelength observatory mainly dedicated to the study of gamma-ray burst (GRBs) and their afterglows. *Swift* is one of NASA's medium explorer (MIDEX) programmes and was launched on November 20, 2004 on a Delta 7320 rocket and injected into a low-Earth orbit. The hardware on-board the satellite has been developed by an international team from the US, the UK and Italy; France, Japan, Germany, Denmark, Spain and South Africa are also scientifically involved in the mission.

The *Swift* satellite (figure 3.4) is composed of three main instruments: a Burst Alert Telescope (BAT; Barthelmy 2004), aimed at identifying GRBs and determining their position with an accuracy of few arcminutes; an Ultraviolet/Optical Telescope (UVOT; Roming et al. 2005); and an X-ray Telescope (XRT; Burrows et al. 2004).

3.4.1 The BAT Instrument

The Burst Alert Telescope (figure 3.5), operating in the 15-150 keV energy range is a large field of view (2 sr), coded aperture instrument with a high sensitivity. It is designed to provide critical GRB triggers and a few arcminute positions. Since its coded aperture

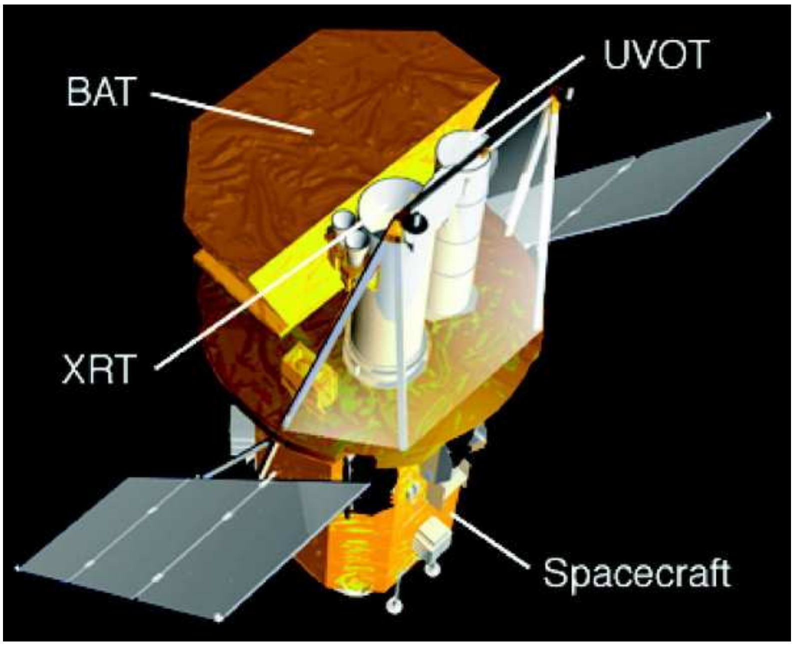

Figure 3.4: A computer generated image of the *Swift* satellite and its main instruments (credits: http://swift.gsfc.nasa.gov/docs/swift/swiftsc.html).

field of view always covers both the XRT and UVOT FOVs, long-lived gamma-ray emission from GRBs can be studied simultaneously with the X-ray and optical instruments. Along with the search for GRBs, BAT is also surveying the hard X-ray sky and monitoring X-ray transients. The BAT accumulates sky maps every 5 minutes; sky images are then searched to detect sources and their positions with a sensitivity of ~1 mCrab.

Despite using BAT data for the analysis (see following chapters), these have not been reduced as part of this thesis work, but have been downloaded from a public database made available by the *Swift* team. Therefore the instrument will not be described in much detail here.

3.4.2 The XRT Telescope

The XRT (see figure 3.6 and table 3.2 for a technical overview) is a focussing X-ray telescope with a 110 cm^2 effective area, a 23 arcmin field of view and an 18 arcsec resolution (HPD), operating in the 0.2-10 keV energy range. It uses a grazing incidence Wolter I telescope that focusses the X-rays onto a CCD at a focal length of 3.5 m.

The instrument has three read-out modes: the Imaging Mode, the Windowed Timing Mode and the Photon Counting Mode. The Imaging Mode produces an integrated image by measuring the total energy deposited per pixel, but does not allow spectroscopy. The Windowed Timing Mode has a high time resolution (2.2 ms); it allows spectroscopy

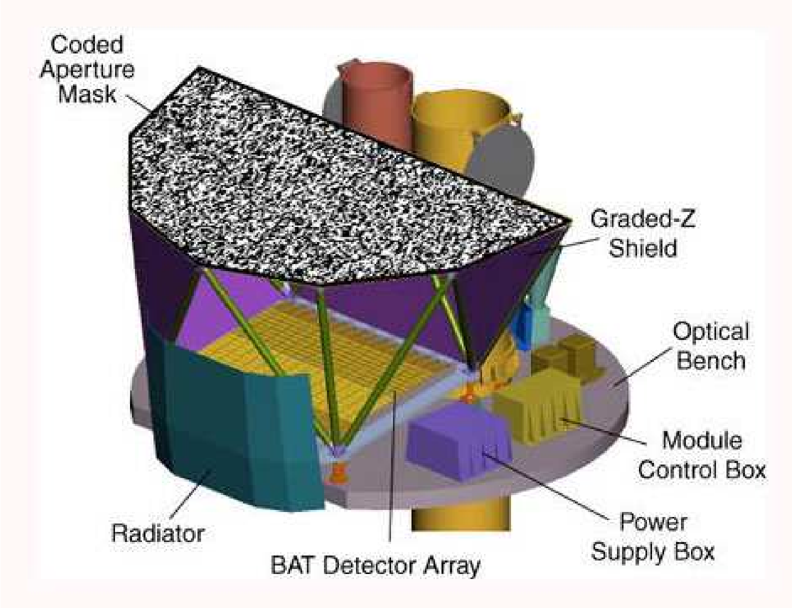

Figure 3.5: A diagram of the Burst Alert Telescope aboard the *Swift* satellite (credits: http://swift.gsfc.nasa.gov/docs/swift/swiftsc.html).

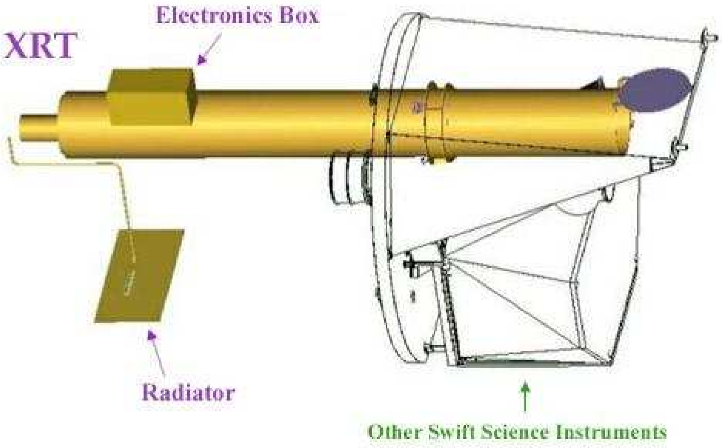

Figure 3.6: A diagram of the X-ray Telescope aboard the *Swift* satellite (credits: http://swift.gsfc.nasa.gov/docs/swift/swiftsc.html).

Telescope:	Wolter I (3.5 m focal length)
Detector:	e2v CCD-22
Detector Format:	600×600 pixels
Pixel Size:	40 μm×40 μm
Readout Modes:	Image Mode (IM) Windowed Timing (WT) Mode Photon-Counting (PC) Mode
Pixel Scale:	2.36 arcsec/pixel
Field of View:	23.6×23.6 arcmin
PSF:	18″ HPD @ 1.5 keV 22″ HPD @ 8.1 keV
Position Accuracy:	3″
Time Resolution	0.14 ms, 1.8 ms or 2.5 s
Energy Range:	0.2-10 keV
Energy Resolution:	140 eV @ 5.9 keV (at launch)
Effective Area:	~125 cm^2 @ 1.5 keV ~20 cm^2 @ 8.1 keV
Sensitivity:	2×10^{-14} erg cm^{-2}s^{-1} in 10^4 sec
Operation:	Autonomous

Table 3.2: XRT Instrument Characteristics.

for bright sources and is most useful for objects with F<10^{-7} erg cm^{-2}s^{-1} (5 mCrab). The Photon Counting Mode is capable of retrieving spectral and spatial information for sources with 2×10^{-14}<F<2×10^{-11} erg cm^{-2} s^{-1} (1 mCrab to 45 mCrab).

The mirror module is composed of 12 nested gold-coated Ni mirrors; the focal plane camera houses an *XMM*/EPIC MOS CCD, which has an image area of 600×602 pixels (40 μm×40 μm in size, corresponding to 2.36 arcsec). The XRT structure is made of an optical bench interface flange and a telescope tube composed by two sections: the forward telescope tube, supporting the star trackers and the telescope doors, and the rear section which houses the focal plane camera.

The main scientific requirements of the XRT instrument are rapid and accurate positioning (<5 arcsec), moderate resolution spectroscopy (>400 eV at 6 keV) and accurate photometry. The centroid of a point source image can be determined to sub-arcsec accuracy in detector coordinates (Hill et al. 2004); the XRT energy resolution at the time of launch was 140 eV at 6 keV. The XRT read-out modes are designed to allow spectroscopy for sources up to ~6×10^{-8} erg cm^{-2} s^{-1} in the 0.2-10 keV energy range. The XRT is also capable of producing accurate photometry and light curves with a time resolution of at least 10 ms.

3.5 *ASCA*

ASCA (Advanced Satellite for Cosmology and Astrophysics, figure 3.7; Tanaka et al. 1994), was launched on February 20, 1993 and inserted into an almost circular orbit, with a perigee of 520 km and an apogee of 620 km and an inclination of 31.1 degrees. The orbital period was about 96 minutes. The satellite ceased its activities in March 2001.

In this thesis only two sources (GRS 1734-292 and NGC 6814, see chapter 7) have been analysed using *ASCA* data.

ASCA, also known as *Astro-D*, was Japan's fourth X-ray mission, built with a large co-operation with the United States which provided part of the scientific payload. It was one of the first satellites to make use of CCDs for astronomy, designed to combine imaging capabilities over a broad energy range, good spectral resolution and a large effective area.

ASCA instrumentation consisted in four identical grazing incidence X-ray telescopes, each equipped with an imaging spectrometer. The angular resolution of the telescopes was quite modest, with a half power diameter of $\sim 3'$ and a PSF of $\sim 1'$. On the telescopes focal planes, there were the detectors: two CCD cameras, the Solid-state Imaging Spectrometers (SIS), and two gas scintillation imaging proportional counters (Gas Imaging Spectrometer, GIS). The SIS had a resolving power $E/\Delta E \sim 50$ at 6 keV and ~ 20 at 1.5 keV. The GIS had a resolving power $E/\Delta E \sim 13$ at 6 keV and ~ 7 at 1.5 keV. The field of view of the detectors was $20' \times 20'$ for the SIS and $50'$ (circular) for the GIS.

ASCA was designed to perform imaging and spectroscopic observations of the sky in the 0.5-10 keV energy range. The satellite's main scientific objectives were the study of X-ray binaries, cataclysmic variables, supernova remnants, active galactic nuclei and clusters of galaxies.

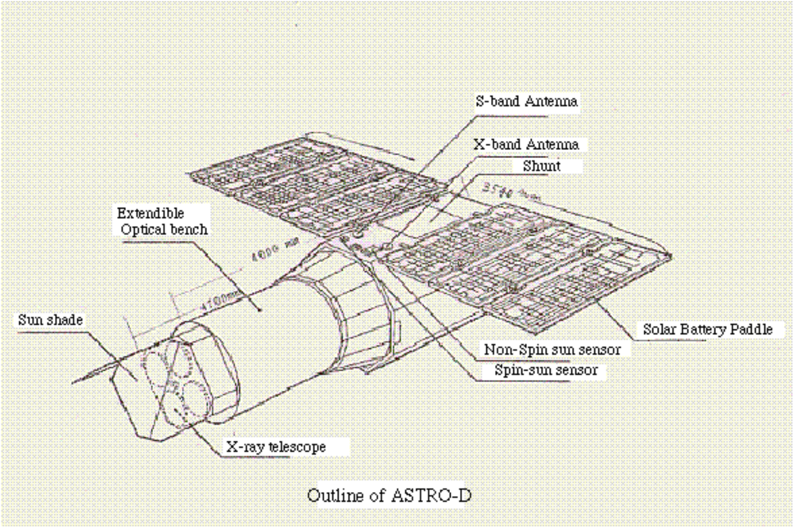

Figure 3.7: A sketch of the *ASCA* satellite. The main components and scientific instruments are labelled (credits: http://heasarc.gsfc.nasa.gov/docs/asca/ascagof.html).

Chapter 4

The *INTEGRAL* AGN Sample

4.1 Introduction

The extragalactic gamma-ray sky has been, so far, poorly explored and up to now only a few surveys have been performed above 10 keV. Among these surveys, there is the *HEAO1/A4* all-sky survey conducted in the 80's in the 13-180 keV band (Levine et al 1984), the survey conducted by the *SIGMA* telescope on board the *GRANAT* satellite in the 35-100 keV band (Revnivtsev et al. 2004a) and more recently those performed by *RXTE/PCA* and *Swift/BAT* in the 8-20 and 14-195 keV respectively (Revnivtsev et al. 2004b; Markwardt et al. 2005).

IBIS has so far surveyed large fractions of the sky at energies above 20 keV, with good sensitivity and positional accuracy. The first year of *INTEGRAL* observations of the Galactic Plane and Centre provided a first sample of 10 gamma-ray selected AGN (Bassani et al. 2004); the second IBIS survey (Bird et al. 2006) enlarged the sample to 32 AGN and the *INTEGRAL*/IBIS extragalcatic survey (Bassani et al. 2006) listed 62 Active Galactic Nuclei detected in the 20-100 keV energy range. More recently, the third IBIS catalogue (Bird et al. 2007) listed more than 420 high energy emitting sources, a large number of which (130) are now firmly identified as AGN. From these source lists, a complete sample of AGN detected above the 5.5σ threshold has been extracted, making it possible and important to study the differences and similarities between different classes of AGN, by measuring the shape of the primary continuum together with the high energy cut-off and the reflection component. Previous broad-band studies of AGN (above all with *BeppoSAX* data) concentrated mostly on incomplete X-ray selected samples (e.g. Perola et al. 2002; Dadina 2007); these were generally made of the brightest objects observed in the X-ray band. The availability of a complete sample is crucial to obtain an unbiased view of the general properties of high energy selected active galaxies.

The present thesis will focus on the broad-band (1-110 keV) spectral analysis of a complete sample of type 1 AGN, combining *XMM-Newton*, *Chandra*, *Swift/XRT*, *ASCA* and *BAT* data together with *INTEGRAL/ISGRI* measurements.

4.2 The Complete Sample

The 35 type 1 sources which will be the object of the present thesis have been selected from the complete sample of AGN extracted from the third IBIS/ISGRI catalogue (Bird et al. 2007), which comprises 421 high energy emitting sources, observed in a systematic analysis of IBIS/ISGRI data spanning more than 3.5 years of operations. Data reported here, in fact, belong to Core Programme and public observations spanning from revolution 12 to revolution 429 inclusive, i.e. the period from launch to the end of April 2006. This represents a significant extension, both in exposure and sky coverage, with respect to the 2^{nd} IBIS catalogue (Bird et al. 2006), which covered the period from February 2003 (rev. 46) to the end of June 2004 (rev. 209) and listed 209 gamma-ray detected sources.

The complete sample has been extracted starting from the 130 AGN listed in the 3^{rd} IBIS/ISGRI catalogue; most of these objects were already identified with active galaxies in the catalogue, while others were subsequently classified as such following optical spectroscopy[1]. From this larger list, a complete sample has been extracted by means of the V/V_{max} test.

The V/V_{max} test was first introduced by Schmidt (1968) as a test of uniformity of distribution in space for a flux-limited sample of objects. It can, however, be used in the opposite sense, that is, assuming that the sample is distributed uniformly in space (and that there is no evolution), it is possible to test if the sample is complete. The test consists of comparing the volumes contained within the distances where the sources are observed (V) with the maximum volumes (V_{max}), defined as those within the distance at which each source would be at the limit of detection. If the sample is not complete, the expected value for $<V/V_{max}>$ is less than 0.5, while when complete it should be equal to 0.5.

In the case of the ISGRI catalogue, the sky exposure, and therefore the limiting sensitivity is a function of position. This can be taken into consideration by using the V_e/V_a variation introduced by Avni & Bahcall (1980). Once again the expected mean value $m=<V_e/V_a>$ will be 0.5 when the sample is complete. The error on each point can be shown to be:

---

[1] For optical classification of *INTEGRAL* sources, including some of the AGN analysed here, please refer to Nicola Masetti's web page at http://www.iasfbo.inaf.it/extras/IGR/main.html

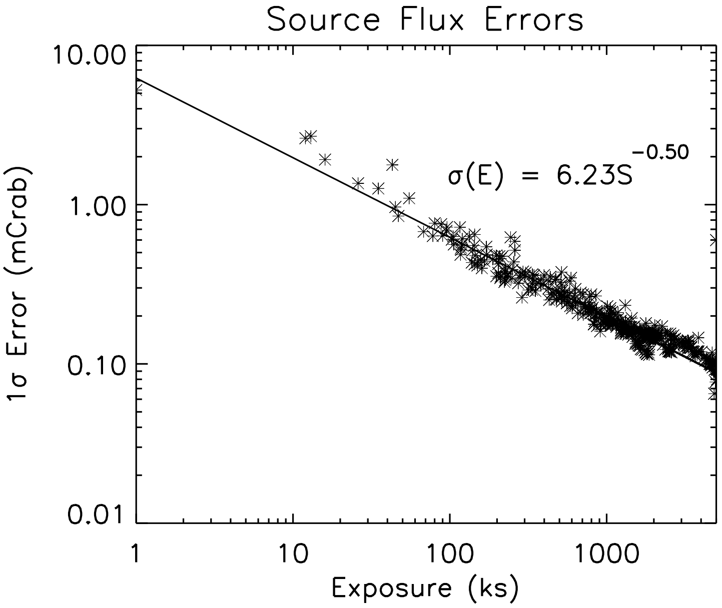

Figure 4.1: The 1σ limiting flux as a function of exposure for the complete 3^{rd} catalogue, fitted with a straight line (in log-log) of slope -0.5. Only for very short exposures (and, for this catalogue very small sky areas) does the data diverge for the fit.

$$\sigma_m(N) = \sqrt{\frac{1/3 - \langle m\rangle + \langle m\rangle^2}{n}} \qquad (4.1)$$

where n is the number of objects in the sample above the significance limit.

For our specific case, the significance for each source given in the catalogue is not that found in the sky map, but a value which is adjusted after the source is detected and a light curve created for it. In applying the V_e/V_a test, the significances used are those which are the basis of finding the source i.e. from the sky map. In practice, this analysis requires the following steps:

- The limiting flux as a function of exposure is calculated using the entire catalogue; the error in every source flux is plotted against the exposure at the position of the source (figure 4.1).
- For a series of limiting significances, in this case from 1σ to 11σ, the V_e/V_a ratio is calculated for each source observed with a significance above this limit. The average value of the ratio is then plotted as a function of the limiting significance (figure 4.2).

Figure 4.3 shows the value of $<V_e/V_a>$ as a function of limiting sensitivity. It can be seen that the increasing trend becomes flat above about 5.5σ. The mean value above this

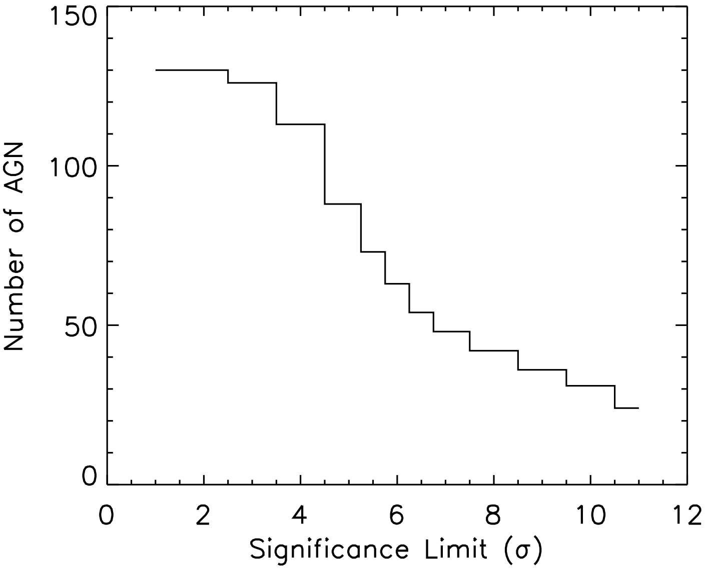

Figure 4.2: The number of AGN in the 3^{rd} ISGRI catalogue as a function of limiting significance.

significance is 0.497±0.020, consistent with the expected value of 0.5. There are 73 AGN detected at a significance higher than this value.

The sample contains 35 type 1 objects, 30 type 2 sources, 3 Narrow Line Seyfert 1s, and 7 Blazars/QSOs (see figure 4.4). In this work, we only concentrate on the first set of objects, i.e. those classified as type 1-1.5. In figure 4.5 the plot of the hard X-ray luminosity (20-100 keV) versus the redshift is shown: the plot gives an estimate of the limiting sensitivity of the sample.

In table 4.1, relevant parameters for each source are listed (coordinates, 20-100 keV flux, 1.4 GHz flux density), together with the optical classification and redshift obtained from NED[2] or from other recent publications. For objects with known distances, 20-100 keV fluxes have been converted to gamma-ray monochromatic luminosities, assuming H_0=71 km $s^{-1}Mpc^{-1}$ and q_0=0 (Spergel et al. 2003). 1.4 GHz information have been obtained from the HEASARC database[3] for 29 objects in the sample; only in the case of IGR J13109-5552, the 1.4 GHz flux was interpolated using the 4.85 and 0.83 GHz fluxes available in the HEASARC radio catalogues (see following chapter).

---

[2] http://nedwww.ipac.caltech.edu/

[3] http://heasarc.gsfc.nasa.gov/

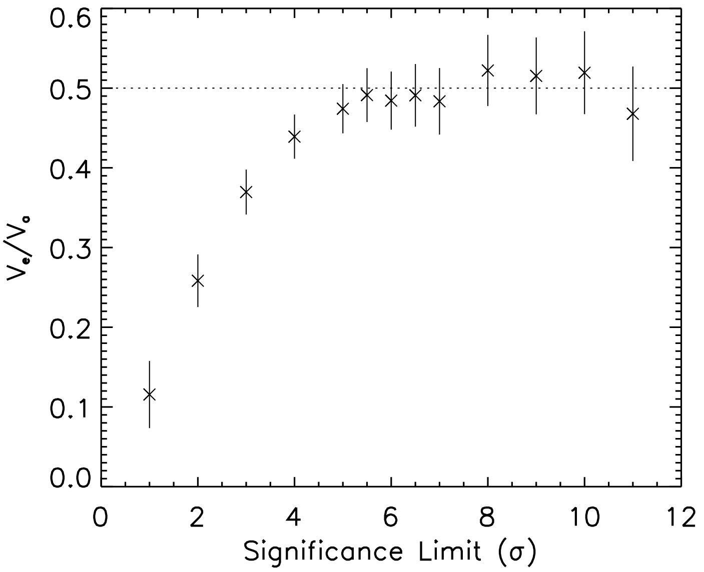

Figure 4.3: The value of <V_e/V_a> as a function of limiting significance.

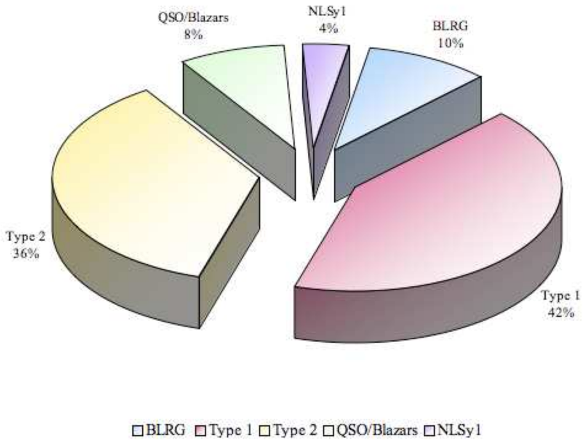

Figure 4.4: Pie diagram showing the different typologies of sources in the *INTEGRAL* AGN complete sample.

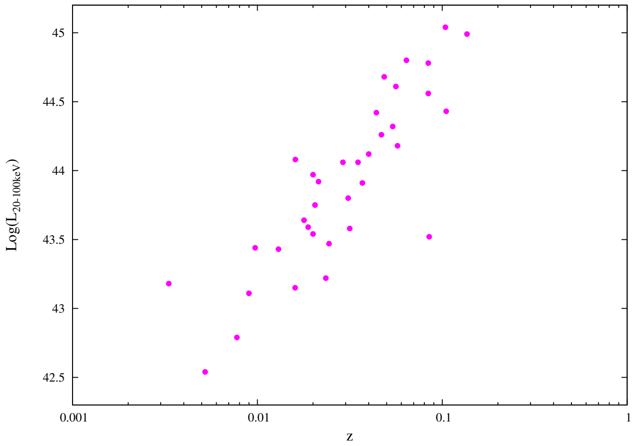

Figure 4.5: The 20-100 keV luminosity versus redshift for optically classified type 1 AGN in the complete sample.

4.3 Data Reduction

The sources in the sample presented in this thesis have all been observed by *XMM-Newton* with the exception of GRS 1734-292 and NGC 6814, observed by *ASCA*, QSO B0241+62 observed by *Chandra* and IGR J00333+6122, Swift J0917.2-6221, Mrk 50, IGR J13109-555, IGR J16119-6033, IGR J17488-3253, 2E 1853.7+1534 and S5 2116+81 for which *Swift/XRT* data have instead been used. For 4U 1344-60 only MOS1 and pn data were available, while for IGR J16482-3036 only MOS1 and MOS2 data. In the cases of MCG+08-11-011 and IC 4329A only pn data were analysed, following Matt et al. (2006) for the former source and Markowitz et al. (2006) for the latter. Table 4.2, reports the observation logs for the sources analysed here, together with the relative exposures (both for the X-ray and *INTEGRAL* measurements).

MOS and PN (Strüder et al. 2001; Turner et al. 2001) data were reprocessed using the *XMM-Newton* Standard Analysis Software (SAS) version 7.0 employing the latest available calibration files. Only patterns corresponding to single, double, triple and quadruple X-ray events for the two MOS cameras were selected (PATTERN≤12), while for the PN only single and double events (PATTERN≤4) were taken into account; the standard selection filter FLAG=0 was applied. Exposures have been filtered for periods of high background and the resulting exposures are listed in table 4.2. Source counts were extracted from circular regions of typically 40″-50″ of radius centered on the source, while background spectra were extracted from circular regions close to the source or from source-free regions of typically 20″ of radius. The ancillary response matrices (ARFs) and the detector response matrices (RMFs) were generated using the *XMM*-SAS tasks *arfgen* and *rmfgen*; spectral channels were rebinned in order to achieve a minimum of 20 counts per

Complete Sample of Type 1 AGN detected above 5.5σ in the 20-40 keV band

Name	**RA**	**DEC**	**z^a**	**F$_{20-100keV}$** **10^{-11} erg cm^{-2}s^{-1}**	**L$_{20-100keV}$** **10^{44} erg s-1**	**F$_{1.4GHz}$** **mJy**	**Ref.**	**Type**
IGR J00333+6122	8.360	61.457	0.105	1.19	2.73	9.2	1	Sy 1.5
QSO B0241+62	41.285	62.48	0.044	1.19	2.73	364.1		Sy 1
B3 B0309+411B	48.273	41.343	0.136	2.57	9.75	360.9		Sy 1/BLRG
3C 111	64.573	38.014	0.0485	9.46	4.75	7726.1		Sy 1/BLRG
LEDA 168563	73.028	49.514	0.029	6.30	1.14	13.4		Sy 1
4U 0517+17	77.676	16.477	0.01788	6.30	4.37	6.0		Sy 1.5
MCG+08-11-011	88.717	46.442	0.0205	6.25	0.57	245.5		Sy 1.5
Mrk 6	103.032	74.423	0.018813	5.02	0.38	269.5		Sy 1.5
IGR J07597-3842	119.923	-38.719	0.04	3.83	1.32	3.8		Sy 1.2
FRL 1146	129.620	-36.013	0.031578	1.76	0.38	19.8		Sy 1.5
Swift J0917.2-6221	139.040	-62.314	0.0573	2.17	1.52	-		Sy 1
NGC 3783	174.733	-37.745	0.00973	13.41	0.28	43.6		Sy 1
NGC 4151	182.636	39.409	0.003319	63.19	0.15	359.6		Sy 1.5
Mrk 50	185.862	2.693	0.023433	1.40	0.17	-		Sy 1
NGC 4593	189.905	-5.353	0.009	7.23	0.13	4.4		Sy 1
IGR J12415-5750	190.377	-57.825	0.0244	2.28	0.29	-		Sy 1
IGR J13109-5552	197.682	-55.863	0.0850	2.42	0.33	512.0	2	Sy 1
MCG-06-30-015	203.995	-34.302	0.007749	4.68	0.06	1.7		Sy 1.2
4U 1344-60	206.883	-60.610	0.013	7.40	0.27	-		Sy 1.5
IC 4329A	207.339	-30.309	0.016054	21.52	1.20	66.4		Sy 1.2
IGR J16119-6036	242.988	-60.658	0.016	2.55	0.14	-		Sy 1
IGR J16482-3036	252.062	-30.590	0.031	3.08	0.64	3.5		Sy 1
IGR J16558-5203	254.010	-52.062	0.054	3.34	2.08	-	3	Sy 1.2
GRS 1734-292	264.377	-29.137	0.0214	8.40	0.83	48.0		Sy 1
2E 1739.1-1210	265.474	-12.215	0.037	2.75	0.81	3.5		Sy 1
IGR J17488-3253	267.217	-32.926	0.02	3.96	0.34	10.5	3	Sy 1
IGR J18027-1455	270.685	-14.916	0.035	4.34	1.14	10.5	4	Sy 1
3C 390.3	280.586	79.781	0.0561	6.06	4.06	11226.0		Sy 1/BLRG
2E 1853.7+1534	283.970	15.618	0.084	2.45	3.64	3.4		Sy 1
NGC 6814	295.657	-10.320	0.005214	5.91	0.03	49.7		Sy 1.5
4C 74.26	310.585	75.145	0.104	4.87	10.97	207.2		Sy1/BLRG
S5 2116+81	318.492	82.072	0.084	4.06	6.02	286.5		Sy 1/BLRG
IGR J21247+5058	321.172	50.972	0.02	10.90	0.94	381.5	4	Sy 1/BLRG
MR 2251-178	343.543	-17.607	0.064	7.28	6.32	16.2		Sy 1
MCG-02-58-022	346.200	-8.666	0.04686	3.91	1.84	32.6		Sy 1.5

^{a}: type and redshift according to NED or quoted reference.

(1): Parisi et al. 2008; (2): Masetti et al. 2008; (3): Masetti et al. 2006; (4): Masetti et al. 2004.

Table 4.1: The *INTEGRAL* Complete Sample of Type 1 AGN.

each bin. For sources affected by pile-up, the central 5″ of the PSF have been excised and spectra have been extracted from annular regions of typically 50″ (external radius).

Chandra data reduction for QSO B0241+62 was performed with CIAO 3.4 and CALDB 3.2.4 to apply the latest gain corrections. Subsequent filtering on event grade and to exclude times of high background resulted in a total exposure of 34 ks. The CIAO script “psextract” was used to generate the spectrum, with appropriate background and response files, of the point source; the source spectrum was extracted using a radius of ∼ 4″ while background files were generated using region of ∼9″. With a count rate of 0.14 counts/frame, the pile-up fraction is insignificant at <10%.

XRT data reduction was performed using the XRTDAS v1.8.0 standard data pipeline package (`xrtpipeline` v. 0.10.3) in order to produce screened event files. All data were collected in the Photon Counting (PC) mode (Hill et al. 2004), adopting the standard grade filtering (0-12 for PC) according to the *XRT* nomenclature. Source data have been extracted using photons in a circular region of typically radius 20″; background data have instead been taken from various uncontaminated regions near the X-ray source, using either a circular region of different radius or an annulus surrounding the source.

ASCA data (spectra and associated files) were downloaded from the TARTARUS database version 3.1[4]. The cross calibration constant between the two *ASCA*-GIS instruments has always been assumed to be 1.

The *INTEGRAL* data reported here consist of several pointings performed by ISGRI (Lebrun et al. 2003) between revolutions 12 and 429, i.e. the period from launch to the end of April 2006. ISGRI images for each available pointing were generated in various energy bands using the ISDC offline scientific analysis software OSA (Goldwurm et al. 2003) version 5.1. Count rates at the position of the source were extracted from individual images in order to provide light curves in various energy bands; from these light curves, average fluxes were then extracted and combined to produce an average source spectrum (see Bird et al. 2007 for details). Analysis was performed in the 20-150 keV band.

In the present analysis we also made use of public *Swift*/BAT spectra, retrieved on the web[5]; spectra are from the first 9 months of operations of the *Swift/BAT* telescope (Baumgartner et al. 2008).

---

[4] http://tartarus.gsfc.nasa.gov

[5] http://swift.gsfc.nasa.gov/docs/swift/results/bs9mon/

Observations Log

Name	**Obs. Date**	**Exp. (PN) (ksec)**	**Exp. (MOS) (ksec)**	**Exp. (*XRT*‡) (ksec)**	**Exp. (*ASCA*) (ksec)**	**Exp. (*Chandra*) (ksec)**	**Exp. (*INTEGRAL*†) (ksec)**
IGR J00333+6122	14/11/2007	-	-	6.04	-	-	1787
QSO B0241+62	06/04/2001 07/04/2001	-	-	-	-	34	372
B3 0309+411	04/09/2005	11.0	19.7/16.1	-	-	-	5067
3C 111	14/03/2001	14.5	7.6/7.1	-	-	-	2006
LEDA 168563	26/02/2007	9.6	10.8/9.4	-	-	-	157
MCG+08-11-011	09/04/2004	10.3	12.4/16.9	-	-	-	48
Mrk 6	27/03/1001	9.0	14.9/7.4	-	-	-	581
IGR J07597-3842	08/04/2006	11.9	14.3/13.3	-	-	-	1049
FRL 1146	12/12/2006	6.9	6.3/7.1	-	-	-	1172
Swift J0917.2-6221	11/11/2005 13/12/2005	-	-	12.9	-	-	1140
NGC 3783	28/12/2000	32.2	35.0/33.9	-	-	-	39
NGC 4151	27/05/2003	10.4	15.8/15.8	-	-	-	449
Mrk 50	14/11/2007 15/11/2007 16/11/2007	-	-	18.3	-	-	1164
NGC 4593	02/07/2000	3.5	6.0 (MOS2)	-	-	-	1040
IGR J12415-5750	01/02/2006	4.0	8.3/6.6	-	-	-	1604
IGR J13109-5552	25/12/2006 28/12/2006	-	-	6.58	-	-	1288
MCG-06-30-015	04/08/2001	98	83.7/92.1	-	-	-	473
4U 1344-60	25/08/2001	28.7	38.7 (MOS1)	-	-	-	1510
IC 4329A	06/08/2003	47.2	44.7/41.9	-	-	-	382
IGR J16119-6036	15/06/2007	-	-	2.5	-	-	1786
IGR J16482-3036	01/03/2006	-	7.0/7.0	-	-	-	2460
IGR J16558-5203	01/0372006	4.8	5.8/5.4	-	-	-	2502
GRS 1734-292	08/09/1998	-	-	-	6.1	-	6087
2E 1739.1-1210	04/04/2006	13.1	14.7/14.7	-	-	-	1515
IGR J17488-3253	02/11/2005	-	-	16.8	-	-	5766
IGR J18027-1455	25/03/2006	14.2	17.5/16.9	-	-	-	2500
3C 390.3	08/10/2004	38.8	32.4/34.60	-	-	-	3058
2E 1853.7+1534	20/07/2007 29/07/2007	-	-	2.6	-	-	785
NGC 6814	04/05/1993	-	-	-	41.7	-	1853
4C 74.26	06/02/2004	25.6	29.0/29.0	-	-	-	1213
S5 2116+81	25/06/2006 17/10/2006	-	-	10.2	- -	- -	1985
IGR J21247+5058	06/11/2005	22.2	24.2/23.6	-	-	-	1067
MR 2251-178	18/05/2002	8.5	13.6/10.9	-	-	-	307
MCG-02-58-022	01/12/2000	7.2	-	-	-	-	320

†: note that for *INTEGRAL* the exposure refer to a number of pointings in the period between launch and April 2006.

‡: total exposure of the summed pha files.

Table 4.2: Observation logs of the sources in the sample.

4.4 Data Analysis Outline

The objective of the present thesis is the analysis of the broad-band spectral data of the complete sample of all but one *INTEGRAL* detected type 1 AGN; the only missing source is 4U 0517+17, for which no public available X-ray data could be found.

This study includes both radio loud (RL) and radio quiet (RQ) objects. The analysis will start with the study of a peculiar source, IGR J21247+5058, which lies on the Galactic plane and was not known to be a type 1 AGN before *INTEGRAL* observations. The peculiarity of this source lies in its strong radio emission and structure, which immediately suggest its classification as a Broad Line Radio Galaxy (BLRG).

This sources served as a landmark to discriminate radio loud from radio quiet AGN, which in this work are analysed separately. Chapter 5 will therefore be centered on IGR J21247+5058, while chapter 6 will focus on the radio loud AGN present in the complete sample, leaving the analysis of the remaining type 1 AGN to chapter 7.

Here and in the following, spectral analysis was performed with `XSPEC` v.11.2.3 (Arnaud 1996) and errors are quoted at 90% confidence level for one parameter of interest ($\Delta\chi^2$=2.71)[6]. Galactic absorption towards each source (Dickey & Lockman 1990) has always been included in each fit, so that the quoted absorbing column densities are always in excess of this Galactic value.

---

[6] A test was also made for checking if systematic errors should be taken into consideration. It resulted that the systematic error could be around or below 2%. Introducing it in our fits does not alter significantly the results of the analysis.

Chapter 5

A case study: the peculiar Broad Line Radio Galaxy IGR J21247+5058

5.1 Introduction

IGR J21247+5058 was initially reported in the first *INTEGRAL* survey catalogue (Bird et al. 2004) and listed in subsequent survey papers. Soon after its discovery, IGR J21247+5058 was associated by Ribó et al. (2004) with the radio source 4C 50.55, also known as GPSR 93.319+0.394, KR2, NRAO 659 or BG 2122+50: this object has the typical morphology of a radio galaxy showing a bright core and two lobes. The estimated position of the core from the NVSS map is RA (J2000)=$21^h24^m39.25^s$ and Dec (J2000)=$+50°58'23.80''$ ($1''$ uncertainty).

Confirmation of the AGN nature of IGR J21247+5058 came via optical observations obtained at the Loiano telescope (Masetti et al. 2004), despite the fact that the optical spectrum of the source looks very peculiar. It has in fact a broad, redshifted H_α complex superimposed onto a "normal" F/G-type Galactic star continuum. While most of the observed features (Na, Ca and Mg) are consistent with redshift z=0 and thus with a Galactic stellar origin, the H_α complex leads to a redshift z=0.02. This feature is very similar to the one observed in another bright radio galaxy, namely 3C 390.3 (Dietrich et al. 1998). The H_α complex, together with the spatially coincident extended radio emission and the detection of strong hard X-ray radiation, strongly indicates the unfortunate situation of a chance alignment between a relatively nearby star and a background radio galaxy. Indeed the *INTEGRAL/IBIS* spectrum of this source is compatible with the canonical AGN spectrum (Molina et al. 2006). Because the only optical line observed is broad, the source was tentatively classified as a Seyfert 1 or alternatively as a broad line radio galaxy (BLRG).

Unfortunately, given the confusion with the nearby star, it is impossible to gain more information on the source optical characteristics with the currently available data (see Masetti et al. 2004); in particular no reliable measurement of the B magnitude can be used to estimate the source radio loudness using the relation RL=log[F(5GHZ)/F(B)]. At the observed redshift, the source luminosity in the 20-100 keV band is 8.5×10^{43} erg s^{-1}, making IGR J21247+5058 one of the brightest AGN in the local Universe[1].

In the following, a detailed radio analysis of the source based on archival VLA data is presented, together with a broad-band spectral analysis of *XMM-Newton* and *Swift*/*XRT* combined with the *INTEGRAL/IBIS* data.

5.2 Radio Observations

At the very low energy part of the electromagnetic spectrum, radio observations provide valuable information on the nature of IGR J21247+5058. Radio images at various resolutions have been presented in several works (e.g. Mantovani et al. 1982, Pandey et al. 2006). In figure 5.1 is shown a 1.4 GHz image of the field of IGR J21247+5058 obtained with data from the VLA archive. The circle indicates the location and positional error of the *INTEGRAL* detection, which clearly points to the nucleus of IGR J21247+5058 as the source of the gamma-ray emission. The radio source has the typical edge-brightened morphology of an FR II radio galaxy, with a central compact core and two large lobes. The size of IGR J21247+5058 is $\sim 9.5'$ and the total flux density at 1.4 GHz is 2.5 Jy. At the redshift proposed for this source, these data correspond to a total extent LS of 230 kpc and a monochromatic radio power $P_{1.4} = 10^{24.4}$W Hz^{-1}. This makes IGR J21247+5058 a typical radio galaxy in size, with a radio power at the lower end of the observed range in FR II sources.

In figure 5.2 is shown the spectrum of the core of IGR J21247+5058 between 610 MHz and 15 GHz. The points between 1.4 and 15 GHz were obtained from data in the VLA archive, while the 610 MHz point is taken from the GMRT data (Pandey et al. 2006). The spectrum is typical of synchrotron self-absorbed radiation, with a peak at about 8 GHz and a low frequency turnover.

The core fraction at 1.4 GHz is about $S_c/S_t = 0.1$, which is suggestive of a moderate Doppler boosting of the base of the jet. In fact, the core is brighter than what would be expected on the basis of the correlation between core and total radio power (Giovannini et al. 1988). From the total flux density at low frequency ($S_{0.4} = 5.4$ Jy, Mantovani et al. 1982), the core flux density should be only $\sim$ 50 mJy at 5 GHz, i.e. about a factor 10

---

[1] Assuming H_0=70 km $s^{-1}$$\mathrm{Mpc}^{-1}$ and a flat Universe.

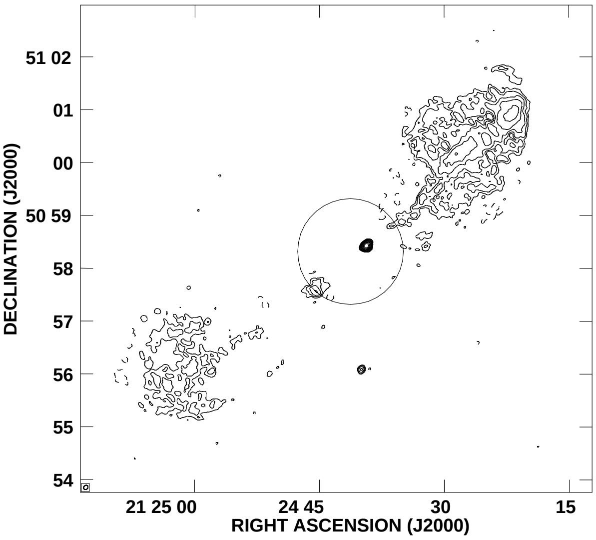

Figure 5.1: A 1.4 GHz image of the field of IGR J21247+5058 from VLA data (in B configuration). Contours are traced at (−1, 1, 2, 4, ...)×0.5 mJy beam^{-1} and the peak is 244 mJy beam^{-1}. The restoring beam is 5.5×4.4 arcsec. The circle shows the ISGRI position and error box of IGR J21247+5058.

less than observed. If we assume a typical Lorentz factor for the radio jet (γ=5, see e.g. Giovannini et al 2001), we can use this constraint to estimate a viewing angle $\theta \sim 35°$. This seems to be small enough to allow us to peer into the BLR and it also explains the broadening of the H_α line. Put altogether, the radio data seem to indicate that the counterpart of IGR J21247+5058 is an FR II broad line radio galaxy.

It is however difficult to guess which is the approaching side of the source. The NW lobe is brighter, but a knot of enhanced brightness is visible in the SE jet at 90″ from the core. If this brightness asymmetry is due to Doppler boosting, then the approaching side would be the SE one. A look at the parsec scale structure would be desirable to better study the properties of the inner jet and define this issue.

It is also interesting to note that a weak feature is clearly detected in several VLA data sets at $\sim 2'$ south of the core (RA = $21^h24^m39.97^s$, Dec = $+50°56'05.4''$). It has a flux of $\sim$ 4 mJy at 1.4 GHz and $\sim$ 2 mJy at 4.8 GHz. This source is probably unrelated to the *INTEGRAL* source, as it falls outside its 90% error circle and it is not detected in X-rays (see next section).

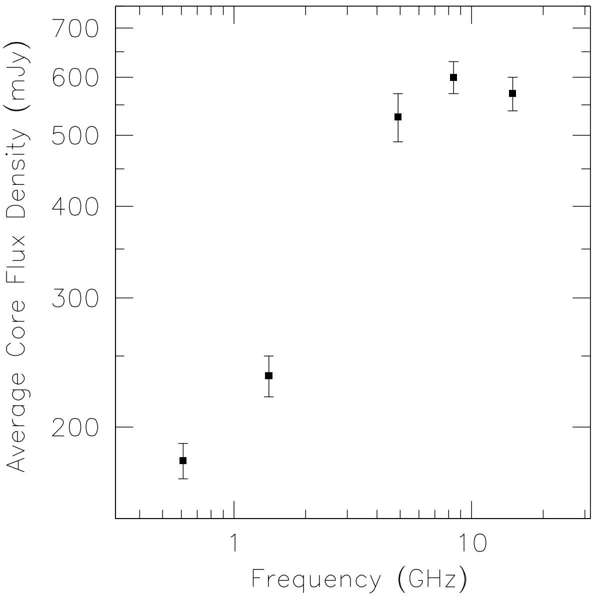

Figure 5.2: Average spectrum of the core of IGR J21247+5058 with VLA data (between 1.4 and 15 GHz) and the GMRT (0.6 GHz). The error bars show the rms of the various measurements considered, as well as the absolute calibration uncertainty.

5.3 X-ray Observations and Data Analysis

IGR J21247+5058 was observed by *XMM-Newton* on 2005 November 6 during orbit 1083, in the *XMM-Newton* Guest Observer Programme. Two other observations are present in the archive, but have not been used due to their poor statistical quality. During this orbit, the EPIC pn (Strüder et al. 2001) exposure was ~25 ks, while the EPIC MOS1 and MOS2 (Turner et al. 2001) exposures were ~27 ks (see table 5.1). The EPIC pn camera was operated in Large Window Mode with a thick filter applied, while the two MOS cameras were both operated in Small Window Mode. MOS and PN data were reprocessed using the *XMM-Newton* Standard Analysis Software (SAS) version 7.0 (see previous chapter for details on the data analysis). Image analysis indicates that a bright source, localised at RA=$21^h24^m39.36^s$ and Dec (J2000)=$+50°58'23.86''$, compatible with the position of the radio core, is detected with high significance, while no emission is seen at the location of the radio lobes nor in correspondence with the radio source located south of the core of IGR J21247+5058. As for the Galactic star which is aligned with the radio galaxy by chance, it could emit X-rays by coronal activity as seen in many stars of similar late spectroscopic type. However, any contamination is likely to be negligible as the star is likely at 2.5 kpc (Masetti et al. 2004), i.e. too far away to provide significant flux if the emission is from a stellar corona.

	Obs date	**Exposures (ksec)**	**Filter**	**Source counts (ct/s)**
XMM-MOS1	06-11-2005	24.2	Thick	1.918±0.009
XMM-MOS2	06-11-2005	23.6	Thick	1.907±0.009
XMM-PN	06-11-2005	22.0	Thick	5.582±0.02
XRT1	17-10-2006	7.2	-	0.4953±0.01
XRT2	25-01-2007	3.7	-	0.3222±0.01
INTEGRAL	Nov. 2002 to Apr. 2006	768	-	1.423±0.04

Table 5.1: Observations log for IGR J21247+5058.

Cross calibration constants pn/MOS1 and MOS2/MOS1 were left free to vary and always found to be close to unity as expected. Data from the three EPIC cameras were initially fitted in the 0.4-10 keV range using a simple power law absorbed only by the Galactic column density (N_H^{gal}=1.11×10^{22} cm^{-2}; see figure 5.3). This model does not yield an acceptable fit (χ^2=4974.7 for 2624 d.o.f.) as evident in figure 5.3 and the resulting power law slope is very flat ($\Gamma=0.94^{+0.01}_{-0.01}$). Since the data to model ratio are indicative of intrinsic absorption, the data were re-fitted adding this component (`wa`$_g$`*wa*po` in `XSPEC`); this new model provides a significant improvement in the fit (χ^2=2526.2 for 2623 d.o.f.), a column density $N_H=0.62^{+0.02}_{-0.02}\times10^{22}$cm^{-2} but a still rather flat spectrum ($\Gamma=1.28^{+0.01}_{-0.01}$). An even better fit ($\chi^2$=2446.1 for 2622 dof) is obtained using an ionised absorber instead of a cold one (`wa`$_g$`*absori*po` in `XSPEC`): the column density in this case is $1.12^{+0.10}_{-0.09}\times10^{22}$cm^{-2} and the ionisation state ξ (= L/nR^2, Done et al. 1992) is $18.1^{+6.8}_{-5.9}$, i.e. the absorber is at most mildly ionised. The slope of the power law hardens but only marginally ($\Gamma=1.33^{+0.02}_{-0.02}$). The absorption (cold or ionised) has then been substituted with a partial covering component (`*wa`$_g$`*pcfabs*po`, see table 5.2). This model provides a $\Delta\chi^2$=103.8 compared to the cold absorption model and a better χ^2 for the same d.o.f. compared to the ionised absorption model; the resulting spectrum has a similar photon index and the same column density as obtained for the ionised absorber model, but the absorption is now colder and covers around 80% of the source. At this stage we also checked the data for the presence of a cold iron line, adding to the partially covering model a narrow Gaussian component, having fixed the width to 10 eV. This model provides a fit improvement (χ^2=2405.9 for 2620 d.o.f. or $\Delta\chi^2$=16.5 for 2 d.o.f.), a line energy at $6.39^{+0.06}_{-0.08}$ keV and an equivalent width (EW) of 21^{+6}_{-10} eV (see figure 5.4 for the confidence contours of the line energy versus line normalisation). The improvement is significant at the 99.9% confidence level; however the EW is rather small, i.e. too close to the capability limits of moderate resolution CCD instruments like *XMM*, calling for some caution in considering the line as a real feature or just local noise. Without going into more details, the important point to stress here is that in IGR J21247+5058 a cold iron line is either very weak or not present. There is also a hint for a line at around 1.7 keV, but again its EW is very small and its energy

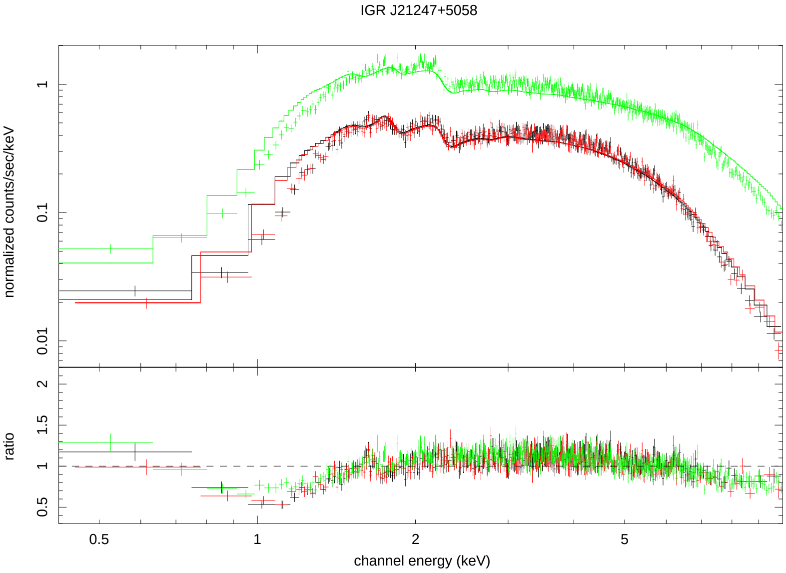

Figure 5.3: The *XMM* data fitted using a simple power law absorbed by Galactic column density.

suspiciously close to background features present in the pn and MOS camera to consider it as a real feature.

Despite the fact that a fit with just one absorber (cold, mildly ionised or partially covering the source) is quite acceptable, the resulting spectrum is still rather flat. Hence, two different scenarios to steepen the *XMM* spectral data have been tried: reflection from neutral material (with the Compton reflection component described by the parameter R=$\Omega/2\pi$; `pexrav` model in `XSPEC`) or an extra layer of absorbing material (again cold, ionized or partially covering the source). In the first case the inclination angle was fixed at 30°, implying a nearly face-on geometry. The reflection component resulting from the fit was small R=$0.59^{+0.45}_{-0.42}$ and the photon index still rather flat (Γ=$1.43^{+0.06}_{-0.06}$); the low value of the reflection parameter, although not well constrained, is consistent with the weak iron line observed in the spectrum of IGR J21247+5058, suggesting that the reprocessing of the power law photons in the accretion disk plays a negligible role in the source. In the second case, the best fit is obtained with another layer of cold material partially covering the source (`wa*pcfabs*pcfabs*po`, see table 5.2). This model provides a power law slope of ~1.6, close to the 1.7 value measured in other BLRG (Sambruna et al. 1999; Grandi et al. 2006), although still flatter than the 1.9 value typically observed in radio quite AGN (Perola et al. 2002). The absorbing column densities are around 9×10^{22} cm^{-2} and 10^{22}cm^{-2}, covering 27% and 83% of the central source. Given the fact that the highest steepening of the spectrum is obtained with a double absorber model and that reflection is either not required or small (also from the weakness of the iron line), we chose the second model as a better description of the *XMM* data. As some excess counts (mostly pn) are

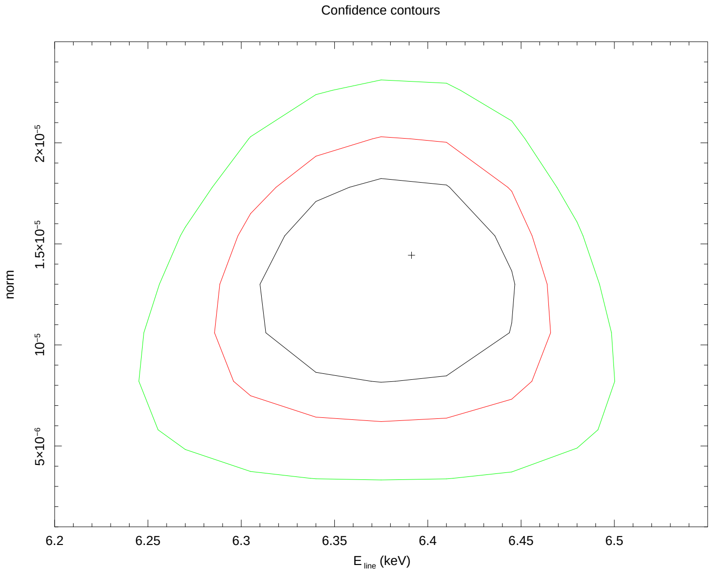

Figure 5.4: The confidence contours of the line energy versus line normalisation.

still visible at low energies, we have further added to this best fit model a soft thermal component (in the form of a black body or a `mekal` model) or a scattered component in the form of a power law; in the latter case the two power laws have the same photon index but different normalisations. In all cases, the excess emission remains and the fits return parameters which are unusual for AGN (a too high temperature and a scattered component with a too high normalisation with respect to the primary continuum). Given the quality of the data at low energies and the weakness of this excess emission, it is beyond the scope of the present thesis to further enquire about this component and its analysis is postponed to when more detailed X-ray observations of IGR J21247+5058 are available.

In order to check if the source could be classified as a radio-loud object, we exploited the X-ray flux measurement and used the R_X=L_r(5GHz)/L_X(2-10 keV) relation (e.g. Terashima & Wilson 2003 and Panessa et al. 2007); to do this we used the VLA 5 GHz measurement of the core component and then compared it to the 2-10 keV flux. Since LogR_X=-3.3, IGR J21247+5058 could be defined a borderline object, as it is radio loud or quiet depending on our choice of the dividing line between these two classes: LogR_X=-4.5 (as in Terashima & Wilson 2003) or -2.8 (as in Panessa et al. 2007). However the LogR_X value of IGR J21247+5058 is fully compatible with those of similar BLRG like 3C 111 (LogR_X=-3.7), 3C 120 (LogR_X=-2.1), 3C 390.3 (LogR_X=-3.1) and 3C 382 (LogR_X=-4.0) (Grandi et al. 2006 and Liu & Zhang 2002), implying that also this new source is very likely a radio loud AGN. It is interesting to note that following one of the criteria for radio loudness proposed by Zamfir et al. (2008) (see also next chapter), IGR J21247+5058 is the weakest FR II galaxy yet reported, having Log(L_{5GHz})~31 erg $s^{-1}Hz^{-1}$, an order of magnitude lower than the usually adopted threshold (see next chapter).

IGR J21247+5058 was also observed with the *XRT* telescope for ~7.2 ks on 2006 October 17 and for 3.7 ks on 2007 January 25 (again, see previous chapter for data analysis details). The log of these two *XRT* observations is also reported in table 5.1.

Due to the lower quality of these data, a simple model, i.e. a power law passing through a single absorption layer partially covering the central source has been employed. The first *XRT* observation (hereafter *XRT1*) provides a power law spectrum with $\Gamma=1.54^{+0.19}_{-0.18}$, moderate intrinsic absorption, a partial covering fraction f=0.74 and a 2-10 keV flux of 6.4×10^{-11} erg $cm^{-2}s^{-1}$ (see table 5.2). To check if the best fit values could be improved, another partial covering absorber was added to the model, but the fit does not produce better results (χ^2=132.2 for 138 d.o.f.).

The second observation (hereafter *XRT2*) is of even poorer quality due to the shorter exposure; it provides slightly different parameters than the first observation (see table 5.2) and a lower 2-10 keV flux of $(3.37\pm0.1)\times10^{-11}$ erg cm^{-2} s^{-1}. Despite the less precise modelling allowed by the *XRT* observations, the comparison between the two *XRT* observations and with the *XMM-Newton* measurement suggests a change in the source absorption properties related to a flux variation. Note that for consistency, also the *XMM* data are modelled here with a single layer of absorption. The change in the absorber properties is evident in figure 5.5, where the contour plots of the column density versus covering fraction are displayed for the three available X-ray observations: in particular while *XRT1* data are fully compatible with the *XMM* one, both differ from the *XRT2* observation parameters. Given that the model used is not the best fit found with the *XMM* data, as a second step the double absorber model has been adopted and then the 3 sets of data compared by means of an accurate parameter space exploration. Due to the lower statistical quality of the *XRT* data, the photon index and the two absorption parameters, each at a time, were fixed to the *XMM* value. The result of this procedure is that the likely change occurring is in the column density of the absorber covering 80% of the source while the other parameters are consistent within errors with each other. However, given the poor quality of the *XRT2* spectrum, i.e. the one that provides evidence for this change in absorption, some caution is needed and further observations required to confirm this observational evidence.

The *INTEGRAL* data have been analysed in the 17-100 keV band (the source count rate in this band is reported in table 5.1). A simple power law provides a good fit to the *IBIS* data (χ^2=8.9 for 10 d.o.f.) and a photon index $\Gamma=2.0\pm0.1$ and a 17-100 keV flux of 1.15×10^{-10} erg cm^{-2} s^{-1}. The *INTEGRAL* spectrum is clearly steeper than the *XMM/XRT*

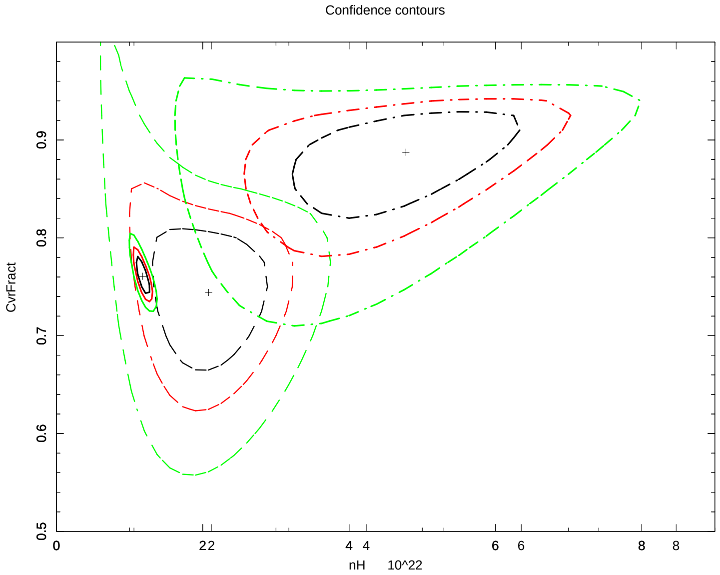

Figure 5.5: Constraints on the absorbing column densities and relative covering fractions for the *XMM* (solid line), *XRT1* (dashed line) and *XRT2* (dashed-dotted line) observations assuming a single absorption layer (`wa`$_g$`*pcfabs*po`).

ones, implying that a cut-off is possibly present and located in the IBIS energy band.

5.3.1 The High Energy Broad-Band Spectrum

X-ray and *INTEGRAL* data were then fitted together in order to obtain an average broad-band spectrum of the source. In the fitting procedure, a multiplicative constant, *C*, has been introduced to take into account possible cross-calibration mismatches between the X-ray and *INTEGRAL* data; this constant has been found to be close to 1 both for *XMM* and *Swift/XRT* using various source typology (Landi et al. 2007; De Rosa et al. 2008; Masetti et al. 2007) so that significant deviation from this value can be confidently ascribed to source flux variability. Initially, the *XMM* and the *IBIS/ISGRI* data were combined together, employing the model (`wa*pcfabs*pacfabs*po`) used for the *XMM* data alone and considered here as our baseline model (we have ignored the iron line at this stage but the results do not change significantly if this component is added to the fit). This model provides a good fit with a photon index of ~1.7, and two absorption layers ($\sim 10^{22}$ and $\sim 10^{23}$ cm^{-2} respectively, table 5.3), covering 84% and 34% of the central source. To check for the presence of a high energy cut-off, we substituted the simple power law with a cut-off power law (`wa*pcfabs*pcfabs*cutoffpl`). The model yields our best fit (χ^2=2354.0, 2628 d.o.f., figure 5.6) and a power law slope around 1.5; a cut-off is indeed present and well constrained at around 75 keV (see table 5.3 and figure 5.7). In the above models the value of *C* is around 0.80, suggesting a good match and no major changes in

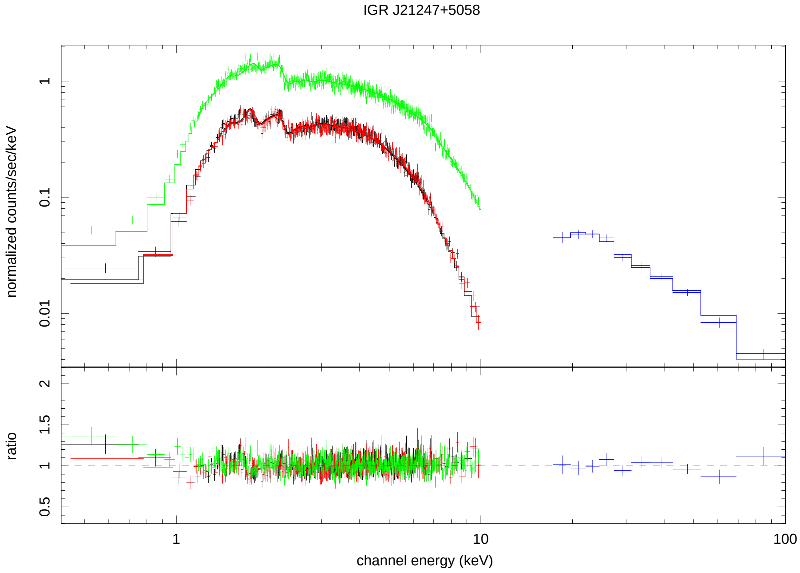

Figure 5.6: *XMM/ISGRI* broad band (0.4-100 keV) spectrum of IGR J21247+5058: the model is a cut-off power-law absorbed both by Galactic column density and by two layers of absorbing material partially covering the source.

flux between the *XMM* and *INTEGRAL* observations. Finally, the broader energy coverage was exploited to check again for the presence of reflection in the source spectrum by adding this component to the previous model (`wa*pcfabs*pcfabs*pexrav`, see table 5.3). The fit shows an improvement (χ^2=2350.9 for 2627 d.o.f., 99.9% confidence level) with respect to the simple double partial covering model (`wa*pcfabs*pacfabs*po`); however, when considering the best-fit model (`wa*pcfabs*pcfabs*cutoffpl`), there is only a marginal improvement in the fit, suggesting that the reflection component is not strongly required by the data. The model gives a power law slope of ∼1.5, the high energy cut-off is around 100 keV and the double absorption layer values are well in agreement with those obtained with no reflection in the model (R=0). This reflection model yields a poorly constrained value of R around 0.4 and a cross calibration constant ∼0.7. We have also tried to find evidence for a jet component in the high energy data introducing a second power law component (`wa*pcfabs*pcfabs*(cutoffpl+po)`) with the photon index of the primary continuum fixed at the canonical 1.7 value for BLRG. Again the fit does not show any improvement (χ^2=2379.2, 2627 d.o.f.), the power law component used to model the jet emission has a slope of $1.50^{+0.16}_{-0.33}$ and the high energy cut-off is consistent with value found in the best fit ($83.5^{+61.6}_{-29.2}$ keV). The values of the column densities and their covering fractions are in agreement with those found in the best fit. It can thus be concluded that the extra jet component is not required by the data and that the source emission is not jet-dominated.

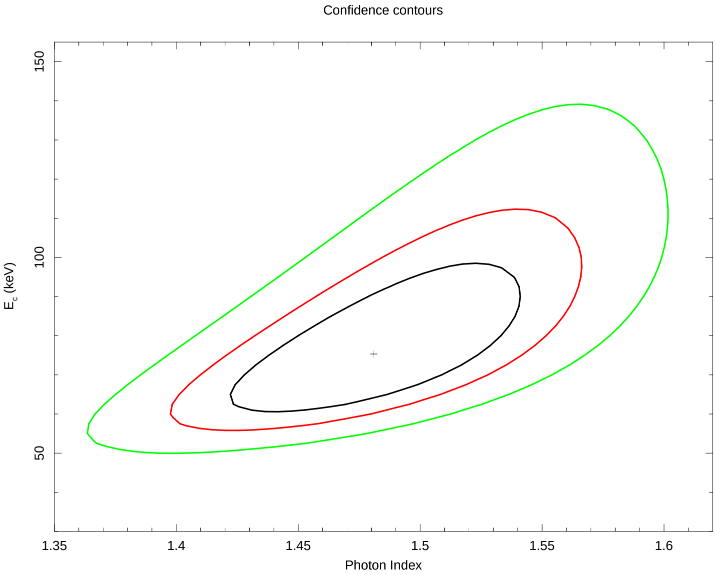

Figure 5.7: Constraints on the primary continuum (power-law photon index) versus the high energy cut-off of IGR J21247+5058.

Next, the best-fit model (`wa*pcfabs*pcfabs*cutoffpl`) was used to fit *XRT* and *INTEGRAL* data. In both *XRT* observations, the fit is good (χ^2=138.8 for 145 d.o.f. and χ^2=47.8 for 54 d.o.f.), the power law slopes are around 1.6 and 1.8 and the high energy cut-off values are not well constrained, although they could be placed above 50 and 80 keV respectively. The partial covering fractions for the *XRT1-2/ISGRI* broad-band spectrum are broadly compatible with those found for the *XMM/ISGRI* spectrum (see table 5.3). It must be pointed out that due to the poor statistical quality of the *XRT* datasets, the values of the partial covering fractions are not well constrained and so errors are evaluated by freezing the parameters related to each layer while calculating the uncertainties for the other. The constant between *XRT1* and *INTEGRAL* spectra is around 0.8, suggesting again agreement between the two sets of data. The constant between the *XRT2* observation and the *INTEGRAL* data is instead higher (1.6), implying that the source could have undergone some minor changes in flux or have changed its absorption properties as discussed in the previous section.

Spectral Fits to *XMM-Newton* and *Swift/XRT*

	Γ	$\mathbf{N}_H^1$ ($\mathbf{10^{22}cm^{-2}}$)	$\boldsymbol{f}_1$	$\mathbf{N}_H^2$ ($\mathbf{10^{22}cm^{-2}}$)	$\boldsymbol{f}_2$	$\mathbf{F}_{2-10keV}$ ($\mathbf{10^{-11}}$ **erg** $\mathbf{cm^{-2}s^{-1}}$)	χ^2 **(dof)**
XMM[a]	$1.35^{+0.02}_{-0.02}$	$1.11^{+0.10}_{-0.10}$	$0.76^{+0.02}_{-0.02}$	-	-	5.1	2422.4 (2622)
XMM[b]	$1.57^{+0.05}_{-0.05}$	$0.99^{+0.12}_{-0.12}$	$0.83^{+0.03}_{-0.02}$	$9.14^{+1.93}_{-1.75}$	$0.27^{+0.04}_{-0.04}$	5.1	2345.8 (2620)
XRT1[a]	$1.54^{+0.19}_{-0.18}$	$2.08^{+0.88}_{-0.84}$	$0.74^{+0.07}_{-0.09}$	-	-	6.4	132.5 (140)
XRT2[a]	$1.94^{+0.39}_{-0.37}$	$4.76^{+1.73}_{-1.67}$	$0.89^{+0.04}_{-0.07}$	-	-	3.3	41.4 (48)

Best fit parameters related to model (a) (`wa*pcfabs*po`) and model (b) (`wa*pcfabs*pcfabs*po`);
Parameters are as following: Γ=Photon index; $\mathbf{N}_H^1$= Column density of first absorber;
$\boldsymbol{f}_1$= Covering fraction of first absorber; $\mathbf{N}_H^2$= Column density of second absorber;
$\boldsymbol{f}_2$= Covering fraction of second absorber; $\mathbf{F}_{2-10keV}$= 2-10 keV Flux
and χ^2 **(dof)**= Chi squared (degrees of freedom).

Table 5.2: Spectral fits to X-ray data for IGR J21247+5058.

Spectral fits to broad-band *XMM-Newton-INTEGRAL*/IBIS and *Swift/XRT-INTEGRAL*/IBIS spectra

	Γ	$\mathbf{N}_H^1$ ($\mathbf{10^{22}cm^{-2}}$)	$\boldsymbol{f}_1$	$\mathbf{N}_H^2$ ($\mathbf{10^{22}cm^{-2}}$)	$\boldsymbol{f}_2$	$\mathbf{E}_c$ **(keV)**	**C**	**R**	χ^2 **(dof)**
XMM/ISGRI[a]	$1.67^{+0.05}_{-0.04}$	$10.96^{+1.81}_{-1.56}$	$0.34^{+0.03}_{-0.03}$	$1.11^{+0.12}_{-0.12}$	$0.84^{+0.02}_{-0.02}$	-	$0.73^{+0.07}_{-0.06}$	-	2403.6 (2629)
XMM/ISGRI[b]	$1.48^{+0.06}_{-0.06}$	$9.47^{+2.14}_{-1.98}$	$0.25^{+0.04}_{-0.05}$	$0.95^{+0.12}_{-0.13}$	$0.82^{+0.03}_{-0.03}$	$75.3^{+25.7}_{-15.9}$	$0.85^{+0.08}_{-0.07}$	-	2354.0 (2628)
XMM/ISGRI[c]	$1.54^{+0.08}_{-0.08}$	$8.19^{+2.27}_{-1.92}$	$0.25^{+0.04}_{-0.05}$	$0.97^{+0.12}_{-0.12}$	$0.83^{+0.03}_{-0.03}$	$99.1^{+54.5}_{-29.1}$	$0.67^{+0.18}_{-0.12}$	$0.42^{+0.47}_{-0.39}$	2350.9 (2627)
XRT1/ISGRI[d]	$1.58^{+0.32}_{-0.25}$	$6.62^{+39.74}_{-6.57}$	$0.13^{+0.08}_{-0.08}$	$1.91^{+0.59}_{-0.49}$	$0.75^{+0.08}_{-0.06}$	>50	$0.78^{+0.32}_{-0.32}$	-	138.8 (145)
XRT2/ISGRI[d]	$1.75^{+0.15}_{-0.20}$	$4.95^{+1.18}_{-1.64}$	$0.77^{+0.06}_{-0.07}$	$0.56^{+1.95}_{-0.13}$	$0.95^{+0.01}_{-0.961}$	>80	$1.59^{+0.56}_{-0.31}$	-	47.8 (54)

Best fit parameters related to model model (a) (`wa*pcfabs*pcfabs*po`), model (b) (`wa*pcfabs*pcfabs*cutoffpl`),
model (c) (`wa*pcfabs*pcfabs*pexrav`) and model (d) (`wa*pcfabs*pcfabs*cutoffpl`);
Parameters are as following: Γ=Photon index; $\mathbf{N}_H^1$= Column density of first absorber;
$\boldsymbol{f}_1$= Covering fraction of first absorber; $\mathbf{N}_H^2$= Column density of second absorber;
$\boldsymbol{f}_2$= Covering fraction of second absorber; $\mathbf{E}_c$= Cut-off energy; **C**=Cross calibration constant;
R= reflection Component; χ^2 **(dof)**= Chi squared (degrees of freedom).

Table 5.3: Spectral fits for IGR J21247+5058 broad-band data.

5.4 Discussion and Conclusions

The radio counterpart of IGR J21247+5058 shows characteristics typical of a Broad Line Radio Galaxy, very likely of the FR II type. The spectrum between 610 MHz and 15 GHz, obtained with VLA and GMRT archival data, is typical of synchrotron self-absorption radiation. Moreover, there is evidence for a moderate Doppler boosting of the base of the jet, based on the ratio between core and total radio power. It can therefore be concluded that the source is certainly radio loud.

The 0.4-100 keV broad-band spectrum of IGR J21247+5058 is well modelled by a power-law continuum with a cut-off at around 70-80 keV, absorbed by two layers of cold material partially covering the central source. A weak iron line is possibly present in the data, while the value of the reflection component is low (R~0.4) and not well constrained. In many ways IGR J21247+5058 behaves like other BLRG which show weak reprocessing components and flatter X/gamma-ray power-law slopes than generally observed in radio quiet broad line galaxies like Seyferts (Grandi et al. 2006); both characteristics are generally (but not solely, see next chapter) interpreted as due to the presence of a beamed jet component in these bright radio sources. The effect of this component is that of contaminating/diluting the Seyfert continuum which is likely present in the source. Alternatively, one has to suppose differences in the accretion disk between BLRG and radio quiet Seyfert galaxies, such as the geometry, flow efficiency or gas state (ionised versus neutral). The high energy cut-off in IGR J21247+5058 inferred by the *INTEGRAL* data is typical of Seyfert galaxies and not of beamed AGN like blazars, which tend to have much higher cut-off energies. We have not found strong evidence for a jet component in our broad-band data, although its presence cannot be excluded. A better way to look for beamed radiation in IGR J212471+5058 is by means of high resolution observations at radio frequencies, which would be extremely important. On the other hand, complex absorption is not a characteristic of classical BLRG and has been observed so far in only another object, i.e. 3C 445 (Sambruna et al. 2007). Both galaxies require cold absorbers partially covering the central source, even though in the case of 3C 445 three layers of obscuring materials are required while only two in IGR J21247+5058 are needed at low energies. However, while 3C 445 shows a strong iron line and a consequent strong reflection component, in the case of IGR J21247+5058 reflection is not required by the data and the iron line is weak or even absent. Several emission lines are also observed at low energies in the spectrum of 3C 445, making it somewhat different from IGR J21247+5058. As for 3C 445, the presence of absorption in IGR J21247+5058 is at odds with its Seyfert 1 classification, but this discrepancy can be circumvented if the “clumpy torus" model recently proposed by Elitzur & Shlosman (2006) and successfully applied to 3C 445 (Sambruna et al. 2007) is also applied to this newly discovered radio galaxy. In this model, the torus is not a continuous toroidal structure but is made of clouds with $N_H \sim 10^{22}$-10^{23} atoms cm^{-2} distributed around the equatorial plane of the AGN. The BLR represents the inner segment of the torus and this is the region where the X-ray absorption is likely to occur (Liu & Zhang 2002). Because of this clumpyness the difference between type 1 and 2 AGN is not only due to orientation but also to the probability of direct view of the active nucleus or, in other words, on how many clouds our line of sight intercepts. Indeed, the inclination to the line of sight inferred from the radio analysis suggests that we are peering directly into the broad line region; moreover, variations in the absorption properties are expected in this scenario, as the torus structure changes due to cloud motion.

Overall it can be concluded that IGR J21247+5058 is a new interesting member of the class of BLRG, with features that are in some respect typical of this class and others which are quite rare for its type: its brightness and proximity make it an ideal laboratory in which to study radio galaxies properties.

In the next chapter, a subsample of seven other BLRG extracted from the complete sample of type 1 AGN detected by *INTEGRAL* will be analysed in detail.

Chapter 6

Broad Line Radio Galaxies

6.1 Introduction

A sample of radio loud AGN has been extracted using the radio and hard X-ray information and data, as well as the source radio morphology. In this way a set of eight radio loud AGN has been identified, i.e. ∼20% of the entire sample; of these, six were secure radio loud objects and two were identified as candidate ones. Finally the remaining 26 radio quiet objects have been analysed (see next chapter). A detailed analysis of the results and comparison between radio quiet and radio loud objects will be presented in the last chapter of the thesis.

Most of what is known about Active Galactic Nuclei (AGN) is essentially based on studies of radio quiet sources, which make up almost 90% of the entire AGN population; as far as radio loud objects are concerned, their nuclear regions are less well studied, mainly because of their lower number densities. It is widely accepted that Seyfert galaxies are powered by accretion onto a supermassive black hole: the observed radiation, spanning the entire electromagnetic spectrum, is produced by a cold accretion disk and by a hot corona, as proposed in the so-called two-phase model (Maraschi & Haardt 1997). In the X-ray domain, the emission of radio quiet Broad Line AGN (Seyfert 1) is, to the first order, well described by a power law of photon index 1.8-2.0, extending from a few keV to over 100 keV; at higher energies there is evidence of an exponential cut-off, the exact value of which is still uncertain (Perola et al. 2002; Risaliti 2002). Secondary features, such as the Fe Kα line and the Compton reflection component are also commonly observed; they are considered to be the effects of reprocessing of the primary continuum and are relatively well understood (Mushotzky et al. 1993). From studies performed on samples of Broad Line Radio Galaxies (BLRG from now on; Sambruna et al. 1999 and Grandi et al. 2006) there is evidence that they show similar optical/UV continuum and emission line characteristics to their radio quiet counterparts, but may display some fundamental differences in their X-ray behaviour. BLRG, in fact, exhibit flatter/harder power law slopes than radio quiet Seyfert 1 galaxies and are also known to have weaker reprocessing features such as Fe Kα lines and Compton reflection components (e.g. Sambruna et al. 1999 and Grandi et al. 2006). The origin of these differences is however far from being understood. A possible cause for the observed diversity could be ascribed to a different disk geometry and/or accretion flow efficiencies, or the presence of jets and beaming effects that contaminate/dilute the AGN component and the reprocessing features; ionised reflection, which naturally produces weaker reprocessing features, has also been considered in the literature (Ballantyne, Ross & Fabian 2002). Now that a large sample of AGN detected above 20 keV by *INTEGRAL* is available, it is possible and important to perform a comparison between different classes of AGN, by measuring the shape of the primary continuum together with the high energy cut-off and the reflection component.

In this chapter the broad-band (1-110 keV) spectral analysis of a sample of seven candidate radio loud type 1 AGN is presented, combining *XMM-Newton*, *Chandra*, *Swift/XRT* and *BAT* data together with *INTEGRAL* measurements.

6.2 The Sample

The definition of radio loudness is rather vague, with different criteria applied in the literature (see Zamfir, Sulentic & Marziani 2008 for a critical discussion). Traditionally, empirical boundaries were set by the radio power density at 5 GHz (P_{5GHz}) (Miller, Peacock & Mead 1990) and the radio (same frequency) to optical B band flux density ratio (R_B) (Kellerman et al. 1989): an AGN is radio loud if $P_{5GHz} \geq 10^{32}$ erg s^{-1} Hz^{-1} and Log[P_{5GHz}/P_B]$\geq$1. In time, different surrogate definitions of both parameters have appeared in the literature involving radio data at different frequencies and comparison with even UV and X-ray fluxes to deal with objects selected in bands other than the optical. More recently Zamfir, Sulentic & Marziani (2008) suggested the use of the source radio morphology as a further criterion to divide radio loud from radio quiet objects. Since FR I morphology is quite rare in broad line radio loud AGN, while double-lobe FR II appearance is much more common, these authors suggest the adoption of this last morphology as a further discriminator, i.e. FR II-like objects are by default radio loud.

The radio loud AGN presented here have therefore been selected on the basis of similar criteria: the radio power density at 1.4 GHz ($P_{1.4GHz}$), the radio (same frequency) to the 20-100 keV flux density ratio (R_{HX}) and the source morphology, again at 1.4 GHz. Because

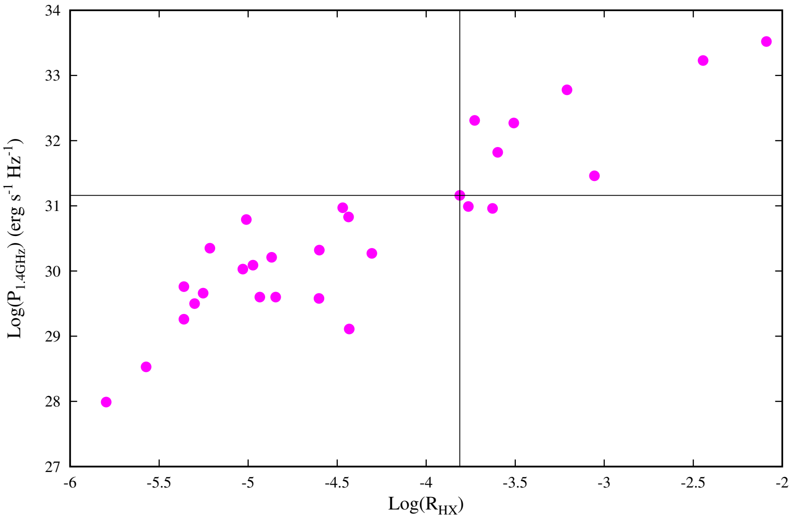

Figure 6.1: 1.4 GHz Power density against the ratio of the 1.4 GHz to 20-100 keV flux density ratio for all most sources in the *INTEGRAL* broad line AGN catalogue. The boundaries on both axis are set by the values of the weakest FR II in the sample (IGR J21247+5058) and are defined by the lines drawn in the figure.

many of these objects are newly discovered, it is difficult to have information for all of them at 5 GHz and/or in the B band, hence the use of the more ready available 1.4 GHz and 20-100 keV data. 1.4 GHz information has been obtained from the HEASARC database[1] for 29 objects in the sample, except in the case of IGR J13109-5552, where the 1.4 GHz flux was extrapolated using the 4.85 and 0.83 GHz fluxes available in the HEASARC database. *INTEGRAL* data were derived from the fluxes reported in Bird et al. (2007; see also chapter 4) and are available for all objects in the sample. Candidate radio loud objects were selected on the basis of their location in the diagram shown in figure 6.1, where the radio quiet/loud boundaries on both axis are set by the weakest FR II source in the sample, i.e. IGR J21247+5058. This source has been fully discussed in the previous chapter and can be now taken as a clear example of a radio loud AGN on the basis of various arguments. In particular it has been classified as an FR II galaxy mainly on the basis of its morphology.

By means of these boundaries, 7 radio loud AGN (excluding IGR J21247+5058 already discussed in the previous chapter) have been identified: QSO B0241+62, B3 0309+411, 3C 111, 3C 390.3, IGR J13109-5552, 4C 74.26 and S5 2116+81 (see table 6.1); note the ambiguous location of two AGN, MCG+08-11-011 and Markarian 6, which are below the adopted boundaries but very close to IGR J21247+5058. Information at 5 GHz and in

---

[1] http://heasarc.gsfc.nasa.gov/

the B band are available for all these sources so that a cross-check can be made on their radio power and radio-to-optical flux density ratio according to the more conventional definition used by Miller, Peacock & Mead (1990) and Kellerman et al. (1989). Both values are listed in table 6.1 for all 7 candidates plus IGR J21247+5058, Markarian 6 and MCG+8-11-011, which are still considered due to their location in figure 6.1: 5 AGN are close or above $P_{5GHz} \geq 10^{32}$ erg s^{-1} Hz^{-1} and in any case all but Mrk 6 and MCG+8-11-011 have a 5 GHz flux density exceeding that of IGR J21247+5058. All the objects, including Mrk 6 and MCG+08-11-011, have instead $Log[P_{5GHz}/P_B] \geq 1$, the limit defined by the radio-to-optical flux density ratio. Next the radio morphology of all 7 radio loud candidate AGN was examined, plus again Mrk 6 and MCG+08-11-011 (see table 6.1).

Name	**Type**	$\mathbf{N}_H^{Gal}$	**Log($\mathbf{P}_{5GHz}$)**	**Log($\mathbf{R}_B$)**	**CD**[‡]
			10^{22} cm^{-2}	**erg s^{-1}Hz^{-1}**	
QSO B0241+62	-	0.75	31.230	2.8-2.9	1.94
B3 0309+411	BLRG, FRII?	0.13	32.322	3.3	1.17
3C 111	BLRG, FRII	0.32	31.919	4.4-5.0	0.04
IGR J13109-5552	-	0.22	31.929	2.7	-
3C 390.3	BLRG, FRII	0.04	32.477	3.7	0.09
4C 74.26	BLRG, FRI/FRII	0.12	31.939	1.9-2.07	0.95
S5 2116+81	BLRG, FR?	0.07	31.771	1.9	1.78
IGR J21247+5058	BLRG, FRII	1.11	31.041	-	0.76
MCG+08-11-011	-	0.20	29.886	1.6	-
Mrk 6	-	0.06	29.934	1.5-1.8	-

[‡]: radio core dominance at 5 GHz, except for B3 0309+411B
for which it is measured at 8 GHz (see references in the text).

Table 6.1: Candidate Radio Loud AGN in the *INTEGRAL* complete sample.

All but 2 sources (i.e. QSO B0241+62 and IGR J13109-5552) are well known Broad Line Radio Galaxies (see table 6.1 and NED; Ballantyne 2005) and show a morphology with two lobes extending from the central nucleus (see for example NVSS contour maps available in NED); the extension of the lobes for B3 0309+411 and 4C 74.26 is more than 1 Mpc, hence their classification as giant radio galaxies (de Bruyn 1989; Riley et al. 1988). These double-lobed objects are classified in the literature as FR II galaxies, with the exception of 4C 74.26 and S5 2116+81, which still have an uncertain/unknown nature. QSO B0241+62 and IGR J13109-5552 have been poorly studied at radio frequencies and their classification is uncertain; both are Seyfert 1 according to NED and Masetti et al. (2008). QSO B0241+62, shows a compact unresolved core in the NVSS map, although high resolution radio imaging indicates a possible double-lobe morphology within this core structure (Tzanetakis et al. 1978). The sky region containing IGR J13109-5552 has not been mapped by the NVSS, but the source is present in the Molonglo Galactic Plane Survey 2^{nd} Epoch (MGPS-2) Compact Source Catalogue (Murphy et al. 2007); a cut-off image of the source shows an unresolved but elongated structure. QSO B0241+62 is reported as a relatively strong source in various radio surveys, has a flat radio spectrum with a α~0.1 [2] (Vollmer et al. 2005) and so almost certainly qualifies as a radio loud AGN. IGR J13109-5552 has less information at radio frequencies but the few available data provide a flat spectrum also in this case (α~0.3).

For completeness, the morphology of Markarian 6 and MCG+08-11-011 have also been checked in the NVSS/NED databases: both sources are similar to QSO B0241+62, i.e. display a compact core which shows, at higher resolution, a clear (in Markarian 6; Kharb et al. 2006) or possible (in MCG+8-11-011, Ulvestad & Wilson 1986) double lobe structure. However their radio spectra are steeper than in the previous two cases and more similar to radio quiet AGN. This evidence, coupled with their lower radio powers argues against a classification as radio loud AGN and therefore both objects are not considered further. They will be analysed, together with the remaining type 1 radio quiet objects of the complete sample, in the following chapter.

In table 6.1 also the 5/8 GHz radio core dominance (CD) is listed. The parameter $CD=S_{core}/(S_{tot}-S_{core})$ is taken from Fan & Zhang (2003); the only exception is B3 0309+411 for which the *CD* parameter has been evaluated using data from Ishwara-Chandra & Saikia (1999); no information on *CD* is available for IGR J13109-5552.

The radio core dominance spans a large range of values from 0.04 to 1.9. Sources with high values of this parameter are those in which the beamed radio emission is emitted in a direction closer to the line of sight; in these sources, jet emission is likely to play a

---

[2] $S_{\nu} \propto \nu^{-\alpha}$

greater role than in sources with smaller values of *CD*. Contrary to expectations, we do not find any convincing correlation between *CD* and either P_r or R_X, indicating that in at least some of our sources a jet component alone cannot be the origin of the source radio brightness. As a final remark, we point out that the radio loud sources analysed in this chapter make up around 20% of the 20-40 keV complete sample of broad line AGN and are therefore a non-negligible fraction of the *INTEGRAL* AGN population.

6.3 Broad-Band Spectral Analysis

The *XMM-Newton*, *Chandra* and *Swift/XRT* data were fitted together with *INTEGRAL* and *Swift/BAT* data using `XSPEC` v.11.2.3 (Arnaud 1996); errors are quoted at 90% confidence level for one parameter of interest ($\Delta\chi^2$=2.71). In the fitting procedure, a multiplicative constant, *C*, has been introduced to take into account possible cross-calibration mismatches between the X-ray and the soft gamma-ray data. When treating the *INTEGRAL* data, this constant C_1 has been found to be close to 1 with respect to *XMM-Newton*, *Swift/XRT* and *Chandra* using various source typologies (e.g. Landi et al. 2007; Masetti et al. 2007), so that significant deviation from this value can be confidently ascribed to source flux variability; also when considering *BAT* data, a cross-calibration constant C_2 different to 1 often means flux variation in the source analysed (see for example Ajello et al 2008 and Winter et al. 2008). In all the fits, Galactic absorption (see table 6.2) has already been taken into account so that any column densities reported in subsequent tables refer to absorption intrinsic to the source.

6.3.1 Towards a First Approximation of the Broad-Band Continuum

The broad-band data have been firstly fitted in the 0.5-110 keV energy range employing a simple power law (absorbed only by Galactic column density) in order to identify typical features of the AGN spectra. Some objects show evidence of excess counts below 1 keV; however, since the study of the soft excess is not the main objective of the present thesis, but rather the understanding of the high energy emission characteristics (photon index, high energy cut-off and reflection) of our sources, the analysis has been focussed in the 1-110 keV energy range. Starting from the simple power law various spectral features were introduced, such as intrinsic absorption and iron line, each time performing an F-test to verify the statistical significance of each added component and to provide a basic model able to describe the data at least to a first approximation (see table 6.2 and residuals with respect to this model in figures 6.2, 6.3, 6.4 and 6.5).

Inspection of figure 6.4 (left panel) suggests that the model employed in table 6.2 does not provide a good description of the data also in the case of 3C 390.3, where the residuals have an unusual concave shape, which may be due to the presence of a low energy component (soft excess) still affecting the spectrum around 2-3 keV. To take this into account an extra component has been added to the simple power law in the form of another power law or a blackbody component: both fits provide an equally significant improvement (typically more than 99%) and more acceptable residuals. The blackbody temperature is slightly higher than typically observed in Seyfert 1 galaxies (Panessa et al. 2008). It is interesting to note that so far no soft excess has been reported for this source, except for an old claim never confirmed afterwards (Grandi et al. 1999); however a *Chandra* image of 3C 390.3 reveals extended soft X-ray emission around the nucleus so that the soft excess photons could be related to this component (Kadler et al. 2004 and figure 7 in Hardcastle & Croston 2005). This source is also known to have a variable column density, as found by a previous work (Grandi et al. 1999); however in this analysis no absorption in excess of the Galactic one could be measured. Due to the evidence found, in the following the model $\texttt{wa}_g\texttt{*wa*(bb+po+zga)}$ is adopted (table 6.3 and figure 6.6) as the basic representation of 3C 390.3 data.

Using the results reported in tables 6.2 and 6.3 some conclusions can already be drawn, as the models employed at this stage provide, to a first approximation, a good description of the broad-band spectra of the sources. In all but 2 AGN (B3 0309+411 and 3C 390.3), an intrinsic absorption component is strongly required by the data, at more than 90% confidence level for IGR J13109-5552 and S5 2116+81 and at more than 99% confidence level for the remaining objects. Note, however, that in 3C 111 the measured absorption could be due to a molecular cloud located between us and the source (Unger et al. 1985) and not intrinsic to the AGN.

The Fe Kα line is detected in all the sources (99% confidence level), except in IGR J13109-5552 and S5 2116+81, but this may be due to *XRT* not being sensitive enough to detect the cold iron line around 6.4 keV. Note that the line is narrow in all sources (hence the line width has been fixed to 10 eV), except in 4C 74.26, in which a quite strong and possibly broad iron line is detected (see also Ballantyne 2005 and Larsson et al. 2008). The equivalent widths (EW) for the iron lines are found to be $\lesssim$100 eV in most AGN. In one source, namely 3C 111, the equivalent width values is close to the capability limits of moderate resolution CCD instruments like *XMM-Newton*, calling for some caution in distinguishing between a real feature or just local noise. If the line is related to reflection, the observed values would imply a low reflection component parameter ($R=\Omega/2\pi$): in this case one may expect to find the EW to R ratio of the order of 100-130 eV (Perola et al.

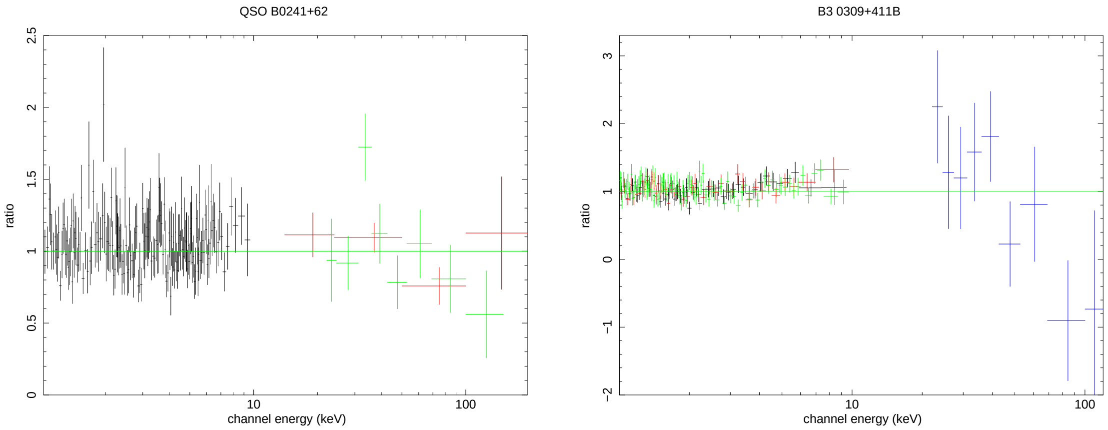

Figure 6.2: Model to data ratios for QSO B0241+62 (left panel) and B3 0309+411B (right panel). The model employed is a simple power law absorbed by both Galactic and intrinsic column density (only in the case of QSO B0241+62) plus a narrow Gaussian component (see table 6.2).

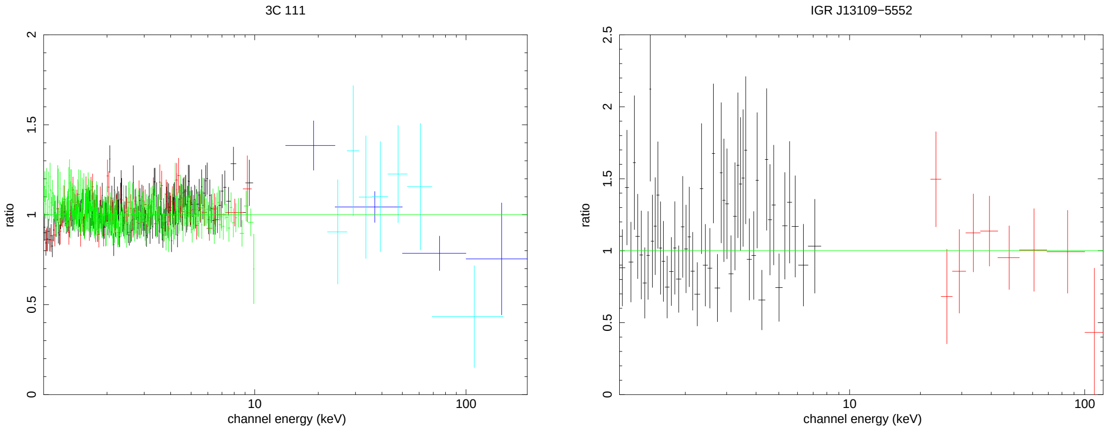

Figure 6.3: Model to data ratios for 3C 111 (left panel) and IGR J13109-5552 (right panel). The model employed is a simple power law absorbed by both Galactic and intrinsic column density plus, in the case of 3C 111, a narrow Gaussian component (see table 6.2).

2002) and consequently values of $R \leq 1$. Finally a note on the cross-calibration constants between the X-ray data and *IBIS/BAT* points: in some sources these constants are not consistent with 1, indicating, as expected, flux variations between the X-ray snap-shot observations and the time-averaged high energy spectral data.

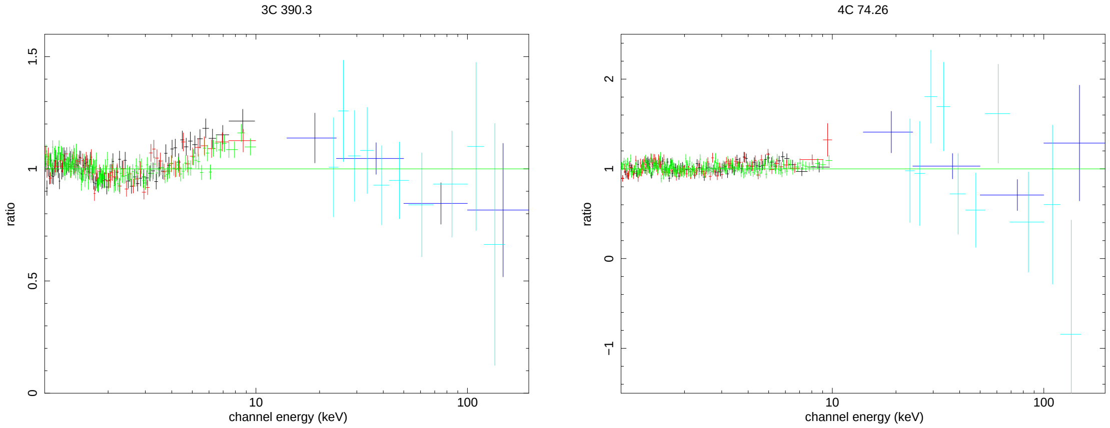

Figure 6.4: Model to data ratios for 3C 390.3 (left panel) and 4C 74.26 (right panel). The model employed is a simple power law absorbed by both Galactic and intrinsic column density (only in the case of 4C 74.26) plus a narrow (3C 390.3) or broad (4C 74.26) Gaussian component (see table 6.2).

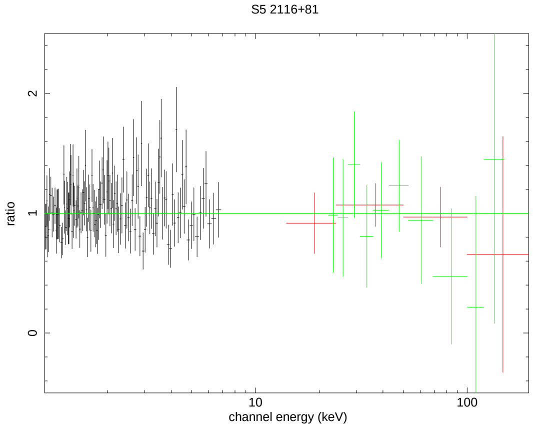

Figure 6.5: Model to data ratios for S5 2116+81. The model employed is a simple power law absorbed by both Galactic and intrinsic column density (see table 6.2).

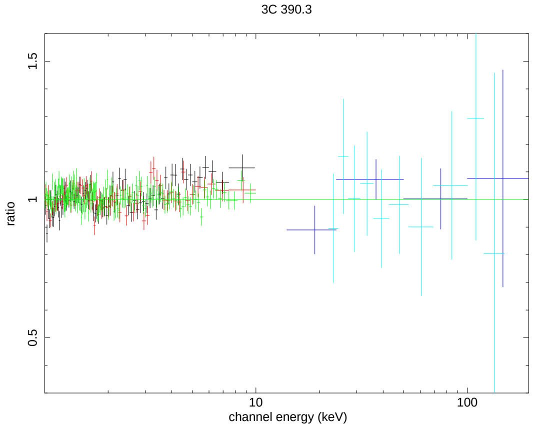

Figure 6.6: Model to data ratio for 3C 390.3. The model used is a simple power law absorbed by Galactic column density plus a blackbody component to model the soft excess and a narrow Gaussian component (see table 6.3).

Spectral Fit Results: $\mathtt{wa}_g$`*wa*(po+zga)`

Name	**N$_H^{gal}$ (10^{22} cm^{-2})**	**N$_H$ (10^{22} cm^{-2})**	Γ	**E$_{line}$ (keV)**	σ **(eV)**	**EW (eV)**	**C$_1^A$**	**C$_2^B$**	χ^2 **(dof)**
QSO B0241+62	0.75	$0.23^{+0.08}_{-0.08}$	$1.65^{+0.07}_{-0.07}$	$6.40^{+0.06}_{-0.05}$	10f	85^{+43}_{-45}	$1.02^{+0.22}_{-0.18}$	$1.32^{+0.32}_{-0.26}$	227.1 (234)
B3 0309+411	0.13	-	$1.82^{+0.03}_{-0.03}$	$6.34^{+0.07}_{-0.09}$	10f	100^{+43}_{-50}	-	$4.65^{+2.11}_{-2.00}$	574.6 (603)
3C 111	0.32	$0.43^{+0.02}_{-0.02}$	$1.69^{+0.02}_{-0.02}$	$6.40^{+0.05}_{-0.05}$	10f	<30	$0.44^{+0.05}_{-0.04}$	$0.54^{+0.11}_{-0.10}$	1245.7 (1498)
IGR J13109-5552	0.22	$0.27^{+0.23}_{-0.27}$	$1.70^{+0.24}_{-0.22}$	-	-	-	-	$2.39^{+1.84}_{-0.99}$	41.2 (55)
3C 390.3	0.04	-	$1.74^{+0.01}_{-0.01}$	$6.44^{+0.02}_{-0.04}$	10f	71^{+8}_{-18}	$0.90^{+0.07}_{-0.07}$	$0.94^{+0.10}_{-0.11}$	2200.4 (2234)
4C 74.26	0.12	$0.12^{+0.01}_{-0.01}$	$1.73^{+0.02}_{-0.01}$	$6.44^{+0.05}_{-0.06}$	183^{+84}_{-65}	103^{+32}_{-25}	$0.54^{+0.09}_{-0.09}$	$0.87^{+0.25}_{-0.25}$	1992.0 (2060)
S5 2116+81	0.07	<0.19	$1.97^{+0.12}_{-0.12}$	-	-	-	$1.52^{+0.60}_{-0.44}$	$2.76^{+1.34}_{-0.95}$	89.1 (128)

A: cross-calibration constant between X-ray data and *BAT*;
B: cross-calibration constant between X-ray data and *INTEGRAL*/*ISGRI*.

Table 6.2: Simple power law fits.

3C 390.3 Spectral Fits Results: $\mathtt{wa}_g$`*(bb+po+zga)`

N$_H$ (10^{22}cm^{-2})	Γ	**kT (keV)**	**E$_{line}^{\dagger}$ (keV)**	**EW (eV)**	**C$_1^A$**	**C$_2^B$**	χ^2 **(dof)**
-	$1.89^{+0.02}_{-0.02}$	$2.41^{+0.22}_{-0.17}$	$6.42^{+0.04}_{-0.03}$	49^{+9}_{-15}	$1.37^{+0.16}_{-0.15}$	$1.58^{+0.24}_{-0.21}$	1970.4 (2232)

†: line width fixed to 10 eV.
A: cross-calibration constant between *XMM* and *BAT*;
B: cross-calibration constant between *XMM* and *INTEGRAL*/*ISGRI*.

Table 6.3: Simple power law fit for 3C 390.3.

6.3.2 Incidence of the High Energy Cut-off

Next a high energy cut-off in the primary power law of the basic model has been introduced (see tables 6.4 and 6.5 for model description in each source case). Only 3C 111 strongly requires a cut-off energy at more than 99% confidence level; the cut-off is localised at around 100 keV. As far as the other sources are concerned, only a lower limit for their cut-off energies could be set at around 60-80 keV, apart from 3C 390.3, where the high energy cut-off could not be constrained at all. It is also interesting to note that the values of C_1 and C_2 tend to be higher when a cut-off energy component is added to the simple power law.

Spectral Fit Results: `wa`$_g$`*wa*(cutoffpl+zga)`

Name	**N$_H$** (10^{22} cm^{-2})	Γ	**E$_{cut}$** (keV)	**E$_{line}$** (keV)	σ (eV)	**EW** (eV)	**C$_1^A$**	**C$_1^B$**	χ^2 **(dof)**	**Prob**[†]
QSO B0241+61	$0.18^{+0.09}_{-0.09}$	$1.58^{+0.09}_{-0.09}$	>78	$6.40^{+0.07}_{-0.05}$	10f	80^{+41}_{-45}	$1.14^{+0.23}_{-0.21}$	$1.54^{+0.39}_{-0.34}$	222.9 (233)	96%
B3 0309+411	-	$1.80^{+0.05}_{-0.05}$	>43	$6.34^{+0.07}_{-0.09}$	10f	99^{+46}_{-47}	-	$6.75^{+3.44}_{-3.81}$	573.9 (602)	91%
3C 111	$0.42^{+0.02}_{-0.02}$	$1.65^{+0.03}_{-0.03}$	110^{+118}_{-40}	$6.40^{+0.05}_{-0.05}$	10f	<30	$0.56^{+0.09}_{-0.08}$	$0.74^{+0.19}_{-0.17}$	1234.2 (1497)	99.9%
IGR J13109-5552	<0.46	$1.55^{+0.31}_{-0.26}$	>58	-	-	-	-	$2.29^{+1.84}_{-0.99}$	39.8 (54)	83%
4C 74.26	$0.11^{+0.01}_{-0.01}$	$1.70^{+0.03}_{-0.03}$	>78	$6.44^{+0.05}_{-0.06}$	184^{+78}_{-66}	104^{+31}_{-26}	$0.63^{+0.16}_{-0.14}$	$1.09^{+0.44}_{-0.37}$	1989.9 (2059)	86%
S5 2116+81	<0.18	$1.95^{+0.14}_{-0.14}$	>81	-	-	-	$1.54^{+0.64}_{-0.44}$	$2.87^{+1.59}_{-1.04}$	89.2 (127)	-

A: cross-calibration constant between X-ray data and *BAT*;
B: cross-calibration constant between X-ray data and *INTEGRAL/ISGRI*.
[†]: fit improvement with respect to table 6.2.

Table 6.4: Cut-off power law spectral fits.

3C390.3 Spectral Fits Results: `wa`$_g$`*(bb+cutoffpl+zga)`

N$_H$ (10^{22}cm^{-2})	Γ	**kT** (keV)	**E$_{cut}$** (keV)	**E$_{line}^{\ddagger}$** (keV)	**EW** (eV)	**C$_1^A$**	**C$_2^B$**	χ^2 **(dof)**	**Prob**[†]
-	$1.89^{+0.02}_{-0.01}$	$2.41^{+0.21}_{-0.16}$	NC	$6.43^{+0.03}_{-0.04}$	48^{+9}_{-14}	$1.37^{+0.16}_{-0.15}$	$1.58^{+0.23}_{-0.11}$	1970.2 (2231)	37%

[‡]: line width fixed to 10 eV.
A: cross-calibration constant between *XMM* and *BAT*;
B: cross-calibration constant between *XMM* and *INTEGRAL/ISGRI*.
[†]: fit improvement with respect to table 6.3.

Table 6.5: Cut-off power law spectral fit for 3C 390.3.

6.3.3 Incidence of the Reflection Component

Finally the reflection component has been introduced in the basic model of tables 6.2 and 6.3 to verify the incidence of this feature in the broad-band data (again refer to tables 6.6 and 6.7 for model description in each source case). The power law has been substituted with the `pexrav` model in `XSPEC`, fixing the inclination angle at 30° (i.e. a nearly face-on geometry as expected in type 1 AGN) and the cut-off energy at 10 000 keV. Taking into consideration the fact that the iron line EW is always $\lesssim$100 eV, we assume that the reflection parameter (R=$\Omega/2\pi$) cannot have very high values; for this reason initially the reflection component was allowed to vary only in the range 0-2. B3 0309+411 and 4C 74.26 require reflection at more than 99% confidence level, while 3C 390.3 and QSO B0241+62 at a lower confidence level (98% and 92% respectively). The reflection component is also significantly required (at more than 99% confidence level) in 3C 111, which also has a high energy cut-off; since in this object the iron line is very weak or possibly even absent, one would expect to observe negligible or low reflection and it could therefore be that a better fit is achieved when both R and E_c are left free to vary (see next section). In S5 2116+81 and IGR J13109-5552 the data only provide a loose lower limit on R, likely due to the low statistical quality of the X-ray data.

The reflection values are all above 0.1 and, when constrained, are typically around 1. Despite being strongly required, R is unconstrained in B3 0309+411 due to the upper bound of 2 set on the reflection; when this bound is removed R is found to be $2.44^{+1.41}_{-1.17}$ and the constant becomes C_2=$2.30^{+1.10}_{-0.94}$. It is also important to note that R tends to be higher than expected on the basis of the measured iron line EW and that the `pexrav` model provides, as expected, smaller values of C_1 and C_2 with respect to the previous two models.

Spectral Fit Results: `wa`$_g$`*wa*(pexrav+zga)`, $0 \leq R \leq 2$, E_c=10 000 keV

Name	**N_H (10^{22} cm^{-2})**	**Γ**	**R**	**E_{line} (keV)**	**σ_{line} (eV)**	**EW (eV)**	**C_1^A**	**C_2^B**	**χ^2 (dof)**	**Prob†**
QSO B0241+61	$0.31^{+0.04}_{-0.10}$	$1.83^{+0.07}_{-0.15}$	>0.37	$6.40^{+0.08}_{-0.03}$	10f	67^{+40}_{-42}	$0.59^{+0.28}_{-0.11}$	$0.74^{+0.36}_{-0.16}$	224.1 (233)	92%
B3 0309+411	-	$1.92^{+0.03}_{-0.04}$	>1.20	$6.33^{+0.09}_{-0.10}$	10f	70^{+41}_{-43}	-	$2.42^{+1.06}_{-0.97}$	560.4 (602)	99.99%
3C 111	$0.48^{+0.03}_{-0.03}$	$1.78^{+0.05}_{-0.06}$	$1.06^{+0.63}_{-0.68}$	$6.40^{+0.07}_{-0.08}$	10f	<30	$0.30^{+0.07}_{-0.04}$	$0.35^{+0.11}_{-0.07}$	1238.5 (1497)	99.7%
IGR J13109-5552	$0.26^{+0.25}_{-0.25}$	$1.75^{+0.23}_{-0.25}$	>0.1	-	-	-	-	$1.30^{+2.69}_{-0.74}$	40.5 (54)	66%
4C 74.26	$0.16^{+0.02}_{-0.02}$	$1.84^{+0.05}_{-0.04}$	$1.30^{+0.67}_{-0.51}$	$6.45^{+0.04}_{-0.06}$	<186	51^{+37}_{-16}	$0.33^{+0.07}_{-0.06}$	$0.54^{+0.16}_{-0.17}$	1977.0 (2059)	99.99%
S5 2116+81	<0.22	$2.03^{+0.20}_{-0.16}$	>0.1	-	-	-	$1.10^{+0.73}_{-0.43}$	$1.97^{+1.51}_{-0.87}$	88.5 (127)	64%

A: cross-calibration constant between X-ray data and *BAT*;
B: cross-calibration constant between X-ray dataand *INTEGRAL/ISGRI*.
†: fit improvement with respect to table 6.2.

Table 6.6: `pexrav` model spectral fits (E_c=10 000 keV).

3C 390.3 Spectral Fits Results: `wa`$_g$`*wa*(bb+pexrav+zga)`, $0 \leq R \leq 2$, E_c=10 000 keV

N_H (10^{22}cm^{-2})	**Γ**	**kT (keV)**	**R**	**$E^\ddagger_{line}$ (keV)**	**EW (eV)**	**C_1^A**	**C_2^B**	**χ^2 (dof)**	**Prob†**
-	$1.89^{+0.03}_{-0.02}$	$2.38^{+0.27}_{-0.22}$	$0.70^{+0.48}_{-0.59}$	$6.43^{+0.03}_{-0.04}$	44^{+10}_{-13}	$0.88^{+0.42}_{-0.13}$	$0.93^{+0.55}_{-0.22}$	1965.4 (2231)	98%

‡: line width fixed to 10 eV.
A: cross-calibration constant between *XMM* and *BAT*;
B: cross-calibration constant between *XMM* and *INTEGRAL/ISGRI*.
†: fit improvement with respect to table 6.3.

Table 6.7: `pexrav` model spectral fit for 3C 390.3 (E_c=10 000 keV).

6.3.4 Constraining Both Reflection and Cut-off Energy

Lastly, the broad-band spectra have been fitted with a cut-off power law reflected from neutral material (`pexrav` model in `XSPEC`, see table 6.8 for model description in each source case). IGR J13109-5552 and S5 2116+81 were removed from the sample, as in both sources the quality of the data allows no such complex fit. Because of the unconstrained value of the reflection fraction in B3 0309+411 when the parameter is allowed to vary only between 0 and 2, the upper bound on R was also raised. Although this model does not always provide a significant improvement with respect to the fits reported in table 6.4 and 6.6, it nevertheless allows a simultaneous estimate of R and E_{cut}. In this way, it has been possible to set constraints on the reflection parameter of 5 objects and on the cut-off of 3; in the cases of B3 0309+411 and 3C 111, these represent the best fit results. Due to the above considerations, in the following discussion only the values reported in table 5 have bee used, with the eventual use of the upper limits on R and E_{cut} obtained for IGR J13109-5552 and S5 2116+81. It is important to note that the values of the parameters listed in table 6.8 are similar to those obtained in previous fits and also that in most sources the cross-calibration constants are now compatible with 1, an indication that the model is appropriate and that variability is not strong or common at high energies (see also Beckmann et al. 2007).

Spectral Fit Results: `wa`$_g$`*wa*(pexrav+zga)`

Name	**N$_H$** (10^{22} cm^{-2}	Γ	**R**	**E$_c$** (keV)	**EW**‡ (eV)	**C$_1^A$**	**C$_2^B$**	χ^2 **(dof)**
QSO B0241+61	$0.21^{+0.15}_{-0.10}$	$1.64^{+0.22}_{-0.14}$	$0.56^{+0.82}_{-0.41}$	>86	73^{+44}_{-42}	$0.85^{+0.44}_{-0.32}$	$1.12^{+0.65}_{-0.48}$	222.2 (233)
B3 0309+411	-	$1.90^{+0.08}_{-0.08}$	$3.48^{+2.24}_{-1.58}$	35^{+91}_{-17}	59^{+42}_{-43}	-	$6.89^{+9.39}_{-3.90}$	554.2 (601)
3C 111	$0.46^{+0.03}_{-0.03}$	$1.73^{+0.06}_{-0.06}$	$0.85^{+0.57}_{-0.58}$	126^{+193}_{-50}	<30	$0.40^{+0.11}_{-0.08}$	$0.52^{+0.19}_{-0.13}$	1227.9 (1497)
3C 390.3	-	$1.89^{+0.03}_{-0.02}$	$0.60^{+0.60}_{-0.44}$	>300	41^{+12}_{-11}	$0.95^{+0.17}_{-0.25}$	$1.01^{+0.39}_{-0.30}$	1966.3 (2231)
4C 74.26	$0.14^{+0.02}_{-0.03}$	$1.79^{+0.06}_{-0.07}$	$1.22^{+0.69}_{-0.70}$	100^{+680}_{-52}	88^{+23}_{-20}	$0.48^{+0.18}_{-0.12}$	$0.86^{+0.50}_{-0.33}$	1976.0 (2060)

‡: line parameters fixed at value obtained in table 3.

A: cross-calibration constant between X-ray data and *BAT*;

B: cross-calibration constant between X-ray data and *INTEGRAL/ISGRI*.

Table 6.8: `pexrav` model spectral fits.

6.4 Comparison with Previous Measurements

Four out of seven sources in the sample have been previously studied over a broad energy range similar to ours, so that a direct comparison is possible. Overall, the parameter values are in good agreement, or compatible within errors, with those found by these previous works. In the case of 3C 111, all observations point to a small reflection and a compatibly low iron line EW (Grandi et al. 2006; Lewis et al. 2005); the results of the present study yield to a slightly higher value of R, but still compatible, within errors, with previous results. A stringent constraint on the high energy cut-off could be placed, located at a slightly lower value than in previous works, although well within the uncertainties found for example by *BeppoSAX* (Grandi et al. 2006).

Comparison for 3C 390.3 with the works by Grandi et al. (2006) and Gliozzi et al. (2003) indicates good agreement on the cut-off energy, although we, as Gliozzi et al., could not place a constraint on this parameter, which is instead found by Grandi and collaborators to be around 250 keV, i.e. still compatible with our lower limit of 300 keV. The value of the reflection parameter is also fully compatible with the result obtained using *BeppoSAX* data (Grandi et al. 1999) but higher (although compatible within relative uncertainties) than that obtained with *RXTE* spectra (Gliozzi et al. 2003).

A very good agreement with previous works is also found for 4C 74.26 (e.g. Ballantyne & Fabian 2005; Grandi et al. 2006 and Larsson et al. 2008), even though a slightly lower, although within errors, value for the cut-off energy is found.

Not much can be said about S5 2116+81 because of the poor statistical quality of the data; however, comparison with *BeppoSAX* data shows that our results do not contradict those found by Grandi et al. (2006).

For QSO B0241+62, B3 0309+411 and IGR J13109-5552 no previous works are available and thus the analysis presented here is the first broad-band study for these 3 AGN.

Chapter 7

Type 1 Radio Quiet AGN

7.1 Introduction

In this chapter, a broad-band spectral analysis in the 1-110 keV energy range of all radio quiet type 1 sources listed in the complete sample will be performed, combining X-ray measurements (from *XMM-Newton*, *XRT* and *ASCA*) and gamma-ray data from both *INTEGRAL* and *BAT*.

Up to now, modelling of the high energy spectra of AGN has focussed on how to reproduce and explain the observed shape of the primary continuum. A good fraction of the proposed models ascribe the power law to the inverse Compton scattering of soft photons in a bath of “hot electrons” (e.g. Maraschi & Haardt 1997). Variations to these basic models depend on the energy distribution of the electrons and their location in relation to the accretion disc.

Measuring both the primary continuum and its cut-off energy is therefore crucial for understanding models and discriminating between them. While the photon index distribution has been well investigated (Matt 2001), observational results on the cut-off energy have so far been limited by the scarcity of measurements above 10-20 keV, with most of the information coming from broad-band spectra provided by the *BeppoSAX* satellite. Analysis of type 1 and 2 AGN (Perola et al. 2002) gives evidence of a wide range of values for the cut-off energy, spanning from 30 to 300 keV and further suggests a possible trend of increasing cut-off energy as the power law photon index increases. However, it is not clear if this effect is due to limitations in the spectral analysis or if it is intrinsic to the sampled source population. Direct *INTEGRAL* measurements now offer the opportunity to obtain further observational results on the primary continuum and the high energy cut-off, providing more refined parameters for AGN modelling.

The analysis will mainly focus on the study of the primary continuum cut-off energy.

Reprocessing features will also be investigated, although not in depth, while features occurring at low energy (such as the eventual soft excess or warm absorber present in some sources) will not be studied. The sample used in the following analysis comprises 27 type 1 sources present in the complete AGN sample, with the exclusion of Narrow Line Seyfert 1s (for a detailed analysis of these objects see Malizia et al. 2008) and Broad Line Radio Galaxies, discussed in the previous chapter. Only one source of the complete sample has been excluded from the analysis, that being 4U 0517+17, for which no X-ray measurement could be found in public archives.

7.2 Broad-Band Spectral Analysis

7.2.1 The Broad Band Continuum: First Approximation

Following the approach adopted in the previous chapter, the broad-band analysis of radio quiet AGN is performed over the restricted energy band 1-110 keV, since the study of low energy features is beyond the scope of the present thesis. In the same way as done in the study of radio loud objects, the first step in the analysis consists of a simple fit, i.e. a power law absorbed by Galactic column density. Intrinsic absorption and iron line components are then added to this model, each time performing an F-test to asses the statistical significance of the added component and to provide a basic model describing the overall spectral shape at least to a first approximation.

This baseline model, whose parameters are reported in table 7.2, provides a good representation of the data in a significant number of sources, as can be seen from figures 7.1 to 7.13, where data to model ratios are shown; Galactic column densities are taken from Dickey & Lockman (1990) and are reported in table 7.2. However in the cases of NGC 3783, MCG-06-30-015 and MR 2251-178, although the model-to-data ratios are quite acceptable, the power law slopes found are flatter than those generally reported in the literature (see Vaughan & Fabian 2004 for MCG-06-30-015; De Rosa et al. 2002 for NGC 3783; Orr et al. 2001 for MR 2251-178). Indeed, if the spectra of these objects are fitted only in the 3-5 and 7-10 keV energy range (as suggested for instance by Vaughan & Fabian 2004 for MCG-06-30-015), so as to ignore all those features occurring at low energies (i.e. warm absorber and soft excess) and/or those occurring around 6 keV (such as the presence of a relativistic iron line), the slopes found are in better agreement with the results presented in the literature (i.e. Γ=2.20 for MCG-06-30-015, Γ=1.94 for NGC 3783, Γ=1.78 for MR 2251-178). Therefore, for these three AGN the fit has been repeated in this more restricted energy range and the results reported in table 7.2 and in figures 7.4

and 7.13 right panel and 7.7 left panel. Note also that from now on, all spectral modelling for these Seyferts will be done over the 3-110 keV band. Note also that MCG-06-30-015 is known to have a relativistic iron line that requires complex modelling to take into account the relativistic effects (Guainazzi et al. 1999; Fabian et al. 2002; Vaughan & Fabian 2004); this is clearly evident in the data-to-model ratio of this source (see figure 7.7, left panel). To take this evidence into account, a simple parametrisation of this feature has been adopted in the form of a narrow Gaussian line, with energy and width fixed to 6.4 keV and 10 eV respectively, plus a `laor` model in `XSPEC` to represent the relativistic iron line (see table 7.3 for details). The fit thus obtained yields acceptable values (see table 7.3) similar to those reported in the literature (e.g. Vaughan & Fabian 2004).

It is also evident from table 7.2 and from some of the ratios shown, that the basic model adopted is not sufficient for a good description of the data in few other cases. For example, despite the cut in the data at 1 keV, LEDA 168563 still shows some excess counts in the data to model ratio (see 7.1 right panel); this soft excess emission has been modelled (following Panessa et al. 2008 who analysed a similar data-set although in a slightly different energy range) with two power laws, one hard ($\Gamma\sim1.6$) and one soft ($\Gamma\sim3.8$). By modifying the baseline model in this way, the fit is much more acceptable (see table 7.4), as are the ratios (see figure 7.16 left panel).

Furthermore, 3 objects in the sample, namely Markarian 6, NGC 4151 and 4U 1344-60, exhibit a very flat power law continuum and show significant deviation at low energies from the absorbed power law plus cold iron line model adopted in table 7.2; from the literature, it is known that all 3 sources are characterised by complex absorption, generally modelled by one or more layers of cold absorbing material totally and/or partially covering the central source (Malizia et al. 2003a for Markarian 6; De Rosa et al. 2007 for NGC 4151; Piconcelli et al. 2006 and Panessa et al. 2008 for 4U 1344-60). All 3 AGN require one layer of absorption partially covering the nucleus; in Markarian 6 and 4U 1344-60 a second layer also partially covering the source is requested, while both NGC 4151 and 4U 1344-60 have also an absorber fully covering the emitting region (see table 7.5 for model description in each source case). The addition of these components in Markarian 6 and 4U 1344-60 highly improves the fit, the power law slopes are steeper and the value of the cross-calibration constants indicates a better match between X and gamma-ray data (see table 7.5 and figure 7.14).

In the case of NGC 4151 though, despite having modified the baseline model to take into account the complex absorber, the data still show excess counts above 1 keV extending up to 3 keV. As described by De Rosa et al. (2007), this source displays a very complex spectral shape in the 1-3 keV region of the spectrum; since the treatment of these

Name	Complex Absorber	Soft Excess (PL or BB)	Broad Fe Line
LEDA 168563	-	√	-
Mrk 6	√	-	-
IGR J07597-3842	-	-	√
FRL 1146	-	-	√
NGC 4151	√	-	-
MCG-06-30-015	-	-	√
4U 1344-60	√	-	-
IC 4329A	-	-	√
IGR J16558-5203	√	-	-

Table 7.1: Peculiar sources in the complete sample.

extra features is beyond the scope of this work, all data below 3 keV have been ignored from now on, as done for MCG-06-30-015, NGC 3783 and MR 2251-178; in doing so, the simple power law plus complex absorption model yields perfectly acceptable results also for NGC 4151 (see table 7.5 and figure 7.15 left panel).

Also IGR J16558-5203 is found to require a layer of cold material partially obscuring the central source (as already found by Panessa et al. 2008) and for this reason the baseline model has been modified accordingly (see table 7.5 and figure 7.15 left panel). Finally, it is worth mentioning that GRS 1734-292 also displays what looks like excess counts at low energies (figure 7.9 right panel). However, this feature is not due to the presence of a soft component, but to the fact that, while the *ASCA* data (when fitted alone) have a very flat power slope, the ISGRI data are instead very steep, due to the presence of a high energy cut-off, clearly evident even when the high energy data are fitted with a simple power law. In fact, when employing a model that takes into account this cut-off energy, the excess counts around 1 keV disappear (see next section); for this reason, the main baseline model has been maintained for GRS 1734-292, without the addition of any extra component to model the data in the low energy region of the spectrum. See table 7.1 for a summary of sources requiring extra components with respect to the baseline model.

The results reported in tables 7.2, 7.3, 7.4 and 7.5 allow for some preliminary conclusions on the general shape of the continua of the sources analysed here. 10 out of 27 objects do not require any intrinsic absorption; 13 objects require an intrinsic column density at more than 99% confidence level and, as already mentioned, 4 sources (Markarian 6, 4U 1344-60, NGC 4151 and IGR J16558-5203) require instead a complex absorber. This represents ~15% of the sample of radio quiet AGN; a similar fraction (one over eight) is also found in radio loud objects. The N_H values are $\lesssim 10^{22}$ cm^{-2}, except in the four sources with complex absorption.

The Fe Kα line is detected in all sources at more than 99% confidence level; no Gaussian component was added to the fit in the cases of the six objects observed by the *XRT* telescope, which is not sensitive enough to detect the cold iron line at around 6.4 keV.

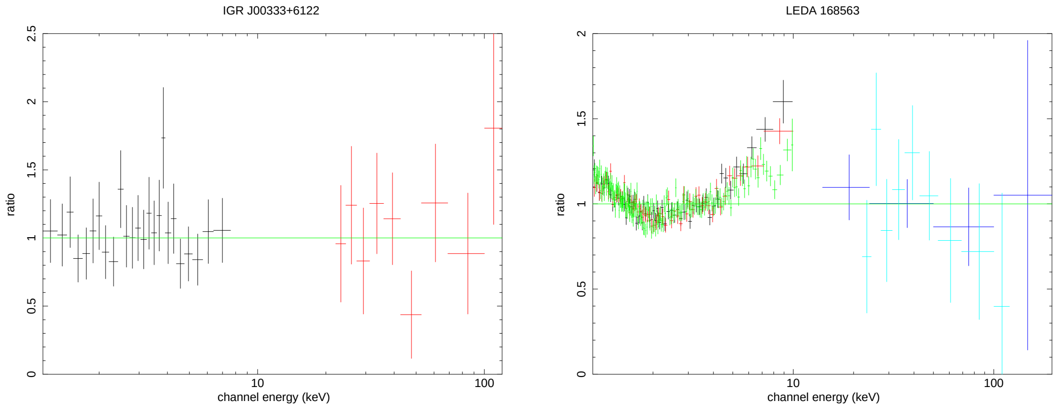

Figure 7.1: Model to data ratios for IGR J00333+6122 and LEDA 168563. The model employed is a simple power law absorbed by Galactic and intrinsic column densities plus a narrow Gaussian component (in the case of LEDA 168563).

Also in the case of GRS 1734-292, observed by *ASCA*, the Fe Kα line is not detected, possibly due to the statistical quality of the available data. The iron line is found always to be narrow (hence its width has been fixed to 10 eV to allow for better constraints on the line parameters), with the exceptions of 3 sources (IGR J07597-3842, FRL 1146 and IC 4329A). In MCG-06-30-015 a narrow plus broad relativistic line is required by the data.

In few cases (like that of IC 4329A) the residuals show some evidence of excess counts around 6.5/7 keV, indicative of the possible presence of a second iron line; however, since these features are not the main objective of the present work, a simple parametrisation of the Fe Kα line has been adopted also in those cases where the presence of a second Gaussian feature around 7 keV is reported in the literature. We have checked that the exclusion of such features does not alter the results of the analysis, by testing their presence in a few sources, but no significant differences were found in the fits with and without these components.

The iron Kα line equivalent widths (EW) are generally found to span a large range of values from a few tens of eV to over 100 eV; note that in some cases the EW is close to the capability limits of moderate resolution CCD instruments like *XMM-Newton*, calling in some caution in these cases.

The photon indices span quite a wide range of values, from 1.56 to 2.30 (in the case of GRS 1734-292), with the mean power law slope being 1.80, with a standard deviation of 0.20.

Finally a comment on the cross calibration constants: figure 7.17 is a plot of C_1 versus C_2 for the simple power law model, which indicates a good match between *BAT* and *INTEGRAL* data. In a number of cases, however, these constants (both or individually) indicate a large mismatch between X-ray and high energy data likely due to variability:

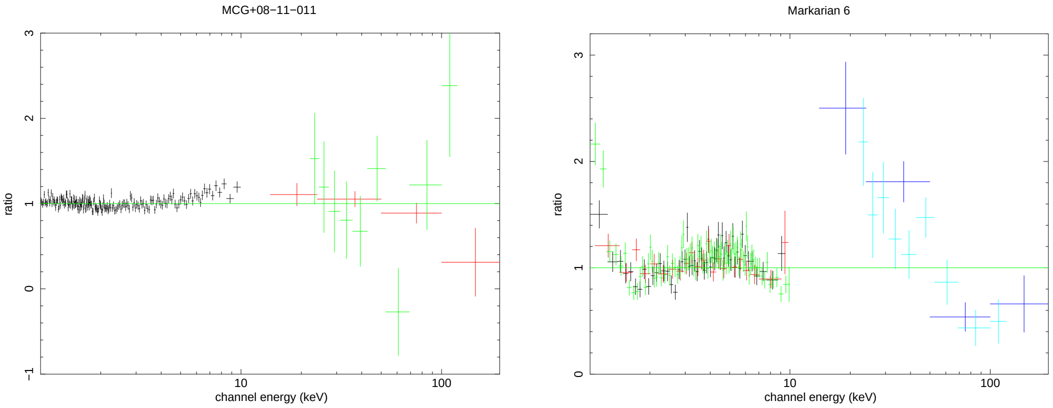

Figure 7.2: Model to data ratios for MCG+08-11-011 and Mrk 6. The model employed is a simple power law absorbed by Galactic and intrinsic column densities plus a Gaussian (narrow or broad) component.

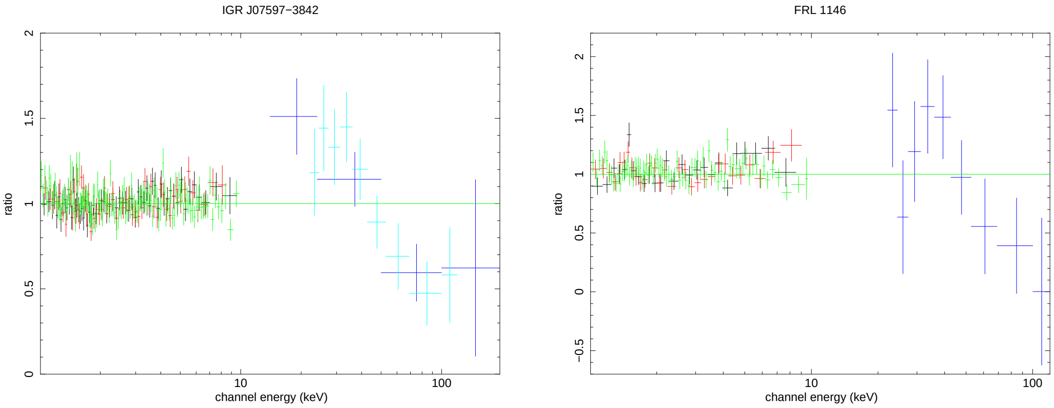

Figure 7.3: Model to data ratios for IGR J07597-3842 and FRL 1146. The model employed is a simple power law absorbed by Galactic and intrinsic column densities plus a broad Gaussian component.

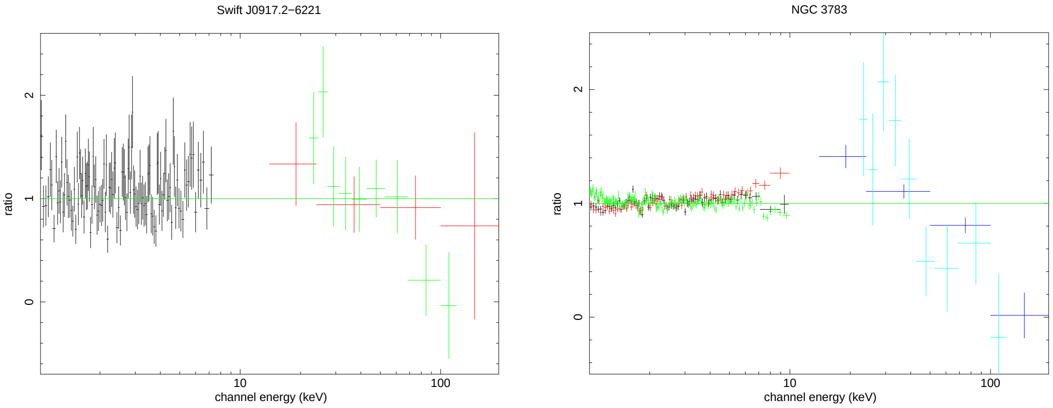

Figure 7.4: Model to data ratios for Swift J0917.2-6221 and NGC 3783. The model employed is a simple power law absorbed by Galactic and intrinsic column densities plus a narrow Gaussian component (in the case of NGC 3783).

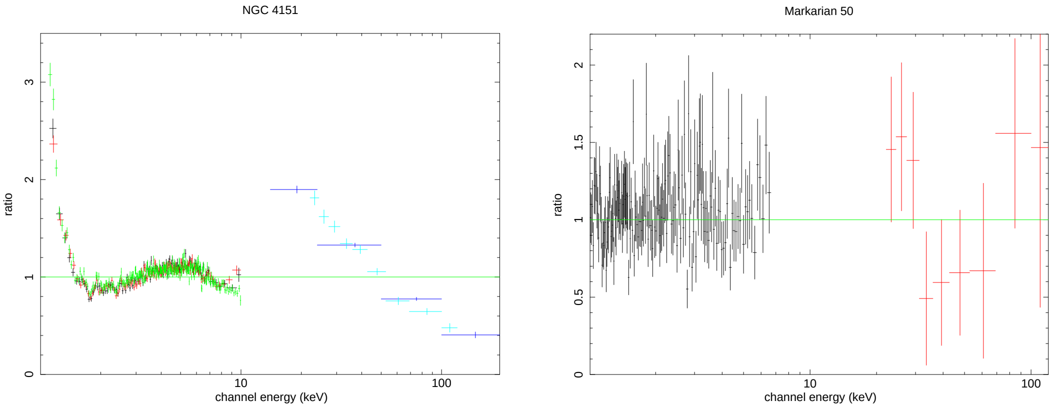

Figure 7.5: Model to data ratios for NGC 4151 and Mrk 50. The model employed is a simple power law absorbed by Galactic and intrinsic column densities plus a narrow Gaussian component (in the case of NGC 4151).

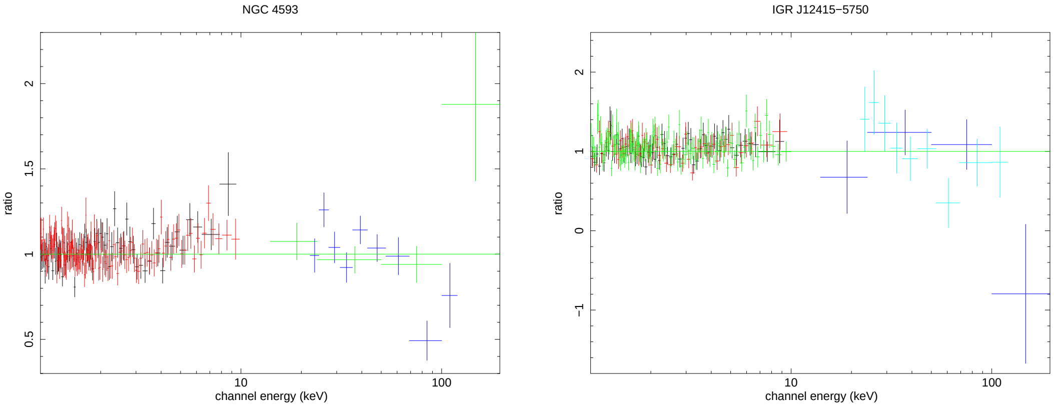

Figure 7.6: Model to data ratios for NGC 4593 and IGR J12415-5750. The model employed is a simple power law absorbed by Galactic and intrinsic column densities plus a narrow Gaussian component.

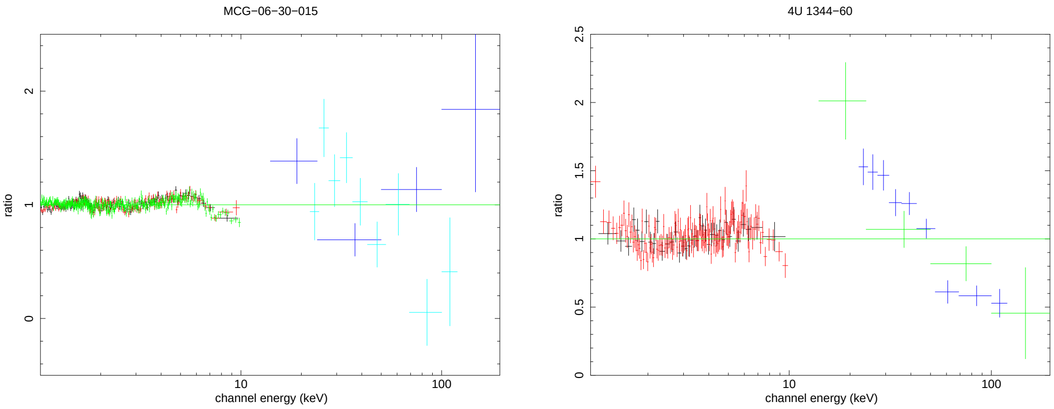

Figure 7.7: Model to data ratios for MCG-06-30-015 and 4U 1344-60. The model employed is a simple power law absorbed by Galactic and intrinsic column densities plus a Gaussian (narrow or broad) component.

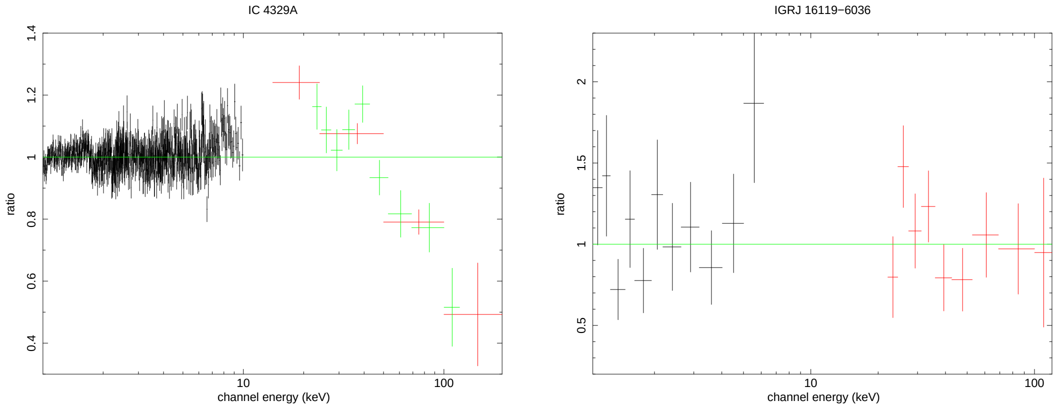

Figure 7.8: Model to data ratios for IC 4329A and IGR J16119-6036. The model employed is a simple power law absorbed by Galactic and intrinsic column densities plus a broad Gaussian component (in the case of IC 4329A).

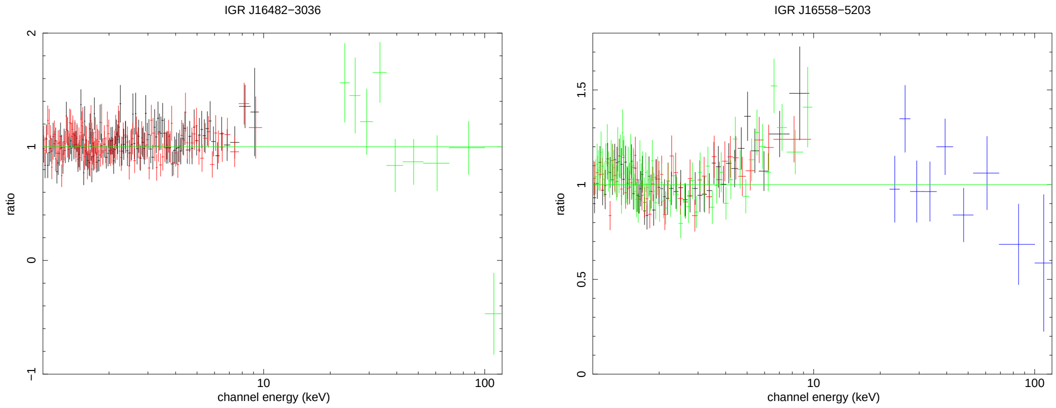

Figure 7.9: Model to data ratios for IGR J16482-3036 and IGR J16558-5203. The model employed is a simple power law absorbed by Galactic and intrinsic column densities plus a narrow Gaussian component.

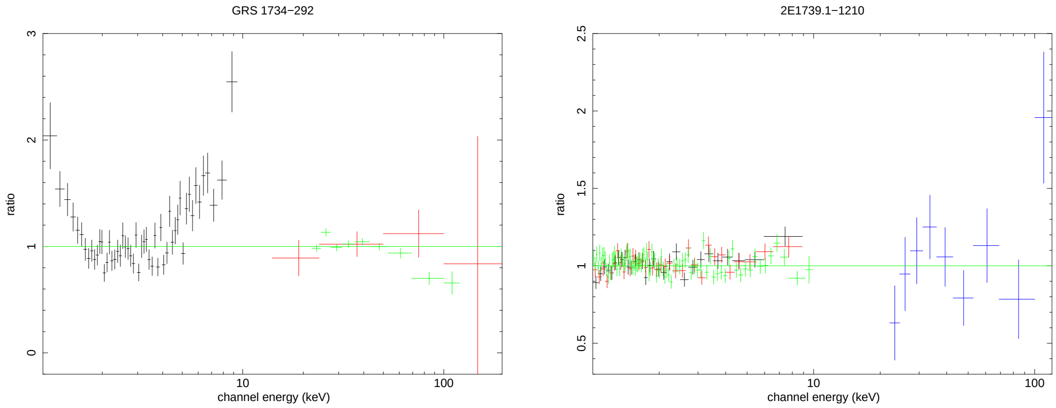

Figure 7.10: Model to data ratios for GRS 1734-292 and 2E 1739.1-1210. The model employed is a simple power law absorbed by Galactic and intrinsic column densities plus a broad Gaussian component (in the case of 2E 1739.1-1210).

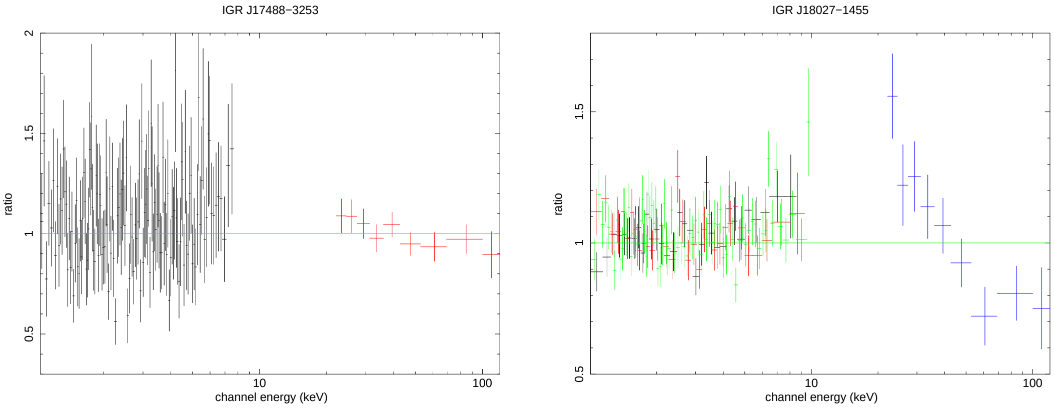

Figure 7.11: Model to data ratios for IGR J17488-3253 and IGR J18027-1455. The model employed is a simple power law absorbed by Galactic and intrinsic column densities plus a narrow Gaussian component (in the case of IGR J18027-1455).

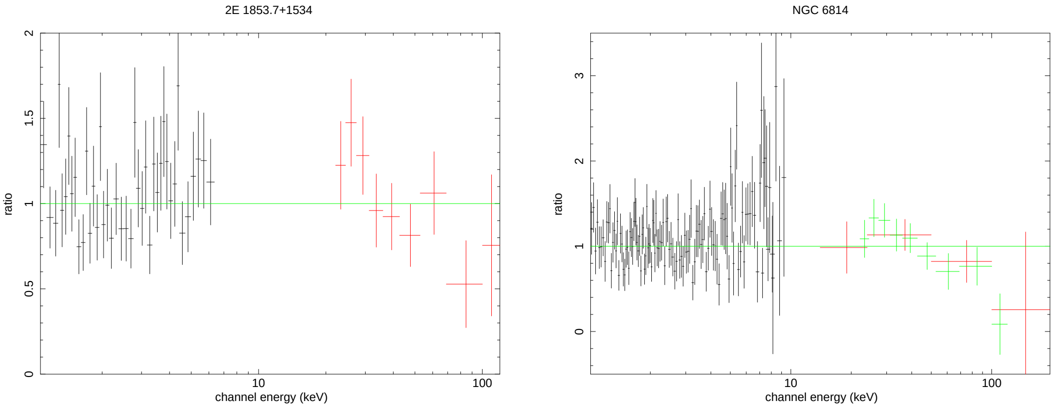

Figure 7.12: Model to data ratios for 2E1853.7+1534 and NGC 6814. The model employed is a simple power law absorbed by Galactic and intrinsic column densities plus a narrow Gaussian component (in the case of NGC 6814).

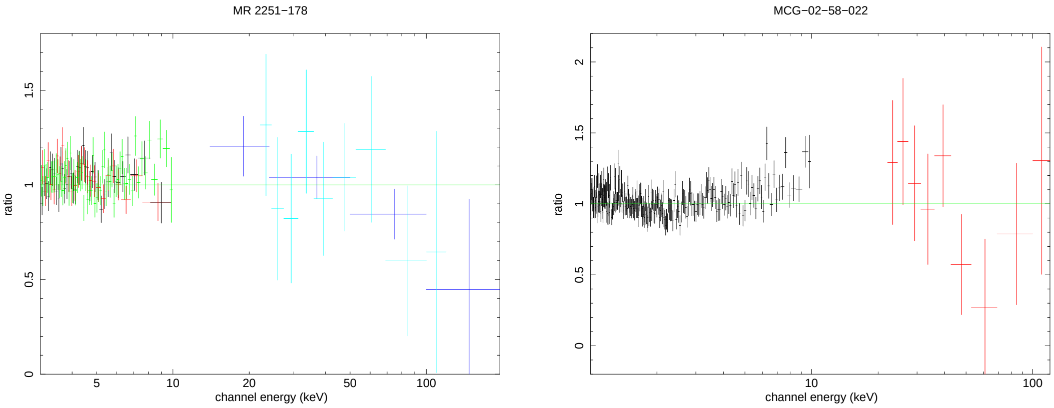

Figure 7.13: Model to data ratio for MR 2251-178 and MCG-02-58-022. The model employed is a simple power law absorbed by Galactic and intrinsic column densities plus a Gaussian (narrow or broad) component.

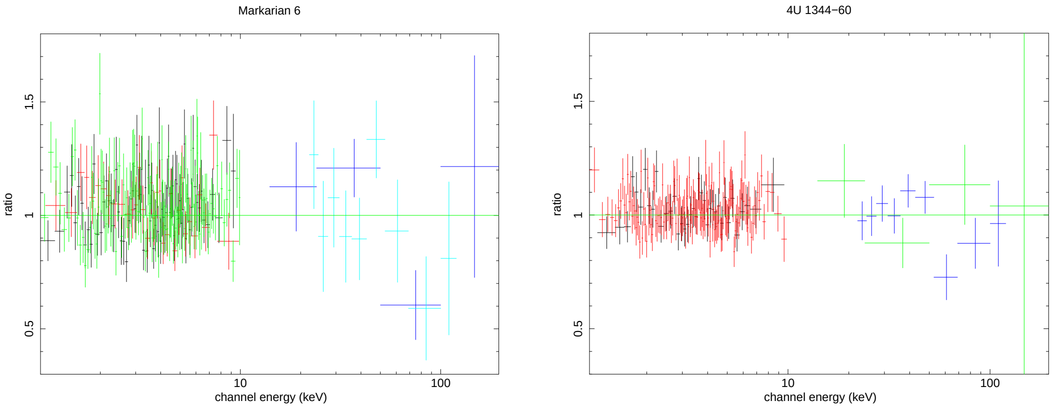

Figure 7.14: Model to data ratio for Mrk 6 and 4U1344-60. The model employed for both sources is a simple power law absorbed by Galactic column density and two layers of material partially covering the central source plus a narrow Gaussian component.

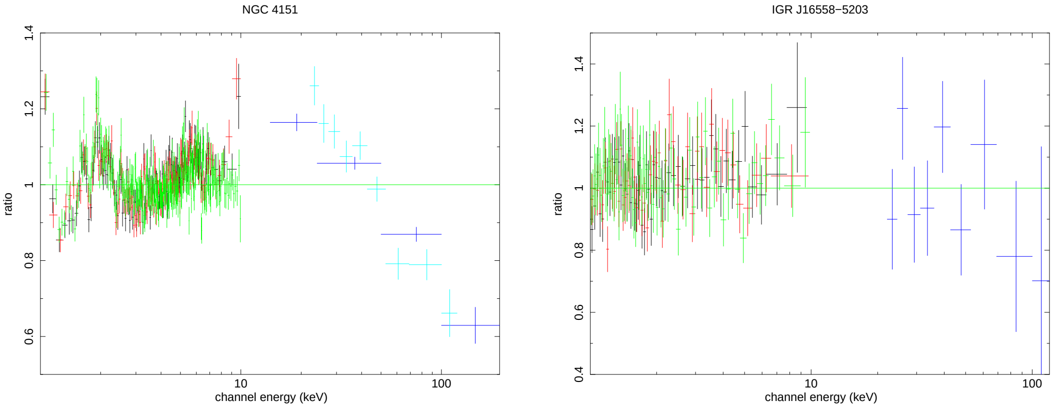

Figure 7.15: Model to data ratio for NGC 4151 (left panel) and IGR J16558-5203 (right panel). The model employed is a simple power law absorbed by Galactic column density and two layers of material totally and partially covering the central source plus a narrow Gaussian component for NGC 4151 and a simple power law absorbed by Galactic column density and a single layer of material partially covering the central source plus a narrow Gaussian line for IGR J16558-5203.

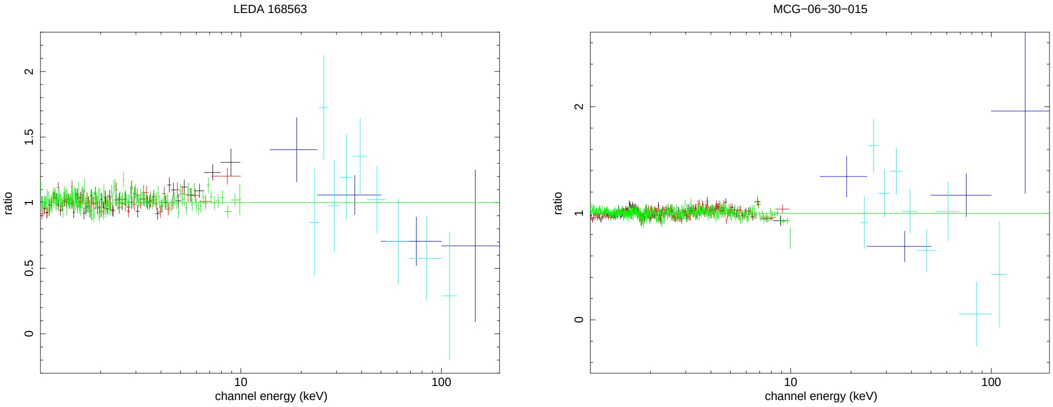

Figure 7.16: Model to data ratio for LEDA 168563 (left panel) and MCG-06-30-015 (right panel). The model employed for LEDA 168563 is a simple power law absorbed by Galactic and intrinsic column density plus a second power law to model the soft excess emission and a narrow gaussian component. The model employed for MCG-06-30-015 is a simple power law absorbed by Galactic and intrinsic column densities plus a narrow Gaussian component fixed at 6.4 keV and a `laor` component to model the relativistic iron line.

for example NGC 6814 has extremely high values of C_1 and C_2, but this is likely due to the long term variability of the source which was already observed in a previous work (Molina et al. 2006), where *ASCA* and *INTEGRAL* data were analysed together, showing a flux change between the X-ray and gamma-ray observation of about a factor of 16. It is clear that in these cases the parameter values might be affected by this large mismatch and have therefore to be treated with some caution. For example, the high value of the iron line EW in NGC 6814 is probably due to this large mismatch between X-ray and gamma-ray data.

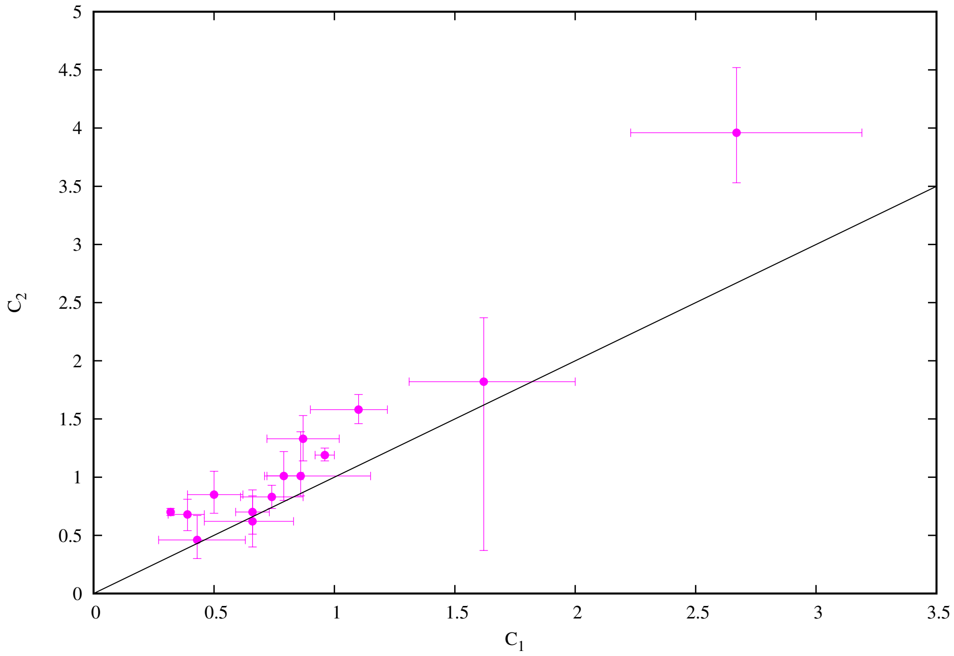

Figure 7.17: Plot of the cross-calibration constants between X- and Gamma-ray data; C_1 is the *XMM/BAT* cross-calibration constant and C_2 is the *XMM/INTEGRAL* one. The 1 to 1 (C_1=C_2) line for the constants is also shown. NGC 6814 has been excluded from the plot (see text for details).

Spectral Fit Results: $\mathtt{wa}_g\mathtt{*wa*(po+zga)}$

Name	$\mathbf{N}_H^G$ **(10^{22} cm^{-2})**	$\mathbf{N}_H$ **(10^{22} cm^{-2})**	Γ	$\mathbf{E}_{line}$ **(keV)**	σ **(eV)**	**EW (eV)**	$\mathbf{C}_1^A$	$\mathbf{C}_2^B$	χ^2 **(dof)**
IGR J00333+6122	0.55	$0.84^{+0.45}_{-0.40}$	$1.76^{+0.30}_{-0.28}$	-	-	-	-	$0.95^{+0.97}_{-0.48}$	18.4 (30)
LEDA 168563	0.54	-	$1.97^{+0.01}_{-0.01}$	$6.41^{+0.05}_{-0.03}$	10f	74^{+16}_{-21}	$0.80^{+0.14}_{-0.13}$	$1.56^{+0.30}_{-0.27}$	2408.0 (1971)
MCG+08-11-011	0.20	-	$1.75^{+0.01}_{-0.01}$	$6.41^{+0.02}_{-0.02}$	10f	125^{+21}_{-22}	$0.66^{+0.07}_{-0.07}$	$0.70^{+0.19}_{-0.19}$	1095.9 (1264)
Mrk 6	0.06	$1.40^{+0.10}_{-0.09}$	$0.92^{+0.05}_{-0.04}$	$6.44^{+0.04}_{-0.04}$	10f	77^{+25}_{-28}	$0.22^{+0.05}_{-0.04}$	$0.24^{+0.05}_{-0.04}$	817.8 (554)
IGR J07597-3842	0.60	-	$1.56^{+0.01}_{-0.01}$	$6.39^{+0.08}_{-0.09}$	192^{+99}_{-79}	112^{+53}_{-30}	$0.74^{+0.13}_{-0.13}$	$0.83^{+0.10}_{-0.10}$	470.8 (459)
FRL 1146	0.40	$0.25^{+0.04}_{-0.04}$	$1.67^{+0.04}_{-0.04}$	$6.33^{+0.06}_{-0.06}$	110^{+109}_{-69}	148^{+62}_{-53}	-	$0.61^{+0.16}_{-0.15}$	509.2 (576)
Swift J0917.2-6221	0.19	$0.43^{+0.12}_{-0.13}$	$1.56^{+0.12}_{-0.13}$	-	-	-	$0.43^{+0.20}_{-0.16}$	$0.46^{+0.21}_{-0.16}$	149.2 (124)
NGC 3783*	0.08	$1.63^{+0.33}_{-0.30}$	$1.73^{+0.04}_{-0.04}$	$6.36^{+0.01}_{-0.01}$	10f	100^{+9}_{-11}	$0.79^{+0.08}_{-0.07}$	$1.01^{+0.21}_{-0.21}$	1650.3 (1769)
NGC 4151*	0.02	$7.07^{+0.17}_{-0.18}$	$1.78^{+0.02}_{-0.02}$	$6.41^{+0.01}_{-0.01}$	10f	65^{+5}_{-6}	$0.31^{+0.01}_{-0.01}$	$0.67^{+0.03}_{-0.03}$	2182.3 (1992)
Mrk 50	0.02	<0.12	$1.94^{+0.12}_{-0.08}$	-	-	-	-	$1.23^{+0.57}_{-0.41}$	159.6 (157)
NGC 4593	0.02	-	$1.86^{+0.02}_{-0.02}$	$6.38^{+0.04}_{-0.04}$	10f	132^{+32}_{-48}	$1.10^{+0.12}_{-0.11}$	$1.58^{+0.13}_{-0.12}$	759.6 (856)
IGR J12415-5750	0.30	-	$1.56^{+0.02}_{-0.02}$	$6.59^{+0.13}_{-0.06}$	10f	102^{+47}_{-50}	$0.66^{+0.21}_{-0.20}$	$0.62^{+0.12}_{-0.12}$	587.5 (682)
MCG-06-30-015*	0.04	$2.34^{+0.23}_{-0.26}$	$2.22^{+0.03}_{-0.04}$	$6.29^{+0.05}_{-0.05}$	354^{+47}_{-43}	170^{+35}_{-19}	$0.98^{+0.17}_{-0.17}$	$1.58^{+0.24}_{-0.24}$	1347.8 (1328)
4U 1344-60	1.07	$1.09^{+0.08}_{-0.06}$	$1.29^{+0.04}_{-0.03}$	$6.41^{+0.03}_{-0.03}$	10f	89^{+20}_{-26}	$0.22^{+0.04}_{-0.03}$	$0.31^{+0.04}_{-0.03}$	898.3 (769)
IC 4329A	0.04	$0.34^{+0.01}_{-0.01}$	$1.79^{+0.01}_{-0.01}$	$6.47^{+0.05}_{-0.05}$	443^{+84}_{-60}	217^{+34}_{-30}	$0.96^{+0.04}_{-0.04}$	$1.19^{+0.06}_{-0.05}$	1786.8 (1617)
IGR J16119-6036	0.23	-	$1.84^{+0.24}_{-0.22}$	-	-	-	-	$5.11^{+5.98}_{-2.60}$	18.8 (17)
IGR J16482-3036	0.18	$0.08^{+0.04}_{-0.04}$	$1.60^{+0.05}_{-0.05}$	$6.45^{+0.08}_{-0.07}$	10f	101^{+49}_{-57}	-	$0.42^{+0.09}_{-0.08}$	456.7 (496)
IGR J16558-5203	0.30	-	$2.00^{+0.02}_{-0.02}$	$6.49^{+0.04}_{-0.04}$	10f	168^{+47}_{-60}	-	$2.72^{+0.35}_{-0.32}$	698.3 (778)
GRS 1734-292	0.77	$1.59^{+0.15}_{-0.14}$	$2.30^{+0.06}_{-0.05}$	-	-	-	$2.67^{+0.52}_{-0.44}$	$3.96^{+0.56}_{-0.43}$	345.8 (113)
2E 1739.1-1210	0.21	$0.09^{+0.02}_{-0.02}$	$1.91^{+0.02}_{-0.02}$	$6.27^{+0.05}_{-0.05}$	10f	47^{+23}_{-23}	-	$1.81^{+0.26}_{-0.24}$	829.3 (871)
IGR J17488-3253	0.53	$0.34^{+0.10}_{-0.10}$	$1.75^{+0.08}_{-0.07}$	-	-	-	-	$1.96^{+0.45}_{-0.35}$	142.2 (137)
IGR J18027-1455	0.50	$0.29^{+0.05}_{-0.04}$	$1.51^{+0.04}_{-0.04}$	$6.41^{+0.02}_{-0.03}$	10f	136^{+36}_{-33}	-	$2.16^{+0.30}_{-0.25}$	824.5 (899)
2E 1853.7+1534	0.39	$0.37^{+0.24}_{-0.21}$	$1.84^{+0.21}_{-0.20}$	-	-	-	-	$1.45^{+1.11}_{-0.60}$	49.6 (47)
NGC 6814	0.13	-	$1.81^{+0.09}_{-0.08}$	$6.38^{+0.16}_{-0.15}$	10f	508^{+252}_{-255}	$13.95^{+4.78}_{-3.88}$	$22.46^{+6.01}_{-5.18}$	220.6 (237)
MR 2251-178*	0.03	$2.55^{+0.77}_{-0.75}$	$1.78^{+0.10}_{-0.10}$	$6.40^{+0.04}_{-0.04}$	10f	46^{+18}_{-20}	$1.62^{+0.38}_{-0.31}$	$1.82^{+0.55}_{-0.45}$	746.8 (863)
MCG-02-58-022	0.04	-	$1.78^{+0.01}_{-0.01}$	$6.33^{+0.04}_{-0.05}$	10f	72^{+19}_{-31}	-	$0.87^{+0.21}_{-0.21}$	898.7 (976)

*: analysed in the 3-110 keV energy range.

A: cross-calibration constant between *XRT/ASCA/XMM* and *BAT*.

B: cross-calibration constant between *XRT/ASCA/XMM* and *INTEGRAL*.

Table 7.2: Simple power law spectral fits.

MCG-06-30-015* **Spectral Fit Results:** `wa`$_g$`*wa*(po+zga+laor`†`)`

$\mathbf{N}_H$ ($\mathbf{10^{22}}$ $\mathbf{cm^{-2}}$)	Γ	$\mathbf{E}_{line}$ **(keV)**	σ **(eV)**	**EW (eV)**	$\mathbf{E}_{line}$ **(keV)**	**EW (eV)**	$\mathbf{C}_1^A$	$\mathbf{C}_2^B$	χ^2 **(dof)**
$1.32^{+0.29}_{-0.28}$	$2.10^{+0.03}_{-0.04}$	6.4f	10f	20^{+6}_{-7}	$6.38^{+0.04}_{-0.04}$	391^{+34}_{-36}	$0.87^{+0.15}_{-0.15}$	$1.33^{+0.20}_{-0.19}$	1304.9 (1328)

*: analysed in the 3-110 keV energy range.

†: the other parameters in the `LAOR` model have been frozen to R_{IN}=1.23r_g, R_{OUT}=400r_g, i=30°, β=-3.

A: cross-calibration constant between *XRT/ASCA/XMM* and *BAT*.

B: cross-calibration constant between *XRT/ASCA/XMM* and *INTEGRAL*.

Table 7.3: Simple power law fit for MCG-06-30-015.

LEDA 168563 Spectral Fit Results: `wa`$_g$`*wa*(po+po+zga)`

$\mathbf{N}_H$ ($\mathbf{10^{22}}$ $\mathbf{cm^{-2}}$)	Γ_1	Γ_2	$\mathbf{E}_{line}$ **(keV)**	σ **(eV)**	**EW (eV)**	$\mathbf{C}_1^A$	$\mathbf{C}_2^B$	χ^2 **(dof)**
-	$3.74^{+0.25}_{-0.31}$	$1.61^{+0.04}_{-0.07}$	$6.42^{+0.06}_{-0.06}$	10f	29^{+15}_{-16}	$0.39^{+0.07}_{-0.08}$	$0.68^{+0.13}_{-0.14}$	1669.8 (1969)

A: cross-calibration constant between *XRT/ASCA/XMM* and *BAT*.

B: cross-calibration constant between *XRT/ASCA/XMM* and *INTEGRAL*.

Table 7.4: Simple power law spectral fit for LEDA 168563.

Spectral Fit Results: `wa`$_g$`*wa*pcfabs*pcfabs*(po+zga)`

Name	$\mathbf{N}_H^{TOT}$ ($\mathbf{10^{22}}$ $\mathbf{cm^{-2}}$)	$\mathbf{N}_H^1$ ($\mathbf{10^{22}}$ $\mathbf{cm^{-2}}$)	$\mathbf{cf}_1$	$\mathbf{N}_H^2$ ($\mathbf{10^{22}}$ $\mathbf{cm^{-2}}$)	$\mathbf{cf}_2$	Γ	$\mathbf{E}_{line}^{\ddagger}$ **(keV)**	**EW (eV)**	$\mathbf{C}_1^A$	$\mathbf{C}_2^B$	χ^2 **(dof)**
Mrk 6	-	$10.15^{+4.20}_{-2.34}$	$0.54^{+0.08}_{-0.07}$	$2.26^{+0.41}_{-0.35}$	$0.93^{+0.01}_{-0.01}$	$1.63^{+0.17}_{-0.09}$	$6.45^{+0.04}_{-0.04}$	65^{+25}_{-27}	$0.86^{+0.29}_{-0.15}$	$1.01^{+0.38}_{-0.17}$	565.1 (551)
4U 1344-60	$1.10^{+0.17}_{-0.17}$	$45.40^{+26.04}_{-13.52}$	$0.47^{+0.09}_{-0.07}$	$5.30^{+2.12}_{-1.58}$	$0.56^{+0.07}_{-0.05}$	$2.01^{+0.13}_{-0.08}$	$6.41^{+0.04}_{-0.04}$	54^{+24}_{-21}	$0.50^{+0.12}_{-0.11}$	$0.85^{+0.20}_{-0.16}$	695.2 (765)
NGC 4151*	$5.88^{+0.49}_{-0.77}$	$31.05^{+10.37}_{-8.85}$	$0.28^{+0.02}_{-0.02}$	-	-	$1.88^{+0.02}_{-0.02}$	$6.41^{+0.01}_{-0.01}$	55^{+4}_{-8}	$0.32^{+0.01}_{-0.01}$	$0.70^{+0.03}_{-0.03}$	2056.2 (1990)
IGR J16558-5203	-	$21.94^{+8.40}_{-5.76}$	$0.47^{+0.05}_{-0.06}$	-	-	$2.18^{+0.05}_{-0.05}$	$6.49^{+0.06}_{-0.05}$	78^{+45}_{-44}	-	$2.59^{+0.50}_{-0.43}$	610.6 (776)

*: analysed in the 3-110 keV energy range.

‡: line width fixed to 10 eV.

A: cross-calibration constant between *XRT/ASCA/XMM* and *BAT*.

B: cross-calibration constant between *XRT/ASCA/XMM* and *INTEGRAL*.

Table 7.5: Partial covering plus power law spectral fits.

7.2.2 The High Energy Cut-Off

Next, a high energy cut-off in the power law has been introduced (`wa`$_g$`*wa*(cutoffpl+zga)`, tables 7.6, 7.7, 7.8 and 7.9). In 15 out of 27 sources a high energy cut-off component is strongly required by the data (at least at 99% confidence level); IGR J18027-1455 and 4U 1344-60 require this component at 96% confidence level, but only in the case of IGR J18027-1455 the high energy cut-off is well constrained (see table 7.2 and 7.5). IGR J12415-5750 requires the component at 89% confidence level and a lower limit on E_c is found. In the remaining objects, the addition of a cut-off energy does not yield any improvement in the fit or the improvement is very marginal. Nonetheless, in five cases (MCG+08-11-011, Mrk 50, IGR J16119-6036, IGR J16558-5203 and MCG-06-30-015) lower limits on E_c could be calculated. The average cut-off energy is around ~100 keV with a standard deviation of ~64 keV. It is also interesting to note that, at least in some cases, the values of C_1 and C_2 tend to be slightly higher when a cut-off energy component is added to the simple power law.

Spectral Fit Results: $\texttt{wa}_g\texttt{*wa*(cutoffpl+zga)}$

Name	**N$_H$** **(10^{22} cm^{-2})**	Γ	**E$_{cut}$** **(keV)**	**E$_{line}$** **(keV)**	σ **(eV)**	**EW** **(eV)**	**C$_1^A$**	**C$_2^B$**	χ^2 **(dof)**	**Prob**♣
IGR J00333+6122	$0.85^{+0.45}_{-0.40}$	$1.76^{+0.30}_{-0.28}$	NC	-	-	-	-	$0.95^{+0.97}_{-0.48}$	18.4 (29)	-
MCG+08-11-011	-	$1.75^{+0.01}_{-0.01}$	>451	$6.41^{+0.02}_{-0.02}$	10f	127^{+19}_{-24}	$0.66^{+0.07}_{-0.07}$	$0.70^{+0.19}_{-0.19}$	1095.8 (1263)	27%
IGR J07597-3842	-	$1.51^{+0.02}_{-0.02}$	71^{+42}_{-20}	$6.39^{+0.08}_{-0.08}$	204^{+113}_{-76}	133^{+48}_{-43}	$1.13^{+0.23}_{-0.22}$	$1.42^{+0.30}_{-0.27}$	445.9 (458)	>99.9%
FRL 1146	$0.22^{+0.05}_{-0.05}$	$1.58^{+0.07}_{-0.09}$	47^{+73}_{-22}	$6.33^{+0.06}_{-0.06}$	110^{+100}_{-69}	147^{+61}_{-53}	-	$1.18^{+0.65}_{-0.41}$	500.8 (575)	99.8%
Swift J0917.2-6221	$0.31^{+0.14}_{-0.13}$	$1.37^{+0.15}_{-0.15}$	46^{+50}_{-19}	-	-	-	$0.56^{+0.28}_{-0.20}$	$0.77^{+0.42}_{-0.28}$	136.2 (123)	99.9%
NGC 3783*	$1.08^{+0.36}_{-0.40}$	$1.58^{+0.06}_{-0.07}$	69^{+36}_{-21}	$6.36^{+0.01}_{-0.01}$	10f	101^{+7}_{-13}	$0.95^{+0.10}_{-0.09}$	$1.40^{+0.34}_{-0.29}$	1620.1(1768)	>99.9%
Mrk 50	<0.12	$1.94^{+0.12}_{-0.11}$	>25	-	-	-	-	$1.23^{+2.05}_{-0.41}$	159.6 (156)	-
NGC 4593	-	$1.84^{+0.02}_{-0.02}$	210^{+308}_{-78}	$6.38^{+0.04}_{-0.04}$	10f	130^{+33}_{-47}	$1.22^{+0.15}_{-0.13}$	$1.81^{+0.22}_{-0.19}$	751.3 (855)	99.8%
IGR J12415-5750	-	$1.54^{+0.03}_{-0.04}$	>68	$6.60^{+0.13}_{-0.07}$	10f	107^{+43}_{-54}	$0.81^{+0.32}_{-0.28}$	$0.80^{+0.30}_{-0.23}$	585.3 (681)	89%
IC 4329A	$0.32^{+0.01}_{-0.01}$	$1.75^{+0.01}_{-0.01}$	122^{+32}_{-21}	$6.48^{+0.05}_{-0.05}$	432^{+78}_{-59}	215^{+32}_{-30}	$1.16^{+0.06}_{-0.06}$	$1.50^{+0.10}_{-0.09}$	1712.4 (1616)	>99.9%
IGR J16119-6036	-	$1.68^{+0.33}_{-0.32}$	>54	-	-	-	-	$4.30^{+5.11}_{-2.21}$	17.4 (16)	73%
IGR J16482-3036	<0.10	$1.51^{+0.06}_{-0.07}$	60^{+57}_{-23}	$6.45^{+0.08}_{-0.08}$	10f	98^{+51}_{-56}	-	$0.73^{+0.27}_{-0.20}$	442.7 (495)	>99.9%
GRS 1734-292	$0.35^{+0.15}_{-0.19}$	$1.38^{+0.10}_{-0.13}$	40^{+5}_{-5}	-	-	-	$0.95^{+0.18}_{-0.18}$	$1.33^{+0.19}_{-0.23}$	166.2 (112)	>99.9%
2E 1739.1-1210	$0.09^{+0.02}_{-0.01}$	$1.90^{+0.03}_{-0.02}$	NC	$6.28^{+0.05}_{-0.05}$	10f	48^{+22}_{-24}	-	$1.79^{+0.27}_{-0.24}$	829.3 (870)	-
IGR J17488-3253	$0.19^{+0.13}_{-0.13}$	$1.58^{+0.13}_{-0.13}$	191^{+282}_{-73}	-	-	-	-	$1.61^{+0.41}_{-0.32}$	134.8 (136)	99.3%
IGR J18027-1455	$0.25^{+0.05}_{-0.05}$	$1.43^{+0.05}_{-0.05}$	99^{+50}_{-29}	$6.41^{+0.02}_{-0.03}$	10f	129^{+37}_{-31}	-	$2.92^{+0.50}_{-0.43}$	820.4 (898)	96%
2E 1853.7+1534	<0.34	$1.47^{+0.28}_{-0.19}$	53^{+69}_{-22}	-	-	-	-	$1.33^{+0.90}_{-0.50}$	39.6 (46)	99.9%
NGC 6814	-	$1.69^{+0.09}_{-0.05}$	70^{+60}_{-25}	$6.38^{+0.20}_{-0.15}$	10f	429^{+235}_{-241}	$16.30^{+5.11}_{-4.53}$	$29.31^{+8.17}_{-8.03}$	206.7 (236)	>99.9%
MR 2251-178*	$1.85^{+0.84}_{-0.88}$	$1.63^{+0.14}_{-0.15}$	90^{+171}_{-41}	$6.39^{+0.04}_{-0.04}$	10f	44^{+20}_{-18}	$1.82^{+0.41}_{-0.36}$	$2.11^{+0.66}_{-0.53}$	740.2 (862)	99.4%
MCG-02-58-022	-	$1.78^{+0.01}_{-0.01}$	NC	$6.33^{+0.05}_{-0.05}$	10f	70^{+21}_{-18}	-	$0.86^{+0.21}_{-0.10}$	898.5 (975)	36%

*: analysed in the 3-110 keV energy range.
A: cross-calibration constant between *XRT/ASCA/XMM* and *BAT*.
B: cross-calibration constant between *XRT/ASCA/XMM* and *INTEGRAL*.
♣: fit improvement with respect to table 7.2

Table 7.6: Cut-off power law spectral fits.

MCG-06-30-015* Spectral Fit Results: `wa`$_g$`*wa*(cutoffpl+zga+laor`†`)`

N_H (10^{22} cm^{-2})	**Γ**	**E_{cut} (keV)**	**E_{line} (keV)**	**σ (eV)**	**EW (eV)**	**E_{line} (keV)**	**EW (eV**	**C_1^A**	**C_2^B**	**χ^2 (dof)**	**Prob$^\clubsuit$**
$1.18^{+0.33}_{-0.32}$	$2.04^{+0.07}_{-0.08}$	>53	6.4f	10f	19^{+7}_{-6}	$6.38^{+0.04}_{-0.04}$	393^{+33}_{-37}	$0.95^{+0.19}_{-0.18}$	$1.60^{+0.42}_{-0.34}$	1302.5 (1327)	88%

*: analysed in the 3-110 keV energy range.

†: the other parameters in the `LAOR` model have been frozen to R_{IN}=1.23r_g, R_{OUT}=400r_g, i=30°, β=-3.

A: cross-calibration constant between *XRT/ASCA/XMM* and *BAT*.

B: cross-calibration constant between *XRT/ASCA/XMM* and *INTEGRAL*.

$^\clubsuit$: fit improvement with respect to table 7.3

Table 7.7: Cut-off power law spectral fit for MCG-06-30-015.

LEDA 168563 Spectral Fit Results: `wa`$_g$`*wa*(cutoffpl+po+zga)`

N_H (10^{22} cm^{-2})	**Γ_1**	**Γ_2**	**E_{cut} (keV)**	**$E^\ddagger_{line}$ (keV)**	**EW (eV)**	**C_1^A**	**C_2^B**	**χ^2 (dof)**	**Prob$^\clubsuit$**
-	$3.40^{+0.29}_{-0.26}$	$1.45^{+0.10}_{-0.13}$	55^{+55}_{-22}	$6.42^{+0.06}_{-0.07}$	27^{+16}_{-15}	$0.53^{+0.13}_{-0.11}$	$1.06^{+0.35}_{-0.26}$	1656.4 (1968)	>99.9%

‡: line width fixed to 10 eV.

A: cross-calibration constant between *XRT/ASCA/XMM* and *BAT*.

B: cross-calibration constant between *XRT/ASCA/XMM* and *INTEGRAL*.

$^\clubsuit$ fit improvement with respect to table 7.4

Table 7.8: Cut-off power law spectral fit for LEDA 168563.

Spectral Fit Results: `wa`$_g$`*wa*pcfabs*pcfabs*(cutoffpl+zga)`

Name	**N_H^{TOT} (10^{22} cm^{-2})**	**N_H^1 (10^{22} cm^{-2})**	**cf$_1$**	**N_H^2 (10^{22} cm^{-2})**	**cf$_2$**	**Γ**	**E_{cut} (keV)**	**$E^\ddagger_{line}$ (keV)**	**EW (eV)**	**C_1^A**	**C_2^B**	**χ^2 (dof)**	**Prob$^\clubsuit$**
Mrk 6	-	$8.89^{+3.62}_{-3.62}$	$0.50^{+0.09}_{-0.11}$	$2.12^{+0.37}_{-0.60}$	$0.92^{+0.01}_{-0.03}$	$1.47^{+0.16}_{-0.20}$	92^{+64}_{-42}	$6.45^{+0.04}_{-0.04}$	64^{+27}_{-25}	$0.97^{+0.21}_{-0.20}$	$1.17^{+0.28}_{-0.25}$	557.4 (550)	>99.9%
4U 1344-60	$1.02^{+0.16}_{-0.25}$	$47.08^{+31.98}_{-21.07}$	$0.40^{+0.12}_{-0.13}$	$5.19^{+2.24}_{-2.38}$	$0.50^{+0.09}_{-0.10}$	$1.80^{+0.23}_{-0.10}$	>86	$6.41^{+0.04}_{-0.03}$	57^{+23}_{-21}	$0.46^{+0.11}_{-0.10}$	$0.78^{+0.18}_{-0.16}$	691.2 (764)	96%
NGC 4151*	$5.13^{+0.85}_{-1.26}$	$21.70^{+14.82}_{-10.43}$	$0.27^{+0.24}_{-0.08}$	-	-	$1.76^{+0.02}_{-0.06}$	276^{+156}_{-78}	$6.41^{+0.01}_{-0.01}$	58^{+4}_{-8}	$0.31^{+0.01}_{-0.01}$	$0.68^{+0.03}_{-0.03}$	2037.6 (1989)	>99.9%
IGR J16558-5203	-	$22.42^{+8.81}_{-5.92}$	$0.47^{+0.05}_{-0.06}$	-	-	$2.17^{+0.05}_{-0.05}$	>112	$6.49^{+0.06}_{-0.05}$	77^{+45}_{-43}	-	$2.77^{+0.73}_{-0.57}$	610.0 (775)	62%

*: analysed in the 3-110 keV energy range.

‡: line width fixed to 10 eV.

A: cross-calibration constant between *XRT/ASCA/XMM* and *BAT*.

B: cross-calibration constant between *XRT/ASCA/XMM* and *INTEGRAL*.

$^\clubsuit$ fit improvement with respect to table 7.5

Table 7.9: Partial covering plus cut-off power law spectral fits.

7.2.3 The Reflection Fraction

Finally, a reflection component has been added to the baseline model, in order to verify its incidence on the overall spectral shape (tables 7.10, 7.11, 7.12 and 7.13). The power law has thus been substituted by the `pexrav` model in `XSPEC`, fixing the inclination angle at 30° (i.e. a nearly face on geometry as expected for type 1 sources) and the cut-off energy at 10 000 keV; the reflection fraction is parametrised as R=$\Omega/2\pi$. The reflection component was allowed to vary between 0 and 2, since the iron line equivalent widths are found to be, for the majority of sources, around 100 eV and consequently the reflection parameter cannot have very high values; indeed for an EW of ~140 one would expect R to be ~1 (George & Fabian 1991; Perola et al. 2002).

14 out of 27 sources require the reflection component at more than 99% confidence level; however, R is well constrained only in 2 objects, possibly due to the choice of boundaries for the parameter. In 4 sources the component is required at more than 95% confidence level, but among these it is constrained only in NGC 4151. The remaining sources do not require this component or they require it at a low confidence level; in these cases only upper/lower limits could be found. In order to place some more stringent constraints on the reflection fraction, especially for those sources which require the component at more than 99% confidence level, the parameter R was left free to vary outside the set boundaries. The fits return acceptable results and the reflection fraction is better constrained for most sources (see last column of table 7.10), except for the objects observed by the *XRT* telescope, for which the poor data quality could play an important role in not allowing a good constraint on R.

Also in the case of GRS 1734-292, if left free to vary outside the set boundaries, R returns very high values, despite the fact the there is no evidence for the presence of an iron line in the data, but again this could be due to the fact that the source strongly requires a low energy cut-off. When considering NGC 6814, if the reflection fraction is left free to vary above 2, its value is very high, likely due to the fact that the source is highly variable and that the cross-calibration constants and the reflection parameter might be linked in the fitting procedure.

The measured values of R span a wide range within the allowed boundaries, with a mean value of 1.44 and a standard deviation of 0.91, a little higher than the value expected considering the measured equivalent widths, found to be all around or slightly above 100 eV. It is worth noting that, while the cross-calibration constants are compatible with 1 (within errors) for most sources when employing a simple power law model or a cut-off power law model, C_1 and C_2 become smaller when the model employed is the `pexrav`.

Spectral Fit Results: `wa`$_g$`*wa*(pexrav+zga)`, $0\leq$R≤2, E$_c$=10 000 keV

Name	**N$_H$** (**10^{22} cm^{-2}**)	**Γ**	**R**	**E$_{line}$** (**keV**)	**σ** (**eV**)	**EW** (**eV**)	**C$_1^A$**	**C$_2^B$**	**χ^2 (dof)**	**Prob$^{♣}$**	**R‡**
IGR J00333+6122	$0.85^{+0.37}_{-0.36}$	$1.76^{+0.30}_{-0.22}$	NC	-	-	-	-	$0.95^{+0.97}_{-0.59}$	18.4 (29)	-	-
MCG+08-11-011	-	$1.85^{+0.01}_{-0.01}$	>1.78	$6.41^{+0.02}_{-0.02}$	10f	95^{+18}_{-22}	$0.32^{+0.04}_{-0.03}$	$0.31^{+0.09}_{-0.09}$	1016.2 (1263)	>99.9%	$2.47^{+0.51}_{-0.51}$
IGR J07597-3842	-	$1.60^{+0.03}_{-0.03}$	$0.81^{+0.59}_{-0.54}$	$6.39^{+0.08}_{-0.09}$	150^{+96}_{-85}	82^{+47}_{-33}	$0.47^{+0.17}_{-0.11}$	$0.52^{+0.17}_{-0.10}$	463.8 (458)	99%	-
FRL 1146	$0.32^{+0.05}_{-0.07}$	$1.83^{+0.05}_{-0.12}$	>0.51	$6.32^{+0.06}_{-0.06}$	<162	107^{+55}_{-45}	-	$0.35^{+0.14}_{-0.08}$	503.3 (575)	99%	$1.90^{+1.93}_{-1.38}$
Swift J0917.2-6221	$0.49^{+0.12}_{-0.13}$	$1.72^{+0.12}_{-0.14}$	>0.95	-	-	-	$0.23^{+0.11}_{-0.09}$	$0.25^{+0.11}_{-0.09}$	142.1 (123)	98%	$7.71^{+9.44}_{-4.81}$
NGC 3783*	$1.55^{+0.34}_{-0.34}$	$1.92^{+0.05}_{-0.08}$	>1.20	$6.36^{+0.01}_{-0.01}$	10f	88^{+8}_{-12}	$0.50^{+0.07}_{-0.03}$	$0.65^{+0.16}_{-0.14}$	1622.9 (1768)	>99.9%	$1.72^{+0.80}_{-0.52}$
Mrk 50	<0.17	$1.94^{+0.25}_{-0.08}$	NC	-	-	-	-	$1.23^{+0.57}_{-0.69}$	159.6 (156)	-	-
NGC 4593	-	$1.94^{+0.02}_{-0.03}$	>1.21	$6.38^{+0.05}_{-0.04}$	10f	89^{+36}_{-37}	$0.53^{+0.12}_{-0.06}$	$0.72^{+0.16}_{-0.06}$	735.1 (855)	>99.9%	$2.94^{+1.66}_{-1.34}$
IGR J12415-5750	-	$1.63^{+0.03}_{-0.05}$	>0.64	$6.60^{+0.14}_{-0.08}$	10f	71^{+46}_{-48}	$0.34^{+0.16}_{-0.11}$	$0.30^{+0.13}_{-0.07}$	578.8 (681)	99.8%	$1.57^{+1.13}_{-0.94}$
IC 4329A	$0.39^{+0.01}_{-0.01}$	$1.92^{+0.01}_{-0.02}$	>1.65	$6.38^{+0.02}_{-0.02}$	81^{+39}_{-33}	55^{+13}_{-10}	$0.51^{+0.03}_{-0.02}$	$0.61^{+0.04}_{-0.03}$	1711.5 (1616)	>99.9%	$1.98^{+0.35}_{-0.33}$
IGR J16119-6036	-	$1.84^{+0.24}_{-0.22}$	NC	-	-	-	-	$1.79^{+6.86}_{-0.95}$	17.7 (16)	67%	-
IGR J16482-3036	$0.14^{+0.04}_{-0.05}$	$1.75^{+0.04}_{-0.09}$	>0.94	$6.45^{+0.09}_{-0.09}$	10f	72^{+48}_{-51}	-	$0.22^{+0.06}_{-0.04}$	446.8 (495)	99.9%	$2.27^{+2.57}_{-1.28}$
GRS 1734-292	$1.35^{+0.13}_{-0.13}$	$2.24^{+0.05}_{-0.05}$	>1.90	-	-	-	$1.05^{+0.21}_{-0.18}$	$1.42^{+0.21}_{-0.16}$	250.6 (112)	>99.9%	$12.49^{+3.07}_{-2.60}$
2E 1739.1-1210	$0.15^{+0.02}_{-0.03}$	$2.05^{+0.03}_{-0.07}$	>0.92	$6.27^{+0.06}_{-0.08}$	10f	28^{+26}_{-20}	-	$1.01^{+0.24}_{-0.14}$	815.6 (870)	>99.9%	$1.94^{+0.99}_{-0.91}$
IGR J17488-3253	$0.29^{+0.11}_{-0.10}$	$1.75^{+0.08}_{-0.08}$	>0.17	-	-	-	-	$0.88^{+0.82}_{-0.27}$	137.7 (136)	96%	-
IGR J18027-1455	$0.36^{+0.04}_{-0.05}$	$1.67^{+0.04}_{-0.07}$	>1.24	$6.41^{+0.02}_{-0.03}$	10f	109^{+36}_{-29}	-	$1.15^{+0.09}_{-0.15}$	823.8 (898)	62%	-
2E 1853.7+1534	$0.38^{+0.21}_{-0.23}$	$1.94^{+0.10}_{-0.22}$	>0.64	-	-	-	-	$0.70^{+0.48}_{-0.33}$	44.1 (46)	98%	-
NGC 6814	-	$1.89^{+0.08}_{-0.08}$	>1.29	$6.38^{+0.22}_{-0.20}$	10f	368^{+225}_{-218}	$6.39^{+2.45}_{-1.85}$	$9.85^{+2.99}_{-2.47}$	209.6 (236)	99.9%	$11.47^{+9.83}_{-5.99}$
MR 2251-178*	$2.54^{+0.78}_{-0.75}$	$1.78^{+0.11}_{-0.10}$	<0.52	$6.40^{+0.04}_{-0.04}$	10f	45^{+19}_{-19}	$1.62^{+0.38}_{-0.41}$	$1.82^{+0.57}_{-0.54}$	746.8 (862)	-	-
MCG-02-58-022	-	$1.87^{+0.01}_{-0.02}$	>1.71	$6.32^{+0.06}_{-0.06}$	10f	43^{+19}_{-23}	-	$0.41^{+0.10}_{-0.10}$	844.5 (975)	>99.9%	$2.87^{+0.86}_{-0.75}$

*: analysed in the 3-10 keV energy range.

‡: value of parameter outside set boundaries.

A: cross-calibration constant between *XRT*/*ASCA*/*XMM* and *BAT*.

B: cross-calibration constant between *XRT*/*ASCA*/*XMM* and *INTEGRAL*.

$^{♣}$: fit improvement with respect to table 7.2.

Table 7.10: `pexrav` model (E$_c$=10 000 keV) spectral fits.

MCG-06-30-015* Spectral Fit Results: `wa`$_g$`*wa*(pexrav+zga+laor`†`)`, 0≤R≤2, E$_c$=10 000 keV

N$_H$ (10^{22} cm^{-2})	Γ	**R**	**E$_{line}$ (keV)**	σ (eV)	**EW (eV)**	**E$_{line}$ (keV)**	**EW (eV)**	**C$_1^A$**	**C$_2^B$**	χ^2 **(dof)**	**Prob$^\clubsuit$**
$1.56^{+0.28}_{-0.29}$	$2.24^{+0.04}_{-0.07}$	$1.14^{+0.59}_{-0.51}$	6.4f	10f	18^{+3}_{-6}	$6.32^{+0.04}_{-0.05}$	295^{+43}_{-47}	$0.63^{+0.13}_{-0.06}$	$0.97^{+0.17}_{-0.14}$	1292.6 (1327)	>99.9%

*: analysed in the 3-110 keV energy range.

†: the other parameters in the `LAOR` model have been frozen to R$_{IN}$=1.23r$_g$, R$_{OUT}$=400r$_g$, i=30°, β=-3.

A: cross-calibration constant between *XRT/ASCA/XMM* and *BAT*.

B: cross-calibration constant between *XRT/ASCA/XMM* and *INTEGRAL*.

$^\clubsuit$: fit improvement with respect to table 7.3.

Table 7.11: `pexrav` model (E$_c$=10 000 keV) spectral fit for MCG-06-30-015.)

LEDA 168563 Spectral Fit Results: `wa`$_g$`*wa*(pexrav+po+zga)`, 0≤R≤2, E$_c$=10 000 keV

N$_H$ (10^{22} cm^{-2})	Γ_1	Γ_2	**R**	**E$^\ddagger_{line}$ (keV)**	**EW (eV)**	**C$_1^A$**	**C$_2^B$**	χ^2 **(dof)**	**Prob$^\clubsuit$**
-	$3.63^{+0.34}_{-0.23}$	$1.59^{+0.06}_{-0.05}$	NC	$6.42^{+0.06}_{-0.06}$	28^{+15}_{-15}	$0.44^{+0.08}_{-0.07}$	$0.65^{+0.12}_{-0.06}$	1669.0 (1968)	67%

‡: line width fixed to 10 eV.

A: cross-calibration constant between *XRT/ASCA/XMM* and *BAT*.

B: cross-calibration constant between *XRT/ASCA/XMM* and *INTEGRAL*.

$^\clubsuit$: fit improvement with respect to table 7.4.

Table 7.12: `pexrav` model (E$_c$=10 000 keV) spectral fit for LEDA 168563.

Spectral Fit Results: `wa`$_g$`*wa*pcfabs*pcfabs*(pexrav+zga)`, 0≤R≤2, E$_c$=10 000 keV

Name	**N$_H^{TOT}$ (10^{22} cm^{-2})**	**N$_H^1$ (10^{22} cm^{-2})**	**cf$_1$**	**N$_H^2$ (10^{22} cm^{-2})**	**cf$_2$**	Γ	**R**	**E$^\ddagger_{line}$ (keV)**	**EW (eV)**	**C$_1^A$**	**C$_2^B$**	χ^2 **(dof)**	**Prob$^\clubsuit$**
Mrk 6	-	$9.94^{+4.23}_{-4.14}$	$0.55^{+0.08}_{-0.07}$	$2.27^{+0.37}_{-0.53}$	$0.93^{+0.01}_{-0.01}$	$1.68^{+0.16}_{-0.12}$	NC	$6.45^{+0.02}_{-0.04}$	62^{+24}_{-28}	$0.74^{+0.32}_{-0.33}$	$0.86^{+0.43}_{-0.40}$	564.5 (550)	55%
4U 1344-60	$1.10^{0.15}_{-0.20}$	$5.37^{+1.91}_{-1.92}$	$0.56^{+0.06}_{-0.07}$	$46.44^{+24.00}_{-18.79}$	$0.45^{+0.10}_{-0.07}$	$2.02^{+0.11}_{-0.10}$	<1.55	$6.41^{+0.04}_{-0.03}$	53^{+23}_{-21}	$0.42^{+0.09}_{-0.15}$	$0.71^{+0.27}_{-0.27}$	694.4 (764)	65%
NGC 4151*	$5.90^{+0.47}_{-0.87}$	$29.80^{+9.89}_{-9.16}$	$0.27^{+0.04}_{-0.02}$	-	-	$1.89^{+0.03}_{-0.02}$	$0.14^{+0.12}_{-0.10}$	$6.41^{+0.01}_{-0.01}$	54^{+5}_{-6}	$0.30^{+0.02}_{-0.01}$	$0.64^{+0.05}_{-0.05}$	2050.5 (1989)	98%
IGR J16558-5203	-	$18.83^{+13.03}_{-6.23}$	$0.33^{+0.14}_{-0.08}$	-	-	$2.20^{+0.05}_{-0.05}$	>0.12	$6.49^{+0.06}_{-0.06}$	67^{+47}_{-40}	-	$1.32^{+1.14}_{-0.23}$	607.4 (775)	96%

*: analysed in the 3-110 keV energy range.

‡: line width fixed to 10 eV.

A: cross-calibration constant between *XRT/ASCA/XMM* and *BAT*.

B: cross-calibration constant between *XRT/ASCA/XMM* and *INTEGRAL*.

$^\clubsuit$: fit improvement with respect to table 7.5.

Table 7.13: Partial covering plus `pexrav` model (E$_c$=10 000 keV) spectral fits.

7.2.4 Constraining the Reflection Fraction and the High Energy Cut-off

Lastly the sources spectra have been fitted with a cut-off power law reflected from neutral material, i.e. the `pexrav` model in `XSPEC` (see table 7.14, 7.15, 7.16 and 7.17 for model description in each source case). IGR J00333+6122, Mrk 50, IGR J16119-6036, IGR J17488-3253 and 2E 1853.7+1534 have been removed from the analysis since the quality of the data does not allow to employ such a complex model. Swift J0917.2-6221 has instead been retained, despite been observed by the *XRT* telescope, because the use of the `pexrav` model yields a significant improvement in the fit. The upper bound on the reflection fraction has also been lifted due to some particular cases.

Although this model is not always the best representation of the data (it is the best fit in 17 sources) and the errors are in some cases higher than in previous models, it has been chosen for the following discussion because it allows a simultaneous estimate of both the reflection fraction and the cut-off energy.

From the tables it is evident that 14 out of 27 objects have very well constrained values of R, while 6 have only upper limits. As far as the high energy cut-off is concerned, 13 sources have well constrained values of the parameter, 5 have lower limits and for 3 sources no constraint at all could be placed on it.

It is also interesting to note that in most cases the cross-calibration constants between *XMM* and *BAT/ISGRI* are consistent (within relative uncertainties) with 1, indicating that flux variability at high energies is not very common in AGN (Beckmann et al. 2007). This, however, is not true in some cases, such as LEDA 168563, where the cross-calibration constant between *XMM* and *BAT* is quite low, indicating that the source might have undergone some change in its flux between the two observations. In fact, when fitting together the *BAT* and *ISGRI* data alone, the cross-calibration constant between the two instruments is not close to one, indicating some variability. The same is observed in 4U 1344-60 and also in NGC 4151, which is well known to be variable. Both C_1 and C_2 are found to be less than 1 in MCG+08-11-011, Swift J0917.2-6221, IGR J12415-5750, IGR J16482-3036 and MCG-02-58-022. C_1 and C_2 are instead found to be much higher than 1 in the case of NGC 6814. It is in fact well known from the literature that this object exhibits strong X-ray flux variability over short (hours; Staubert et al. 1994) as well as long (days and years; Mukai et al. 2003) timescales. In a recent paper (Molina et al. 2006), the cross-calibration constant between *ASCA* and *INTEGRAL* was found to be 16, with *INTEGRAL* providing a higher flux than *ASCA*. In the present analysis, the constants are found to be ~8 (*ASCA/BAT*) and ~12 (*ASCA/INTEGRAL*), confirming previous re-

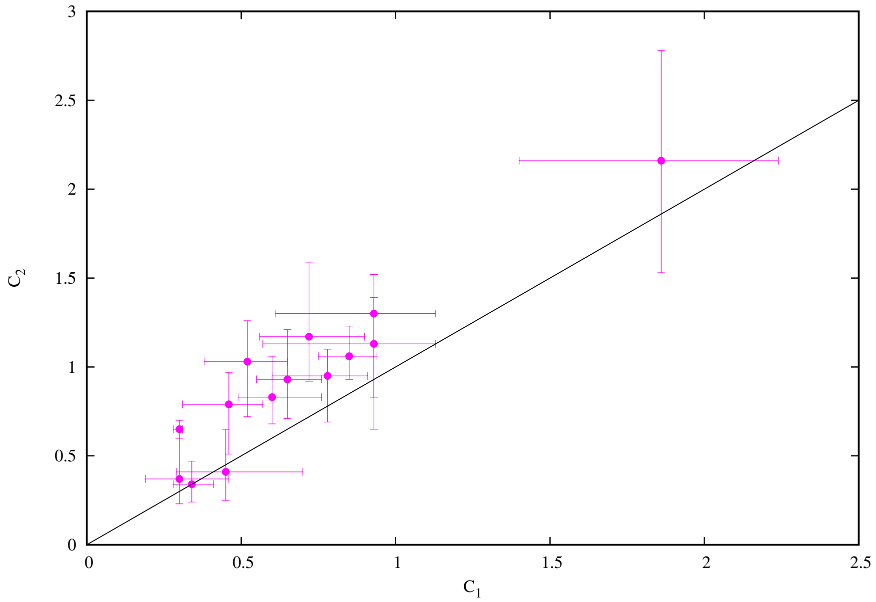

Figure 7.18: Plot of the cross-calibration constants between X and Gamma-ray data; C_1 is the *XMM/ASCA/XRT* and BAT cross-calibration constant and C_2 is the *XMM/ASCA/XRT* and INTEGRAL one. The 1 to 1 (C_1=C_2) line for the constants is also shown. NGC 6814 has been excluded from the plot (see text for details). The constants refer to the `pexrav` model of tables 7.14, 7.15, 7.16 and 7.17

sults and also suggesting that between the two *INTEGRAL* observations (the first one was made between Feb. 2003 and Sep. 2004) and the *BAT* measurement, the source might have undergone once again a change in its high energy flux. It is also worth noting that the present measurement and the one reported in Molina et al. (2006) are the first ones not contaminated by a nearby Galactic source, confirming that the observed flux variation is entirely due to the Seyfert galaxy.

In figure 7.18, a plot of the cross-calibration constants between X-ray and *BAT* (C_1) and X-ray and ISGRI (C_2) data is shown, together with the 1 to 1 line between these two quantities. Since some variances are expected between C_1 and C_2, due to differences in observation times and average fluxes obtained/measured by *BAT* and ISGRI, the good match between C_1 and C_2 is surprising and once again suggests that flux variability is rare at high energies in AGN. Giving a closer look, we find however some discrepancies due to the fact that, while C_2 clusters around 1 (a sign that the spectral match between X-ray and ISGRI data is quite good) C_1 clusters at a lower value of 0.6-0.7; this is an indication that *BAT* spectra may have some systematics when compared to lower energy data.

In the following section, a comparison with results present in the literature is conducted, using the parameter values obtained by employing the `pexrav` model just discussed.

Spectral Fit Results: `wa`$_g$`*wa*(pexrav+zga)`

Name	**N$_H$ (10^{22} cm^{-2})**	**Γ**	**E$_c$ (keV)**	**R**	**EW† (eV)**	**C$_1^A$**	**C$_2^B$**	**χ^2 (dof)**
MCG+08-11-011	-	$1.86^{+0.02}_{-0.03}$	>126	$2.54^{+0.53}_{-0.54}$	92^{+15}_{-26}	$0.34^{+0.07}_{-0.06}$	$0.34^{+0.13}_{-0.10}$	1012.2 (1263)
IGR J07597-3842	-	$1.56^{+0.03}_{-0.03}$	70^{+30}_{-13}	$0.92^{+0.67}_{-0.30}$	89^{+31}_{-35}	$0.78^{+0.13}_{-0.18}$	$0.95^{+0.15}_{-0.26}$	435.7 (458)
FRL 1146	$0.28^{+0.07}_{-0.08}$	$1.71^{+0.12}_{-0.13}$	59^{+194}_{-31}	$1.31^{+0.69}_{-1.27}$	127^{+45}_{-52}	-	$0.71^{+0.57}_{-0.30}$	498.0 (576)
Swift J0917.2-6221	$0.41^{+0.13}_{-0.14}$	$1.60^{+0.14}_{-0.35}$	83^{+210}_{-45}	<10.65	-	$0.30^{+0.16}_{-0.11}$	$0.37^{+0.23}_{-0.14}$	135.3 (122)
NGC 3783*	$1.16^{+0.37}_{-0.37}$	$1.75^{+0.09}_{-0.09}$	98^{+79}_{-34}	$1.23^{+0.63}_{-0.57}$	87^{+11}_{-9}	$0.65^{+0.11}_{-0.10}$	$0.93^{+0.28}_{-0.22}$	1605.3 (1768)
NGC 4593	-	$1.92^{+0.01}_{-0.01}$	>222	$1.77^{+0.85}_{-0.76}$	91^{+37}_{-37}	$0.60^{+0.16}_{-0.11}$	$0.83^{+0.23}_{-0.15}$	732.4 (855)
IGR J12415-5750	-	$1.62^{+0.05}_{-0.06}$	>67	$1.85^{+1.19}_{-1.01}$	81^{+27}_{-59}	$0.45^{+0.25}_{-0.16}$	$0.41^{+0.24}_{-0.16}$	576.4 (681)
IC 4329A	$0.35^{+0.01}_{-0.01}$	$1.81^{+0.03}_{-0.03}$	152^{+51}_{-32}	$0.70^{+0.35}_{-0.31}$	181^{+30}_{-33}	$0.85^{+0.12}_{-0.10}$	$1.06^{+0.17}_{-0.13}$	1699.4 (1617)
IGR J16482-3036	$0.10^{+0.06}_{-0.07}$	$1.65^{+0.10}_{-0.15}$	97^{+158}_{-50}	$1.53^{+1.84}_{-1.51}$	82^{+45}_{-61}	-	$0.38^{+0.36}_{-0.12}$	439.9 (495)
GRS 1734-292	>0.21	$1.36^{+0.17}_{-0.06}$	39^{+17}_{-3}	<0.84	-	$0.93^{+0.20}_{-0.32}$	$1.30^{+0.22}_{-0.47}$	166.1 (111)
2E 1739.1-1210	$0.15^{+0.03}_{-0.03}$	$2.05^{+0.07}_{-0.06}$	NC	$1.81^{+1.02}_{-0.84}$	26^{+36}_{-19}	-	$1.02^{+0.20}_{-0.17}$	815.5 (870)
IGR J18027-1455	$0.30^{+0.08}_{-0.08}$	$1.55^{+0.13}_{-0.11}$	192^{+167}_{-63}	$0.90^{+0.60}_{-0.35}$	117^{+37}_{-31}	-	$1.72^{+0.78}_{-0.56}$	818.6 (898)
NGC 6814	-	$1.80^{+0.09}_{-0.09}$	116^{+203}_{-53}	$7.04^{+12.43}_{-3.90}$	315^{+217}_{-219}	$7.62^{+2.87}_{-2.19}$	$12.52^{+6.98}_{-3.41}$	201.2 (236)
MR 2251-178*	$2.15^{+0.64}_{-1.21}$	$1.68^{+0.10}_{-0.21}$	109^{+104}_{-44}	<0.35	45^{+19}_{-19}	$1.86^{+0.38}_{-0.46}$	$2.16^{+0.62}_{-0.63}$	740.6 (862)
MCG-02-58-022	-	$1.88^{+0.01}_{-0.02}$	NC	$2.90^{+1.00}_{-0.77}$	45^{+25}_{-27}	-	$0.38^{+0.09}_{-0.09}$	856.3 (975)

*: analysed in the 3-110 keV energy range.

†: line parameters fixed at value obtained with simple PL.

A: cross-calibration constant between *XRT/ASCA/XMM* and *BAT*.

B: cross-calibration constant between *XRT/ASCA/XMM* and *INTEGRAL*.

Table 7.14: `pexrav` model spectral fits.

MCG-06-30-015* Spectral Fit Results: `wa`$_g$`*wa*(pexrav+zga+laor`†`)`

N$_H$ (10^{22} cm^{-2})	**Γ**	**E$_{cut}$ (keV)**	**R**	**EW (eV)**	**EW (eV)**	**C$_1^A$**	**C$_2^B$**	**χ^2 (dof)**
$1.48^{+0.33}_{-0.37}$	$2.18^{+0.10}_{-0.11}$	>76	$0.78^{+0.52}_{-0.52}$	21^{+7}_{-8}	312^{+46}_{-56}	$0.72^{+0.18}_{-0.16}$	$1.17^{+0.42}_{-0.25}$	1296.1 (1327)

*: analysed in the 3-110 keV energy range.

†: the other parameters in the `LAOR` model have been frozen to R_{IN}=1.23r_g, R_{OUT}=400r_g, i=30°, β=-3.

A: cross-calibration constant between *XMM* and *BAT*.

B: cross-calibration constant between *XMM* and *INTEGRAL*.

Table 7.15: `pexrav` model spectral fit for MCG-06-30-015.

LEDA 168563 Spectral Fit Results: `wa`$_g$`*wa*(pexrav+po+zga)`

N_H (10^{22} cm^{-2})	Γ_1	Γ_2	E_{cut} (keV)	R	EW† (eV)	C_1^A	C_2^B	χ^2 (dof)
-	$3.50^{+0.25}_{-0.36}$	$1.49^{+0.11}_{-0.18}$	63^{+59}_{-30}	<0.53	28^{+15}_{-17}	$0.52^{+0.13}_{-0.14}$	$1.03^{+0.23}_{-0.31}$	1656.8 (1968)

A: cross-calibration constant between *XMM* and *BAT*.

B: cross-calibration constant between *XMM* and *INTEGRAL*.

Table 7.16: `pexrav` model spectral fit for LEDA 168563.

Spectral Fit Results: `wa`$_g$`*wa*pcfabs*pcfabs*(pexrav+zga)`

Name	N_H^{TOT} (10^{22} cm^{-2})	N_H^1 (10^{22} cm^{-2})	cf$_1$	N_H^2 (10^{22} cm^{-2})	cf$_2$	Γ	E_c (keV)	R	EW† (keV)	C_1^A	C_2^B	χ^2 (dof)
Mrk 6	-	$8.12^{+4.76}_{-2.83}$	$0.49^{+0.10}_{-0.06}$	$2.04^{+0.61}_{-0.49}$	$0.91^{+0.02}_{-0.02}$	$1.42^{+0.20}_{-0.14}$	82^{+202}_{-43}	<1.22	57^{+25}_{-23}	$0.93^{+0.20}_{-0.36}$	$1.13^{+0.26}_{-0.48}$	560.7 (550)
4U 1344-60	$1.02^{+0.16}_{-0.25}$	$5.17^{+2.28}_{-2.36}$	$0.50^{+0.09}_{-0.11}$	$46.76^{+32.37}_{-21.08}$	$0.40^{+0.12}_{-0.14}$	$1.81^{+0.20}_{-0.21}$	>108	<0.80	57^{+23}_{-21}	$0.46^{+0.11}_{-0.15}$	$0.79^{+0.18}_{-0.28}$	691.2 (764)
NGC 4151*	$5.28^{+0.74}_{-1.22}$	$22.44^{+13.67}_{-10.42}$	$0.25^{+0.21}_{-0.07}$	-	-	$1.77^{+0.06}_{-0.05}$	307^{+245}_{-94}	<0.20	56^{+5}_{-6}	$0.30^{+0.01}_{-0.02}$	$0.65^{+0.05}_{-0.05}$	2037.8 (1989)
IGR J16558-5203	-	$18.56^{+16.17}_{-9.10}$	$0.32^{+0.06}_{-0.07}$	-	-	$2.20^{+0.06}_{-0.06}$	NC	$2.20^{+1.08}_{-0.96}$	68^{+44}_{-43}	-	$1.27^{+0.26}_{-0.21}$	607.4 (775)

*: analysed in the 3-110 keV energy range.

†: line parameters fixed at value obtained with simple PL.

A: cross-calibration constant between *XMM* and *BAT*.

B: cross-calibration constant between *XMM* and *INTEGRAL*.

Table 7.17: Partial covering plus `pexrav` model spectral fits.

7.3 Comparison with Previous Results

In order to check the validity of the analysis just presented, the sample has been compared to data already present in the literature, including also the Broad Line Radio Galaxies analysed in the previous chapter. In particular, the fit results are compared with *BeppoSAX* observations analysed over a similar energy range and employing a similar model to ours by Dadina (2007). It must be noted that not all the sources presented in this thesis have been previously observed by other instruments and that only some of them have been studied over a broad energy range by *BeppoSAX*. As far as these sources are concerned, in the work by Dadina (2007) we find 12 of the AGN presented here, namely 3C 111, MCG+08-11-011, Markarian 6, NGC 3783, NGC 4154, NGC 4593, MCG-06-30-015, IC 4329A, 3C 390.3, S5 2116+81, MR 2251-178 and MCG-02-58-022.

As can be seen from figure 7.19, the photon indices obtained with the present analysis are in good agreement with the values found by Dadina (2007), except for Markarian 6 and MR 2251-178, for which we find a very flat power law slope, also when compared to other work (Malizia et al. 2003a for Mrk 6, in which they found $\Gamma\sim$1.6; Orr et al. 2001 for MR 2251-178 who found $\Gamma\sim$1.6); in the case of 3C 390.3 and S5 2116+81 Dadina found flatter slopes than in our analysis (see previous chapter). A good agreement is also found, within the (sometimes) large errors, for the high energy cut-off and the reflection fraction, although for some sources only upper limits are available (see figure 7.20). However, in one case, that of MCG+08-11-11, a much higher value of *R* than that found by Dadina is obtained; *R* is also higher than the ones reported by Perola et al. (2002) with *BeppoSAX* observations (R=$1.09^{+-0.80}_{-0.39}$) and also by Matt et al. (2006) who analysed *XMM* data only and found R=$1.51^{+0.13}_{-0.09}$.

As far as the other sources in the sample are concerned, 8 of them have already been analysed by Panessa et al. (2008) using the same data-set analysed here, but in a broader energy range (0.5-150 keV) and without the addition of the *BAT* data. The sources are LEDA 168563, IGR J07597-3842, FRL 1146, 4U 1344-60, IGR J16482-3036, IGR J16558-5203, 2E 1739.1-1210 and IGR J18027-1455 and overall we can conclude that our results are wholly compatible with those reported in Panessa et al. (2008).

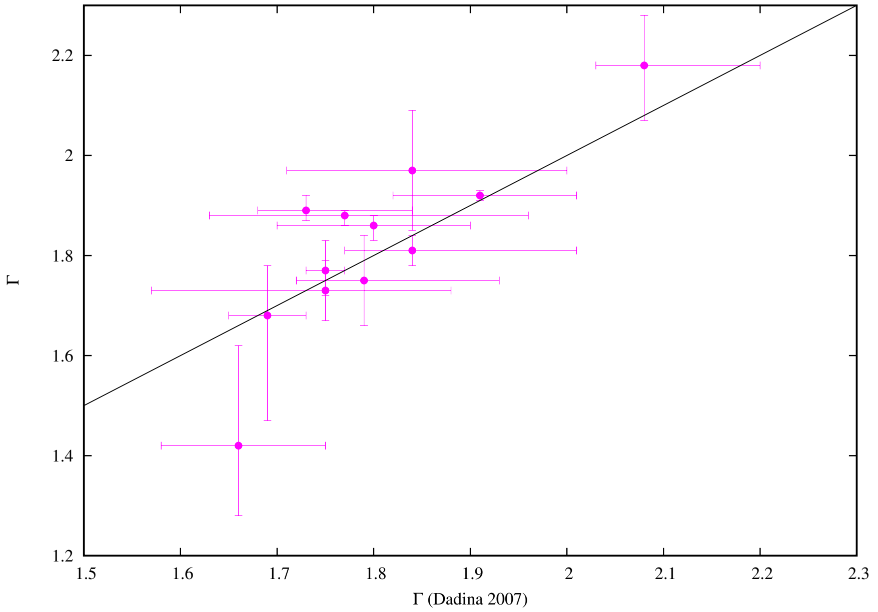

Figure 7.19: The plot shows the photon index values obtained by Dadina (2007) using *BeppoSAX* data versus the results presented here; the solid line represents a ratio of 1 for the two values of Γ. The values are in good agreement except for MR 2251-178.

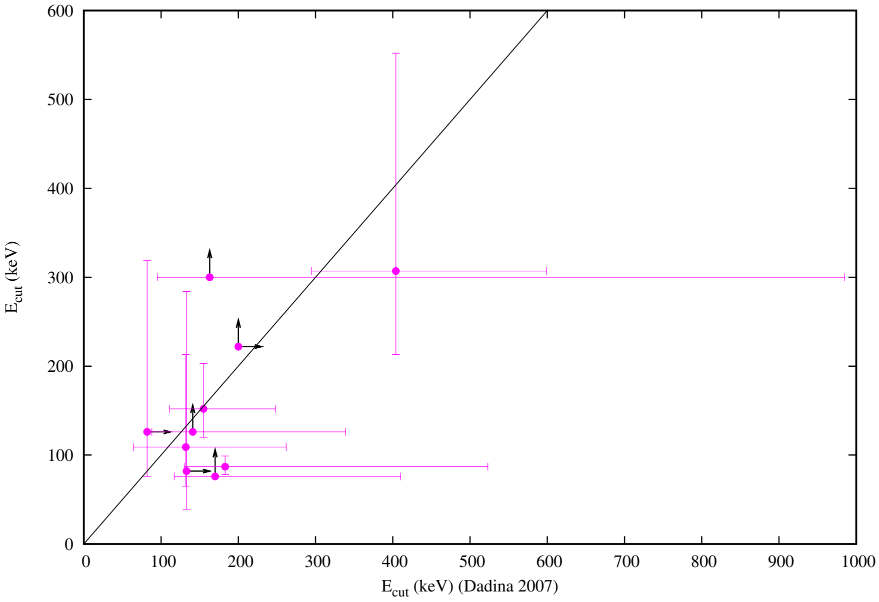

Figure 7.20: The plot shows the high energy cut-off values obtained by Dadina (2007) using *BeppoSAX* data versus the results presented here; the solid line represents a ratio of 1 for the two values of E_{cut}.

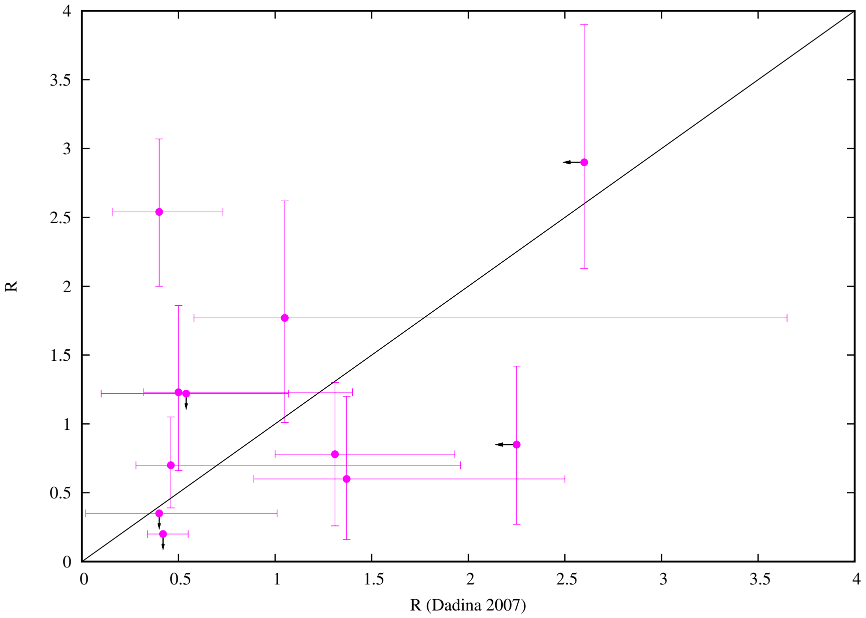

Figure 7.21: The plot shows the reflection fraction values obtained by Dadina (2007) using *BeppoSAX* data versus the results presented here; the solid line represents a ratio of 1 for the two values of *R*.

Chapter 8

Implications of the X- and Gamma-ray Studies and General Conclusions

8.1 Introduction

It is now widely accepted that the Cosmic X-ray Background (CXB) is the product of the integrated emission of point-like extragalactic sources, most of them now resolved below 10 keV thanks to the survey studies conducted both by *XMM-Newton* and *Chandra*. It has also been shown that most of the sources contributing to the CXB are AGN, both unobscured and obscured (e.g. Barger et al. 2005), as already predicted by AGN synthesis models (Comastri et al. 1995). However, while at low energies the shape and the intensity of the CXB is quite well understood (Hickox & Markevitch 2006), at higher energies, around 30 keV or above, these quantities are less well studied and hence the AGN contribution is less defined. Recent analyses of *BeppoSAX, INTEGRAL* and *Swift* data have allowed a better estimate of the CXB spectrum above 10 keV (see Ajello et al. 2008 and references therein). All these measurements agree with an early HEAO A1 result and are consistent within their systematic uncertainties. Such consistency is not present with data at lower energies, where the measured spectrum may be up to ~40% larger. Synthesis models need now to take this discrepancy into consideration.

According to AGN synthesis models (e.g. Comastri et al. 2006), several parameters must be taken into account to describe the shape of the CXB above 30 keV. These are the covering fraction and the geometry of the cold dense gas responsible for the reflection hump seen around 30 keV; the fraction of highly obscured AGN (Compton Thick sources with $N_H \geq 10^{24} cm^{-2}$); the high energy cut-off observed in the primary continuum emission, the exact value of which, as already mentioned, is still not well determined. Some recent models (Gilli et al. 2007) also propose the average power law photon index (and its spread in values) as another important parameter that needs to be considered when describing the CXB.

It is therefore clear that the determination of these parameters over wide samples of sources, and particularly over a wide range of energies (above all up to 100 keV and beyond), is important in order to obtain a firm description of the AGN contribution to the CXB and hence a better understanding of the accretion history of the Universe. Broad-band spectral analysis not only provides information on the cut-off energy but also allows the study of the reflection component. It must also be emphasised that broad-band spectra are the only way to provide simultaneous information on most AGN spectral components and consequently a better estimate of the primary power law photon index.

The determination of the slope of the continuum emission of AGN and its high energy cut-off, besides being a key element in CXB synthesis models, is also essential for spectral modelling of AGN, since these two parameters are deeply linked to the physical characteristics of the Comptonising region around the central nucleus. Although broad-band measurements of AGN have been made in the past, mainly with the *BeppoSAX* satellite (e.g. Perola et al. 2002 and Dadina 2007), these were for the most part related to X-ray bright AGN and did not pertain to a complete sample of sources. In this work we attempt to do this analysis for the first time using a hard X-ray selected sample of type 1 active galaxies.

In this chapter the results of the analysis performed in this thesis will be explored, firstly by taking an overview look at the general properties of the sample studied and then by comparing radio quiet and radio loud sources. Finally the sample and its properties will be discussed in the framework of spectral modelling and AGN contribution to the Cosmic Diffuse Background.

8.2 The Complete Sample: General Properties

In this section the mean properties of the complete sample of radio loud and radio quiet type 1 sources will be explored. In table 8.1 a list is presented for the entire sample of type 1 AGN, with the results of the analysis performed in this thesis, in terms of absorption, photon indices, cut-off energies, reflection fractions and iron line equivalent widths. The cross-calibration constants between X-ray data and BAT (C_1) and ISGRI (C_2) are also listed. The values reported in table 8.1 refer to the `pexrav` model, with R and E_{cut} as free variables (see also previous chapters).

The distribution of the intrinsic column densities, as reported for all the sources in table

Radio Quiet AGN-`pexrav` model

Name	**N$_H$ (10^{22} cm^{-2})**	**Γ**	**E$_c$ (keV)**	**R**	**EW[†] (eV)**	**C$_1^A$**	**C$_2^B$**
IGR J00333+6122	$0.85^{+0.45}_{-0.40}$	$1.76^{+0.30}_{-0.28}$	NC	<1.15	-	-	$0.95^{+0.97}_{-0.60}$
LEDA 168563[♣]	-	$1.49^{+0.11}_{-0.18}$	63^{+59}_{-30}	<0.53	28^{+15}_{-17}	$0.52^{+0.13}_{-0.14}$	$1.03^{+0.23}_{-0.31}$
MCG+08-11-011	-	$1.86^{+0.02}_{-0.03}$	>126	$2.54^{+0.53}_{-0.54}$	92^{+15}_{-26}	$0.34^{+0.07}_{-0.06}$	$0.34^{+0.13}_{-0.10}$
Mrk 6	complex[‡]	$1.42^{+0.20}_{-0.14}$	82^{+202}_{-43}	<1.22	57^{+25}_{-23}	$0.93^{+0.20}_{-0.36}$	$1.13^{+0.26}_{-0.48}$
IGR J07597-3842	-	$1.56^{+0.03}_{-0.03}$	70^{+30}_{-13}	$0.92^{+0.67}_{-0.30}$	89^{+31}_{-35}	$0.78^{+0.13}_{-0.18}$	$0.95^{+0.15}_{-0.26}$
FRL 1146	$0.28^{+0.07}_{-0.08}$	$1.71^{+0.12}_{-0.13}$	59^{+194}_{-31}	$1.31^{+0.69}_{-1.27}$	127^{+45}_{-52}	-	$0.71^{+0.57}_{-0.30}$
Swift J0917.2-6221	$0.41^{+0.13}_{-0.14}$	$1.60^{+0.14}_{-0.35}$	83^{+210}_{-45}	<10.65	-	$0.30^{+0.16}_{-0.11}$	$0.37^{+0.23}_{-0.14}$
Mrk 50	<0.12	$1.94^{+0.12}_{-0.08}$	>25	<1.76	-	-	$1.23^{+0.57}_{-0.41}$
NGC 3783[⋆]	$1.16^{+0.37}_{-0.37}$	$1.75^{+0.09}_{-0.09}$	98^{+79}_{-34}	$1.23^{+0.63}_{-0.57}$	87^{+11}_{-9}	$0.65^{+0.11}_{-0.10}$	$0.93^{+0.28}_{-0.22}$
NGC 4151[⋆]	complex[‡]	$1.77^{+0.06}_{-0.05}$	307^{+245}_{-94}	<0.20	56^{+5}_{-7}	$0.30^{+0.01}_{-0.02}$	$0.65^{+0.05}_{-0.05}$
NGC 4593	-	$1.92^{+0.01}_{-0.01}$	>222	$1.77^{+0.85}_{-0.76}$	91^{+37}_{-37}	$0.60^{+0.16}_{-0.11}$	$0.83^{+0.23}_{-0.15}$
IGR J12415-5750	-	$1.62^{+0.05}_{-0.06}$	>67	$1.85^{+1.19}_{-1.01}$	81^{+27}_{-59}	$0.45^{+0.25}_{-0.16}$	$0.41^{+0.24}_{-0.16}$
MCG-06-30-015[⋆]	$1.48^{+0.33}_{-0.37}$	$2.18^{+0.10}_{-0.11}$	>76	$0.78^{+0.52}_{-0.52}$	312^{+46}_{-56}	$0.72^{+0.18}_{-0.16}$	$1.17^{+0.42}_{-0.25}$
4U 1344-60	complex[‡]	$1.81^{+0.20}_{-0.21}$	>108	<0.80	57^{+23}_{-21}	$0.46^{+0.11}_{-0.15}$	$0.79^{+0.18}_{-0.28}$
IC 4329A	$0.35^{+0.01}_{-0.01}$	$1.81^{+0.03}_{-0.03}$	152^{+51}_{-32}	$0.70^{+0.35}_{-0.31}$	181^{+30}_{-33}	$0.85^{+0.12}_{-0.10}$	$1.06^{+0.17}_{-0.13}$
IGR J16119-6036	-	$1.84^{+0.24}_{-0.22}$	>54	NC	-	-	$5.11^{+5.98}_{-2.60}$
IGR J16482-3036	$0.10^{+0.06}_{-0.07}$	$1.65^{+0.10}_{-0.15}$	97^{+158}_{-50}	$1.53^{+1.84}_{-1.51}$	82^{+45}_{-61}	-	$0.38^{+0.36}_{-0.12}$
IGR J16558-5203	complex[‡]	$2.20^{+0.06}_{-0.06}$	NC	$2.20^{+1.08}_{-0.96}$	68^{+44}_{-43}	-	$1.27^{+0.26}_{-0.21}$
GRS 1734-292	>0.21	$1.36^{+0.17}_{-0.06}$	39^{+17}_{-3}	<0.84	-	$0.93^{+0.20}_{-0.32}$	$1.30^{+0.22}_{-0.47}$
2E 1739.1-1210	$0.15^{+0.03}_{-0.03}$	$2.05^{+0.07}_{-0.06}$	NC	$1.81^{+1.02}_{-0.84}$	26^{+36}_{-19}	-	$1.02^{+0.20}_{-0.17}$
IGR J17488-3253	$0.34^{+0.10}_{-0.10}$	$1.59^{+0.15}_{-0.11}$	>118	<1.14	-	-	$1.63^{+0.40}_{-0.75}$
IGR J18027-1455	$0.30^{+0.08}_{-0.08}$	$1.55^{+0.13}_{-0.11}$	192^{+167}_{-63}	$0.90^{+0.60}_{-0.35}$	117^{+37}_{-31}	-	$1.72^{+0.78}_{-0.56}$
2E 1853.7+1534	<0.39	$1.47^{+0.41}_{-0.20}$	53^{+295}_{-21}	<11.40	-	-	$1.33^{+0.90}_{-0.83}$
NGC 6814	-	$1.80^{+0.09}_{-0.09}$	116^{+203}_{-53}	$7.04^{+12.43}_{-3.90}$	315^{+217}_{-219}	$7.62^{+2.87}_{-2.19}$	$12.52^{+6.98}_{-3.41}$
MR 2251-178[⋆]	$2.15^{+0.64}_{-1.21}$	$1.68^{+0.10}_{-0.21}$	109^{+104}_{-44}	<0.35	45^{+19}_{-19}	$1.86^{+0.38}_{-0.46}$	$2.16^{+0.62}_{-0.63}$
MCG-02-58-022	-	$1.88^{+0.01}_{-0.02}$	NC	$2.90^{+1.00}_{-0.77}$	45^{+25}_{-27}	-	$0.38^{+0.09}_{-0.09}$

Radio Loud AGN-`pexrav` model

Name	**N$_H$ (10^{22} cm^{-2})**	**Γ**	**E$_c$ (keV)**	**R**	**EW[†] (eV)**	**C$_1^A$**	**C$_2^B$**
QSO B0241+61	$0.21^{+0.15}_{-0.10}$	$1.64^{+0.22}_{-0.14}$	>86	$0.56^{+0.82}_{-0.41}$	73^{+44}_{-42}	$0.85^{+0.44}_{-0.32}$	$1.12^{+0.65}_{-0.48}$
B3 0309+411	-	$1.90^{+0.08}_{-0.08}$	35^{+91}_{-17}	$3.48^{+2.24}_{-1.58}$	59^{+42}_{-43}	-	$6.89^{+9.39}_{-3.90}$
3C 111	$0.46^{+0.03}_{-0.03}$	$1.73^{+0.06}_{-0.06}$	126^{+193}_{-50}	$0.85^{+0.57}_{-0.58}$	<30	$0.40^{+0.11}_{-0.08}$	$0.52^{+0.19}_{-0.13}$
IGR J13109-5552	<0.46	$1.55^{+0.31}_{-0.26}$	>58	<5.1	-	-	$1.83^{+3.56}_{-1.03}$
3C 390.3[♠]	-	$1.89^{+0.03}_{-0.02}$	>300	$0.60^{+0.60}_{-0.44}$	41^{+12}_{-11}	$0.95^{+0.17}_{-0.25}$	$1.01^{+0.39}_{-0.30}$
4C 74.26	$0.14^{+0.02}_{-0.03}$	$1.79^{+0.06}_{-0.07}$	100^{+680}_{-52}	$1.22^{+0.69}_{-0.70}$	88^{+23}_{-20}	$0.48^{+0.12}_{-0.18}$	$0.86^{+0.50}_{-0.33}$
S5 2116+81	<0.24	$2.03^{+0.26}_{-0.20}$	>85	<4.0	-	$1.10^{+0.97}_{-0.47}$	$1.96^{+2.17}_{-0.89}$
IGR J21247+5058	complex[‡]	$1.54^{+0.08}_{-0.08}$	99^{+54}_{-29}	$0.42^{+0.47}_{-0.39}$	<30	-	$0.67^{+0.18}_{-0.12}$

A: cross-calibration constant between *XMM/Chandra/XRT/ASCA* and *BAT*.

B: cross-calibration constant between *XMM/Chandra/XRT/ASCA* and *INTEGRAL*.

[⋆]: analysed in the 3-110 keV energy range.

[†]: line parameters fixed at value obtained with simple PL.

[♣]: the model employed is `wa`$_g$`*wa*(po+pexrav+zga)`.

[♠]: the model employed is `wa`$_g$`*wa*(bb+pexrav+zga)`.

[‡]: see chapter 7 and 5 (IGR J21247+5058) for details on the complex absorbers.

Table 8.1: Spectral results for the `pexrav` model for all the type 1 sources in the complete sample.

8.1, shows a peak around Log(N$_H$)=21-22, with the sources characterised by complex absorption occupying the tail towards higher values of N$_H$ (figure 8.1). Note that for sources requiring complex absorption, the value of the intrinsic column density is relative to the layer with the highest covering fraction. The weighted average[1] for the absorbing column density is N$_H$=(3.24±0.08)×10^{21} cm^{-2} (standard deviation σ=4.2×10^{22} cm^{-2}),

---

[1] Because in our results the errors on all the parameters are asymmetric, to evaluate the error on the weighted mean of the parameters, the arithmetical mean of the errors has been used.

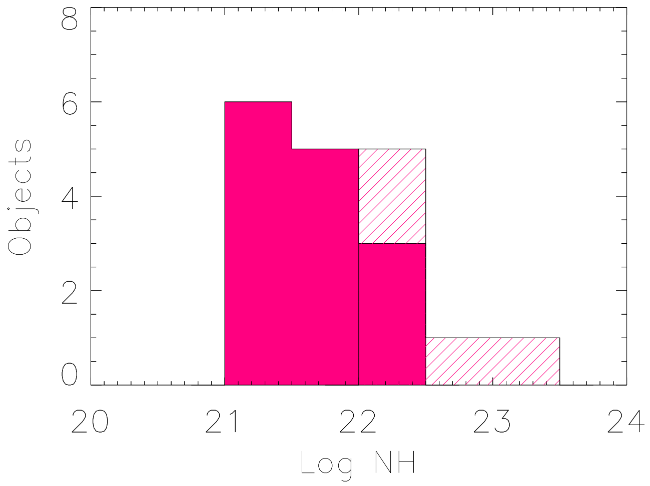

Figure 8.1: Intrinsic Column Density Distribution for the sample analysed here. The dashed histogram represents sources requiring complex absorption, for which the value of N_H with the larger covering fraction has been used.

lower than the mean value of 3.98×10^{22} cm^{-2} found by Dadina (2008) for the type 1 sources listed in his work.

The distribution of the photon indices for the entire sample is shown in figure 8.2, where it can be seen that the majority of the sources fall in the range 1.5-2.0. Indeed, the weighted average photon index for the whole sample is 1.86±0.01 with a standard deviation of 0.20. It is worth noting that this value is close to the generally accepted canonical photon index for type 1 AGN of 1.9. Our mean power law slope is also similar to the value found by Dadina (2008), who employed the same model used in this analysis but with *BeppoSAX* observations of a sample of 43 type 1 AGN and found a mean value of 1.89±0.03.

The mean value (excluding upper limits) for the high energy cut-off is 104 keV (standard deviation σ~64 keV); the distribution of values for this parameter shows a tail extending to higher energies (see figure 8.3). Because of the large asymmetry in the errors on E_c, it is difficult to evaluate an appropriate error on the cut-off energy. The value found in the present analysis is lower than the mean value of 230±22 keV found by Dadina (2008) and also than the value provided by the mean *BeppoSAX* spectrum obtained by Malizia et al. (2003b). Again this may be related to the fact that this study employs for the first time a complete sample, whereas in the past similar studies employed bright randomly chosen AGN.

The sample has also been tested against the correlation found by a number of authors

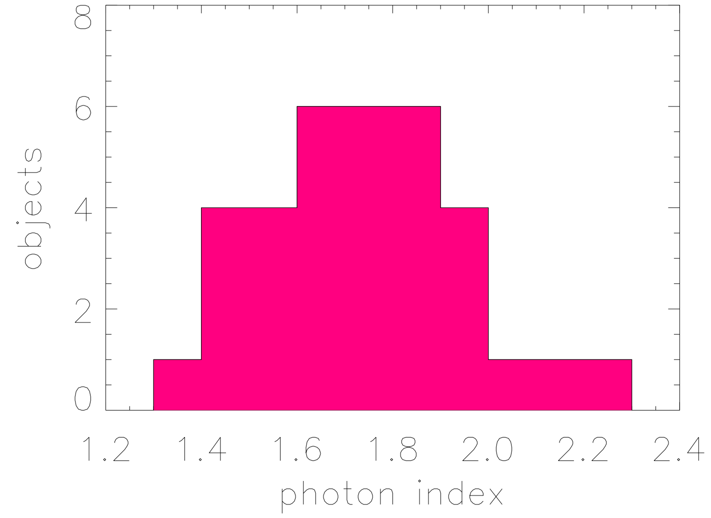

Figure 8.2: Photon index distribution of the type 1 sources analysed here.

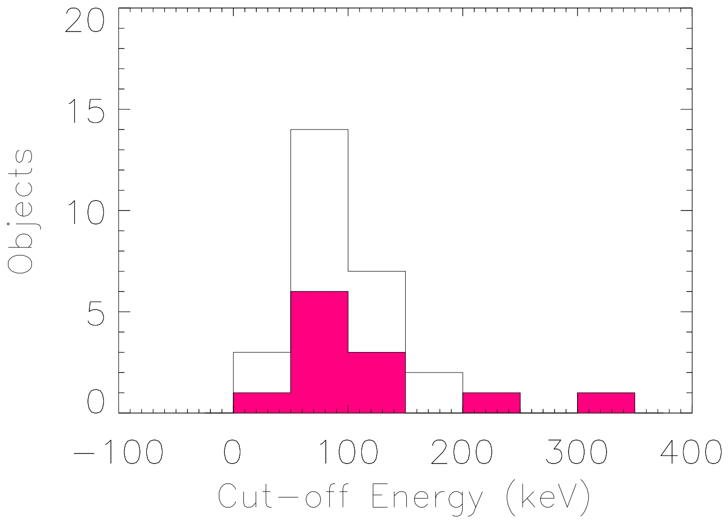

Figure 8.3: High energy cut-off distribution for the type 1 sources presented here. Upper limits are represented by the filled magenta histogram.

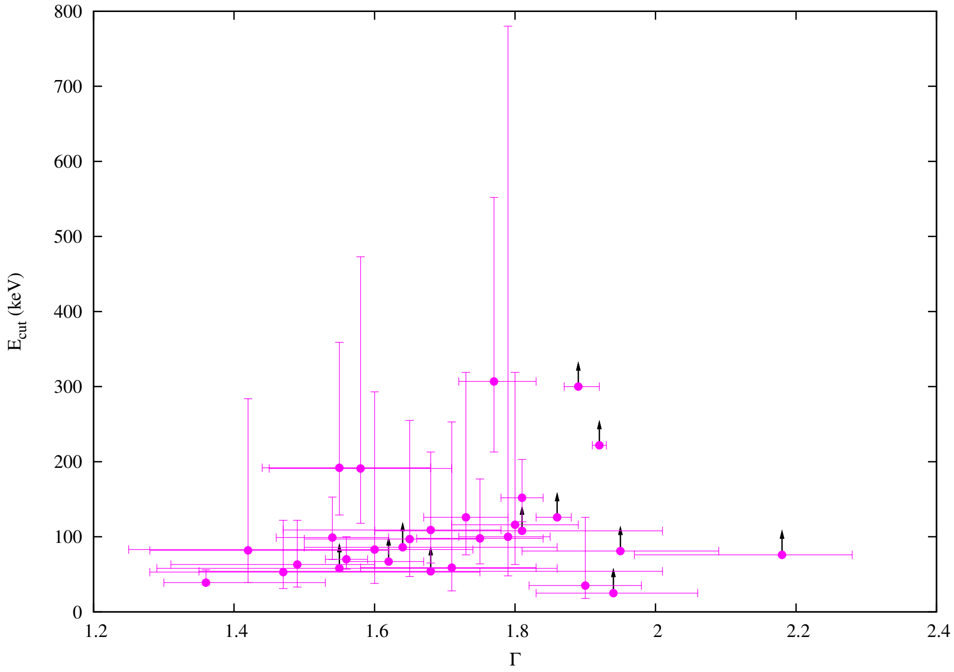

Figure 8.4: High energy cut-off vs. photon index for both RQ and RL objects. No trend of increasing cut-off energy with higher Γ values is found.

between the photon index and the high energy cut-off. First claimed by Piro (1999), it was further discussed by Matt (2001) and Petrucci et al. (2001), taking advantage of the broadband *BeppoSAX* observations of AGN. At present, this correlation is still debated, since previous work found that the two parameters are not independent in the fitting procedure, with Γ increasing as the cut-off energy decreases (Perola et al. 2002).

Figure 8.4 shows a plot of the photon index versus the high energy cut-off, but no evident trend is found between these two quantities. The use of a Pearson statistical test to the two sets of data also returns a low correlation coefficient of $r\sim0.23^2$ (if upper limits are ignored r is 0.30); note that this test does not take into account the relative uncertainties on the parameters values. Studying the distribution in the parameter space of these two quantities is also an indirect way of testing that the results of our analysis are not strongly affected by the interplay between Γ and E_c.

As far as the reflection fraction is concerned, the weighted mean (excluding again upper limits) found in this study is 1.08±0.14 (standard deviation σ=0.85), consistent, within uncertainties, with the value of 1.23±0.11 reported by Dadina (2008); indeed, the distribution of the reflection fractions shows a peak around 1 (figure 8.5), with a tail extending to higher values of R of up to 3. It must be noted, however, that there could be

---

[2] The square of the correlation coefficient r is conventionally used as a measure of the association between two variables.

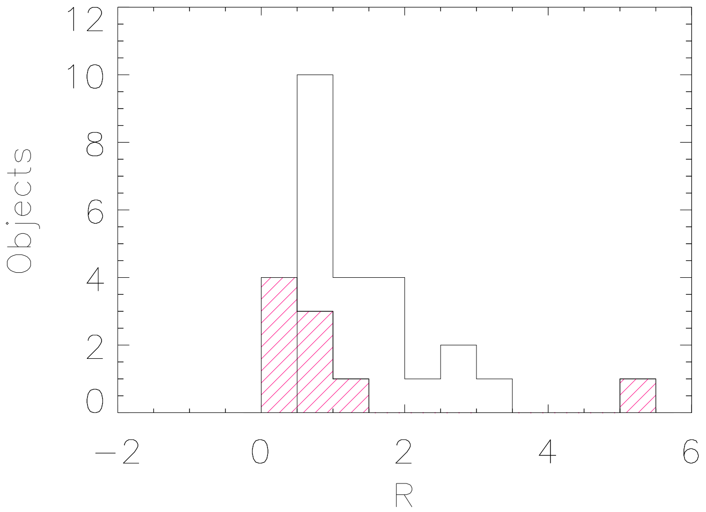

Figure 8.5: Reflection fraction distribution for radio quiet and radio loud objects. Upper/lower limits are represented by the dashed histogram.

few sources in the sample, like NGC 6814 and B3 0309+411, where a large value of the reflection fraction may be the result of a large mismatch between X-ray and soft gamma ray data due to flux variability. The only other outlier with respect to the main group of AGN is Swift J0917.2-6221, for which, however, we only have a loose upper limit on R. Since R and the cross-calibration constant are strongly related in the fitting procedure, it is important to test if a correlation exists between these two quantities. Indeed, from figure 8.6 (upper panel) it can be inferred that a correlation between the reflection fraction and the cross-calibration constant exists, as also suggested by applying a Pearson test to the parameter space of figure 8.6 which returns a strong correlation coefficient of $r\sim0.83$ (not considering upper limits). However if NGC 6814 and B3 0309+411 (and all the upper limits) are removed (see figure 8.6 lower panel) r becomes $\sim$-0.44, implying that the two sources are those providing a high value of r. Furthermore, if all upper limits are taken into account, then $r\sim0.43$, with NGC 6814 and B3 0309+411 included, and $\sim$-0.39 with them removed. This suggests that at most a weaker correlation is present and the estimate on R is not too dependent on the value of C.

A correlation was also searched for between the photon index and the reflection fraction. Zdziarski et al. (1999) proposed that such a correlation might be explained assuming that the cold medium, responsible for the reflection and surrounding the corona, affects the hardness (i.e. the slope) of the X-ray spectrum. In this framework, the soft photons, emitted from the cold medium and irradiating the X-ray source, serve as seeds for Comp-

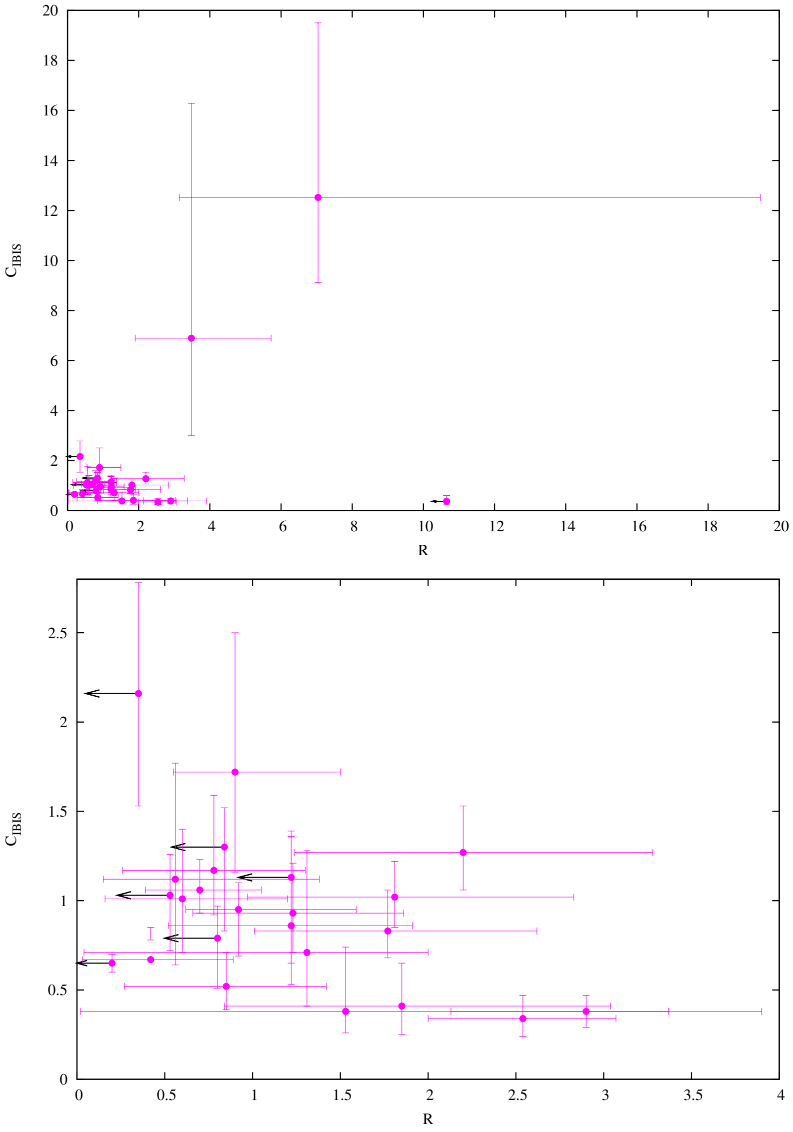

Figure 8.6: *Upper Panel*: reflection fraction vs. cross-calibration constant between X-ray and IBIS data. *Lower Panel*: a zoom of the plot for small values of R.

ton upscattering. This implies that the larger is the solid angle subtended by the reflector, the stronger is the flux of the soft photons and therefore the stronger the cooling of the plasma. In the case of thermal plasma, the larger the cooling by seed photons, the softer the resulting X-ray power law spectrum. A correlation between Γ and R has also been seen by Petrucci et al. (2001), who, employing a `pexrav` model, confirmed that the higher is the temperature of the corona (which is directly linked also to the cut-off energy), the larger is the reflection fraction. However, these authors, found also that using a different model that takes into account anisotropic Comptonisation, the trend is reversed and larger reflection corresponds to lower temperatures. Besides, the two parameters R and Γ are strongly linked in the fitting procedure and therefore a trend in the parameter space may not be entirely physical. Figure 8.7 is a plot of R vs. Γ for our set of AGN; the Pearson test applied to the two datasets (excluding upper limits on the parameters) gives in our case a small correlation coefficient of ~0.21, which becomes even smaller if upper limits are considered (r=0.05). This is contrary to what found by Dadina (2008) who found a correlation between Γ and R. We have also looked for a correlation between the reflection fraction and the high energy cut-off (see figure 8.8) by applying again the Pearson test to our data: the correlation coefficient is ~-0.17 (with and without considering the upper limits on R and E_c), again indicative of no correlation between the spectral parameters.

We can therefore conclude that we do not find any evidence for correlations between the various spectral parameters Γ, R and E_c, an indication this that the interplay between these quantities does not have an important part in the fitting and has not introduced spurious relations in our analysis[3].

The distribution of iron line equivalent widths is shown in figure 8.9; the weighted mean value of EW is 64±4 eV (σ~77 eV), Indeed, if the iron line emission is entirely associated with the optically thick material of the disk, one would expect the line EW to correlate with the reflection fraction. Figure 8.10 shows a plot of R vs. EW for the entire sample; the Pearson test applied to these two sets of data, excluding upper limits, returns only a correlation coefficient of ~0.41 (if upper limits are considered r is 0.46), suggesting, if anything, a very weak correlation. In some cases, as observed in B3 0309+411 and 4C 74.26 for RL sources and MCG+08-11-011, 2E 1739.1-1210 and MCG-02-58-022 for RQ objects, the observed iron line EW is too small for the reflection measured: a possible explanation resides in the scatter expected in the EW values due to a variation in the iron abundance, or to a possible anisotropy of the source seed photons which might affect the observed spectrum (Petrucci et al. 2001; Merloni et al. 2006). For a given value of R, the EW could also differ according to the value of the power law photon index: up to Γ=2,

---

[3] Unless our errors on each parameter are large enough to mask any physical or systematic effect.

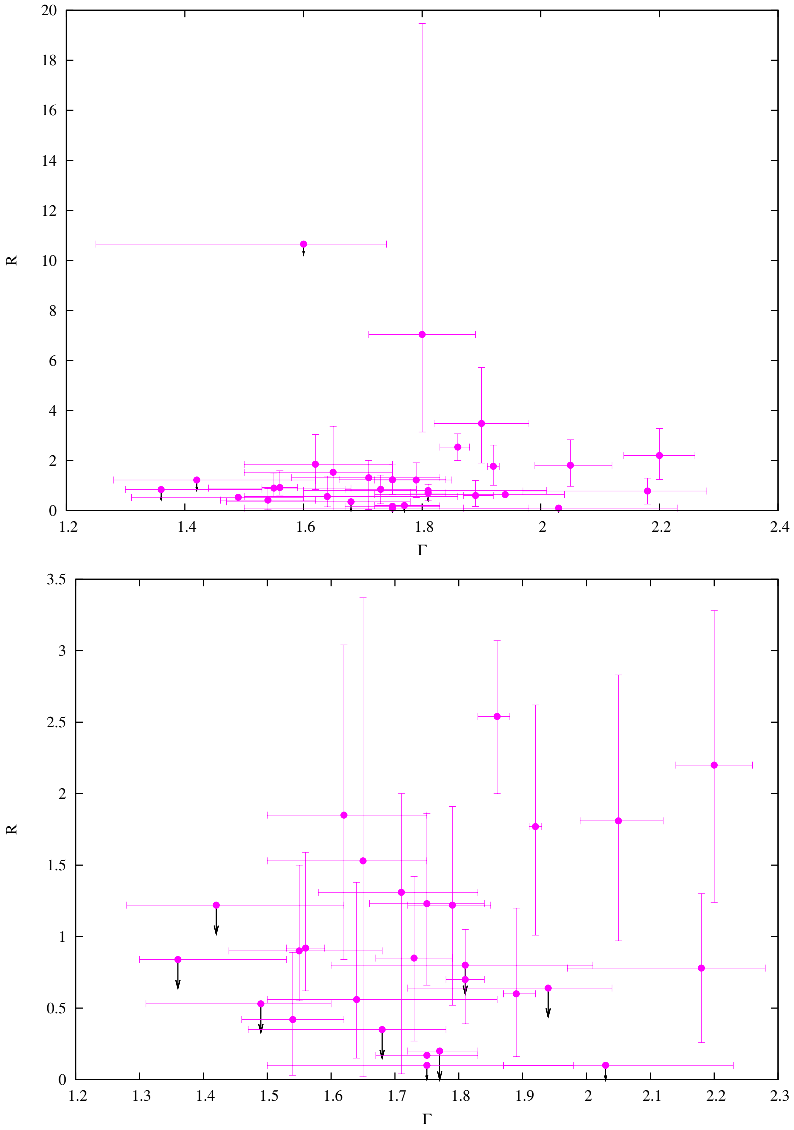

Figure 8.7: *Upper Panel*: reflection fraction vs. photon index for the AGN in our sample. *Lower Panel*: a zoom of the plot for low values of *R*. Swift J0917.2-6221, B3 0309+411 and NGC 6814 have been excluded.

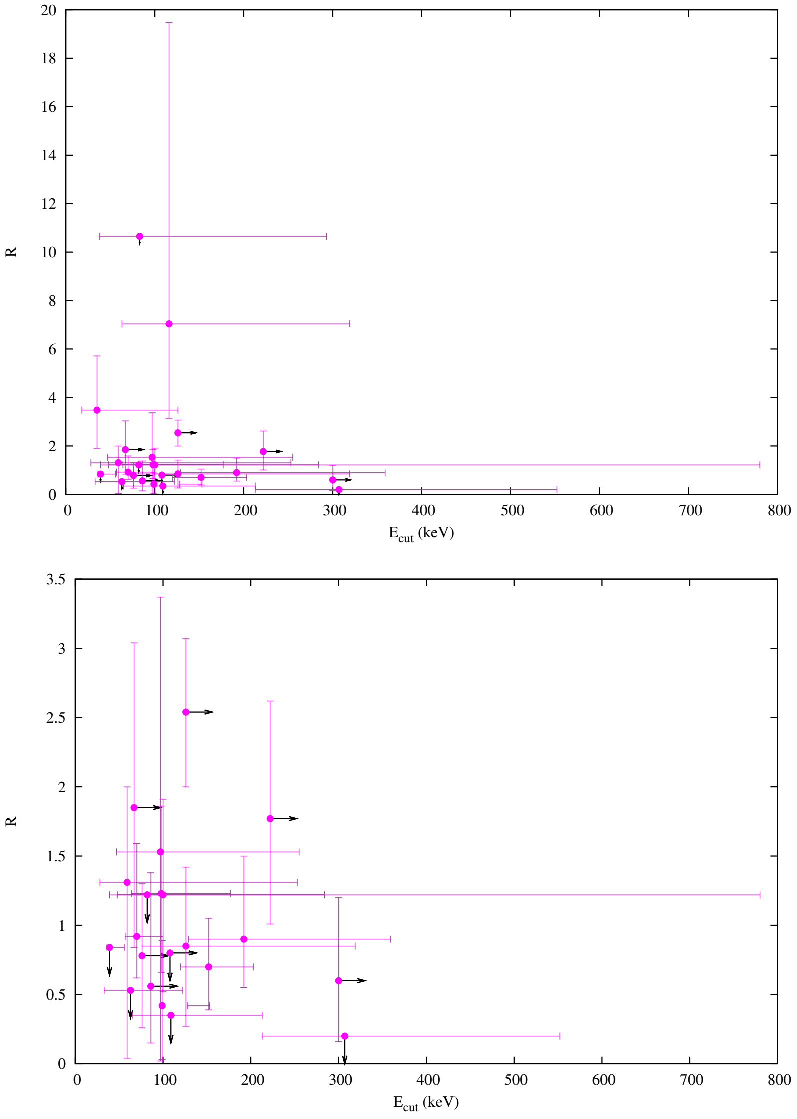

Figure 8.8: *Upper Panel*: High energy cut-off vs. the reflection fraction for the complete sample of type 1 AGN. *Lower Panel*: a zoom of the plot excluding source with very high R (NGC 6814 and Swift J0917.2-6221).

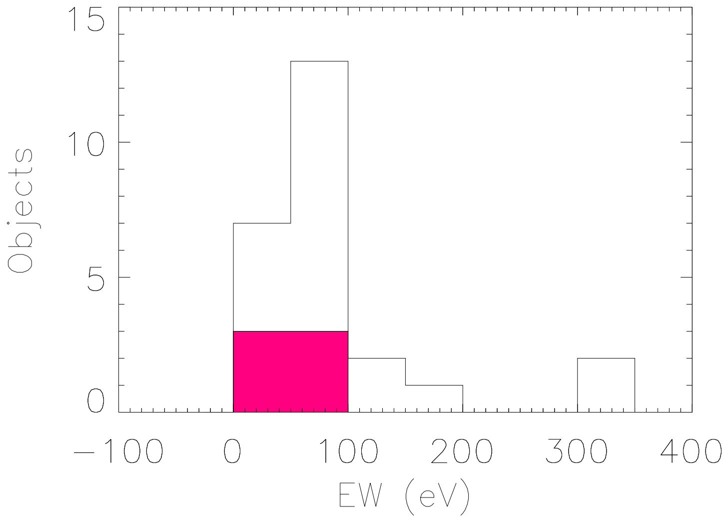

Figure 8.9: Iron Line Equivalent Width (EW) distribution. RQ sources are represented by the empty histogram, while RL sources by the filled magenta histogram

the EW decreases as the spectrum steepens, while above Γ=2 the trend is reversed (Perola et al. 2002; Mattson, Weaver & Reynolds 2007). B3 0309+411, 4C 74.26. MCG+08-11-011, 2E 1739.1-1210 and MCG-02-58-022 have all steep spectra and so a lower EW than expected on the basis of the measured *R* value is not surprising. It is also worth mentioning that in the sample presented here, we found that most sources have narrow Fe Kα lines, with only ~15% of the sample requiring a broad line. This fraction is lower than the one found by Guainazzi et al. (2006) for a sample of AGN observed by *XMM*, in which at least 25% of the objects require a broad iron line.

8.3 RL and RQ Sources

In the following the distribution of the fit parameters of Radio Loud (RL) and Radio Quiet (RQ) AGN presented in this thesis will be discussed (see table 8.1).

The power law slopes are found to be similar for both type of sources. Only one BLRG, i.e. IGR J21247+5058 (see chapter 5), is found to require complex absorption in the form of two layers partially obscuring the central emitting region; this source has also a very flat power law continuum (Γ=1.54). Up to very recently, the only other BLRG known to show a similar spectral complexity regarding absorption was 3C 445 (Sambruna et al. 2007), for which three layers of cold material were required to model the spectrum. Amongst radio quiet AGN, 4 sources (Mrk 6, 4U 1344-60, NGC 4151 and IGR J16558-

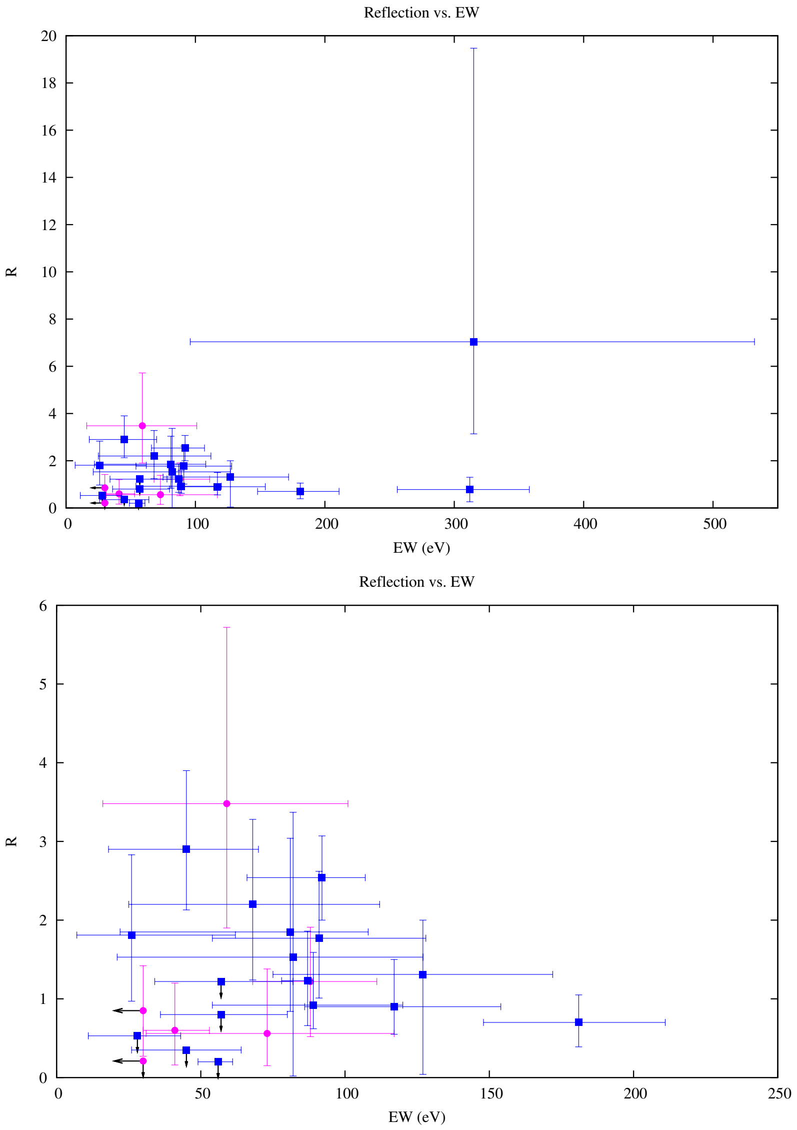

Figure 8.10: *Upper Panel*: Reflection fraction vs. Equivalent Width for RL and RQ sources. *Lower Panel*: a zoom of the plot in the region of low EW and R (NGC 6814 and MCG-06-30-015 have been excluded). Magenta circles are RL sources, blue boxes are RQ objects.

5203) are instead characterised by complex absorption, in the form of one or more layers of partially covering material, but only one, i.e. Markarian 6, exhibits a flat power law continuum (Γ=1.42). The intrinsic absorption measured in BLRG is generally small or absent ($\lesssim 2\times10^{21}$ atoms cm^{-2}), except in the cases of 3C 111 and IGR J21247+5058; in 3C 111, however, the extra absorption is probably due to intervening material between us and the source (Unger et al. 1985).

A similar result regarding absorption is also found for the radio quiet type 1 AGN analysed here: intrinsic column densities are generally small, with some of the sources not requiring any form of absorption at all. The exceptions are those sources requiring complex absorption, where the measured column densities can reach orders of 10^{22}-10^{23} atoms cm^{-2}. It is interesting to note that complex absorption is found in both populations and in similar proportions (~15% in RQ sources and ~12% in RL AGN). The analysis performed here suggests that objects with complex absorption are present within the population of broad line AGN, independent of them being radio quiet or radio loud.

As far as BLRG are concerned, Grandi et al. (2006) found evidence in their data for a correlation between absorption and radio core dominance (*CD*), with more absorbed objects showing lower *CD* values. The data presented here do not show such a trend; there is also no indication of a correlation between photon index or absorption and L_{HX}[4] using both RQ and RL objects.

As already described in the previous section, the high energy cut-off spans a wide range of values from ~30 up to ~300 keV, both for radio quiet and radio loud objects, as already found in other works on radio quiet AGN (e.g. Molina et al. 2006 and Panessa et al. 2008), showing that under this aspect the two populations behave in a similar way. For BLRG, the possibility of a correlation between the high energy cut-off and the core dominance or the L_{HX} ratio has also been explored, but no trend could be found for these parameters.

As far as the reflection fraction is concerned, in BLRG very low values for this component, typically below 1, are found, except in two cases (namely B3 0309+411 and 4C 74.26); as expected in these sources, the EW of the iron line is $\lesssim$100 eV. In radio quiet AGN, on the other hand, generally higher values (around or above 1) of this parameter are found, with some sources displaying reflection fractions higher than 2, despite the measured EW being around or below 100 eV in most cases.

As shown by the results reported here (see table 8.1) and as already observed by a number of authors (for instance Grandi et al. 2006 and Sambruna et al. 1999), the reprocessing features in BLRG tend to be, on average, quite weak with respect to their radio

---

[4] Note that L_{HX} has been defined in chapter 6 as $L_{1.4GHz}/L_{20-100keV}$

quiet counterparts. In the EW vs. reflection plot shown in figure 8.10, it is evident that radio loud AGN are more confined to a region of the plot characterised by low values of EW and to a lesser extent of *R*, whereas radio quiet objects tend to be more spread over both axis. This evidence does not seem to be related to the radio core dominance, suggesting that any dilution of the reprocessing features in RL objects, at least for those studied in this work, is not caused by the presence of a jet. Since the observed difference is not striking, an accretion flow origin for the X/gamma-ray emission is a likely explanation for the production of the reprocessing features in the RL sources studied here; this agrees well with some of them being classified as FR II sources, i.e. the BLRG most closely resembling radio quiet AGN (Evans et al. 2006). Within this scenario, it is still possible that a different geometry and/or accretion flow efficiency involving the disk provides the condition for weaker reflection components in BLRG. Alternatively, weak reflection features might be the result of reprocessing in an ionised accretion disk, as suggested by Ballantyne, Ross & Fabian (2002); this would alleviate the need for a change in accretion disk geometry and provide a more similar environment for both radio loud and radio quiet AGN.

8.4 The Complete Sample: Spectral Modelling

Determining the photon indices and cut-off energies of a large, complete sample of AGN is very important for spectral modelling. So far, models have generally focus on how to reproduce and explain the observed primary continuum. A good fraction of the proposed models ascribe the power law to the inverse Compton scattering of soft photons off hot electrons. Variations to this baseline model depend on the energy distribution of these electrons and their location in relation to the accretion disk, often a hot corona above the disk. Within this scenario, the power law photon index and high energy cut-off are directly linked to the temperature and optical depth of the Comptonising hot plasma. Knowing these two quantities can therefore provide vital information for understanding all the characteristics of the plasma near the central engine. The values of Γ and E_{cut} are linked to the Comptonising hot plasma temperature kT_e and optical depth τ, according to the relation proposed by Petrucci et al. (2001):

$$\Gamma - 1 \simeq \left\{ \frac{9}{4} + \frac{m_e c^2}{kT_e \tau (1 + \tau/3)} \right\}^{1/2} - \frac{3}{2} \tag{8.1}$$

The plasma temperature kT_e is estimated as $kT_e = E_{cut}/2$ if $\tau \lesssim 1$ and $kT_e = E_{cut}/3$ if $\tau \gg 1$. In our sample the mean value of E_{cut} is ~104 keV, with most objects falling within the range 50-150 keV; thus the observed range of E$_{cut}$ implies a range of plasma temperatures from 20 to 80 keV. Equation 8.1 (solved for both low and high values of τ and E$_{cut}$ and assuming our average value of Γ=1.86) has therefore acceptable solutions for τ in the range 2 to 5. These results are in good agreement with what previously found for a small sample of Seyfert 1 galaxies studied by Petrucci et al. (2000) and indicate that the plasma has a typical temperature of (50±30) keV and is not too thick (τ<5). Available models should be able to explain and cover the observed range of values.

8.5 The Complete Sample: Cosmic Diffuse X-ray Background

A fundamental input parameter for CXB synthesis models is the broad-band spectral shape of type 1 AGN. The main spectral component is, as we have found, a power law with an exponential roll over at high energies. The average slope of the power law component is generally taken to be Γ = 1.9, mainly from observations performed at low energies or, over a broad band, by *BeppoSAX*; there seems to be no significant redshift dependence of Γ up to high value of z. Up to now the dispersion around this mean photon index value has generally been neglected (σ=0), but recently Gilli et al. (2007) have shown that the modelled CXB spectrum can be hardened, especially near its 30 keV peak, by accounting for a dispersion in photon indices. Choosing a σ of 0.2 (for Γ=1.9) increases the 30 keV flux by about 16%, but still it under predicts the observed CXB; a larger dispersion would provide a better match with the CXB data below 10 keV but excess background flux above 10 keV. Clearly the dispersion of Γ values becomes an important observational parameter to measure. Since observations above 10 keV have been less frequent up to now, due to the lack of instrumental sensitivity, the cut-off energy is, together with the reflection bump, a parameter poorly constrained. While it is well known that an exponential cut-off must be present around a few hundreds of keV, in order not to violate the present level of the CXB above 100 keV, values of 200 keV and up to 500 keV have been used in the past. This was mainly based on *BeppoSAX* observations which indicate a relatively large spread in E$_c$ from about 50 keV up to about 500 keV (Perola et al. 2002; Dadina 2008). A better constraint on E$_c$ is therefore a very important result for which modellers of CXB are waiting.

The characteristic hard slope and the 40 keV break of the CXB indicate, besides the existence of heavily absorbed objects, the presence of at least some reflection in AGN spectral energy distributions (SEDs), and CXB synthesis models typically use a reflection fraction R ~ 1 (Gilli et al. 2007; Gandhi et al. 2007). Clearly the higher the reflection, the less important becomes the contribution of Compton thick AGN, which are being found in small percentage in the local Universe both by *Swift* and *INTEGRAL* (Ajello et al. 2008; Bassani et al. 2006).

Making the above choices of parameters and carefully adjusting them by comparing the model predictions with the really measured CXB spectrum, it is possible to reproduce a self-consistent picture, where the CXB is simply due to the integrated emission of absorbed and unabsorbed AGN; it is also evident that within this delicate interplay between parameters, a small variation of one of the parameter can violate one or more of the observational constraints. A detailed modelling of the CXB using results reported here is beyond the scope of the present thesis, but clearly our data, which focussed for the first time on a complete sample of AGN, are able to provide key information on the AGN average continuum slope and dispersion and a better definition of the other two parameters used (R and E_c). We confirm that the primary continuum is a power law with slope in the range 1.8-1.9 and having a dispersion of 0.2, while the reflection fraction is around 1. All these values have been adopted in the recent work of Gilli et al. (2007), where however a higher cut-off energy (200 keV) than obtained in this analysis has been assumed. This choice of E_c is basically driven by the intensity and the shape of the CXB spectrum above the peak, which cannot be exceeded. A higher cut-off energy is not allowed (if the mean and dispersion of the photon index distribution remain 1.9 and 0.2 respectively) because in this case the contribution of unobscured and Compton-thin AGN saturates the CXB emission at 100 keV and underestimates the 30 keV peak by about 20%. When trying to add Compton-thick sources to fit the 30 keV emission, the CXB at 100 keV is then overestimated. A global fit to the CXB spectrum with higher values of E_c, for example 300 keV, can still be achieved but, in order to reduce the model prediction at 100 keV with respect to that at 30 keV, one has to assume a null dispersion in the photon index distribution, which is at variance with what observed. It was therefore concluded by Gilli and co-workers that the average cut-off energy cannot be higher than 200 keV; in fact a lower value, as we observe, would violate some of the constraints discussed above. On the basis of what has been discussed, we therefore believe that the value of Γ=1.86 with a dispersion of 0.2 and a cut-off energy with a narrow range of values around 100 keV could provide a self-consistent modelling of the CXB. The implementation of the information provided in this thesis is clearly very important for CXB synthesis models and represents the following step of this work.

8.6 Conclusions

This thesis presented, for the first time, the broad-band spectral analysis of a complete sample of type 1 AGN, detected by *INTEGRAL* in the hard X-ray band. This is a major step forward in the analysis of the spectral features of AGN, since previous studies mainly focussed on small samples of X-ray bright type AGN.

In chapter 5, the peculiar Broad Line Radio Galaxy (BLRG) IGR J21247+5058 has been analysed in depth. Archival radio observations have shown that this source, detected for the first time at high energies by *INTEGRAL*, is a quite powerful radio source, with two lobes extending from the central nucleus. Combined X-ray (*XMM* and *XRT*) and *INTEGRAL* broad-band spectral analysis has also shown the very peculiar nature of IGR J21247+5058. The source, in fact, is characterised by complex absorption in the form of two layers of cold material partially obscuring the central nucleus, a peculiarity this one that has so far been observed only in another Broad Line Radio Galaxy, i.e. 4C 445 (Sambruna et al. 2007).

In chapter 6, a subsample of seven BLRG has been investigated. Broad-band spectra, obtained by combining *Chandra, XMM* and *XRT* data with *INTEGRAL* data, have been analysed in order to understand the differences, if any, between BLRG and radio quiet AGN. Our analysis showed that the reprocessing features (i.e. the reflection component and the iron line equivalent width) tend to be, on average, quite weak in BLRG with respect to their radio quiet counterparts. This difference is not, however, striking, suggesting that jet emission, often taken as the main difference between RL and RQ sources, is not responsible for the observed differences. An accretion flow origin for the X/gamma-ray emission is the more likely explanation for the production of the reprocessing features in the RL sources studied here.

In chapter 7, the broad-band spectral analysis on the remaining radio quiet type 1 sources has been performed. Also among radio quiet sources we have found four AGN requiring complex absorption, in the form of one or more layers of obscuring material, suggesting that this characteristic may be common in the radio loud and radio quiet populations.

From a general point of view, the results presented in this thesis may be summerised as follows:

- Absorbing column densities are generally small or absent (both for RL and RQ sources), except in those cases where complex absorption is required.
- The average photon index is 1.86, close to the generally accepted canonical value of 1.9.

- The mean high energy cut-off is 104 keV, lower than the values found in other works on broad-band spectra of Seyfert 1 galaxies. However, the values of cut-off energy span a wide range from 50 keV up to 150 keV.

- The average reflection fraction is close to 1, in line with previous measurements and with the assumed value for synthesis models of the CXB.

- The iron lines detected in our sources tend to be narrow, with only 15% of the sample requiring a broad Fe line. The EW are generally below or around 100 eV, in general agreement with the measured reflection fractions. Some sources, however, display steeper power law slopes and lower than expected values of the EW. This could be explained, for a given value of R, considering the value of the power law photon index: up to Γ=2, the EW decreases as the spectrum steepens, while above Γ=2 the trend is reversed, as observed in our sources.

- The average cut-off energy and spectral index provide an estimate on the temperature and optical depth of the plasma where the hard X-ray emission originates. The temperature is about 50 keV and the optical depth varies in the range 2-5, implying a not too thick Comptonising plasma.

- Finally, our result could provide a new self-consistent set of parameters for synthesis models of the Cosmic Diffuse X-ray Background.

Appendix A

Best fit plots for type 1 radio loud sources.

In the following the best fit plots for the type 1 radio loud sources analysed in chapter 6 are shown.

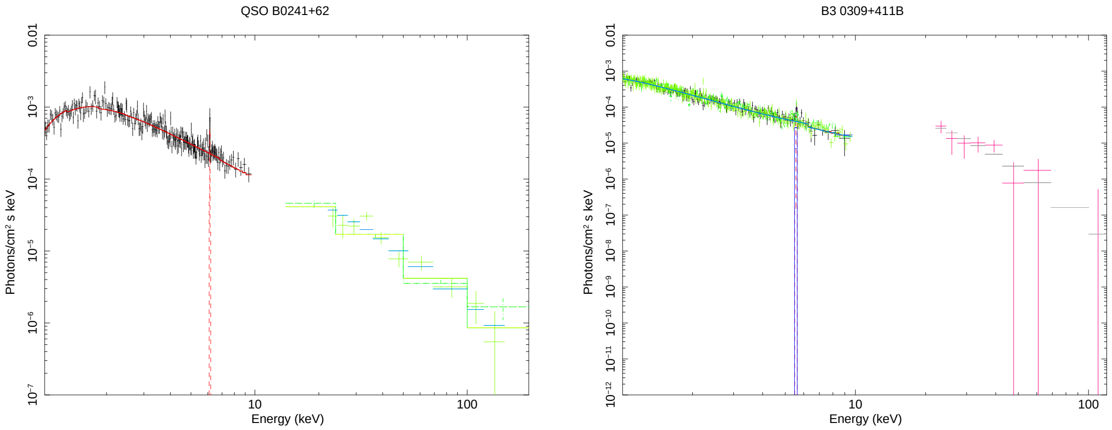

Figure A.1: Best fit plots for QSO B0241+62 (left panel) and B3 0309+411 (right panel). The model is a cut-off power law absorbed both by Galactic and intrinsic column density for QSO B0241+62 and by Galactic column density only for B3 0309+411, reflected by neutral material plus a narrow Gaussian component describing the iron line.

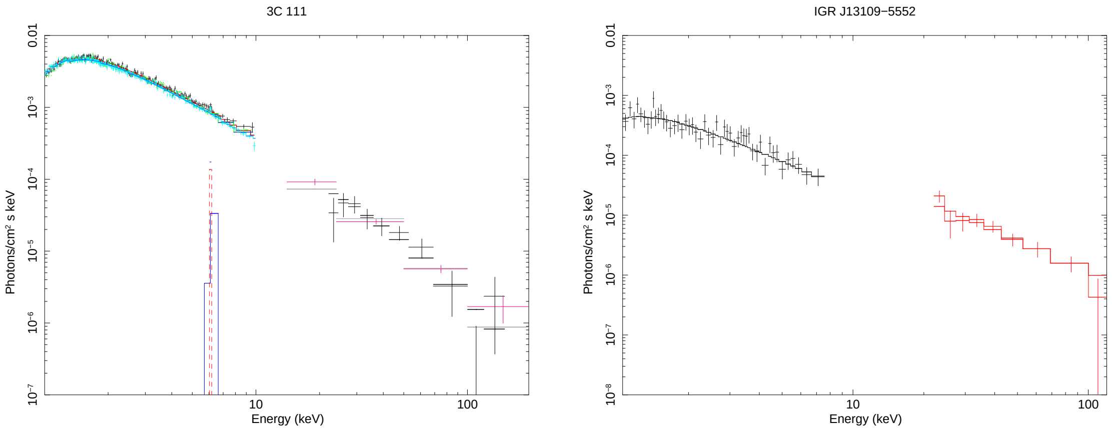

Figure A.2: Best fit plots for 3C 111 (left panel) and IGR J13109-5552 (right panel). 3C 111 is best described by a cut-off power law absorbed by Galactic and intrinsic column densities reflected by neutral material. IGR J13109-5552 is best modelled by a simple power law absorbed both by Galactic and intrinsic column densities.

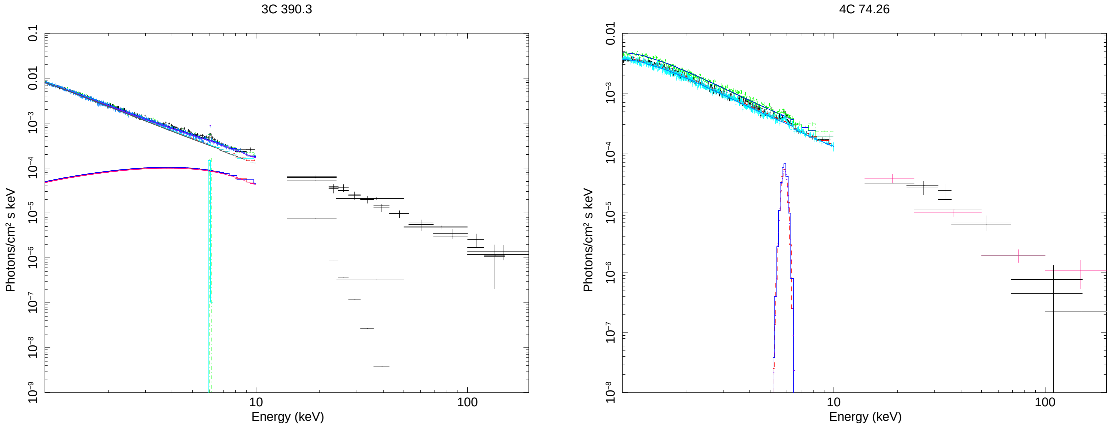

Figure A.3: Best fit plots for 3C 390.3 (right panel) and 4C 74.26 (left panel). 3C 390.3 is best described by an exponentially cut-off power law reflected by cold material and absorbed only by Galactic column density plus a blackbody component to model the soft excess, plus a narrow Gaussian component describing the iron line. 4C 74.26 is modelled with an exponentially cut-off power law reflected by neutral material absorbed by Galactic and intrinsic column densities plus a broad Gaussian component describing the iron line.

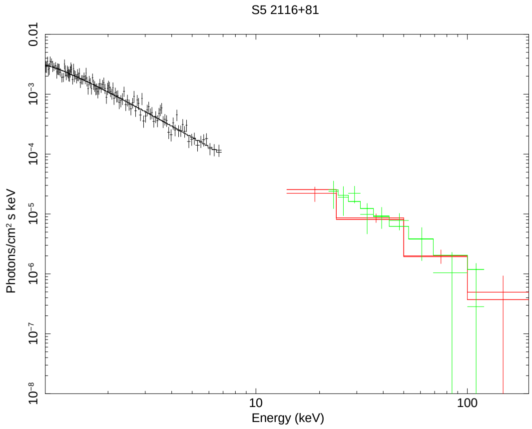

Figure A.4: Best fit plots for S5 2116+81. The best fit model is a simple power law, absorbed both by Galactic and intrinsic column densities.

Appendix B

Best fit plots for type 1 radio quiet sources.

In the following the best fit plots for the type 1 radio quiet sources analysed in chapter 7 are shown.

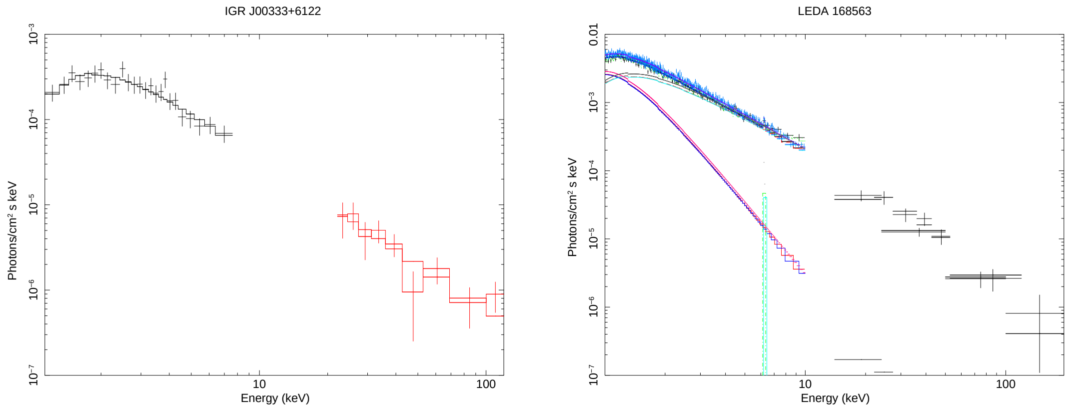

Figure B.1: Best fit plots for IGR J00333+6122 (left panel) and LEDA 168563 (right panel). The model employed is a simple power law absorbed by Galactic and intrinsic column densities for IGR J00333+6122 and a cut-off power law reflected from neutral material plus a second power law to model excess counts at low energies and a narrow Gaussian component for LEDA 168563.

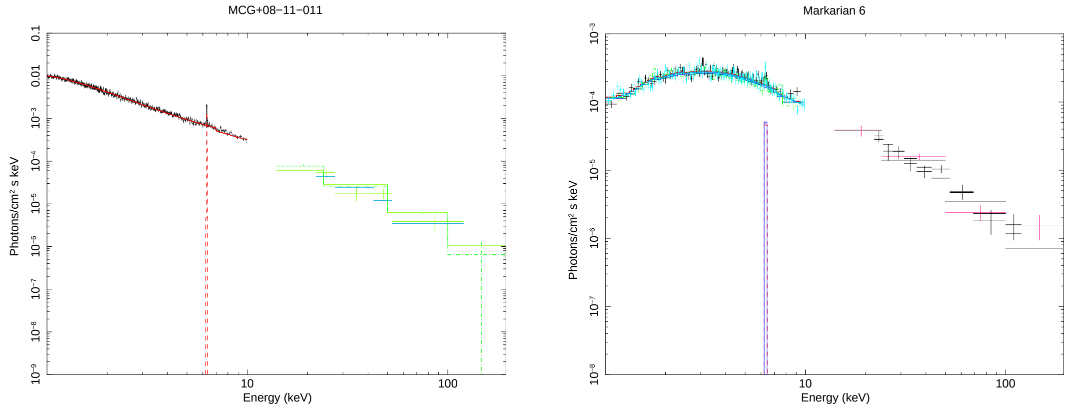

Figure B.2: Best fit plots for MCG+08-11-011 (left panel) and Mrk 6 (right panel). The model is cut-off power law reflected from neutral material and absorbed by Galactic column density plus a narrow Gaussian line for MCG+08-11-011. For Mrk 6 the model is a cut-off power law absorbed by two layers of cold material partially obscuring the central source plus a narrow Gaussian line.

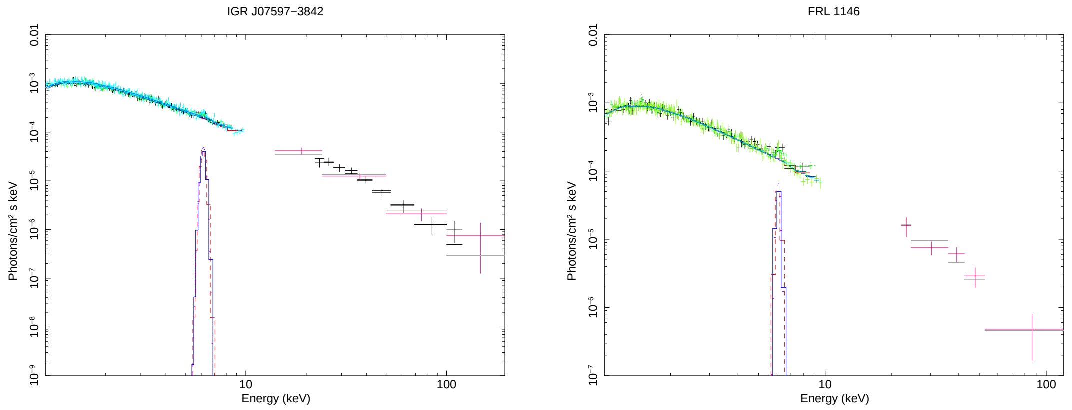

Figure B.3: Best fit plots for IGR J07597-3842 (left panel) and FRL 1146 (right panel). The model is a cut-off power law reflected from neutral material and absorbed by Galactic and intrinsic (in the case of FRL 1146) column densities plus a broad Gaussian component.

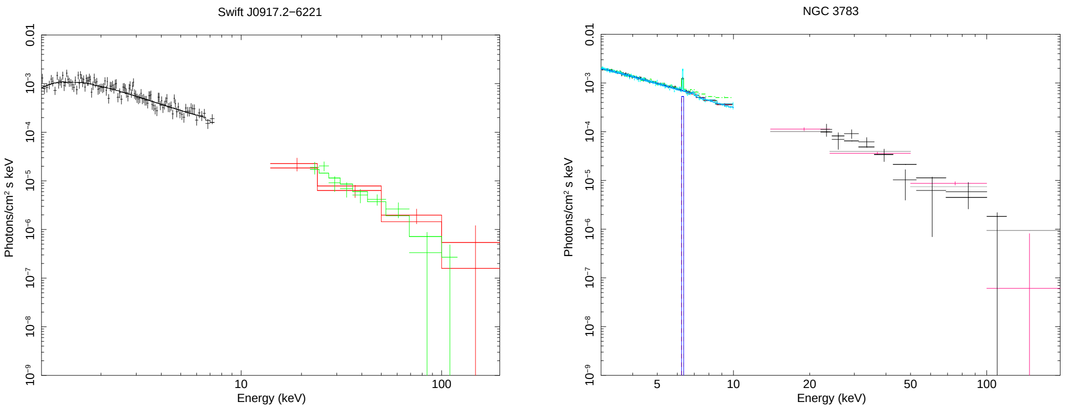

Figure B.4: Best fit plots for Swift J0917.2-6221 (left panel) and NGC 3783 (right panel). The model is a cut-off power law reflected from neutral material and absorbed by Galactic and intrinsic column densities plus a narrow Gaussian component in the case of NGC 3783.

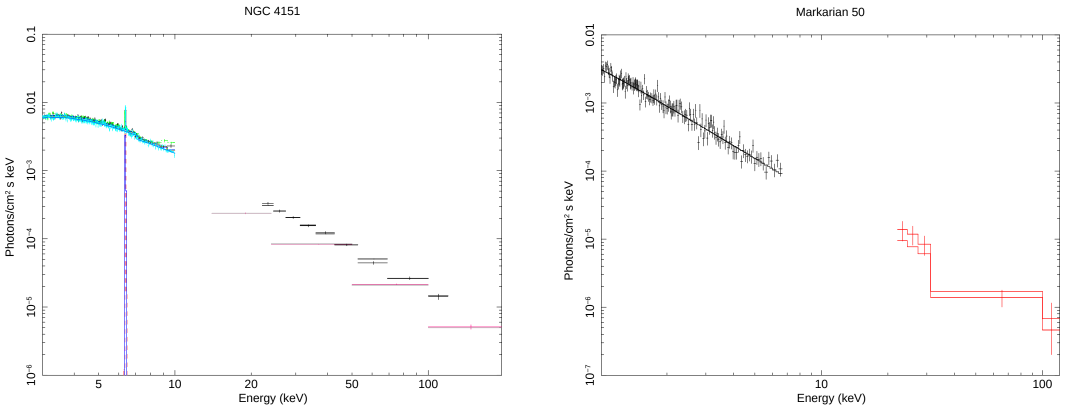

Figure B.5: Best fit plots for NGC 4151 (left panel) and Mrk 50 (right panel). The model employed for NGC 4151 is cut-off power law reflected from neutral material and absorbed by Galactic column density and by two layers, one totally and the other partially covering the central source, of cold material plus a narrow Gaussian line. For Mrk 50 the model is a simple power law absorbed both by Galactic and intrinsic column densities.

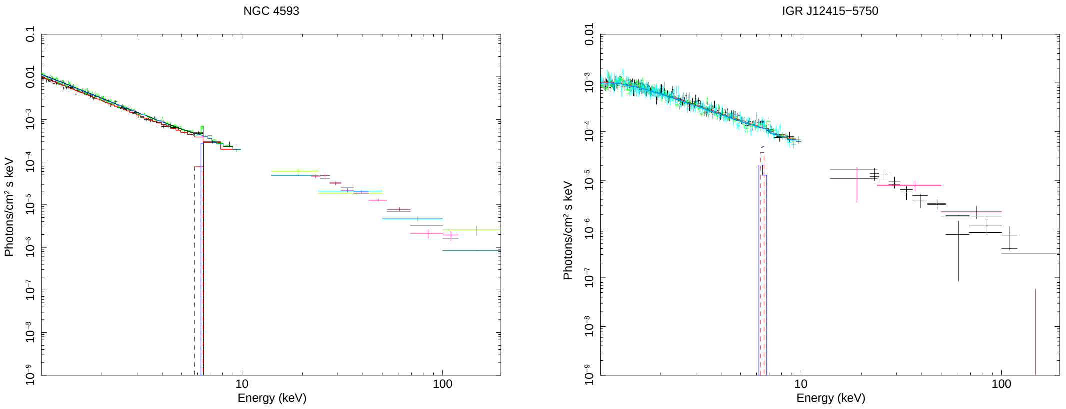

Figure B.6: Best fit plots for NGC 4593 (left panel) and IGR J12415-5552 (right panel). The model employed is a cut-off power law reflected from neutral material and absorbed only by Galactic column density plus a narrow Gaussian component.

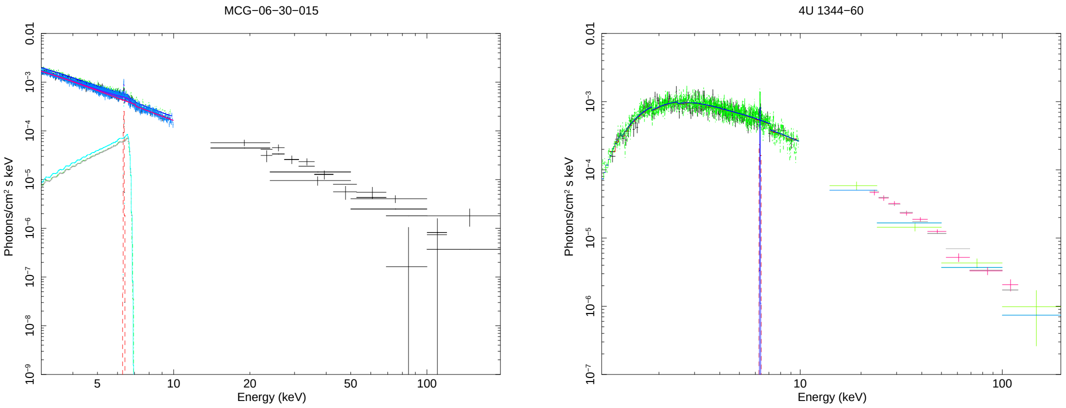

Figure B.7: Best fit plots for MCG-06-30-015 (left panel) and 4U 1344-60 (right panel). The model employed for MCG-06-30-015 is a cut-off power law reflecte from neutral material absorbed both by Galactic and intrinsic couln densities plus a narrow Gaussian component and a `LAOR` model to parametrise the relativistic iron line. The model for 4U 1344-60 is a cut-off power law reflected from neutral material and absorbed by three layers of material, one totally and two partially covering the central source, plus a narrow Gaussian component.

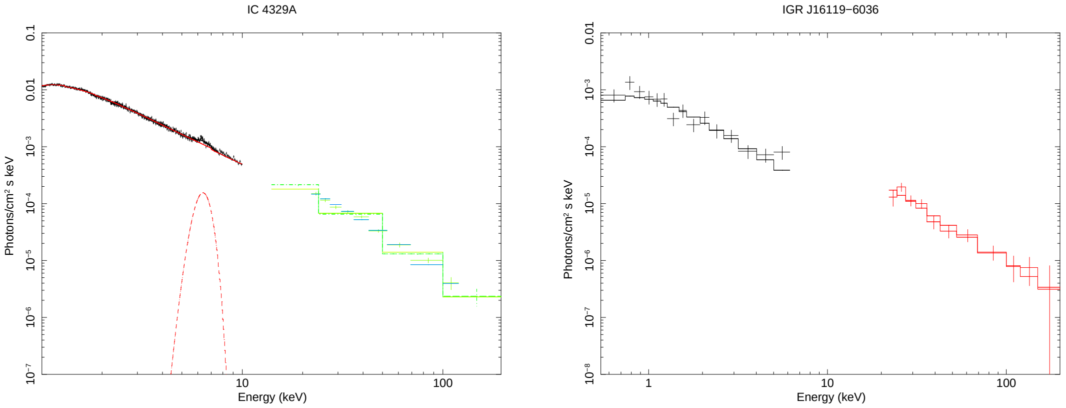

Figure B.8: Best fit plots for IC 4329A (left panel) and IGR J16119-6036 (right panel). The model used for IC 4329A is a cut-off power law reflected from neutral material and absorbed by Galactic and intrinsic column densities plus a broad Gaussian component. For IGR J16119-6036 the model used is a simple power law absorbed only by Galactic column density.

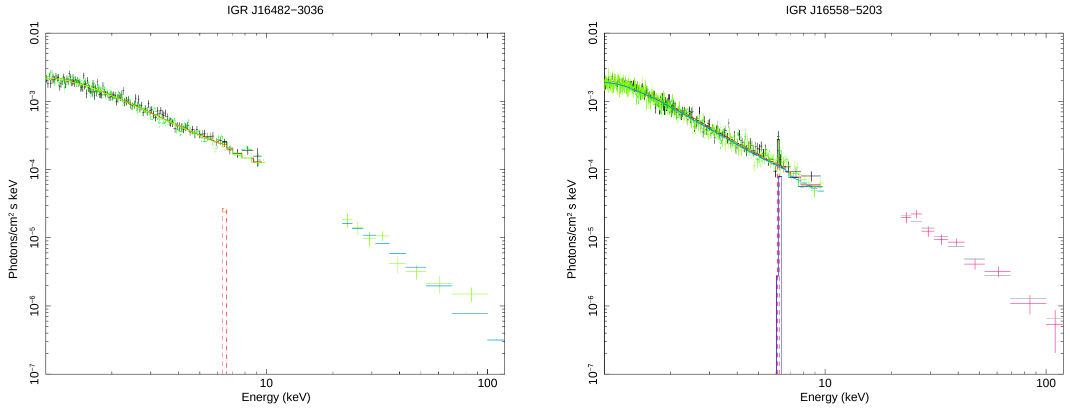

Figure B.9: Best fit plots for IGR J16482-3036 (left panel) and IGR J16558-5203 (right panel). The model employed for IGR j16482-3036 is a cut-off power law reflected from neutral material and absorbed both by Galactic and intrinsic column densities plus a narrow Gaussian component. For IGR J16558-5203 the model is again a cut-off power law reflected from neutral material and absorbed by a partially covering layer of cold material plus a narrow Gaussian line.

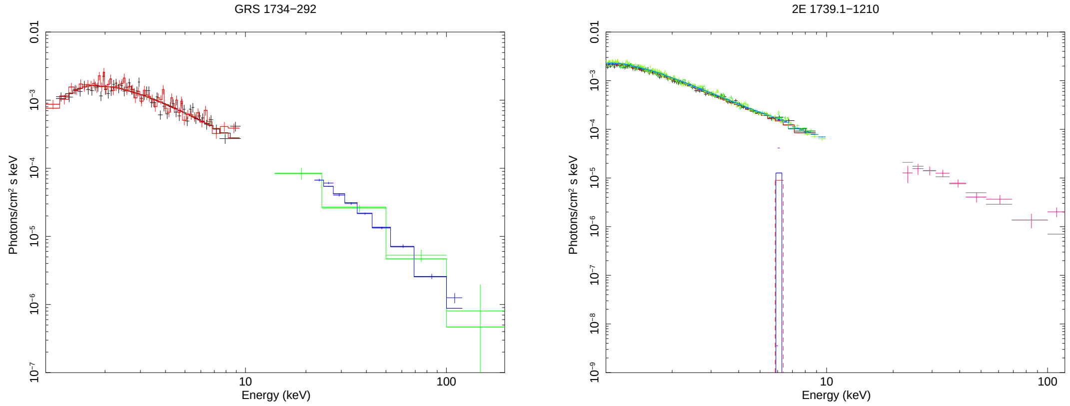

Figure B.10: Best fit plots for GRS 1734-292 (left panel) and 2E 1739.1-1210 (right panel). The model is a cut-off power law reflected from neutral material and absorbed by Galactic and intrinsic column densities plus, in the case of 2E 1739.1-1210, a narrow Gaussian component.

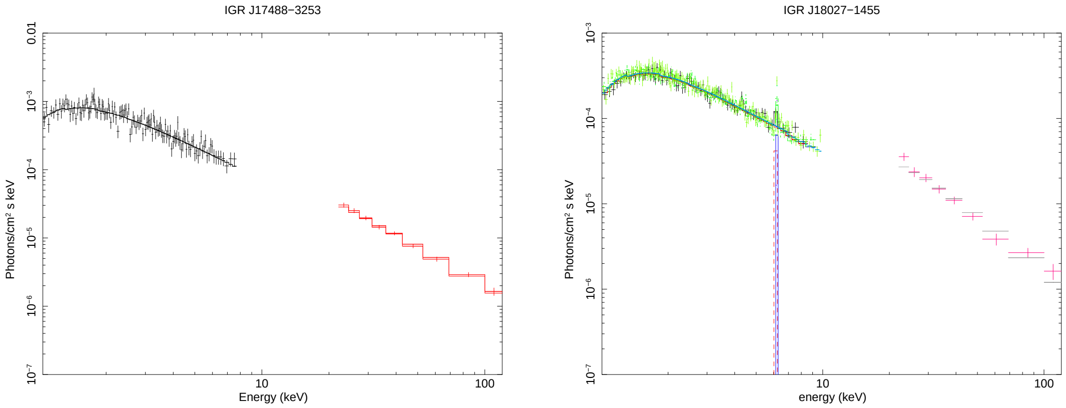

Figure B.11: Best fit plots for IGR J17488-3253 (left panel) and IGR J18027-1455 (right panel). The model used for IGR J17488-3253 is a cut-off power law absorbed both by Galactic and intrinsic column densities. For IGR J18027-1455 the model is a cut-off power law reflected from neutral material and absorbed both by Galactic and intrinsic column densities plus a narrow Gaussian component.

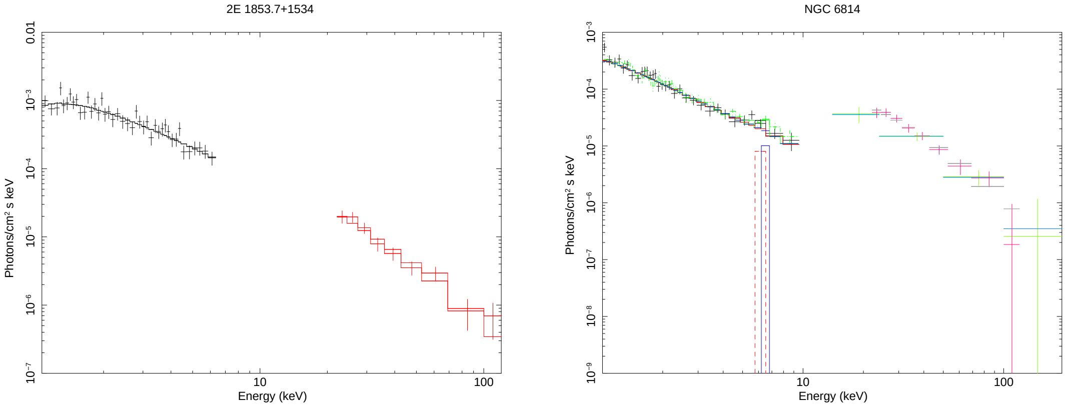

Figure B.12: Best fit plots for 2E 1853.7+1534 (left panel) and NGC 6814 (right panel). The model employed for 2E 1853.7+1534 is a cut-off power law absorbed by Galactic and intrinsic column densities. For NGC 6814 the model is a cut-off power law reflected from neutral material absorbed by Galactic column density plus a narrow Gaussian component.

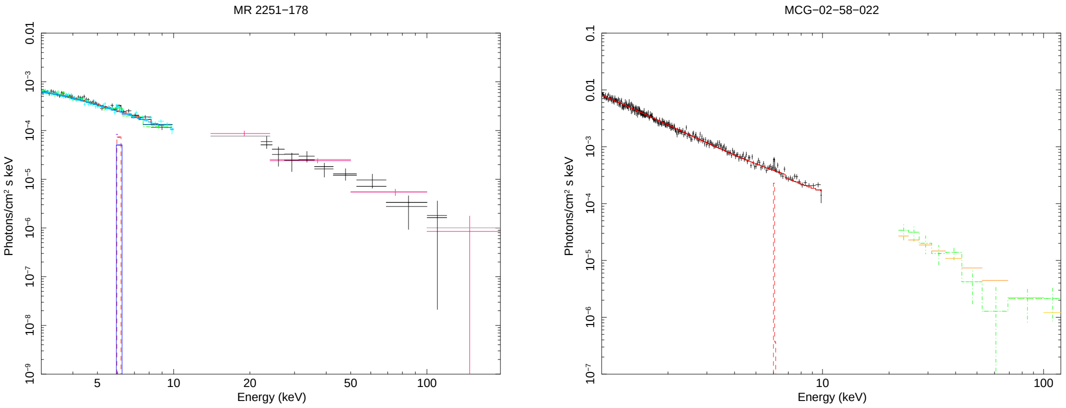

Figure B.13: Best fit plots for MR 2251-178 (left panel) and MCG-02-58-022 (right panel). The model employed is a cut-off power law reflected from neutral material absorbed by Galactic and intrisic (in the case of MR 2251-178) column densities plus a narrow Gaussian component.

Bibliography

Ajello M., Rau A., Greiner J. et al. 2008, ApJ, 673, 96

Anderson J.M. & Ulvestad J.S. 2005, ApJ, 627, 674

Antonucci R.R. & Miller J.S. 1985, ApJ, 297, 621

Arnaud K. A. 1996, Astronomical Data Analysis Software and Systems V, eds Jacoby G. and Barnes J., p.17, ASP Conf Series vol. 101

Avni Y. & Bahcall J.N. 1980, ApJ, 235, 694

Ballantyne, D. R., Ross, R. R., Fabian, A. C. 2002, MNRAS, 332, 45

Ballantyne D.R. 2005, MNRAS, 362, 1183

Ballantyne D.R & Fabian A.C. 2005, ApJ, 622, 97

Barger A.J., Cowie L.L., Mushotzky R.F. et al. 2005, AJ, 129, 578

Barthelmy S.D. 2004, SPIE, 5165, 169

Barvainis R., Lehr J., Birkinshaw M. et al. 2005, ApJ, 618, 108

Bassani L., Malizia A., Stephen J.B. et al. 2004, ESAP, 552, 139

Bassani L., Molina, M., Malizia A. et al. 2006, ApJ, 636, 65

Baumgartner W., Tueller J., Mushotzky R. et al. 2008, ATel 1429

Beckmann V., Barthelmy S.D., Courvoisier T.J.-L. et al. 2007, A&A, 475, 827

Bianchi S., Matt G., Balestra I. et al. 2004, A&A, 422, 65

Bird A. J., Barlow E. J., Bassani L. et al. 2004, ApJ 607, 33

Bird, A.J., Barlow E.J., Bassani L. et al. 2006, ApJ, 636, 765

Bird A. J., Malizia A., Bazzano A. et al. 2007, ApJS, 170, 175

Blustin A.J., Branduardi-Raymont G., Behar E. et al. 2002, A&A, 392, 453

Branduardi-Raymont G., Sako M., Kahn S.M. et al. 2001, A&A, 365, 162

Brinkman B.C., Gunsing T., Kaastra J.S. et al. 2000, SPIE, 4012, 81

Burrows D.N., Hill J.E., Nousek J.A. et al. 2004, SPIE, 5165, 190

Cappi M., Matsuoka M., Comastri A. et al. 1997, A&A, 325, 954

Cappi M., Panessa F., Bassani L. et al. 2006, A&A, 446, 459

Clavel J., Wamsteker W., Glass I.S. 1989, ApJ, 337, 236

Comastri A., Setti G., Zamorani G., Hasinger G. 1995, A&A, 296, 1

Comastri A., Gilli R., Hasinger G. 2006 invited talk at the meeting“Gamma Wave 2005”, Bonifacio, September 2005. To be published in “Experimental Astronomy”

Contini M & Viegas S.M. 2000, ApJ, 535, 721

Dadina M. 2007, A&A, 461, 1209

Dadina M. 2008, A&A, 485, 417

de Bruyn A.G. 1989, A&A, 226L, 13

Deluit S. & Courvoisier T. J.-L. 2003, A&A, 399, 77

De Rosa A., Piro L., Fiore F. et al. 2002, A&A, 387, 838

De Rosa A., Piro L., Perola G.C. et al. 2007, A&A, 463, 903

De Rosa A., Bassani L., Ubertini P. et al. 2008, A&A, 483, 749

Dickey J.M. & Lockman F.J. 1990, ARA&A, 28, 215

Dietrich M., Peterson B.M., Albrecht P. et al. 1998, ApJ Suppl. Ser. 115, 185

Done C., Mulchaey J.S., Mushotzky R.F. et al., 1992, ApJ, 395, 275

Efstathiou A. & Rowan-Robinson M. 2001 in proceedings of “QSO hosts and their environments”ed. Marqéz I., Masegosa J. et al. Kluver Academic Plenum Publishers xvii, p.376

Elitzur M. & Shlosman I. 2006, ApJL, 648, 101

Elitzur M. 2008, NewAR, 52, 274

Elvis M., Wilkes B.J., McDowell J.C. et al. 1994, ApJS, 95, 1

Evans D.A., Worral D.M., Hardcastle M.J. et al. 2006, ApJ, 642, 96

Fabian A.C., Iwasawa K., Reynolds C.S. & Young A.J. 2000, PASP, 112, 1145

Fabian A.C., Vaughan S., Nandra K. et al. 2002, MNRAS, 335, 7

Fan J.H. & Zhang J.S. 2003, A&A, 407, 899

Fiore F., Pellegrini S., Matt G. et al. 2001, ApJ, 556, 150 357

Gandhi P., Fabian A.C., Suebsuwong T. et al. 2007, MNRAS, 382, 1005

Garmine G.P., Bautz M.W., Ford P.G. et al. 2003, SPIE, 4851, 28

Gehrels N., Chincarini G., Giommi P. et al. 2004, ApJ, 611, 1005

George I.M. & Fabian A.C. 1991, MNRAS, 249, 352

George I.M., Turner T.J., Yaqoob T. et al. 2000, ApJ, 531, 52

Ghisellini G., Haardt F. & Matt G. 1994, ApJ, 432, 95

Gilli R., Comastri A., Hasinger G. 2007, A&A, 463, 79

Giovannini G., Feretti L., Gregorini L. et al. 1988 A&A, 199, 73

Giovannini G., Cotton W.D., Feretti L. et al. 2001, ApJL, 522, 97

Gliozzi M., Sambruna R.M., Eracleous M. 2003, ApJ, 584, 176

Goldwurm A., David P., Fochini l: et al. 2003, A&A, 411, 223

Gondoin P., Aschenback B.R., Bejersbergen M.W. et al. 1998, SPIE, 3444, 278

Granato G.L. & Danese L. 1994, MNRAS, 268, 235

Grandi P., Guainazzi M., Haardt F. et al. 1999, A&A, 343, 33

Grandi P., Urry C.M., Maraschi L. et al. 2000, AdSpR, 25, 485

Grandi P., Malaguti G., Fiocchi M. 2006, ApJ, 642, 113

Greenhill J.R., Moran J.M, Greenhill L.J. et al. 1996, ASPC, 103, 193

Gros A., Goldwurm A., Cadolle-Belle M. et al. 2003, A&A, 411, 179

Guainazzi M., Perola G.C., Matt G. et al. 1999, A&A, 346, 407

Guainazzi M., Bianchi S., Dovčiak M. 2006, AN, 327, 1032

Guilbert P.W. & Rees M.J. 1988, MNRAS, 233, 475

Haardt F. & Maraschi L. 1993, ApJ, 413, 507

Haardt F., Maraschi L. & Ghisellini G. 1994, ApJ, 449, 13

Hardcastle M.J. & Croston J.H. 2005, MNRAS, 363, 649

Heckman T., Krolik J.H., Hewer G. et al. 1995, ApJ, 452, 549

Hickox R.C. & Markevitch M. 2006, ApJ, 645, 95

Hill J.E., Burrows D. N. Nousek J.A. et al. 2004, SPIE, 5165, 217

Ho L.C. & Ulvestad J.S. 2001, ApJS, 133, 77

Ho L.C. & Peng C.Y. 2001, ApJ,555,650

Ishwara-Chandra C.H. & Saikia D.J. 1999, MNRAS, 309, 100

Iwasawa K. & Taniguchi Y. 1993, ApJ, 413, 15

Johnson W.N., Zdziarski A.A., Madejski G.M. et al. 1997, AIPC, 410, 283

Kadler M., Ros E., Kerp J., Kovalev Y.Y., Zensus J.A. 2004, Proc. 7th European VLBI Network Symposium Edited by R. Bachiller, F. Colomer, J.-F.; Desmurs, and P. de Vicente, 23

Kaspi S., Brandt W.N., Netzer H. et al. 2001, ApJ, 554, 216

Kellerman K.I., Sramek R., Schimidt M. et al. 1989, AJ, 98,1195

Kharb P., O'Dea C.P., Baum S.A. et al. 2006, ApJ, 652, 177

Kinkhabwala A., Sako M., Behar E. et al. 2002, ApJ, 575, 732

Kormendy J. & Richstone D. 1995, ARA&A, 33, 581

Krolik J.H. & Kriss G.A. 1995, ApJ, 447, 512

Krolik J.H. 1998, ApJ, 498, 13

Kukula M.J., Pedlar A., Baum S.A. & O’Dea C.P. 1995, MNRAS, 276, 1262

Labanti C., Di Cocco G., Ferro G. et al. 2003, A&A, 411, 149

Landi R., De Rosa A., Dean A. J. et al. 2007, MNRAS, 380, 926

Larsson J., Fabian A.C., Ballantyne D.R & Miniutti G. 2008, MNRAS, 388, 1037

Lebrun F., Leray J.P., Lavocat P. et al. 2003, A&A, 411, 141

Levenson N.A., Krolik J.H., Życki P.T. et al. 2002, ApJ, 573, 81

Levine A.M., Lang F.L., Lewin W.H.G. et al. 1984, ApJS, 54, 581

Lewis K.T., Eracleous M., Gliozzi M. et al. 2005, ApJ, 622, 816

Liu F.K. & Zhang H. 2002, A&A, 381, 757

Lund N., Brandt S., Budtz-Jorgensen C. et al. 2003, A&A, 411, 231

Maccacaro T., Perola G.C. & Elvis M. 1982, ApJ, 257, 47

Maiolino R. & Rieke G.H. 1995, ApJ, 454, 95

Maiolino R., Salvati M., Marconi A. & Antonucci R.R. 2001a, A&A, 375, 25

Maiolino R., Marconi A., Salvati M. et al. 2001b, A&A, 365, 28

Malizia A., Bassani L., Capalbi M. et al. 2003a, A&A, 406, 105

Malizia A., Bassani L., Stephen J.B. et al. 2003b, ApJ, 589, 17

Malizia A., Bassani L., Bird A.J. et al. 2008, MNRAS, 389, 1360

Mantovani F., Nanni M., Salter C. J. et al. 1982, A&A, 105, 176

Manzo G., Giarrusso S., Santangelo A. et al. 1997, A&AS, 122, 341

Maraschi L. & Haardt F. 1997, ASPC, 121, 101

Market T.H., Canizares C.R., Dewey D. et al. 1994, SPIE, 2280, 168

Markowitz A., Reeves J.N., Braito V. 2006, ApJ, 646, 783

Markwardt C. B., Tueller J., Skinner G. K. et al. 2005, ApJ, 633, 77

Masetti N., Palazzi E., Bassani L. et al. 2004, A&A, 426, 41

Masetti N., Malizia A., Dean A.J. et al. 2006, ATel 957

Masetti N., Landi R., Pretorius M.L. et al. 2007, A&A 470, 331

Masetti N., Mason E., Morelli L. et al. 2008, A&A, 482, 113

Mas-Hesse M., Gimenéz A., Culhane L. et al. 2003, A&A, 411, 261

Matt G., Perola G.C. & Piro L. 1991, A&A, 247, 25

Matt G. 2000, A&A, 355, 31

Matt G. 2001, AIPC, 599, 209

Matt G. 2002, RSPTA, 360, 2045

Matt G., Braito V., Brusa M. et al. 2003, MmSAIt, 74, 367

Matt G., Bianchi S., De Rosa A. et al. 2006, A&A, 445, 451

Mattson B.J., Weaver K.A. & Reynolds C.S. 2007, ApJ, 664, 101

Merloni A., Malzac J., Fabian A.C. & Ross R.R. 2006, MNRAS, 370, 1699

Miller L., Peacock J.A. & Mead A.R.G. 1990, MNRAS, 244, 207

Mineo T., Fiore F., Laor A. et al. 2000, A&A, 361, 695

Molina M., Bassani L., Malizia A. et al. 2006, MNRAS, 371, 821

Molina M., Giroletti M., Malizia A. et al. 2007, MNRAS, 382, 937

Mukai K., Hellier C., Madejski G. et al. 2003, ApJ, 597, 479

Murray S.S., Chappell J.H., Kenter A.T. et al. 2000, SPIE, 4140, 144

Murphy T., Mauch T., Green A. et al. 2007, MNRAS, 382, 382

Mushotzky R.F., Done C. & Pounds K. 1993, ARA&A, 31, 71

Nandra K. & Pounds K.A. 1994, MNRAS, 268, 405

Narayan R., Mahadevan R. & Quataert E. 1998, in “Theory of black hole accretion disk”ed. Abramowicz M.A., Bjornsson G. & Pringle J., Cambridge University Press, p.148

Ogle P.M., Marshall H.L., Lee J.C. & Canizares C.R. 2000, ApJ, 545, 81

Orr A., Barr P., Guainazzi M. et al. 2001, A&A, 376, 413

Padmanabhan U. & Yaqoob T. 2003, IAUS, 214, 265

Pandey M., Manchanda R.K., Rao A.P. et al. 2006 A&A, 446, 471

Panessa F., Barcons X., Bassani L. et al. 2007, A&A, 467, 519

Panessa F., Bassani L, De Rosa A. et al. 2008, A&A, 483, 151

Parisi P., Masetti N., Landi R. et al. 2008, ATel 1540

Perola G.C., Matt G., Cappi M. et al. 1999, A&A, 351, 937

Perola G. C., Matt G., Fiore F. et al. 2000, A&A, 358, 117

Perola G.C., Matt G., Cappi M. et al. 2002, A&A, 389, 802

Petrucci P.O., Haardt F., Maraschi L. et al. 2000, ApJ, 540, 131

Petrucci P.O., Haardt F., Maraschi L. et al. 2001, ApJ, 556, 716

Petrucci P.O. 2002, in “Proceedings of the 5th Italian AGN meeting”, Como, June 11-14 2002, ed. I. Cagnoni

Piconcelli E., Sánchez-Portal M., Guainazzi M. et al. 2006, A&A, 453, 839

Pier E.A. & Krolik J.H. 1992, ApJ, 401, 99

Piro L. 1999, AN, 320, 236

Pounds K. & Reeves J. 2002, in Proceedings of the Symposium on “New visions of the X-ray Universe in the XMM-Newton and Chandra era”, 26/30-11-2002, ESTEC, The Netherlands

Reeves M.J. & Turner M.J.L. 2000, MNRAS, 316, 234

Revnivtsev M.G., Sunyaev R.A., Gilfanov M.R. et al. 2004a, AstL, 30, 527

Revnivtsev, M., Sazonov S., Jahoda K. & Gilfanov M. 2004b, A&A, 418, 927

Reynolds C.S. 1997, MNRAS, 286, 513

Ribó M., Combi J. A., Mirabel I. F. 2004, ATel 235

Riley J.M., Warner P.J., Rawlings S. et al. 1988, MNRAS, 236, 13

Risaliti G., Maiolino R. & Salvati M. 1999, ApJ, 522, 157

Risaliti G. 2002, A&A, 386, 379

Risaliti G., Elvis M. & Nicastro F. 2002, ApJ, 571, 234

Roming P.W.A., Kennedy T.E., Mason K.O. et al. 2005, SSRV, 120, 95

Rowan-Robinson M. 2001, NewAR, 45, 631

Sako M., Kahn S.M., Behar E. et al. 2001, A&A, 365, 168

Sambruna R.M., Eracleous M., Mushotzky R.F. 1999, ApJ, 526, 60

Sambruna R.M., Reeves J.M. & Braito V. 2007, ApJ, 665, 1030

Schmidt M. 1968, ApJ, 151, 393

Shakura N.I. & Sunyaev R.A. 1973, A&A, 24, 337

Spergel D.N., Verde L., Peiris H.V. et al. 2003, ApJS, 148, 175

Staubert R., Koenig M., Friedrich S. et al. 1994, A&A, 288, 513

Stern B.E., Poutanen J. Svensson R. et al. 1995, ApJ, 449, 13

Strüder L. Briel U., Dennerl K. et al. 2001, A&A, 365, 18

Suganuma M., Yoshii Y., Kobayashi Y. et al. 2006, ApJ, 639, 46

Tanaka Y., Inoue H. & Holt S.S. 1994, PASJ, 46, 37

Terashima Y. & Wilson A.S. 2003, ApJ, 583, 145

Tran H.D. 2001, ApJ, 554, 19

Turner T.J., George I.M., Nandra K.A. & Mushotzky R.F. 1997, ApJ, 488, 164

Turner M.J.L., Abbey A., Arnaud M. et al. 2001, A&A, 365, 27

Tzanetakis A., Spencer R.E., Masson C.R. et al. 1978, MNRAS, 185, 63

Ubertini P., Lebrun F., Di Cocco G. et al. 2003, A&A, 411, 131

Ulrich M.H., Maraschi L. & Urry C.M. 1997, ARA&A, 35, 445

Ulvestad J.S. & Wilson A.S. 1986, MNRAS, 218, 711

Unger V., Nguyen Q.R., Mauron N. et al. 1985, A&A, 146, 123

Urry C.M. & Padovani P. 1995, PASP, 107, 803

Vaughan S. & Fabian A.C. 2004, MNRAS, 348, 1415

Vedrenne G., Roques J.P., Schoenfelder V. et al. 2003, A&A, 411, 63

Vollmer B., Davoust E., Dubois P. et al. 2005, A&A, 436, 757

Weintgartner J.C. & Murray N. 2002, AAS, 201, 4911

Wilkes B.J., Schimdt G.D., Cutri R.M. et al. 2002, ApJ, 569, 1

Winkler C., Courvoisier T., Di Cocco G. et al. 2003, A&A, 411, 49

Winter L.M., Mushotzky R.F., Tueller J. & Markwardt C. 2008, ApJ, 674, 686

Zamfir S., Sulentic J.W. & Marziani P. 2008, MNRAS, 387, 856

Zdziarski A.A., Ghisellini G., George I.M. et al. 1990, ApJ, 363, 1